

DEUTSCHES ELEKTRONEN-SYNCHROTRON
Ein Forschungszentrum der Helmholtz-Gemeinschaft



DESY-THESIS-2017-042
October 2017

Energy-Dependent Proton Damage in Silicon

by

E. M. Donegani

ISSN 1435-8085

NOTKESTRASSE 85 - 22607 HAMBURG

DESY behält sich alle Rechte für den Fall der Schutzrechtserteilung und für die wirtschaftliche Verwertung der in diesem Bericht enthaltenen Informationen vor.

DESY reserves all rights for commercial use of information included in this report, especially in case of filing application for or grant of patents.

To be sure that your reports and preprints are promptly included in the
HEP literature database
send them to (if possible by air mail):

DESY Zentralbibliothek Notkestraße 85 22607 Hamburg Germany	DESY Bibliothek Platanenallee 6 15738 Zeuthen Germany
---	---

ENERGY-DEPENDENT PROTON DAMAGE IN SILICON

Dissertation

zur Erlangung des Doktorgrades
an der Fakultät für Mathematik, Informatik
und Naturwissenschaften
Fachbereich Physik
der Universität Hamburg

vorgelegt von
Elena Maria Donegani
aus Como, Italien

Hamburg
2017

*To Paolo,
Gabriella,
Chiara.*

Gutachter der Dissertation:

Prof. Dr. Erika Garutti
Dr. Eckhart Fretwurst

Zusammensetzung der Prüfungskommission:

Dr. Eckhart Fretwurst
Prof. Dr. Erika Garutti
Prof. Dr. Wolfgang Hansen
Prof. Dr. Daniela Pfannkuche
Prof. Dr. Norbert Wermes

Vorsitzende der Prüfungskommission:

Prof. Dr. Daniela Pfannkuche
29/09/2017

Datum der Disputation:

Vorsitzender Fach-Promotionsausschusses Physik

Prof. Dr. Wolfgang Hansen

Leiter des Fachbereichs Physik:

Prof. Dr. Michael Potthoff

Dekan der Fakultät MIN:

Prof. Dr. Heinrich Graener

Contents

Abstract	vii
Kurzfassung	ix
Introduction	1
I First part - Literature overview	5
1 Fundamentals properties of silicon sensors	7
1.1 Intrinsic silicon	7
1.1.1 Crystal structure	8
1.1.2 Energy bands	10
1.1.3 Intrinsic charge carrier concentrations	13
1.2 Extrinsic silicon	16
1.2.1 Low temperatures	18
1.3 The p ⁺ n-junction as building block	19
1.4 Silicon for particle detection	21
2 Highlights on silicon sensors exposed to proton beams	25
2.1 Milestones in the history of silicon sensors	25
2.2 Silicon sensors in space	27
2.2.1 The space mission PAMELA	27
2.3 Silicon sensors for HEP	31
2.3.1 The CMS Si-tracker for HL-LHC	32
2.4 Silicon sensors for proton therapy	35

2.4.1	pCT: proton imaging with silicon sensors	37
3	Proton-induced bulk damage to Si sensors	43
3.1	Interactions of protons in silicon	43
3.1.1	$E_p < 10$ MeV	44
3.1.2	$E_p > 10$ MeV	44
3.2	Quantification of bulk damage	47
3.2.1	NIEL hypothesis	47
3.2.2	Displacement Per Atoms: DPA	51
3.3	Radiation-induced bulk defects	52
3.3.1	Defects classification	53
3.3.2	SRH carrier statistics	54
3.3.3	Defect occupation under reverse bias	57
3.3.4	Defect occupation under forward bias	58
3.4	Impact of bulk-defects on sensor properties	59
3.4.1	Evolution of bulk-defects with annealing	62
II	Second part - Experimental work	65
4	Investigated silicon samples and experimental methods	67
4.1	Proton irradiations	67
4.1.1	23 MeV protons @ KIT	68
4.1.2	188 MeV protons @ AGOFIRM	68
4.1.3	23 GeV protons @ CERN	69
4.2	Test Structures	70
4.2.1	Geometry and bulk properties	70
4.3	IV measurements	73
4.4	CV(f,T) measurements	74
4.5	Thermally Stimulated Current (TSC) measurements	74
4.5.1	The TSC method	74
4.5.2	The TSC setup	76
4.6	Summary of performed measurements	79
5	“Macroscopic” approach	81
5.1	Results of IV measurements	81
5.1.1	Representative examples of reverse IV	83
5.1.2	$IV(E_{protons})$	85
5.1.3	$I(\phi_{neq})$ dependence at V_{LL}	87
5.1.4	$I(\phi_{neq})$ dependence above total depletion	90
5.1.5	Volume current annealing	92

5.1.6	Representative examples of forward IV	94
5.2	Results of CV measurements	98
5.2.1	Doping profiles before irradiation	98
5.2.2	Annealing and type inversion	99
5.2.3	The initial rise method	102
5.2.4	Analysis of CV(f,T)	102
5.2.5	Capacitance in forward bias	103
6	“Microscopic” approach	109
6.1	TSC measurement settings	109
6.1.1	Filling current	110
6.1.2	Heating rate β	111
6.2	Analysis of TSC spectra ($T_{fill} = 10$ K)	114
6.2.1	Background and leakage current subtraction	114
6.2.2	Defect concentrations	116
6.3	Bulk defects after proton irradiation	120
6.3.1	E(30K): oxygen-dependent IR	124
6.3.2	B_iO_i : boron removal	128
6.3.3	Deep hole-traps	130
6.3.4	The V_n -group	131
6.4	Analysis of TSC spectra (with $T_{fill} > 10$ K)	132
6.5	Impact of defect clusters	137
7	Microscopic vs. Macroscopic	143
7.1	TSC vs. IV	143
7.2	TSC vs. CV (initial rise method)	144
7.3	TSC vs. C(f) at low bias	145
7.4	Simulations vs. Measurements of bulk defects	149
7.4.1	TCAD Input files	149
7.4.2	Simulation of single trap	151
7.4.3	Simulation with a set of bulk defects	156
	Conclusions & outlooks	163
A	List of measured devices	169
B	Density of states	171
C	List of TSC parameters	173
D	List of α values	175

E Error from trapezoidal rule	177
F TCAD steering file	181
List of acronyms	185
Bibliography	189
Acknowledgments	202

Abstract

Non Ionizing Energy Loss (NIEL) in the sensor bulk is a limiting factor for the lifetime of silicon detectors. In this work, the proton-energy dependent bulk-damage is studied in n- and p-type silicon pad diodes. The samples are thin ($200\ \mu\text{m}$ thick), and oxygen enriched (bulk material types: MCz, standard or deep-diffused FZ). Irradiations are performed with 23 MeV, 188 MeV and 23 GeV protons; the 1 MeV neutron equivalent fluence assumes selected values in the range $[0.1, 3] \cdot 10^{14}\ \text{cm}^{-2}$.

In reverse bias, Current-Voltage (IV) and Capacitance-Voltage (CV) measurements are performed to electrically characterise the samples; in forward bias, IV and CV measurements point out the transition from lifetime to relaxation-like semiconductor after irradiation. By means of Thermally Stimulated Current (TSC) measurements, 13 bulk defects have been found after proton irradiation.

Firstly, TSC spectra are analysed to obtain defect concentrations after defect filling at the conventional temperature $T_{fill} = 10\ \text{K}$. Secondly, temperature dependent capture coefficients of bulk defects are explained, according to the multi-phonon process, from the analysis of TSC measurements at higher filling temperatures ($T_{fill} < 130\ \text{K}$). Thirdly, a new method based on the SRH statistics and accounting for cluster-induced shift in activation energy is proposed; it allows to fully characterise bulk defects (in terms of activation energy, concentration and majority capture cross-section) and to distinguish between point- and cluster-like defects.

A correlation is noted between the leakage current and the concentration of three deep defects (namely the V_2 , V_3 and H(220K) defects), for all the investigated bulk materials and types, and after all the considered proton energies and fluences. At least five defects are found to be responsible for the space charge, with positive contributions from the E(30K) and B_iO_i defects, or negative contributions from three deep acceptors H(116K), H(140K) and H(152K).

Kurzfassung

Der nicht ionisierende Energieverlust (NIEL) im Sensorsubstrat ist ein limitierender Faktor für die Lebensdauer von Siliziumdetektoren. In dieser Arbeit werden Kristalldefekte in Abhängigkeit von der Protonenenergie in n- und p-dotierten Flächendioden untersucht. Die Dioden sind dünn ($200\ \mu\text{m}$ dick) und mit Sauerstoff angereichert (Substratmaterial: MCz, Standard oder tief diffundiertes FZ). Die Bestrahlungen wurden mit Protonen von 23 MeV, 188 MeV und 23 GeV mit Teilchenfluenzen (1 MeV Neutronenäquivalent) im Bereich von $[0.1, 3] \cdot 10^{14}\ \text{cm}^{-2}$ durchgeführt.

Zur elektrischen Charakterisierung der Dioden wurden in Sperrrichtung Strom-Spannungs (IV) und Kapazitäts-Spannungs (CV) Messungen durchgeführt; in Durchlassrichtung zeigen IV- und CV-Messungen den Übergang von *lifetime* zu *relaxation*-artigem Halbleiter nach der Bestrahlung.

Mit Hilfe von *Thermally Stimulated Current* (TSC) Messungen wurden nach Protonenbestrahlung 13 Kristalldefekte gefunden.

Zuerst werden TSC-Spektren analysiert, um Defektkonzentrationen nach der Defektfüllung bei der konventionellen Temperatur von $T_{fill} = 10\ \text{K}$ zu erhalten.

Danach werden temperaturabhängige Einfangkoeffizienten von Kristalldefekten nach dem Multi-Phonon-Prozess aus der Analyse von TSC-Messungen bei höheren Fülltemperaturen ($T_{fill} < 130\ \text{K}$) bestimmt. Zuletzt wird eine neue Methode auf Basis der Shockley-Read-Hall-Statistik unter Berücksichtigung der cluster-induzierten Verschiebung der Aktivierungsenergie vorgeschlagen. Sie erlaubt es, Kristalldefekte in Bezug auf Aktivierungsenergie, Konzentration sowie Wirkungsquerschnitte der Majoritätsladungsträger vollständig zu charakterisieren und zwischen punkt- und clusterähnlichen Defekten zu unterscheiden.

Es ist eine Korrelation zwischen dem Leckstrom und der Konzentration von drei tiefen Defekten (dem V_2 , V_3 und H(220K)) für alle untersuchten Substratmateri-

alen und -typen und für alle betrachteten Protonenergien und -fluenzen festgestellt worden. Mindestens fünf Defekte sind für die Raumladung verantwortlich, mit positiven Beiträgen aus den E(30K) und B_iO_i Defekten sowie negativen Beiträgen von drei tiefen Akzeptoren H(116K), H(140K) und H(152K).

Introduction

“Every effect of particles or radiation can be used as a working principle for a particle detector”, was once said by Prof. Dr. Claus Grupen.

The building block of a silicon sensor is: a p-n junction operated in reverse bias. The working principle is: electron-hole pairs creation by ionization or direct excitation; as a result, charge carriers induce a current in the electrodes, as long as they drift in the electric field and reach a biasing contact.

However, it should be kept in mind that there is a price to be paid: intense particle beams strongly affect properties and performance of irradiated particle detectors. This is particularly true for silicon sensors exposed to hadron beams, for which the leakage current is increased, the electric field is severely altered and the efficiency in charge collection is significantly reduced.

In the past, most of the investigations were performed regarding the bulk damage of silicon sensors after electron, photon and neutron irradiations. In particular, data and knowledge of proton-induced bulk-damage in silicon are quite limited, especially in p-type sensors. Therefore, this work investigates the proton-energy dependent damage in n- and p-type silicon pad diodes, after irradiation with protons of 23 MeV, 188 MeV and 23 GeV. The 1 MeV neutron equivalent fluence assumes selected values in the range $[0.1, 3] \cdot 10^{14} \text{ cm}^{-2}$. The silicon pad diodes are 200 μm thick and oxygen enriched (the bulk materials are: MCz, standard or deep-diffused FZ).

Three type of measurements are performed: Current - Voltage (IV(T)) and Capacitance - Voltage (CV(f,T)) measurements in order to electrically characterized the samples; Thermally Stimulated Current (TSC) measurements are performed to characterize the proton-induced bulk defects. In addition, IV and CV measurements under forward bias identify the possible transition from lifetime- to

relaxation-like semiconductor after irradiation.

The thesis work is structured in two parts:

Part I - Literature overview:

Chapter 1 deals with fundamental properties and working principles of silicon sensors which are widely used as particle detectors in many research fields. **Chapter 2** summarizes the history of silicon sensors, and provide representative examples of silicon sensors exposed to proton beams: in space experiments, in High Energy Physics, and for Proton Therapy.

The topic of proton-induced bulk damage in silicon sensors is addressed in **Chapter 3**, summarizing the interactions of protons in silicon according to the proton energy, and quantifying the bulk damage according to the NIEL hypothesis or in terms of DPA units. The statistics of recombination and generation of holes and electrons through defect levels is reviewed according to the Shockley-Read-Hall (SRH) model. The impact of bulk defects on fundamental sensor properties, and their evolution with annealing, is then presented with focus on the leakage current, space charge distribution and charge collection efficiency.

Part II - Experimental results:

Chapter 4 deals with the irradiation conditions with 23 MeV, 188 MeV and 23 GeV protons, with highlights on the newly irradiations performed with 188 MeV protons. The irradiated MCz, standard and deep-diffused FZ pad diodes are studied with three experimental techniques: IV(T)/CV(f,T) and TSC. The corresponding results are described in **Chapter 5** and **Chapter 6**, respectively. Firstly, from IV(T) characteristics in reverse bias it is demonstrated that leakage current is proportional to the neutron equivalent fluence, for all the investigated proton energies, bulk materials, and annealing. Secondly, CV characteristics in reverse bias are analyzed with the new “initial rise method”. In addition, the activation energy of a main deep donor in p-type material is derived from the frequency- and temperature-dependent capacitance characteristics. Type inversion from n- to p-type is noted for deep-diffused FZ after exposure to 23 MeV or 188 MeV protons with fluences of $7 \cdot 10^{13} \text{ cm}^{-2}$. (No deep-diffused FZ diodes are available for the present study). In addition, IV and CV measurements are also performed in forward bias for a physical insight about relaxation-like semiconductors after irradiation: ohmic IV curves at the maximum resistivity, and a negative diffusion capacitance, respectively.

Thirdly, at least 13 bulk defects are detected by means of TSC measurements in all the proton-irradiated samples. The very same bulk defects are found after irradiation with various proton energies, bulk materials and type, a part for the B_iO_i defect which is responsible for the boron removal in p-type sensors. Bulk material, proton energy, fluence and annealing dependences are discussed. Three methods are implemented in Python to analyze TSC spectra:

a) With $T_{fill} = 10 \text{ K}$ and forward injection, i.e. the conventional approach of the

last decades, to calculate defect concentrations;

b) With $T_{fill} = 10$ K and light illumination, with an occupation-dependent activation energy for cluster defects. This new approach to the analysis of TSC spectra is based on the SRH statistics and allows to fully characterize bulk defects (i.e. in terms of activation energy, concentration and majority capture cross-section). Moreover, it allows to distinguish between point- and cluster-like defects;

c) With defect filling at higher temperatures ($10 \text{ K} < T_{fill} < 130 \text{ K}$), and accounting for the temperature-dependent capture coefficients according to the multi-phonon process.

Following the results from chapter 5 and chapter 6, the relation between bulk defects and sensors properties are given in **Chapter 7**:

- From IV vs. TSC measurements, regarding the leakage current;
- From CV (at low frequency and low temperature) vs. TSC measurements, regarding the space charge contributions;
- From $C(f,T)$ at low bias to extract the activation energy of the dominant deep donor in p-type sensors after proton irradiation.

The main defects with impact on the leakage current and the space charge concentration are simulated in TCAD, in order to suggest a set of (six) relevant bulk defects for further development of a radiation damage model based on measured bulk defects.

Part I

Literature overview

Fundamental properties of silicon sensors

Silicon was discovered by the Swedish chemist Jöns Jacob Berzelius in 1824, and since nearly forty years it is the material of choice for a variety of solid state devices and in many different physics fields [1]. About 98% percent of all semiconductor devices are in fact fabricated with silicon, such as integrated circuits, microprocessors and memory chips [2].

This chapter summarizes the fundamental properties of silicon in equilibrium, i.e. when no external forces such as voltage, electric or magnetic fields, nor temperature gradients are applied. Firstly, the case of pure silicon with no impurity atoms nor defects will be described in section 1.1. Secondly, the properties of extrinsic silicon (with specific impurity atoms) will be introduced in section 1.2 in order to understand the basic device structure of silicon sensors (subs. 1.3).

The wide use of silicon as a detection medium is due to its striking performance both for position and energy determination (section 1.4), and highly benefits from the fast development of the technology for integrated circuits [3, 4].

1.1 Intrinsic silicon

This section deals with the basic properties of intrinsic silicon, i.e. a pure single-crystal material with no impurities nor lattice defects (subs. 1.1.1). In crystalline materials, outer-shell atomic levels exhibit an energy band structure (subs. 1.1.2). It is important to note that for an intrinsic semiconductor, the concentration of electrons in the conduction band is equal to the concentration of the holes in the valence band (subs. 1.1.3). The electrical conductivity is entirely dependent on thermally generated carriers. Properties and effects of radiation-induced defects in the crystal lattice will be discussed in chapter 3, since crystal damage is the main concern for the silicon sensor's longevity.

1.1.1 Crystal structure

Silicon is the second most abundant element (after oxygen) in the Earth's crust [5], making up 27% of the lithosphere by mass [6]. Silicon has three stable isotopes (^{28}Si , ^{29}Si and ^{30}Si), with relative abundances of 92.23%, 4.67% and 3.10%, respectively [7]. Silicon naturally occurs in the form of silicon dioxide (quartz), or more complex compounds (silicates). The “pure” silicon element can be industrially produced either in the amorphous or crystalline form, the latter one having a well-structured periodic arrangement of atoms.

The primitive cell of a silicon crystal is shown in fig. 1.1(a): such building block (with cube side $a_0 = 5.431 \text{ \AA}$) can be repeated in all the three dimension to form the overall crystal lattice. Each atom is covalently bonded to four other atoms in a tetrahedral configuration, also known as sp^3 -hybridization, with an angle between the atom bonds of 109.5° . The periodic arrangement of silicon atoms results in two interpenetrating face-centered-cubic (fcc) Bravais lattices, one displaced from the other by a translation of $\frac{a_0}{4}(1, 1, 1)$ along a body diagonal: atoms are located at each corner, at the center of the cube and additionally on each face plane. Such structure can be described with just two basis atoms located at $(0,0,0)$

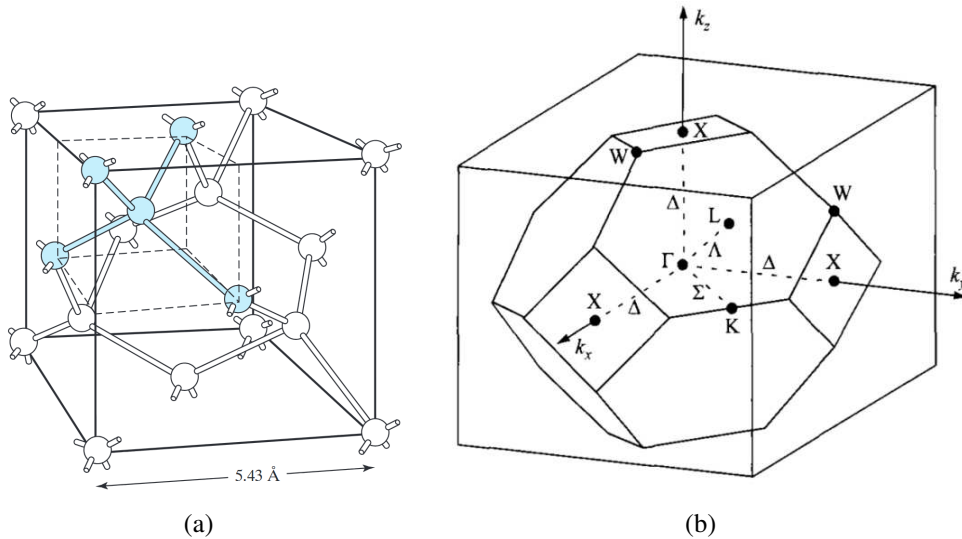


Figure 1.1: Primitive cells in a silicon crystal: (a) the crystallographic unit cell (a cube with edge length $a_0 = 5.431 \text{ \AA}$), and (b) its reciprocal lattice in the momentum space (Wigner-Seitz cell). Figures taken from [8] and [9], respectively.

and at $\frac{a_0}{4}(1, 1, 1)$, and three basis vectors:

$$\mathbf{a}_1 = \frac{a_0}{2} \begin{pmatrix} 0 \\ 1 \\ 1 \end{pmatrix}, \quad \mathbf{a}_2 = \frac{a_0}{2} \begin{pmatrix} 1 \\ 0 \\ 1 \end{pmatrix}, \quad \mathbf{a}_3 = \frac{a_0}{2} \begin{pmatrix} 1 \\ 1 \\ 0 \end{pmatrix}. \quad (1.1)$$

The lattice is invariant under translations involving lattice vectors of the form:

$$\mathbf{R}_{ijk} = i\mathbf{a}_1 + j\mathbf{a}_2 + k\mathbf{a}_3. \quad (1.2)$$

The most important symmetry points and lines are shown in tab. 1.1. In crystallography, the Miller indices are usually exploited to represent a crystal direction $[hkl]$ perpendicular to a crystal plane (hkl) . In fig. 1.2, the three main planes in a cubic crystal are shown. The crystal orientation deeply affects the mechanical, physical, chemical and electronic properties of crystalline materials. The orientation-dependent properties have an impact also on the device fabrication, as summarized in table 1.2. Alternatively, it is possible to visualize a primitive cell in the reciprocal lattice of the momentum space. This is for example the case of the so-called Wigner-Seitz cell, which is obtained by drawing a line from one reference lattice point ($\Gamma = (0, 0, 0)$), depicted in fig. 1.1(b)) to all its nearest neighbors, together with the perpendicular bisector planes for each of the lines. The volume enclosed by these planes is the Wigner-Seitz-cell; for silicon, it has the shape of a truncated octahedron. In the reciprocal space, the unit cell corresponding to the Wigner-Seitz cell is called Brillouin zone (see fig. 1.1(b)).

Point name	Point coordinates	Axis name	Axis coordinates
X	$\frac{2\pi}{a}(\pm 1, 0, 0)$ $\frac{2\pi}{a}(0, \pm 1, 0)$ $\frac{2\pi}{a}(0, 0, \pm 1)$	Δ	$\langle 1, 0, 0 \rangle$
L	$\frac{2\pi}{a}(\pm \frac{1}{2}, \pm \frac{1}{2}, \pm \frac{1}{2})$	Λ	$\langle 1, 1, 1 \rangle$
K	$\frac{2\pi}{a}(\pm \frac{3}{4}, \pm \frac{3}{4}, 0)$ $\frac{2\pi}{a}(0, \pm \frac{3}{4}, \pm \frac{3}{4})$ $\frac{2\pi}{a}(\pm \frac{3}{4}, 0, \pm \frac{3}{4})$	Σ	$\langle 1, 1, 0 \rangle$

Table 1.1: Symmetry axis and points in a Wigner-Seitz cell.

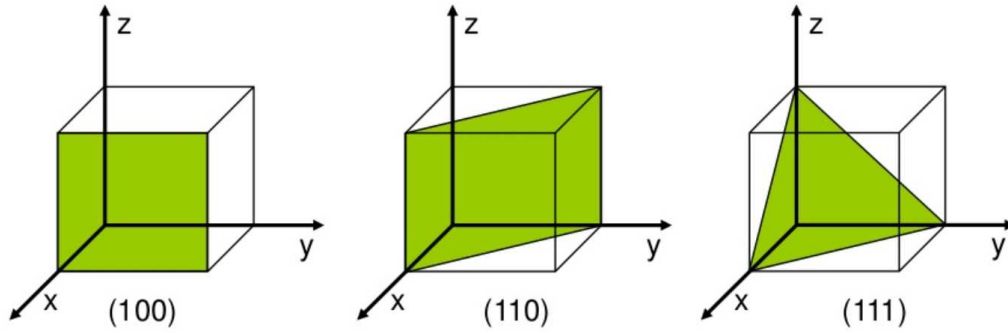


Figure 1.2: Miller indices representative for the three main planes in a cubic crystal: (a) (100), (b) (110), and (c) (111).

Factor	$\langle 100 \rangle$	$\langle 110 \rangle$	$\langle 111 \rangle$
Grown-crystal quality	G	P	E
Growth-rate	E	A	G
Crystal production cost	E	P	E
Mechanical strength	G	G	E

Table 1.2: Practical comparison of silicon wafers with different orientation (E=excellent, G=good, A=acceptable, P=poor). Summarized from [10].

The basis vectors in the reciprocal lattice are obtained from the relation $\mathbf{b}_i \cdot \mathbf{a}_j = 2\pi\delta_{ij}$ as follows:

$$\mathbf{b}_1 = \frac{2\pi}{a_0} \begin{pmatrix} -1 \\ 1 \\ 1 \end{pmatrix}, \quad \mathbf{b}_2 = \frac{2\pi}{a_0} \begin{pmatrix} 1 \\ -1 \\ 1 \end{pmatrix}, \quad \mathbf{b}_3 = \frac{2\pi}{a_0} \begin{pmatrix} 1 \\ 1 \\ -1 \end{pmatrix}. \quad (1.3)$$

General reciprocal lattice vectors can be expressed in the form:

$$\mathbf{G}_{lmn} = l\mathbf{b}_1 + m\mathbf{b}_2 + n\mathbf{b}_3. \quad (1.4)$$

The reciprocal lattice (with just one atom per primitive cell) allows to derive an approximate solution of the Schrödinger equation in a crystal, as if one-electron was in a spherically symmetric crystal potential (see next section 1.1.2).

1.1.2 Energy bands

The spatial periodicity of a lattice is responsible for the establishment of the so-called energy bands. In fact, it is well known that electrons in an isolated atom can only possess discrete energy levels. If many atoms are brought together at

distances comparable to the orbital radius, the wave-functions of the orbiting electrons start to overlap. This overlapping is then responsible for the introduction of hybrid quantized energy levels, which split into two different levels because of the mutual interaction of the two atoms. In crystalline solids, the overall number of split levels can be considered as a quasi-continuum of energy states, better known as a band.

More precisely, the rules of quantum mechanics have to be applied to the case of a periodic crystal. In principle, the full Hamiltonian of the crystal should contain not only the one-electron potentials (for the electrons-atomic nuclei interactions), but also pair potentials (for the electron-electron interactions). In reality, an effective one-electron potential $U(\mathbf{r})$ can be exploited to simplify the case, if all the electrons are assumed to be independent [11]. Therefore, for a lattice-periodic Hamiltonian satisfying the condition $\hat{H}(\mathbf{r} + \mathbf{R}) = \hat{H}(\mathbf{r})$ (for all vectors of the Bravais lattice), the Bloch's theorem provides the one-electron wave function:

$$\Psi_{n\mathbf{k}} = e^{i\mathbf{k}\cdot\mathbf{r}} u_{n\mathbf{k}}(\mathbf{r}), \quad (1.5)$$

where $u_{n\mathbf{k}}(\mathbf{r} + \mathbf{R}) = u_{n\mathbf{k}}(\mathbf{r})$ is a lattice-periodic function. The corresponding energies $E_n(\mathbf{k})$ are continuous function in the Bloch vector \mathbf{k} , for each band index n , and constitute the energy bands. Bloch vectors are restricted to the first Brillouin zone and can also be applied to non-electronic excitations such as phonons.

It is relevant to note that a completely filled band does not contribute to conduction (electrons can not move anywhere else); whereas electrons are free to move in a partially filled band, so that a current flow can be established.

Three types of bands can be outlined:

- *Valence* band, generally made up of occupied molecular orbitals, thus the electrons are tightly bound to the lattice atoms. The highest energy level is called E_V ;
- *Conduction* band, generally made up of empty molecular orbitals, so that electrons are free to move. These electrons actually contribute to the conductivity of the material. The lowest energy level is called E_C ;
- “*Forbidden*” band without energy levels. Since it is localized between the valence and the conduction band, the energy difference is called energy gap ($E_g = E_V - E_C$).

Fig. 1.3 shows the energy bands $E_n(\mathbf{k})$ for silicon which has $E_g = 1.12$ eV at room temperature and under normal atmospheric pressure [9]. In particular, the Γ line points out that the top of the valence band and the bottom of the conduction band do not occur at the same \mathbf{k} . Therefore, in addition to the energy E_g , there must be a transition in the momentum space, i.e. phonon needs to be exchanged with the

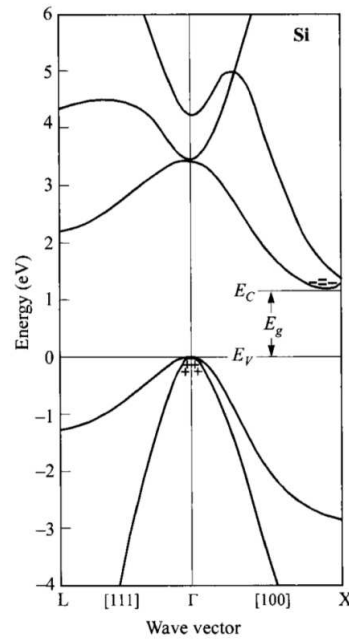


Figure 1.3: Simplified band structure of silicon [9].

lattice to satisfy the \mathbf{k} conservation. For this reason silicon is said to be an *indirect* band gap semiconductor; the dominant recombination process is a transition via localized energy states in the forbidden energy bandgap [9], as it will be described in detail in chapter 3. According to the value of the energy gap E_g ¹, solid-state materials can be classified at least in three different categories:

1. *Insulators* ($E_g > 4$ eV): the valence band is fully occupied and separated from the conduction band by a large energy gap. The thermal energy at 300 K (~ 25 meV) is definitely not enough to excite the electron from the valence to the conduction band;
2. *Conductors* (no E_g): conduction and valence bands overlap, therefore there is no energy gap. Even at low temperatures electrons can be easily excited to the conduction band. Thermally excited electrons can jump into the conduction band thus contributing to a current flow if an electric field is applied;
3. *Semiconductors* ($E_g \sim 1$ eV): at 0 K a semiconductor is primarily an insulator. At room temperature, the valence band is nearly filled, whereas the conduction band is nearly empty. Given the small E_g , even a slight temperature increase or an optical excitation is sufficient to promote electrons from the valence to the conduction band.

¹ E_g is temperature dependent, see subs. 1.2.1.

Section 1.1.3 deals with the properties of intrinsic silicon that is pure silicon with no impurity atoms nor lattice defects, which will be later presented in chapter 3. All the mentioned properties are considered to be independent of time and not affected by any external force (such as voltage, electric field, magnetic field or temperature gradients). The detailed band structure is simplified and grouped into just two distinct bands: the valence and the conduction bands.

1.1.3 Intrinsic charge carrier concentrations

At any temperature above 0 K there is a finite probability that an electron in a semiconductor lattice is promoted to the conduction band, leaving behind a “hole” (positively charged). Electrons and holes are two distinct types of mobile carriers, with opposite electrical charge. Their contributions to the charge flow (i.e. the current) are related to the number of electrons in the conduction band and the number of holes in the valence band, respectively.

The distribution (with respect to energy) of electrons in the conduction band is given by the density of allowed quantum states in the conduction band times the probability $f_F(E)$ that a state is occupied by an electron [12]:

$$n(E) = g_C(E) f_F(E). \quad (1.6)$$

The density of states $g_C(E)$ in the conduction band is:

$$g_C(E) = \frac{m_n^* \sqrt{2m_n^*(E - E_C)}}{\pi^2 \hbar^3} \quad \text{while } E \geq E_C, \quad (1.7)$$

where \hbar the reduced Planck constant ($\hbar = 1.0546 \cdot 10^{-24}$ eV·s) and m_n^* is the “effective mass” of an electron in a crystal. At thermal equilibrium and at the absolute temperature T , the probability that a state with energy E is occupied by an electron can be described with the Fermi-Dirac statistics:

$$f_F(E) = \frac{1}{1 + e^{\frac{E - E_F}{k_B T}}}, \quad (1.8)$$

where k_B is the Boltzmann constant ($k_B = 8.617 \cdot 10^{-5}$ eV/K). The Fermi energy E_F is defined as an energy level that has a probability of 50% of being filled with electrons, notwithstanding the possibility of residing in the forbidden gap.

Likewise, the total number of holes in the valence band is given by the density of allowed quantum states in the valence band multiplied by the probability that a state is not occupied by an electron:

$$p(E) = g_V(E) [1 - f_F(E)], \quad (1.9)$$

with the density of states $g_V(E)$ in the valence band given by:

$$g_V(E) = \frac{m_p^* \sqrt{2m_p^*(E_V - E)}}{\pi^2 \hbar^3} \quad \text{while } E \leq E_V, \quad (1.10)$$

where m_p^* is the effective hole mass.

The Fermi energy does not need to correspond to an allowed energy; in an intrinsic semiconductor at $T > 0$ K, E_F is approximately halfway between E_C and E_V (fig. 1.4). In fact, the thermal energy is sufficient to promote an electron to the conduction band: such creation of electron-hole pairs implies that the number of electrons in the conduction band is equal to the number of holes in the valence band. If the electron and hole effective masses were equal, then $g_c(E)$ and $g_v(E)$ would be symmetrical functions about the midgap energy (the energy midway between E_C and E_V). Therefore, the Fermi energy must be at the midgap energy in order to obtain equal electron and hole concentrations. Since the effective masses of the electrons and hole are not exactly equal, $g_c(E)$ and $g_v(E)$ are not exactly symmetrical about the midgap energy. This is the reason why the Fermi level for an intrinsic semiconductor is slightly shifted from the midgap energy, resulting in equal electron and hole concentrations. The thermal-equilibrium concentration of electrons n_0 may be found by assuming that the Fermi energy remains within the forbidden-energy bandgap and by integrating equation 1.6 over the conduction band energy ²:

$$n_0 = \int_{E_C}^{\infty} g_c(E) f_F(E) dE. \quad (1.11)$$

If $E_C - E_F \gg kT$, then it is also true that $E - E_F \gg kT$ for the electrons in the conduction band ($E > E_C$). The Fermi probability function can be thus reduced to the Maxwell-Boltzmann approximation:

$$f_F(E) = \frac{1}{1 + e^{\frac{E - E_F}{k_B T}}} \approx e^{\frac{[-(E - E_F)]}{kT}}. \quad (1.12)$$

The thermal-equilibrium density of electrons in the conduction band n_0 is now:

$$n_0 = \int_{E_C}^{\infty} \frac{4\pi(2m_n^*)^{3/2}}{h^3} \cdot \sqrt{E - E_C} \cdot e^{\frac{[-(E - E_F)]}{kT}} dE. \quad (1.13)$$

A variable change from T to $\eta = \frac{E - E_C}{kT}$ simplifies the integral calculation to:

$$n_0 = \frac{4\pi(2m_n^* kT)^{3/2}}{h^3} \cdot e^{\frac{[-(E_C - E_F)]}{kT}} \int_0^{\infty} \eta^{1/2} e^{-\eta} d\eta. \quad (1.14)$$

²The upper limit of integration should be the top of the allowed conduction band energy. However, it is correct to replace it with ∞ because the Fermi probability function rapidly approaches zero with increasing energy, as indicated in fig. 1.4.

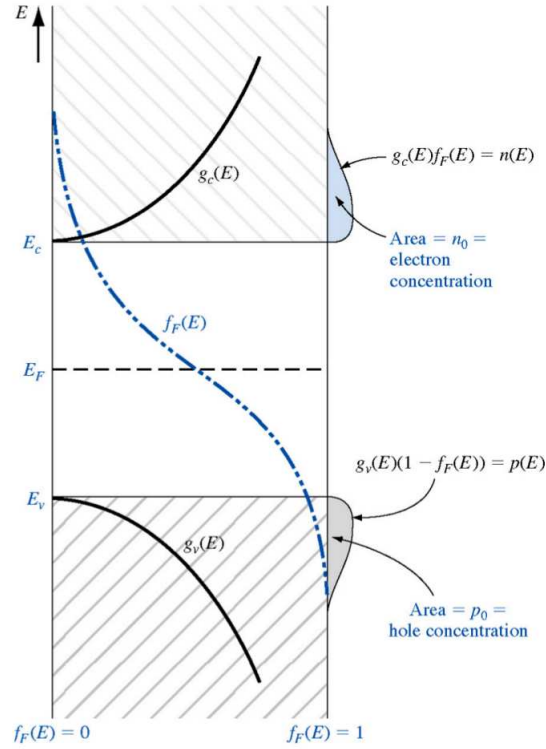


Figure 1.4: Density of states functions, Fermi-Dirac probability function, and electron and hole concentration if E_F is near the midgap energy [13].

Remembering that $\int_0^\infty \eta^{1/2} e^{-\eta} d\eta = \frac{1}{2}\sqrt{\pi}$, the eq. 1.14 becomes:

$$n_0 = 2 \left(\frac{2\pi m_n^* kT}{h^2} \right)^{3/2} e^{\frac{-(E_c - E_F)}{kT}}. \quad (1.15)$$

The thermal-equilibrium electron concentration in the conduction band is usually expressed as:

$$n_0 = N_C e^{\frac{-(E_c - E_F)}{kT}}, \quad (1.16)$$

being N_C the effective density of states function in the conduction band:

$$N_C = 2 \left(\frac{2\pi m_n^* kT}{h^2} \right)^{3/2}. \quad (1.17)$$

Similar calculations can be performed to find out the thermal-equilibrium concentration of holes in the valence band p_0 :

$$p_0 = N_V e^{\frac{-(E_F - E_v)}{kT}}, \quad (1.18)$$

being N_V the effective density of state function in the valence band:

$$N_V = 2 \left(\frac{2\pi m_p^* kT}{h^2} \right)^{3/2}, \quad (1.19)$$

where N_C and N_V are constant for a given semiconductor material at a fixed temperature; they are both of the order of 10^{19} cm^{-3} for silicon at $T=300 \text{ K}$ [12].

The fact that electron and hole concentrations are equal for an intrinsic semiconductor ($n_0 = p_0 = n_i$) can be exploited to calculate the position of the intrinsic Fermi-level E_{Fi} :

$$N_C e^{\frac{-(E_C - E_{Fi})}{kT}} = N_V e^{\frac{-(E_{Fi} - E_V)}{kT}}. \quad (1.20)$$

Taking the natural log of both sides of eq. 1.20 and solving for E_{Fi} provides:

$$E_{Fi} = \frac{1}{2}(E_C + E_V) + \frac{1}{2}kT \ln \left(\frac{N_V}{N_C} \right). \quad (1.21)$$

Alternatively, the definitions of N_C and N_V provide another expression for E_{Fi} :

$$E_{Fi} = \frac{1}{2}(E_C + E_V) + \frac{3}{4}kT \ln \left(\frac{m_p^*}{m_n^*} \right). \quad (1.22)$$

The first term is exactly the midgap energy E_{midgap} . If the electron and hole effective masses were equal, then the intrinsic Fermi level would be exactly in the middle of the bandgap. Since $m_p^* \neq m_n^*$, the intrinsic Fermi level shifts away from the band with the larger density of states.

For the sake of brevity, just a unique intrinsic carrier concentration n_i is usually adopted:

$$n_i^2 = n_0 p_0 = N_C N_V e^{\frac{-(E_C - E_V)}{kT}} = N_C N_V e^{\frac{-E_g}{kT}}. \quad (1.23)$$

Two important conclusions can be drawn: firstly, the intrinsic carrier concentration is strongly dependent on the temperature (doubling about every 11°C); secondly, $n_i \approx 10^{10} \text{ cm}^{-3}$ at $T = 300 \text{ K}$ [9], whereas the volume density of atoms in silicon is roughly of the order of $10^{22} \text{ atoms/m}^3$. This means that only 1 out of 10^{12} silicon atoms is ionized [14].

1.2 Extrinsic silicon

Since the number of thermally generated carriers are generally very small in intrinsic silicon at room temperature, a much larger number can be introduced by replacing a silicon atom with either (see fig. 1.5):

- A *donor*, i.e. a group V element (e.g. phosphorus or arsenic), resulting in more electrons in the conduction band. $E_c - E_d$ is the donor ionization energy;
- An *acceptor* i.e. a group III element (e.g. boron), resulting in extra holes in the valence band. $E_a - E_v$ is the acceptor ionization energy.

Donor impurity atoms “donate” the extra valence electrons to the conduction band, providing excess electrons to the intrinsic semiconductor. These electrons in excess increase in turn the electron carrier concentration of silicon, which is therefore labeled as n-type. Similarly, acceptor impurities “accept” electrons from valence band. The excess of holes increase the hole carrier concentration, which is labeled as p-type. Therefore, four types of charged species in a doped (or extrin-

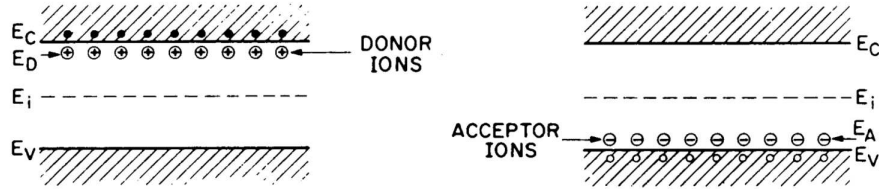


Figure 1.5: Shallow energy levels for (left) n-type silicon with positive ionized donors, and (right) p-type silicon with negative ionized acceptors [15].

sic) semiconductor have to be taken into account: electrons, holes, positive donor ions, and negative acceptor ions. Their densities are represented by the symbols n , p , N_d and N_a , respectively.

In extrinsic silicon the Fermi level has to be adjusted to guarantee the charge neutrality. If the temperature is higher than the ionization temperature of the joint impurities, most of the donors and acceptors are ionized, and the following approximation for the neutrality condition holds [9]:

$$n + N_a = p + N_d. \quad (1.24)$$

It is therefore possible express the concentration of electrons in the conduction band and the concentration of holes in the valence band as follows:

- n-type silicon:
$$\begin{cases} n = \frac{1}{2} \left(N_d - N_a + \sqrt{(N_d - N_a)^2 + 4n_i^2} \right) \\ p = \frac{n_i^2}{n} \approx \frac{n_i^2}{N_d} \end{cases},$$
- p-type silicon:
$$\begin{cases} n = \frac{n_i^2}{p} \approx \frac{n_i^2}{N_a} \\ p = \frac{1}{2} \left(N_a - N_d + \sqrt{(N_a - N_d)^2 + 4n_i^2} \right) \end{cases}.$$

If the number of dopants in silicon are substantially larger than the intrinsic concentration n_i , the position of the Fermi level in extrinsic semiconductor is:

- n-type: $\begin{cases} N_d - N_a \gg n_i \\ N_d \gg N_a \end{cases} \rightarrow n \approx N_d \text{ and } E_C - E_F = k_B T \ln \left(\frac{N_C}{N_d} \right),$
- p-type: $\begin{cases} N_a - N_d \gg n_i \\ N_a \gg N_d \end{cases} \rightarrow p \approx N_a \text{ and } E_F - E_V = k_B T \ln \left(\frac{N_V}{N_a} \right).$

In n-type material, the Fermi level is located in the upper half of the bandgap, whereas in p-type materials it is located in the lower half of the bandgap. It has to be mentioned that a semiconductor can be doped with both donors and acceptors; the resulting free charge carrier concentration is then called effective doping concentration N_{eff} :

$$N_{eff} = N_d^+ - N_a^- . \quad (1.25)$$

The impact of proton irradiation on N_{eff} will be presented in the dedicated theory chapter 3, and the results from measurements of macroscopic sensor parameters will be shown in chapter 5 for Si sensors with various bulk materials.

Nowadays, many different silicon sensors can be produced, but, despite their differences, they all rely on the same basic structure and operating principle: the asymmetric p^+n junction, operated under reverse bias (section 1.3).

1.2.1 Low temperatures

The case of low temperature will be of importance in chapter 6. Let's consider for example the case of n-type bulk material: at very low temperature, most of the donor atoms can be still occupied by electrons, and $E_F > E_d$. This phenomenon is called freeze-out, for all the fifth electrons are bound to the original donor. As a result, the carrier concentration is significantly less than the dopant concentration:

$$n = \left(\frac{N_C N_d}{2} \right)^{1/2} e^{-(E_C - E_d)/2kT} . \quad (1.26)$$

The Fermi level is also dependent on the temperature: fig. 1.6 shows the Fermi level E_F as a function of the absolute temperature T and for different doping concentrations (N_d and N_a for n- and p-type silicon, respectively). At low temperature, the Fermi level is near the band edges of silicon.

In addition, the energy gap E_g of silicon is temperature dependent too, and decreases as the temperature is increased [16]:

$$E_g(T) = E_g(0) - \frac{\alpha \cdot T^2}{T + \beta_g} , \quad (1.27)$$

being $E_g(0) = 1.1602$ eV, $\alpha_g = (4.9 \pm 0.2) \cdot 10^{-4}$ eV/K⁻¹ and $\beta_g = (655 \pm 49)$ K.

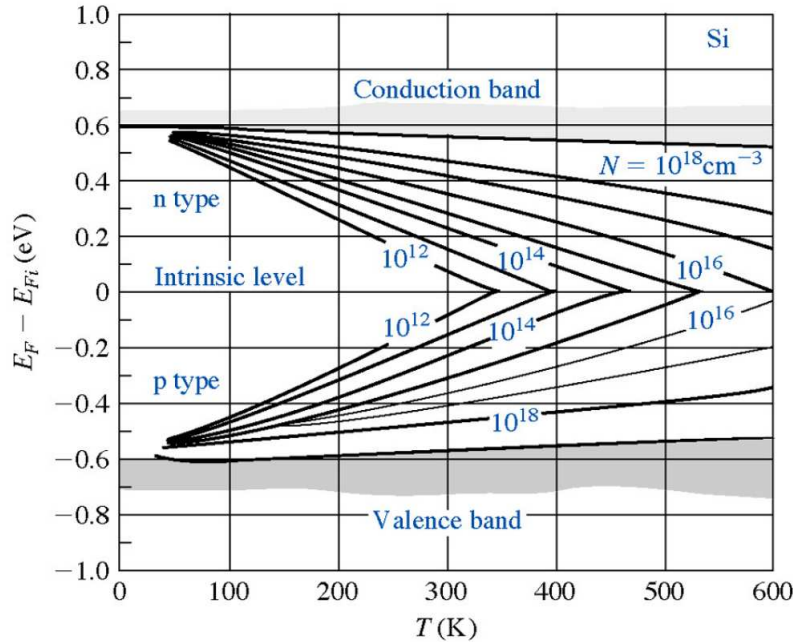


Figure 1.6: Fermi level as a function of temperature and doping [13].

1.3 The p⁺n-junction as building block

Doped semiconductors can be exploited as particle detectors if particles deposit their energy in a carrier-free active volume, and the resulting signal is read out at the edges of such volume. This can be accomplished with a reverse-biased p⁺n-junction (i.e. a single crystal doped with both acceptor and donor atoms).

When a p-type and a n-type semiconductor are joined together, a p⁺n-junction is formed (fig. 1.7(a)). The Fermi level has to be constant all along the junction, so there should be a band bending across the junction to maintain the equilibrium. The bending results from the diffusion of free electrons from the n-type side (where they are “in excess”), to the p-side of the junction, and vice versa for the holes. The migration of carriers creates a potential barrier that contrasts further diffusion of electrons and holes, until a dynamic equilibrium is established. The so-called built-in potential, i.e. the electrostatic potential corresponding to the potential barrier is given by

$$V_{bi} = \frac{kT}{q} \ln \frac{N_A N_D}{n_i^2}, \quad (1.28)$$

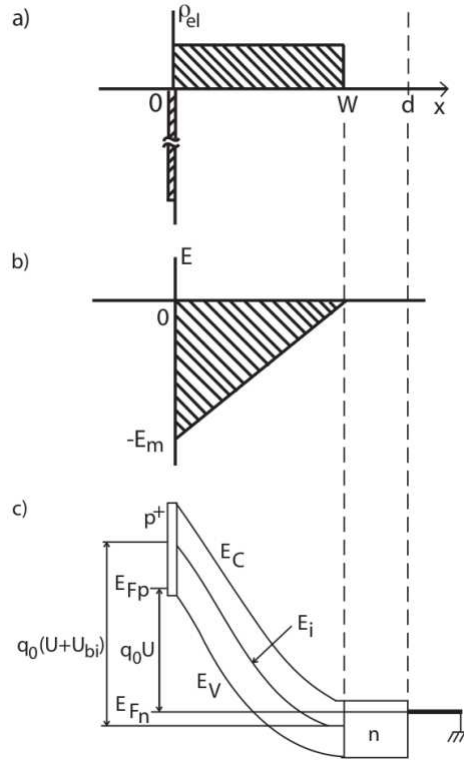


Figure 1.7: Schematic representation of a p^+n junction in the abrupt junction approximation: (a) charge density, (b) electric field strength and (c) electron potential energy [17].

where n_i is the intrinsic carrier density, q is the electronic charge, $N_A(N_D)$ is the acceptor (donor) concentration, respectively. Eq. 1.28 clearly points out that the built-in potential strongly depends on the doping concentration. Typical values of $N_A = 10^{16} \text{ cm}^{-3}$ and $N_D = 10^{12} \text{ cm}^{-3}$ would lead to a $V_{bi} = 0.458 \text{ V}$, so V_{bi} is in the order of few hundreds mV.

A linear electric field (fig. 1.7(b)) distribution is the solution of the Poisson's equation applied to an abrupt³ p^+n junction, under the boundary condition $E(x = W) = 0$:

$$\begin{cases} -\frac{d^2\Phi(x)}{dx^2} = \frac{\rho_{el}}{\epsilon_{Si}\epsilon_0} = \frac{q_0 N_{eff}}{\epsilon_{Si}\epsilon_0} \\ E(x = W) = -\frac{d}{dx}\Phi(x = W) = 0 \end{cases} \rightarrow E(x) = \frac{q_0 N_{eff}}{\epsilon_{Si}\epsilon_0}(x - W), \quad (1.29)$$

where ϵ_0 and ϵ_{Si} are the permittivity of vacuum ($8.854 \cdot 10^{-14} \text{ F/cm}$) and the dielectric constant for silicon (11.9 [9]), respectively. The maximum of the E-field

³ The transition region between the n - and p -type parts is so sharp that the variation in impurity concentration can be considered a single discontinuous change.

occurs at the metallurgical junction. The consequent potential shows a parabolic dependence as a function of the distance x (fig. 1.7(c)):

$$\Phi(x) = -\frac{1}{2} \frac{q_0 N_{eff}}{\epsilon_{Si} \epsilon_0} (x - W)^2, \quad (1.30)$$

where x_n and x_p are the widths of the depletion zone on the n- and p-side, respectively; W is the total width of the depletion region:

$$W = x_p + x_n = \sqrt{\frac{2\epsilon_{Si}\epsilon_0 V_{bi}}{q_0} \cdot \frac{N_a + N_d}{N_a N_d}}. \quad (1.31)$$

Since the expression p^+n junction denotes a higher doping density in the p-side with respect to the n-side ($N_a \gg N_d$), the following approximation can be performed:

$$W \approx x_n \approx \sqrt{\frac{2\epsilon_{Si}\epsilon_0 V_{bi}}{q_0 N_d}}. \quad (1.32)$$

Typical values for $N_a = 10^{16} \text{ cm}^{-3}$, $N_d = 10^{12} \text{ cm}^{-3}$ and $V_{bi} = 500 \text{ mV}$ would imply that W is only $25 \mu\text{m}$ [18]. Such thickness can be increased by applying an external reverse bias V_{ext} (of the same sign of V_{bi}):

$$\begin{cases} \Phi(x) = -\frac{1}{2} \frac{q_0 N_{eff}}{\epsilon_{Si} \epsilon_0} (x - W)^2 \\ \Phi(x = 0) = V_{bi} + V_{ext} \end{cases} \rightarrow W(V_{ext}) = \sqrt{\frac{2\epsilon_{Si}\epsilon_0}{q_0 |N_{eff}|} \cdot (V_{bi} + V_{ext})}. \quad (1.33)$$

A typical value for N_{eff} in the order of 10^{12} cm^{-3} would lead to a more useful depletion thickness of hundreds of μm for the n-side, by applying an external voltage of $V_{ext} = 100 \text{ V}$ [18].

The usefulness of the p^+n junction will become clear for the various silicon sensors presented in chapter 2; moreover, in chapter 4 the basic principles will be applied in order to derive two main physical quantities generally measured for understanding device and material characteristics: the junction current and capacitance (see section 3.4).

The present chapter ends with subs. 1.4, featuring the most important advantages of extrinsic silicon for particle detection.

1.4 Silicon for particle detection

In many different physics fields, several features make extrinsic silicon a useful material for particle detection:

1. The small energy band gap (1.12 eV at T=300 K), which allows MIPs⁴ to produce a large number of charge carriers $N_{e,h}$. The typical signal charge is 3.5 fC (22000 electrons) for MIPs traversing 300 μm of silicon;
2. The moderate band gap with respect to the thermal energy at room temperature (25.9 meV) allows operation at room temperature; therefore cooling is only necessary in ultra-low noise applications [19];
3. The high intrinsic energy resolution $\frac{\Delta E}{E}$:

$$\frac{\Delta E}{E} = 2.35 \sqrt{\frac{Fw}{E}}, \quad (1.34)$$

where E is the energy of the impinging particle, F the Fano factor (0.1 for silicon). The average energy w required to create an electron-hole pair is just 3.6 eV for silicon, whereas ≈ 30 eV or even ≈ 300 eV are necessary for most of the gaseous detectors and scintillators, respectively;

4. The possibility of achieving high position resolution (below 10 μm), by segmenting a p^+n junction into many small regions;
5. The high charge mobility that enables fast collection times (of typically 10-20 ns for 300 μm thick sensors [20]);
6. The good mechanical stability and at the same time the low Z number, a characteristic especially important for tracking sensors, where multiple scattering has to be minimized;
7. The possibility of growing Si-based layers (e.g. SiO_2 and Si_2N_3) for surface passivation;
8. The possible integration with readout electronics given the identical material involved;
9. The large scale availability at relatively low cost.

The use of fully depleted sensors based on the p^+n junctions as described in section 1.3 is probably one of the most common, mainly thanks to the favorable detection efficiency and the high sensitivity to MIPs. Furthermore, such device structure (replicated in linear arrays or in two-dimensional matrices of p^+n junctions) requires a relatively small number of processing steps and guarantees the

⁴ A Minimum Ionizing Particle is a particle whose average energy loss rate in matter is close to the minimum.

high quality of the final product. To measure the position of the incident particle, the area of the p^+ region is usually segmented into many small regions (strip or pixel) which are separately read out. The position resolution depends on the strip spacing and the read-out method. As long as only digital information is used (taking the center position of the strip as the measured coordinate)⁵, the position resolution can be calculated starting from:

$$\langle \Delta x^2 \rangle = \frac{1}{p} \int_{-p/2}^{p/2} x^2 dx = \frac{p^2}{12}, \quad (1.35)$$

where p is the strip pitch. This means that the root-mean-square deviation from the true coordinate is:

$$\sigma_x = \sqrt{\langle \Delta x^2 \rangle} = \frac{p}{\sqrt{12}}. \quad (1.36)$$

Substantial improvements can be reached with analog readout, collecting charges on more than one strip. The coordinate is found by interpolation, e.g. by the center-of-gravity method. The expected resolution would then becomes:

$$\sigma_x \approx \frac{p}{SNR}, \quad (1.37)$$

with SNR being the signal-to-noise ration of the system.

The alternative readout of the backside n^+ contact electrode (as sketched in the bottom part of fig. 1.8), or another junction type like n^+p might be an option in harsh radiation environments, where the issue of type inversion (from n - to p -type) arises after irradiation. Besides type inversion, trapping of charge carriers by radiation-induced defects is an additional issue. Hence, different choices for the bulk material are provided as representative examples in chapter 2. The impact of harsh radiation environments on the bulk properties and the sensor performance will be then addressed in chapter 3.

⁵If effects of track inclination and charge diffusion are neglected.

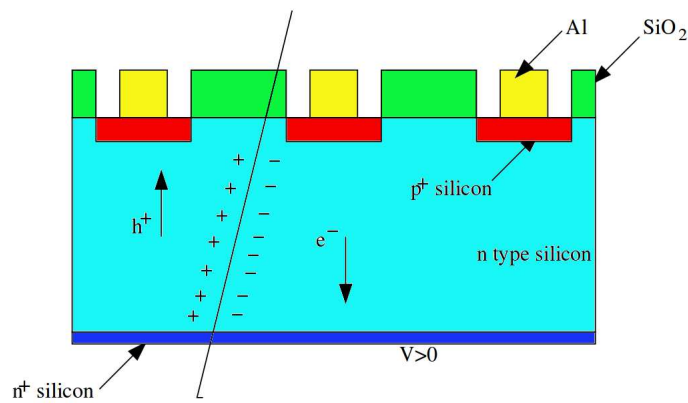


Figure 1.8: Typical layout of an AC coupled microstrip silicon detector (with n-type bulk). Electron-hole pairs from the ionization of a crossing charged particle, drift to the electrodes on the sensor planes in the presence of an electric field. Holes are collected by the p⁺ strips, which are capacitively coupled to aluminum readout strips. The intrinsic signal is shaped and amplified in the subsequent readout electronics.

Highlights on silicon sensors exposed to proton beams

Section 2.1 briefly summarizes the development of high position resolution silicon detectors since the 1980s. After nearly four decades, there exist numerous types of silicon sensors that are “variations on the original theme” to accomplish the required position resolution, energy scale, time structure and signal. Silicon detectors have found use in many fields of physical research, starting from investigations at the very large scale ($\geq 10^{28}$ m) of the Universe [21]. The PAMELA satellite was chosen as a representative application of double sided silicon sensors in space (section 2.2). On the other extreme ($\leq 10^{-20}$ m), silicon sensors are at the heart of many particle physics experiments; the CMS detector is the largest largest silicon detector built so far, and it was chosen as an example involving hybrid pixel sensors (section 2.3).

Many other research fields are benefiting from silicon sensors originally developed for nuclear physics and later especially for High Energy Physics (HEP): mechanical engineering, crystallography and medicine to name a few. In section 2.4, the promising application of microstrip silicon sensors for proton Computed Tomography is mentioned, which represents the “ultimate aspiration for radiotherapy” [22]. Details are provided in the bibliography section; here the focus is on the very silicon bulk and the proton field involved.

2.1 Milestones in the history of silicon sensors

In many different physics fields, ranging from high energy physics (HEP) to astroparticle physics, tracking particle trajectories plays a fundamental role. In fact, all the information regarding e.g. the production point, the flight direction, the particle momentum (or the charge sign of the particle in the presence of a magnetic

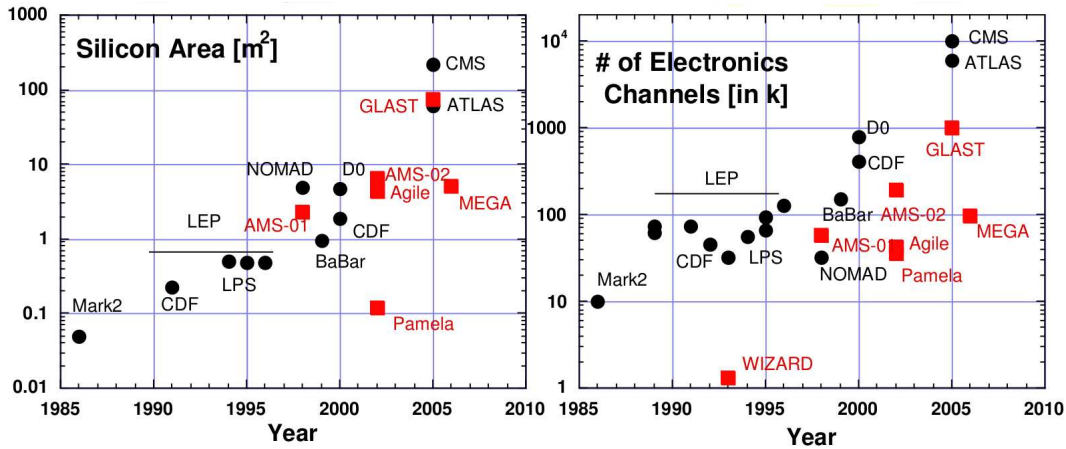


Figure 2.1: Main HEP (black circles) and space experiments (red squares) involving silicon sensors, showing the exponential growth of (a) the silicon area and (b) the number of electronics channel as a function of time [21].

field) can be deduced from the accurate reconstruction of the particle trajectory. Before the application of silicon detectors, typical tracking detectors were either bubble chambers (in use until about 1984) or Multi-Wire Proportional Chambers (MWPC, invented in 1968). However, bubble chambers had long dead-time (of $\approx 1/20$ s), and required time-consuming work by eye of “scanning (wo)men”. The MWPCs were the first “electronic” detectors in the sense that the reconstruction of tracks was performed by a computer, but resolution of about $100 \mu\text{m}$.

In the early 1970s, the formulation of the Standard Model (SM) of particle physics was finalized, predicting three generations of quarks and leptons [23],[24]. In particular, particles containing heavy quarks were expected to decay quickly: B-mesons (containing b-quarks) have lifetimes τ_b of ≈ 1.6 ps, and D-mesons (containing c-quarks) have lifetimes τ_c even shorter than 1 ps. The theoretical expectations were indeed challenging for that time, given the fact that a lifetime in the order of 0.1 ps implies a flight path of only few tenths of μm ($c\tau_c = 30 \mu\text{m}$). No sensor technology could yield such demanding position-resolution, particle-separation and short dead-time.

The turning point in the history of position-sensitive detectors dates back to the early 1980s, with the invention of the planar technology for the production of silicon detectors [25]. Such technique allows the segmentation of a side of the p^+n junction. Signals from such “segments” can be exploited to determine the position of the particle hit. The improvement from “macro-segments” to microstrips was straightforward, and devoted to precise tracking and vertex reconstruction.

The crucial role of silicon sensors in many relevant space missions (section 2.2) and High Energy Physics experiments (HEP, section 2.3) is impressively summa-

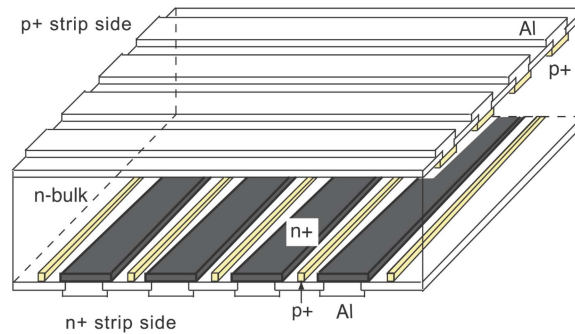


Figure 2.2: Cross-sectional view of a DSSD. Each high resistivity n-type silicon detector is segmented into microstrips on both sides: p^+ strips on the junction side (x-view), and n^+ strips on the ohmic side (y-view). Each n^+ strip is surrounded by a floating p^+ implantation to be isolated from adjacent strips. Aluminum electrodes are directly coupled on each strip with ohmic contacts [28].

rized in fig. 2.1. Both the detector area and the number of electronics channels involved have been following an exponential growth during nearly three decades, according to a version of Moore's law [3]. It is worth noticing that space telescopes such as AMS-02 (to investigate antimatter in cosmic rays and dark matter) and GLAST (for gamma-ray astronomy) are now instrumented with as much Si-area as in accelerator-based experiments.

2.2 Silicon sensors in space

In 1987, silicon strip detectors have been proposed for space experiments [26]. The replacement of gaseous detectors with silicon strip detectors indeed prolonged the lifetime of space missions, while shortening dead times (from ms to μ s) for better investigation of transient astronomical events. For instance, the AGILE Gamma-ray Imaging Detector (GRID) was characterized by a trigger based exclusively on silicon detectors and the shortest ever dead time for gamma-rays detection ($\leq 200 \mu$ s) [27].

2.2.1 The space mission PAMELA

Here we briefly outline the case of PAMELA [29], which represents a mirable synthesis for typical Si-sensors in satellite-born experiments:

- A 0.43 T permanent *magnet spectrometer*, equipped with six planes of *Double-Sided Silicon Detectors* (DSSD, fig. 2.2), providing two indepen-

dent impact coordinates from a single plane, minimizing the multiple scattering while maximizing the spatial resolution: $(3.0 \pm 0.1) \mu\text{m}$ in the x view while $(11.5 \pm 0.6) \mu\text{m}$ in the y view. The particle charge and rigidity¹ up to 1.2 TV/c can be measured;

- A Si/W sampling *electromagnetic calorimeter* (ECAL), with 22 pairs of *single-sided silicon sensor* planes ($380 \mu\text{m}$ thick) interleaved with 22 planes of tungsten absorber plates ($16.3X_0$). Two consecutive Si-layers are orthogonal, therefore 2D spatial information is achieved. An imaging calorimeter distinguishes electrons and protons from their corresponding antiparticles (see fig. 2.3), with a separation factor of the order of 10^5 and 90% efficiency in selecting electrons and positrons above 10 GeV/c.

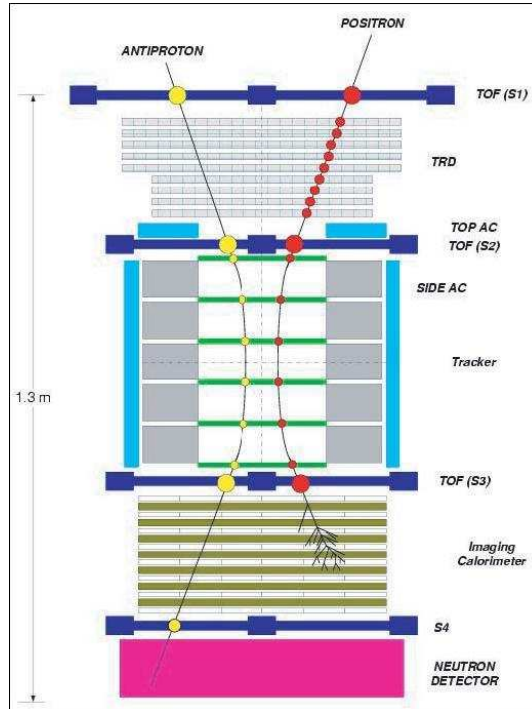


Figure 2.3: Working principle of PAMELA: a Time Of Flight (TOF) apparatus for the trigger signal, a magnetic spectrometer with anti-coincidence shield, and the ECAL. In the bottom part, the scintillator plane (S4) and a neutron detector provide information for not fully contained showers. The apparatus is 1.3 m high, has a mass of 470 kg and an average power consumption of 355 W [30].

¹The rigidity of a particle is defined as $R = cp/Ze$, where p is the momentum, c the light speed, Z the absolute charge and e the electron charge. The magnetic spectrometer actually measures the deflection of the particle, which is defined as R^{-1} .

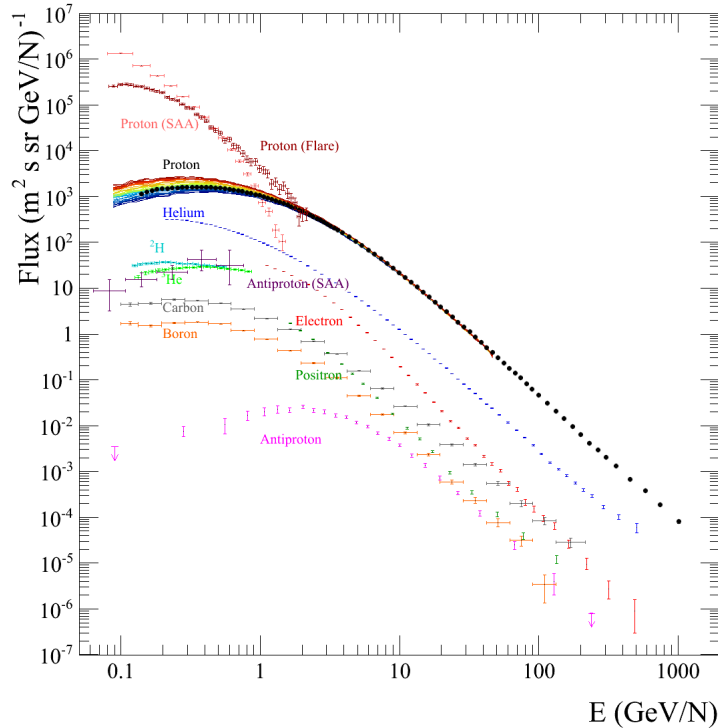


Figure 2.4: Fluxes of different particle species measured by PAMELA [32].

The PAMELA's legacy regarding the physics of cosmic rays (origin, components, acceleration and propagation) can be found in [31]. Hereby the focus will be restricted to the proton component in the space radiation environment (see fig. 2.4). First of all, the Galactic Cosmic Ray (GCR) background radiation permeates the interplanetary space and approximately consists of 85% protons, 14% helium, and 1% heavier particles. Additionally, solar Particle Events (SPE) from fast coronal mass ejections can occasionally cause much larger fluxes of particles, and especially high energy protons. Peak flux during an SPE may be two or five orders of magnitude greater than the background, within hours of the event onset. Periods of enhanced flux may last for days, with successive peaks due to multiple events and enhancements during shock passage. Satellites can be exposed to fluxes of particles (with $E > 10$ MeV) up to $4 \cdot 10^4$ protons/cm²/sec/ster. The spectra of remarkably large proton events are shown in fig. 2.5; in all cases, a steep decline is present up to few hundreds of MeV proton energy [33].

Lower energy protons can be captured by the Earth's magnetic field and trapped into the pole-to-pole Van Allen belts. In particular, there is a region off the Brazil coast where the radiation belts are closest to the Earth's surface: the South At-

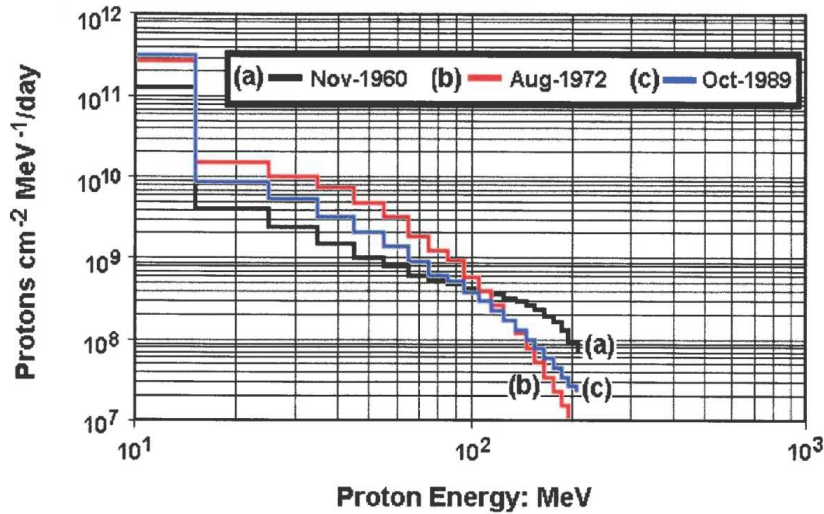


Figure 2.5: Typical spectra during three extremely large solar proton events [33].

lantic Anomaly (SAA). In the SAA, the flux of protons can be up to 30 times higher than at the equator [34]. The trapped radiation belts are not static [33]: their altitude distribution and intensity are greatly dependent on solar activity and prone to hourly, daily and seasonal changes. In addition, the magnetic field of the Earth changes and may reverse itself in the course of geological times. Significant proton fluxes with energies of hundreds of MeV are usually measured, as quantified in the previously mentioned fig. 2.4.

Besides low energy protons, it is worth mentioning the recent discovery of PeV protons by the High Energy Stereoscopic System (HESS) [35]. The most likely source is the supermassive black hole Sagittarius A* at the center of the the Milky Way.

We conclude that device degradation in space is inevitable because of ionization and displacement damage, but the actual issues arise from single-event effects (SEEs, reversing the logic state of a memory element) or single event latch-up (SEL, with dangerous high currents from intense charge trails). During passage through the SAA, SEEs create such a high background that sensors are unusable. Out in space, satellites are vulnerable too: protons degrade solar panel efficiency, onboard electronic circuitry and increase the noise in star-tracking systems.

However, it is worth noticing that radiation damage to silicon detectors and read-out chips in space is not a concern as it is actually for the accelerator-based experiments such as at Tevatron or at LHC [34]. For instance, the total dose after the 5 year GLAST mission is expected to be 10 Gy [36]. An actual challenging radiation environment (with higher fluxes of more energetic protons) is the case of CMS (section 2.3.1).

2.3 Silicon sensors for HEP

In the case of HEP experiments, the use of silicon for tracking was pioneered by the NA-11 group at CERN [37], for tagging heavy flavor c-quarks, and measuring lifetimes and masses of charm mesons (D^0 , D^\pm and D_s^\pm). NA-11 employed 8 silicon detectors for a total active area of 24 cm^2 with 1200 strips (providing a resolution of $4.5 \mu\text{m}$) [38]. On one hand, the small dimension of the active area was remarkable, but on the other hand the ratio between the detector surface to the nearby electronics surface was 1:300. It was clear that the miniaturization of the read-out components was the only way for larger-scale systems. Such compactness was achieved thanks to the Very-Large-Scale Integration (VLSI) electronics, directly coupled to the strips with wire bonding [39]. VLSI chips had typically up to 128 readout channels, with integrated pre-amplifier, shaper, pipeline and multiplexer. One of the first application of the VLSI advancement is the Mark-II experiment at SLC [40, 41], for the measurement of the B-meson lifetime. Small silicon detectors (up to three layers) were dedicated to the vertexing, while outer gaseous detectors were meant for tracking.

Meanwhile in Europe, all four experiments at the Large Electron Positron collider (LEP) at CERN included silicon vertex detectors. The scientific goals were the lifetime measurements and identification of c-quarks, b-quarks, and the tau-lepton.

The use of stand-alone tracking with silicon sensors began during the second run of the CDF detector at Tevatron [42, 43], for the discovery of the top quark. This was the first time ever that a silicon detector was used at a hadron collider, with unprecedented high collision rates, large number of tracks and radiation damage for sensors and readout chips.

After many decades of R&D, silicon sensors are still placed at the heart of many collider experiments around the world. The history of silicon sensors culminates with the four main experiments of the Large Hadron Collider (LHC), at the European Organization for Nuclear Research (CERN). The storage ring has a circumference of 26.7 km, hosting two separate proton-proton (or Pb-Pb ion) beams.

The LHC was designed for a center-of-mass energy of $\sqrt{s} = 14 \text{ TeV}$ and a proton-proton luminosity $L = 10^{34} \text{ cm}^{-2}\text{s}^{-1}$. Four main detectors are located at specific interaction points: ALICE [44] is investigating the quark-gluon plasma produced in heavy ion collisions, while LHCb [45] is probing the current knowledge of the SM through precise measurement of CP violation in b-hadrons and other rare decays. ATLAS [46] and CMS [47] are multi-purpose detectors to study proton-proton, proton-lead and lead-lead collisions at the TeV scale. The Compact Muon Solenoid experiment (CMS, section 2.3.1) tests the SM at the TeV scale and searches for physics beyond the SM; moreover, it thoroughly studies the electroweak symmetry breaking and the top quark. With an active silicon area

$p_T < 100$ GeV/c in the barrel region.

A right-handed coordinate system has been chosen in CMS, with the x-axis pointing to the center of the LHC ring, the y-axis pointing up, the z-axis pointing in the beam direction (counter-clockwise). The pseudorapidity η is defined as:

$$\eta = -\ln \left[\tan \left(\frac{\theta}{2} \right) \right], \quad (2.3)$$

with the polar angle θ measured with respect to the z-axis. The CMS tracking system is designed to reconstruct high- p_T muons, isolated electrons and charged hadrons with high momentum resolution and an efficiency better than 98% in the range $|\eta| < 2.5$. The CMS experiment [47, 49] has a silicon-only cylindrical tracker (fig. 2.6), which relies on silicon pixels for vertexing and track seeding, and outer strips for tracking at larger level arm:

1. The Pixel Tracker comes with a barrel section (three layers of open-ended cylindrical parts, at 4.4, 7.3 and 10.2 cm distance from the beam axis) and end-caps (two disks at each end of the barrel section). The total silicon area is about 1 m², with 66 million readout channels. The pixels are n⁺-in-n oxygenated <111> silicon substrate ($\rho \approx 2\text{k}\Omega\text{cm}$). Each pixel is bump bonded to read out chips (ROCs) [50]. The pixel dimensions are: 100 μm in the r- ϕ direction, 150 μm in the z direction, and 285 μm in thickness. The vertex resolution is 10 μm in each spatial direction with analog readout [51]. The tracker is a key-element for discriminating between primary and secondary vertices; this is especially relevant for b- and τ -tagging;
2. The Silicon Strip Tracker (SST, distant up to 116 cm from the beam axis) surrounds the pixel detector. The SST is composed of p⁺-n strip sensors, with variable strip pitch (from 80 to 183 μm , according to the different hit rates in the various tracker components). In total, the SST silicon area is 206 m² with 9.5 million readout channels. The SST measures the momentum of the charged particles resulting from the collisions. The resolution in p_T is 2.8% for muons with $p_T = 100$ GeV/c.

After a full operation period of 10 years at $L = 10^{34} \text{ cm}^{-2}\text{s}^{-1}$, the inner and outer strip tracker are exposed to integrated fluences ϕ_{neq} of 10^{14} and 10^{13} cm^{-2} , respectively. The pixel detector are subjected to $\phi_{neq} = 3 \times 10^{14} \text{ cm}^{-2}$ per year [53]. The choice of sensor type and layer number results from a trade-off between tracking efficiency, material budget, cost and radiation hardness:

- On one hand, the more layers the easier is the track reconstruction; on the other hand, the more material the bigger is the multiple scattering;

- Small pixels are mandatory in the innermost tracker for unambiguous hit recognition and 3D vertex reconstruction;
- n-on-n pixels (with the p^+n junction on the back side) were chosen for three main reasons [51]: the higher mobility of electrons, the still high signal charge at moderated bias voltage (<600 V) even after high hadron fluences, and the possibility of implementing a guard ring scheme in the back side (keeping all sensor edges at ground potential);
- The n-type bulk of silicon strip sensors undergoes type inversion within the radiation environment of LHC. A possible strategy to delay type inversion is by starting from relatively low resistivity silicon. In addition, the CMS tracker is operated at $T=263$ K (to minimize reverse annealing) and warmed up during maintenance period (to exploit beneficial annealing);
- Surface degradation was minimized by the use of $\langle 100 \rangle$ oriented silicon wafers with fewer dangling bonds than standard $\langle 111 \rangle$ silicon.

Several upgrades are scheduled for the coming years, including the High Luminosity HL-LHC in 2025 (see summary in table 2.1). It is expected that the HL-LHC will reach hadron fluences up to 10^{16} neq·cm⁻² (after 10 years of operation at the integrated luminosity of 3000 fb⁻¹, see fig. 2.8(a)). This implies an increased occupancy, higher pile-up (140 overlapping events for a bunch-crossing interval of 25 ns) and unprecedented radiation levels. For instance, a radiation dose of 10 MGy is expected for the first new pixel layer located at about 3 cm from the beam.

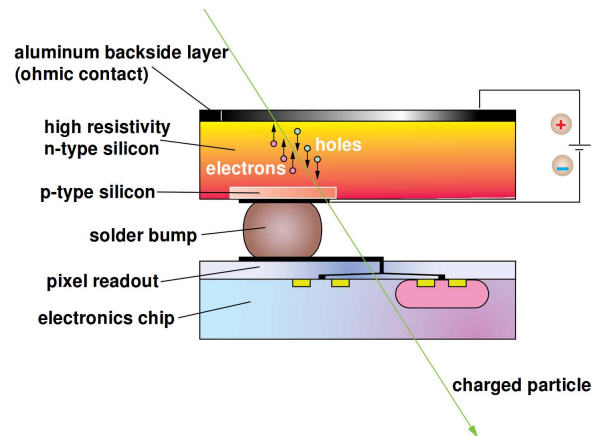


Figure 2.7: Hybrid pixel detector [52]: (top) the sensitive volume (formed by a fully depleted high resistivity silicon substrate), (middle) the solder bump, connected to the readout electronics (bottom).

CMS Phase	Pixel size	Sensor type	Radiation
Phase 0 (initial)	$(100 \times 150) \mu\text{m}^2$	2D, 300 μm	0.15 MGy, $L=150 \text{ fb}^{-1}$ ($R=42 \text{ mm}$)
Phase I (2016/17)	$(100 \times 150) \mu\text{m}^2$	2D, 300 μm	1.2 MGy, $L=500 \text{ fb}^{-1}$ ($R=29 \text{ mm}$)
Phase II (2025)	$(50 \times 50), (25 \times 100) \mu\text{m}^2$	2D/3D, thinner	$\approx 10 \text{ MGy}$, $L=3000 \text{ fb}^{-1}$ ($R=30 \text{ mm}$)

Table 2.1: The planned CMS tracker updates, summarized from [54].

The energy spectra of protons, neutrons and pions expected in the HL-LHC were simulated by the CMS BCRM group (fig. 2.8(b)-2.8(e)). Most of the protons have an energy in the range 0.01–10 GeV. The more the distance from the interaction point, the higher the proton energy, which can be up to $\approx 20 \text{ GeV}$.

Since the current tracker cannot work in such radiation environment, new silicon materials, readout chip and sensor designs were investigated in the framework of LHC and particularly RD50. Together with the ATLAS collaboration it has been established a common R&D effort for the development of readout chip in the 65 nm CMOS technology, for replacing the not sufficiently radiation tolerant $0.25 \mu\text{m}$ chips [54] and to withstand a dose of $\approx 10 \text{ MGy}$ at a hit rate of 2 GHz/cm^2 . The CMS collaboration has been leading two R&D programs on thin n-on-p planar and 3D silicon sensors². In chapter 4, various $200 \mu\text{m}$ thick silicon sensors will be described, while the results of macroscopic and microscopic investigations will be provided in chapter 5 and chapter 6, respectively.

It is noteworthy that the very same silicon detectors meeting the LHC challenges can be tailored for special applications in a wide range of scientific and industrial applications as well. One of the areas to benefit most has been medical physics; in the section 2.4, the focus will be on promising silicon sensors for better assuring patient safety and efficacy of proton therapy treatments.

2.4 Silicon sensors for proton therapy

Any new technology to be implemented for radiotherapy treatments is expected to: speed up and simplify commissioning of new radiotherapy facilities, and accomplish more comprehensive Quality Assurance (QA). During the treatment itself, it should reduce the uncertainties on beam characteristics (e.g. energy and profile),

²3D sensor with column-like electrodes might be an option in view of minimizing trapping of charge carriers by radiation-induced bulk defects. In fact, a decreased electrode spacing would reduce the trapping probability. 3D sensors can be operated at low voltages, but the high channel capacitances are the main disadvantage.

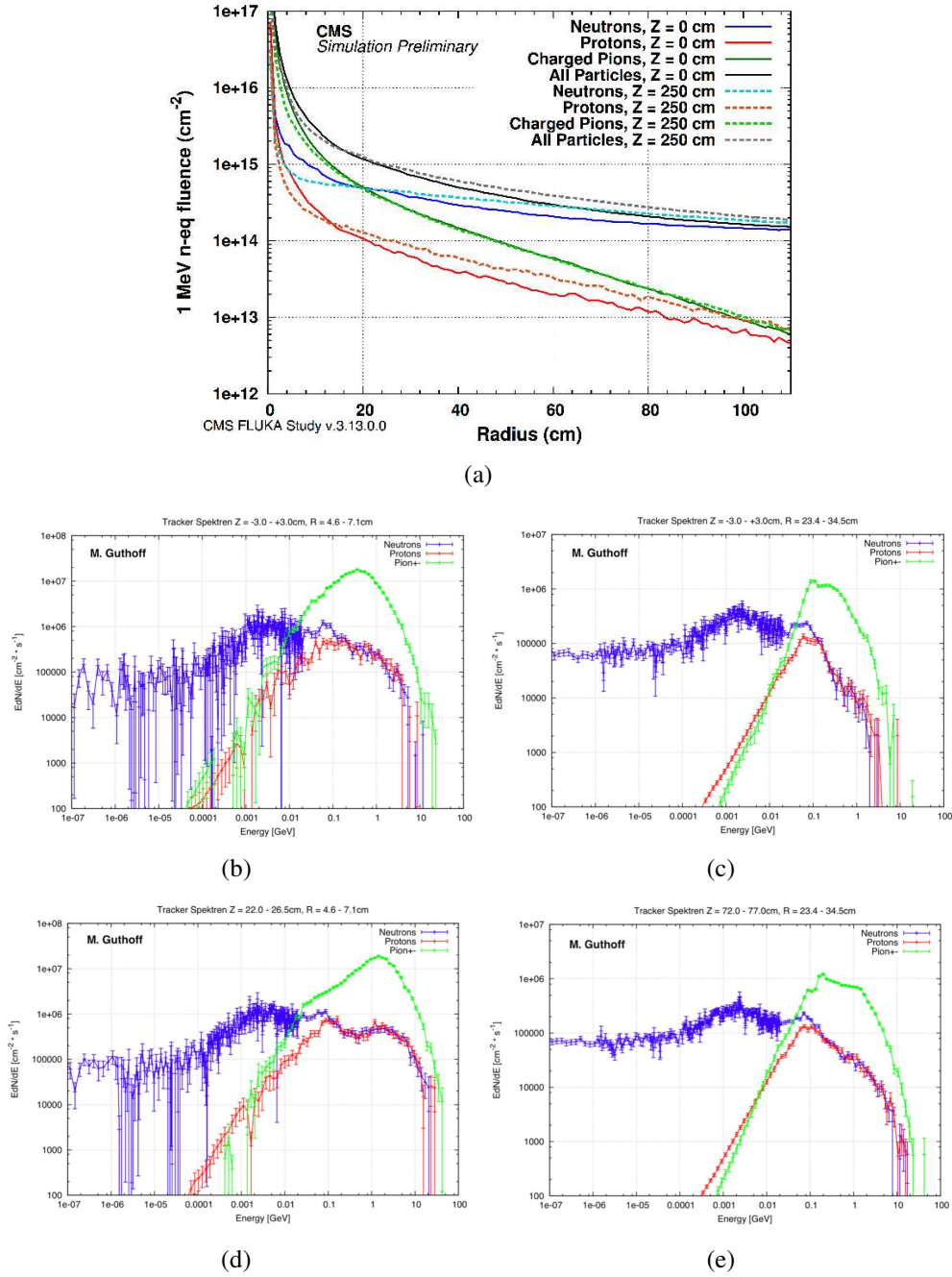


Figure 2.8: FLUKA simulated (a) 1 MeV neq fluence in the CMS tracker, after primary p-p collisions at 7 TeV per beam, for an integrated luminosity of 3000 fb^{-1} [55]. Bottom four plots: energy spectra for neutrons, pions, and protons in the CMS (b)–(c) pixel tracker, and (d)–(e) SST.

possibly providing real-time feedback on the actual delivered dose with optimal time and spatial resolution. Any detector system should be ideally insensitive to any change in temperature, humidity, and magnetic fields in the treatment room. All in all, the detector system should not suffer from degradation due to radiation exposure, and maintain its function within 1% of the specified performance values at least for one year, ideally for more than 5 years [56].

Recalling that the quality and effectiveness of any radiotherapy treatment results from an accurate dose delivery and the full tumor coverage, the former implies stable beam currents, while the beam energy is responsible for the penetration depth.

Silicon sensors are expected to become key-elements for beam monitoring: this is the case of the LHCb VELO microstrip detector [45, 57], that is undergoing R&D for a new non-invasive and real-time beam monitoring during treatment of ocular carcinomas at the Clatterbridge Cancer Center (CCC, Wirral UK). Monitoring of beam intensity and profile would be extremely useful not only for dose assessment, but also for controlling the accelerator operations thereby the patient safety. In fact, a beam monitor would detect early signs of beam instabilities, provide feedback for beam optimization and protect both equipment and patient against instabilities or any possible accident [58].

Silicon sensors are expected to contribute not only for instrumenting the control system of therapeutic proton beams, but also as key element in new imaging technologies for even more advanced particle therapy treatments. As a promising example of the potential role of silicon sensors for proton Computer Tomography is reported in section 2.4.1.

2.4.1 pCT: proton imaging with silicon sensors

Proton therapy is a type of cancer therapy which employs the favorable depth-dose characteristics of protons: after an entrance plateau, the protons lose the absolute greatest part of their residual energy over a small distance (the so-called “Bragg peak”). By tuning the energy of the beam, the position of the Bragg peak can be changed to fully cover the tumor site, whilst sparing the normal tissue beyond it. For therapeutic applications, the typical proton kinetic energy extends from around 60 MeV (corresponding to a range of 3 cm in water) to 230 MeV (i.e. 33 cm in water) [59].

Proton therapy is usually indicated for hard to reach tumors (for example, in the brain, lung, head and neck), and especially childhood cancers for it minimizes risks and side effects in comparison to conventional radiotherapy. Accurate planning and pre-treatment verification of the patient dose are necessary to achieve the best dose conformality. In other words, a safe and successful proton therapy

treatment strictly relies on accurate range $R(E)$ prediction and verification:

$$R(E) = \int_0^E \left(\frac{dE'}{dx} \right)^{-1} dE', \quad (2.4)$$

where E is the initial kinetic energy of the proton. The energy loss rate dE/dx can be related to the proton energy loss ΔE over a track length l via the following approximation [60]:

$$\Delta E = \int_0^l \frac{dE}{dx} dx \approx \sum_0^n \rho_i \left(\frac{dE}{dx} \right)_i \Delta l, \quad (2.5)$$

where x is the unit density-weighted track length. Since $x = \rho \cdot l$, the formula 2.5 points out that a measurement of the energy loss is essentially a measurement of the density distribution of the traversed material. The summation in eq. 2.5 denotes that the continuous transport is approximated by calculation in discrete steps.

Nowadays, dose calculations for proton therapy treatments are based on X-ray Computed Tomography (CT) images, and the patient's position with respect to the treatment beam is checked with standard X-ray radiographs. It should be noted that the conversion from electron density into proton stopping power is a major source of inaccuracy, leading to systematic range errors of 1.6% (for soft tissue), 2.4% (for bone) and even up to 5.0% in lung [61]. For optimum accuracy, it would be better to directly image the patient with protons and provide as input for dose planning a 3D map of the proton stopping power: this is the fundamental idea underlying proton Computed Tomography (pCT). A pCT scanner should track every single proton before and after the patient, and measure the residual proton energy (and/or range). The range uncertainty would be reduced by using protons of energy as high as to pass through the patient [62], with the Bragg peak located in the energy range detector. A proton beam of 250 MeV should be enough for a head scan, while proton energies up to 350 MeV would be necessary for an adult trunk [63].

In a rotational scan, the integrated stopping power has to be determined for every view by a measurement of the energy loss, which can be expressed with the critical parameter in pCT - i.e. the Water-Equivalent Path Length (WEPL):

$$WEPL = \int_{E_{out}}^{E_{in}} \frac{dE}{S_{water}(E)} = \int_0^l RSP(\vec{r}) dl, \quad (2.6)$$

where E_{in} the initial proton energy, E_{out} is the residual energy, and l represents the particle path. By computing the left-hand side of eq. 2.6 (using the Bethe-Bloch

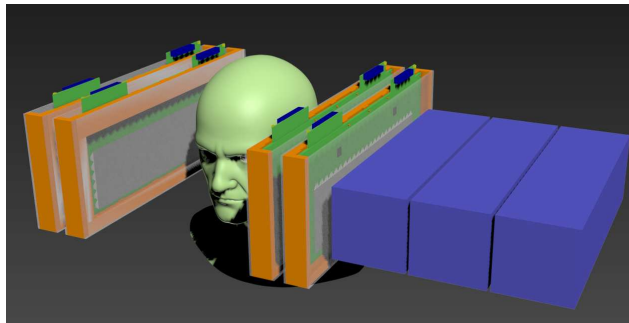


Figure 2.9: Conceptual schema of pCT for a head scan: the proton direction is measured before and after the patient with silicon sensors; the proton energy loss is measured by a calorimeter [66].

formula or, alternatively, by calibrating the WEPL), an image of the Relative Stopping Power (RSP) can be obtained. The RSP of a particle in a material is defined as the ratio between the stopping power of the particles in the given material $S_{material}$ to that of water S_{water} [64].

The pCT method has the potential to achieve higher spatial resolution in comparison to conventional X-ray CT [65]; it would also reduce or eliminate CT artifacts due to metal or dental implants with high Z materials. In addition, a pCT scan has the potential to detect subtle differences in the density of the tissues along the beam path. In fact, tumor tissue have typically a higher density than the surrounding normal tissues, and therefore the tumor boundaries might be defined without injection of contrast medium into the patient. Beyond the use of pCT for treatment planning, it could also be used to verify the position of the patient, and to take into account the tumor shrinkage or changes in the patient's anatomy. The absorbed dose for a pCT head scan was estimated to be a few mGy [67], therefore it is likely that the pCT investigation can be repeated as a quick check before each proton dose fraction. For comparison, diagnostic X-ray CT scanner or X-ray Cone Beam CT (CBCT) deliver a dose of 40 mGy [68].

The use of protons for imaging was originally proposed already in 1963 by Allan Cormack [69], inventor of the X-ray CT, too, but many challenges are not solved yet, starting from the lack of an accelerator delivering the proton energy and intensity in the ranges of interest for pCT and treatment as well [63].

All in all, three phenomena are responsible for the intrinsic limitation of pCT: the Multiple Coulomb Scattering (MCS) of protons off the atom nuclei (limiting the spatial resolution), the energy loss straggling (reducing the electron density resolution), and nuclear interactions (introducing noise and additive dose to the patient). For example, a 200 MeV proton traversing 20 cm of water would have a lateral straggling $\sigma_x = 0.37$ cm, an angular straggling $\sigma_\theta = 41$ mrad and energy

Proton beam	Energy	$200 \text{ MeV} \leq E \leq 330 \text{ MeV}$
	Energy spread	$\approx 0.1\%$
	Beam intensity	10^7 - 10^8 protons/s
Accuracy	Spatial resolution	$< 1 \text{ mm}$
	Electron density resolution	$< 1\%$
	Distance from patient	10 cm
	Installation	$< 10 \text{ min}$
Time efficiency	Verification	$< 5 \text{ min}$
	Reconstruction	$< 10 \text{ min}$
Reliability	Radiation hardness	$> 1000 \text{ Gy}$
	Stability	$< 1\%$
Safety	Imaging dose	$< 20 \text{ mGy}$

Table 2.2: Design specification for a pCT system with therapeutic application in proton therapy, summarized from [61] and [62].

stragglings $\sigma_E = 2.2 \text{ MeV}$ [61].

The main requirements for pCT are summarized in table 2.2; in the following we report on the promising role of silicon sensors for pCT in order to overcome some of the pCT challenges concerning the position and WEPL resolution. Exploratory tests with p-on-n Silicon Strip Sensor (SSD) demonstrated the feasibility of proton imaging in the energy range 20-300 MeV [60]. The particle position can be obtained from the traversed strip number. The steep energy dependence of the stopping power (shown in fig. 2.10) is exploited to obtain the proton energy from a specific energy deposit, using the Time Over Threshold (TOT) technique. The energy measurement was possible up to an input charge of 100 fC, corresponding to the average charge deposited by 17 MeV protons in 400 μm thick silicon sensor [60]. Nowadays, the benchmark pCT system is the prototype realized by the American pCT collaboration, which approaches readiness for clinical applications after more than a decade long extensive pre-clinical tests [70].

The scanner consists of 2+2 SSDs for tracking protons, followed by a five plastic scintillators read out by PMT with a WEPL resolution of 3 mm.

The first remarkable achievement of the pCT collaboration is the realization of a silicon-based tracker with a large uniform sensitive area to image standard QA and head phantoms. A total area of $(36 \times 9) \text{ cm}^2$ is achieved with four slim-edge SSDs in a row. Since wafer sizes are currently limited to 6 inches and the active sensor area is usually surrounded by a 1 mm wide dead edge area, image artifacts are inevitable if sensors are overlapping or butted against each other. Slim edges can be obtained with the Scribe-Cleave-Passivate (SCP) treatment involving Laser + XeF_2 scribing, then cleaving and passivating with Nitrogen Plasma-Enhanced

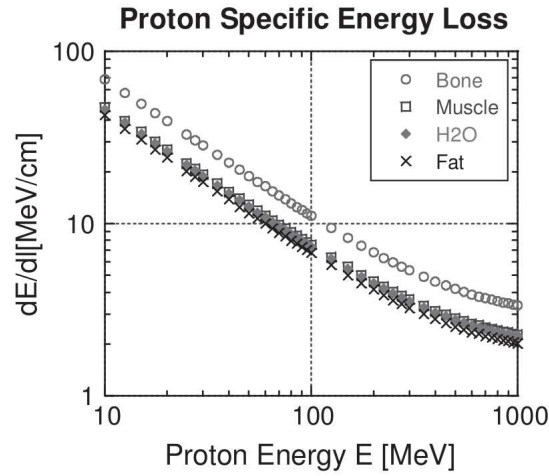


Figure 2.10: Proton specific energy loss as a function of energy for bone, muscle, water and fat. The energy dependence is exploited to obtain the particle energy [60].

Chemical Vapor Deposition (PECVD) nitride for n-type and Atomic-Layer Deposited (ALD) alumina for p-type sensors. The SCP process reduces the width of the dead edge area from 1 mm to less than $200 \mu\text{m}$ [71].

Fig. 2.11 shows an SSDs sensor before and after the SCP treatment. After the removal of the guard ring, the leakage current is less than 100 nA at the depletion voltage of 100 V. Individual strip currents and CCE on the strips next to the slim edge are essentially unchanged before and after the SCP treatment [72]. The pCT collaboration developed fast electronics and a DAQ system reliably operating at approximately 1 MS/s data rates; one single continuous scan takes about 6 min. It was calculated that at least 100 protons in every 1 mm^3 voxel and in each of the 180 views are necessary; moreover, a head-size object requires ca. $7 \cdot 10^8$ protons. A crude estimation after 10 years long operation would lead to:

$$7 \cdot 10^8 \frac{\text{protons}}{\text{image}} \cdot 3 \frac{\text{image}}{h} \cdot 12 \frac{h}{\text{day}} \cdot 300 \frac{\text{day}}{\text{year}} \cdot 10 \text{year} \approx 8 \cdot 10^{13} \text{ protons.} \quad (2.7)$$

As a final remark, it should be noted that tracking imagers are not compatible with passive scattered proton beams and have a slow image acquisition speed, currently making them impractical for clinical use. In contrast, integrating systems are compatible with both passive and pencil-beam scanning, too - with image acquisition time short enough for clinical use. Again, various detectors have been proposed but all of them have limitations: for example, plastic nuclear track detectors require an unsuitable developing process; CMOS or a combined system of CCD camera and scintillator detectors provide a relatively low energy resolution. Re-

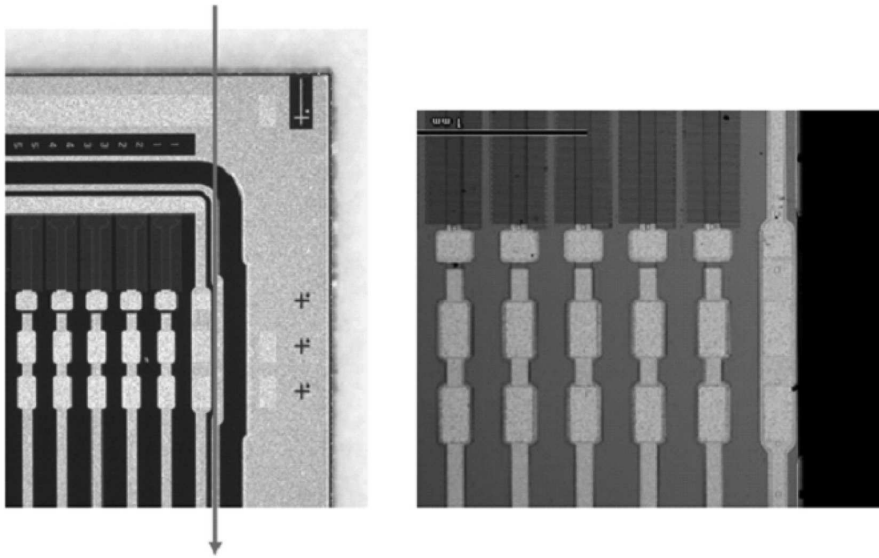


Figure 2.11: (a) A p-on-n sensor with strip pitch of $228 \mu\text{m}$; the vertical line represents the planned cut between the bias line and guard ring. (b) The SCP-treated sensor with slim edge of less than $250 \mu\text{m}$ and without guard ring [73].

cent results demonstrated the feasibility of using silicon diode arrays for proton imaging [74]. The prototype detector is composed of four monolithic silicon sensor modules - each of which is 64 mm in length and comprises 64 pixels. When placed along the central axis of the proton beam, the position of the beam's Bragg peak along the diode array correlates with the Water Equivalent Thickness (WET) of the object being imaged. The resolution and maximum error in WET measurements were found to be 2.0 and 1.5 mm, respectively [74].

The new detector design would be a low-cost solution that “could find its way into clinical application much sooner than the more technologically demanding solutions based on individual proton tracking” [75].

Proton-induced bulk damage to silicon sensors

After summarizing the fundamentals of silicon sensors in chapter 1 and providing representative examples of silicon sensors exposed to proton beams in three different physics research areas in chapter 2, the topic of proton-induced bulk damage in silicon sensors is presented.

At the beginning, an overview on the basic interactions of protons in silicon is provided according to the proton energy (section 3.1), with focus on Non-Ionizing Energy Losses (NIEL). Radiation damage by various particles with different energies is usually scaled and compared under the assumption of the so-called NIEL hypothesis (section 3.2); strength and weaknesses of such concept are discussed. In addition, another phenomenological approach to quantify the radiation damage via the number of displaced atoms (DPA) is described as well.

Radiation-induced bulk defects (classified in section 3.3) affect sensor properties and performance (as summarized in section 3.4).

3.1 Interactions of protons in silicon

Rutherford scattering dominates the interaction of protons in silicon at kinetic energies below 10 MeV (subsection 3.1.1), while higher energy protons mainly undergo nuclear elastic scattering and nuclear reactions (subsection 3.1.2).

In the following, it is assumed that an atom is displaced from its lattice site whenever it receives a kinetic energy equal or greater than E_d i.e. the threshold energy for displacement ($E_d \approx 25$ eV for silicon).

The first displaced atom is called Primary Knock-on Atom (PKA); the formed vacancy-interstitial (V-I) pair is called Frenkel pair. The defect density ρ_d result-

ing from irradiation of a target material with atomic density N is expressed with:

$$\rho_d = N\sigma n, \quad (3.1)$$

where σ is the cross-section for a defect-producing interaction and n is the number of resulting defects after the interaction.

3.1.1 $E_p < 10$ MeV

At proton energies below about 10 MeV, Coulomb interactions dominate the production of displaced atoms from their lattice sites. The differential cross-section for elastic scattering of protons (i.e. Rutherford scattering) is:

$$\frac{d\sigma_{el}}{d\Omega} = \frac{1}{(4\pi\epsilon_0)^2} \left(\frac{Ze^2}{2mc^2} \right)^2 \frac{1-\beta^2}{\beta^4} \csc^4(\theta/2), \quad (3.2)$$

where $\beta = v/c = pc/E$ (being p and E are the momentum and the energy of the proton); θ is the scattering angle and m the rest mass of the proton. The target silicon atom has a charge number Z .

Corrections for the reduction of the Coulomb potential because of the electrostatic screening of the nuclear charges by the space charge of the innermost electron shells are included in the Ziegler, Biersack, Littmark (ZBL) screened Coulomb potential [76]. These corrections are especially important below 0.1 MeV.

Therefore, the great part of the incident particle energy is lost due to ionization of lattice atoms. However, ionization losses will not lead to any relevant changes in the silicon lattice: the bulk damage is rather caused by protons with $E_p > 10$ MeV, as described in detail in the next section, given its relevance for the present work.

3.1.2 $E_p > 10$ MeV

At proton energies higher than 10 MeV, nuclear scattering is not negligible. In particular, non-elastic scattering starts to contribute to the total cross-section above 20 MeV, dominating at energies higher than 100 MeV. At even higher proton energies, many different reaction channels are responsible for secondary reaction products; in particular, fragmentation and spallation of the target nuclei may occur. In silicon, protons with energy greater than about 10 MeV mainly undergo the following two mechanisms [77]:

1. **Nuclear elastic collisions** between the incident proton and the PKA; elastic scattering dominates below 50 MeV. After penetrating the electron cloud of the target atom, the proton interacts with an unscreened silicon nucleus

via Coulomb repulsion. The integrated Mott-Rutherford cross-section addresses collisions that displace an atom from its lattice position:

$$\sigma_e = \frac{\pi b^2}{4\gamma^4} \left((\varepsilon - 1) - \beta^2 \ln \varepsilon + \pi \alpha \beta \left[2 \left(\varepsilon^{1/2} - 1 \right) - \ln \varepsilon \right] \right), \quad (3.3)$$

where:

$$\left\{ \begin{array}{l} \gamma = (1 - \beta^2)^{-1/2}, \\ b = \frac{2Ze^2}{mc^2\beta^2}, \\ \varepsilon = E_m/E_d, \\ \alpha = Ze^2/\hbar c, \\ E_m = \frac{2E(E + 2mc^2)}{(1 + m/M)^2 (Mc^2) + 2E}. \end{array} \right.$$

In the above mentioned formulas, m , v and E refer to the proton mass, velocity and energy, respectively; M and Z to the silicon mass and charge number; the maximum energy transfer to the silicon nucleus is E_m . Recalling that an energy greater than E_d must be transferred to the recoil nucleus and considering those interactions with $E_m \gg E_d$ (i.e. $\varepsilon \gg 1$), the average energy \bar{E} transferred to a PKA is therefore:

$$\bar{E} = E_d (\ln \varepsilon - \beta^2 + \pi \alpha \beta). \quad (3.4)$$

Given the logarithmic dependence on E , the average energy \bar{E} does not depend on the energy E of the incident proton: as a result, \bar{E} varies in the range 100-200 eV for proton energies between 10 MeV and 1.8 GeV.

Before coming to rest, the PKA may produce in turn other defects in the lattice; assuming that about half of the initial energy goes into defect production, the total number of displacements n_e is roughly:

$$n_e \approx \frac{1}{2} \frac{\bar{E}}{E_d}. \quad (3.5)$$

Combining all the equations for σ_e , \bar{E} and n_e it is possible to yield the elastic contribution to the defect density:

$$\rho_e \approx \frac{\pi b^2 N \varepsilon}{8\gamma^2} (\ln \varepsilon - \beta^2 + \pi \alpha \beta), \quad (3.6)$$

if only the contribution to ε by the first addend in eq. 3.3 is considered.

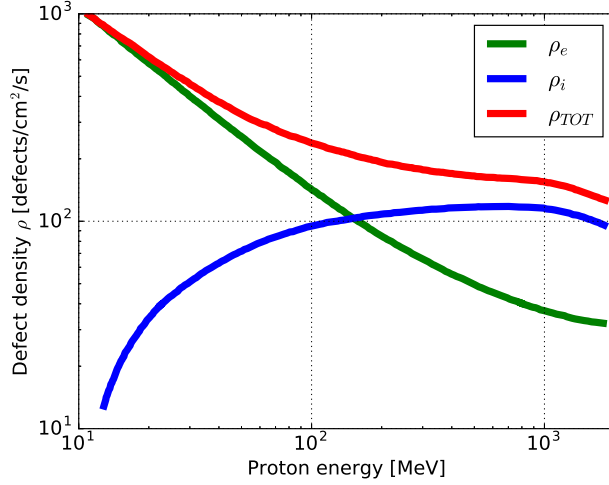


Figure 3.1: Theoretical defect density ρ in silicon as a function of incident proton energy [77], as a result of elastic (ρ_e) and inelastic (ρ_i) collisions.

2. **Inelastic collisions** are the dominant defect-producing mechanisms, especially for proton energies $E_p > 150$ MeV (see fig. 3.1). In particular, spallation of the target nucleus is of primary importance at proton energies higher than 200 MeV: the incident proton collides with individual nucleons in the target nucleus and generate a “cascade” with ejection of few fast nucleons. Nucleons are primarily emitted in the same direction of the incident proton; their energy distribution is roughly $E^{-1/2}$, from about 5 MeV up to the energy of the incident proton. Since the residual nucleus is left in an excited state, it “evaporates” nucleons with an average energy of 10-15 MeV. This is the so-called “evaporation” portion of the spallation interaction. To summarize, the defect density ρ_i from inelastic scattering results from five main contributions:

$$\rho_i = N\sigma_i [n_{RN} + (mpn)_{FP} + (mpn)_{FN} + (mpn)_{SP} + (mpn)_{SN}], \quad (3.7)$$

due to recoiling nuclei (RN), fast hadrons in the cascade phase (FP and FN), and slow hadrons from the evaporation phase (SP and SN). The number of emitted nuclei is m ; p is the geometric probability factor that the emitted particle actually interacts before leaving the target.

In the case of proton interactions with silicon, (p,n) and (p, γ) nuclear reactions are possible, but it should be noticed that the (p,n) reactions typically have three orders of magnitude higher cross-section than (p, γ) reactions. The produced radionuclides decay by emitting positrons or by the electron capture process. Nuclear reactions with dopant impurities or electrodes metals are negligible [78].

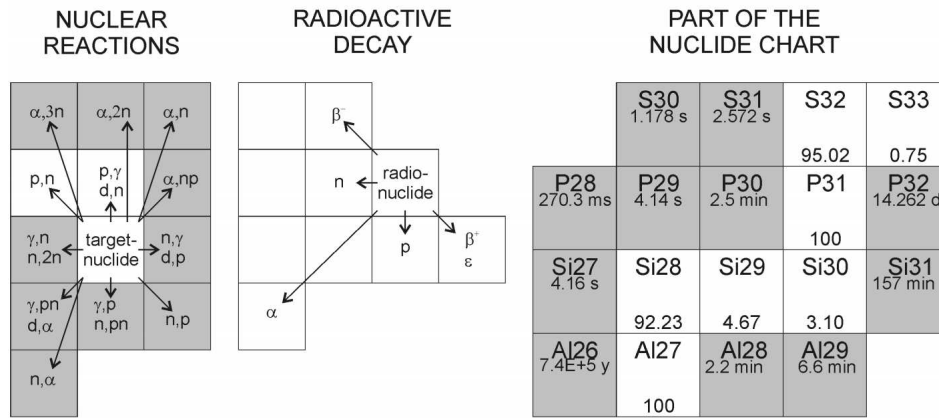


Figure 3.2: Nuclear reactions: (left) proton-induced reactions are shown in white cells, (middle) decay scheme of the radionuclides, (right) part of the nuclide chart with silicon-related radionuclides [78].

The next section 3.2 deals with two models for quantifying and comparing radiation damage effects for the bulk of silicon sensors: NIEL and DPA.

3.2 Quantification of bulk damage

Nowadays, NIEL-based calculations are the standard reference to quantify and compare radiation damage by different particles at various energies and fluences (section 3.2.1). In section 3.2.2, another approach for predicting the radiation damage by means of the Displacement Per Atom (DPA) unit is presented.

3.2.1 NIEL hypothesis

The concept of NIEL was developed in order to quantify and compare displacement damage effects after irradiation of semiconductor and optical devices. The basic assumption is that the amount of defects induced in the silicon bulk linearly scales with the energy imparted during displacing collisions. It has to be mentioned that recombination of the created vacancy-interstitial pairs and the final evolution of primary defects into stable defects is not taken into account.

The NIEL concept is defined as [79]:

$$NIEL(E) = \frac{N_A}{A_L} \cdot D(E), \quad (3.8)$$

where N_A is Avogadro's number of particles per mole and A'_L is the molar mass of the lattice atoms, i.e. a quantity with units of [kg/mole] and equal to the mass of Avogadro's number of particles. The most important physical quantity involved in the NIEL definition is the displacement damage cross-section $D(E)$ [79]:

$$D(E) = \sum_i \sigma_i(E) \cdot \int_{T_{min}}^{T_{max}} dE_R \int_{-1}^1 d\mu \cdot f_i(E, \mu, E_R) \cdot {}^{ion}T_{dam}(E_R). \quad (3.9)$$

The summation is over all the open reaction channels i with cross-section $\sigma_i(E)$, where E is the energy of the incident particle. The integration is done over all possible recoil energies E_R above the displacement threshold, and the possible emission angles ($\mu = \cos(\theta)$). The function $f_i(E, \mu, E_R)$ represents the probability for generating a PKA with recoil energy starting from a particle with energy E undergoing the i -reaction. Finally, ${}^{ion}T_{dam}(E_R)$ is the displacement partition function for the emitted ion in the i^{th} -reaction with energy E_R . It should be noted that $T_{min} = E_d$ in some publications, while in other references $T_{min} = 0$ instead. In the latter case, if an energy less than the displacement threshold is imparted, the PKA remains in its lattice position but energy does go into phonons - hence, it is considered to be part of the non-ionizing component.

The displacement damage cross-sections $D(E)$ for neutrons, protons, pions and

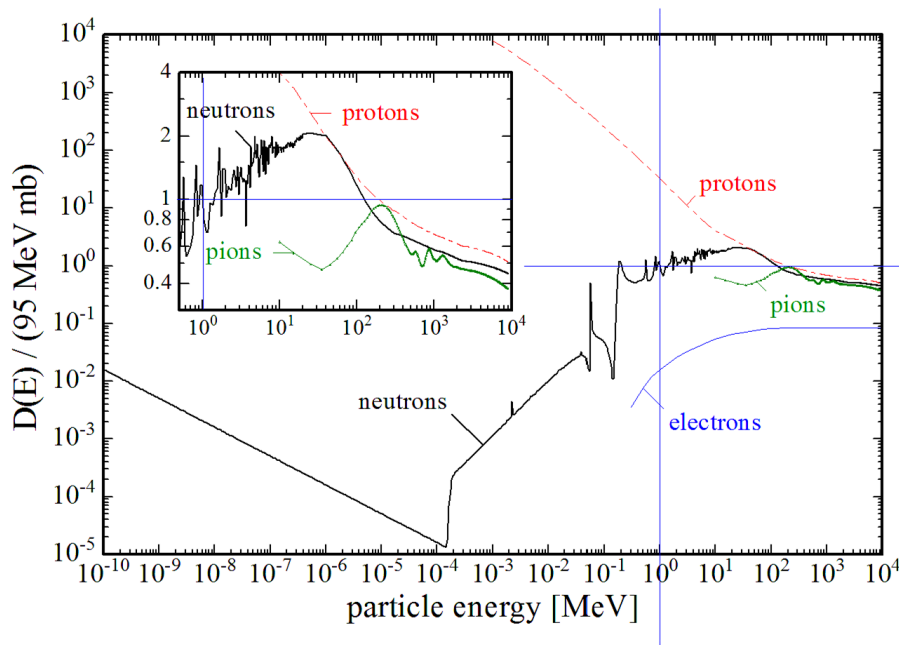


Figure 3.3: Displacement damage cross-section for neutrons, protons and pions from [80] and [17].

electrons are shown in fig. 3.3. In the energy range between (10^{-4} , 10^4) MeV, the proton $D(E)$ decreases monotonically as a function of the proton energy E .

The proton damage function is dominated by Coulomb interactions at lower energies, so it is larger than the neutron's one. For energies in the GeV range, proton and neutron damage functions share common values since they undergo the same nuclear reactions.

In the specific case of protons, it is worth noticing that in literature there are not only earlier results by M. Huhtinen [81] and G. P. Summers [82] from the 1990s, but also more recent calculations by I. Jun [83] from 2003 and M. Guthoff [84] from 2014, as collected in fig. 3.4. The differences in the published NIEL values are mainly due to the different inelastic reaction models implemented in the radiation transport codes (TRIM in [82], FLUKA in [85] or MCNPX in [86]). NIEL values in [81] were obtained from a fit to experimental data. The NIEL values adopted in the present work are therefore included in tab. 3.1. The damage caused by different particles is usually compared to the damage caused by neutrons, taking the NIEL of 1 MeV neutrons as the reference point (95 MeV·mb). The damage efficiency of any particle type with a given energy is expressed via

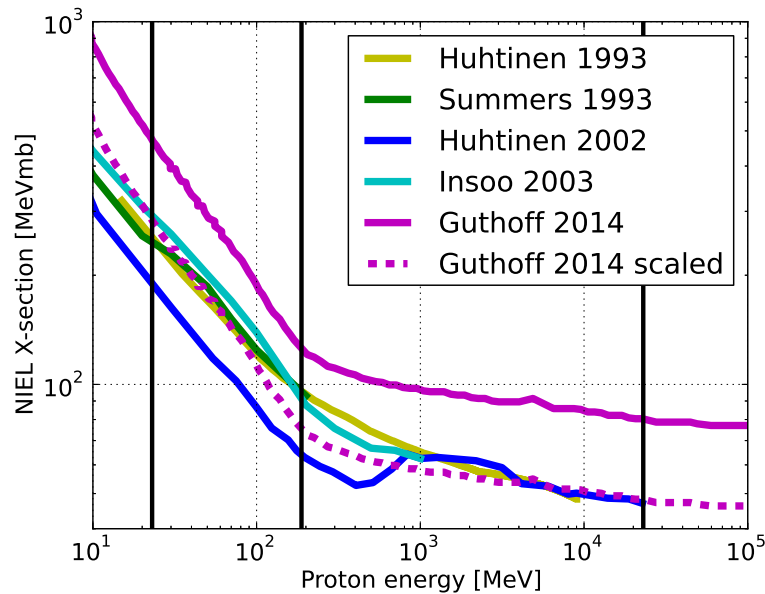


Figure 3.4: Energy-dependence of NIEL for protons in silicon. Guiding lines are overlaid in black at relevant energies for the present work (23 MeV, 188 MeV and 23 GeV protons). Data are taken from [81]→[87].

the hardness factor κ :

$$\kappa = \frac{\int D(E)\phi(E)dE}{D(E_n = 1MeV) \cdot \int \phi(E)dE}. \quad (3.10)$$

It follows that a neutron equivalent fluence ϕ_{neq} corresponds to an actual particle fluence ϕ (in cm^{-2}) as given by:

$$\phi_{neq} = \kappa\phi. \quad (3.11)$$

NIEL-based calculations are the standard reference for comparing radiation damage by various particles of different energies. In particular, the NIEL scaling hypothesis has been experimentally demonstrated for standard FZ p-on-n silicon sensors after irradiation with protons, neutrons and pions [89]. However, there are still some open issues about its widespread applicability.

Since bulk damage from NIEL interactions is primarily responsible for the degradation of the performance of silicon sensors in HEP experiments like at the LHC, the changes in the macroscopic sensor properties (e.g. leakage current) are expected to be proportional to the NIEL. However, violation of the NIEL scaling has already been observed in [87].

A possible explanation is that the NIEL scaling account for the total displacement energy, without discriminating point-like from cluster defects, which are highly disordered regions with high density of defects (see section 6.3.4). It is in fact assumed that the macroscopic damage is due to a limited number of different defects. It is true that the creation of vacancies and interstitial depends only on the NIEL, but it is possible that more complex defects are formed according to the material characteristics (for instance in oxygen- or carbon-enriched materials). Experimental data are not always available for the many different material and devices currently under investigation. This work is part of an ongoing effort to investigate the impact of proton damage in three different silicon devices of different doping (n- and p-type), as it will be shown in section 5.1.

Proton energy	NIEL (MeV mb)	HF -	DPA - [84]
23 MeV	192 [87]	2.0 [88]	$4.36 \cdot 10^{-21}$
188 MeV	67 [81]	0.70	$1.42 \cdot 10^{-21}$
23 GeV	70 [89]	0.62 [89]	$1.01 \cdot 10^{-21}$

Table 3.1: List of NIEL, hardness factors and DPA values for the proton energies of interest for the present work.

3.2.2 Displacement Per Atoms: DPA

A different approach to the issue of radiation damage was proposed by Norget-Robinson-Torrens (NRT) in 1975 [90], by calculating the number of displacements per atom (DPA). The DPA unit of measurement was introduced to quantify how many times an atom is displaced on average during irradiation [85]. A DPA of 10^{-22} means that one atom out of 10^{22} was displaced from its lattice site [84]. The DPA values are directly related to the number of created Frenkel pairs N_F :

$$DPA = \frac{A}{N_A \rho} N_F, \quad (3.12)$$

where ρ is the material density (in g/cm^3), A is the mass number and N_A is the Avogadro number [85]. The number of Frenkel pairs N_F can be found according to the NRT theory [91]:

$$N_F = \kappa(T) \frac{\xi(T)T}{2E_d}, \quad (3.13)$$

where T the kinetic energy of the primary knock on atom; $\kappa(T)$ is the displacement efficiency (including the possible recombination of Frenkel pairs), and $\xi(T)$ the Lindhard partition function describing the fraction of energy that goes to non-ionizing interactions. DPA values due to protons in silicon are shown in fig. 3.5

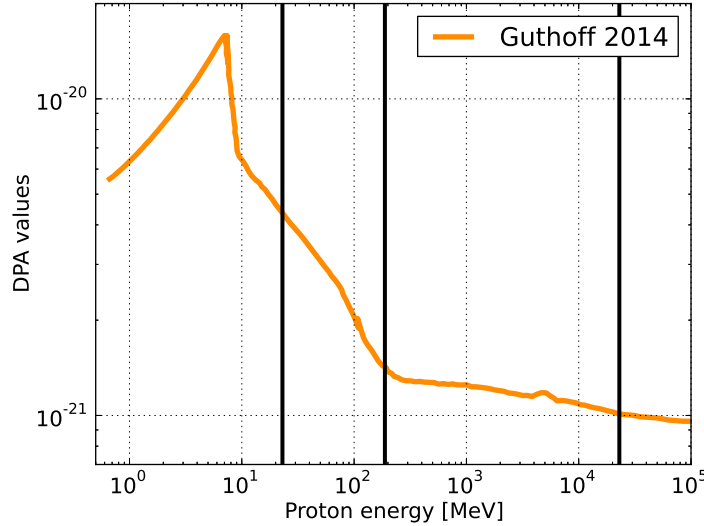


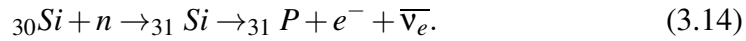
Figure 3.5: DPA values as a function of proton energy [84]. Guiding lines are overlaid in black at relevant energies for the present work (23 MeV, 188 MeV and 23 GeV protons).

as a function of the proton energy. DPA values for proton energies of interest in the current work can be found in tab. 3.1.

In comparison to NIEL-based calculations, DPA calculations rely only on interactions which actually produce lattice defect, while phonon interactions are disregarded. This is the reason why protons at lower momentum (below 100 MeV/c) produce less radiation damage in DPA calculations than in NIEL calculations. Moreover, DPA-based calculations take recombination of Frenkel pairs into account [84], a further improvement with respect to the NIEL-based calculations. In fact, vacancies and interstitials may recombine with each other, if their distance is smaller than a few lattice constant: 60% of the Frenkel pairs can recombine [92]. In disordered regions, the recombination level can be up to 95% [93].

3.3 Radiation-induced bulk defects

Radiation-induced atom-displacements can create several not only point-like defects (like interstitials or vacancies), but also more complex combinations of these two (e.g. di-vacancies V_2 , di-interstitials I_2 or even triple-vacancies V_3). Some examples of typical radiation-induced defects after irradiation of a Si lattice are depicted in fig. 3.6. Concerning nuclear reactions, the following representative reaction may take place:



It follows that diffusing silicon atoms or vacancies may combine with impurity atoms like phosphorus, oxygen or carbon. A classification of radiation-induced

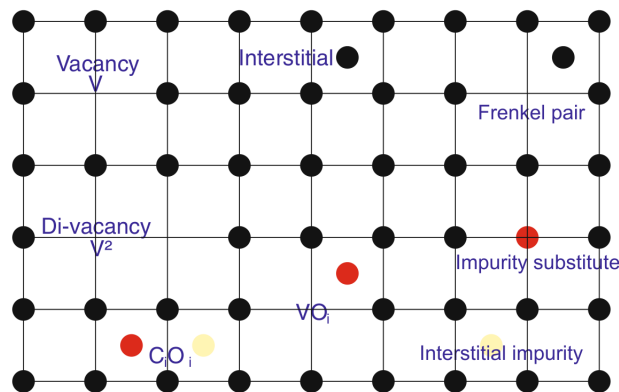


Figure 3.6: Simplified illustration of typical radiation-induced defects in a silicon crystal lattice [15].

bulk-defects in silicon is proposed in section 3.3.1, which will be useful for the investigations of proton-induced defects presented in chapter 6.

3.3.1 Defects classification

This section deals with important defects in silicon sensors, which are either related to the bulk material or caused by the exposure to radiation.

The most prominent impurities in high-purity silicon are oxygen, carbon and the doping atoms (phosphorus or boron). A review of these impurities is summarized as follows from [94] and [95]:

- **Oxygen** is introduced during the growth process and additional oxygen enrichment treatments. Oxygen dimers (O_{2i}) contribute to the formation of Thermal Donors (TD), depending on the oxygen concentration of the material and the heat treatment;
- **Carbon** is present in silicon sensors as substitutional (C_s) or interstitial (C_i). While C_s is electrically inactive, C_i is mobile at room temperature and contributes to the formation of $C_i C_s$ or $C_i O_i$;
- **Phosphorus** is usually a substitutional atom, replacing Si atoms. It can combine with other defects or impurities like carbon to form stable centres like the VP centre;
- **Boron** is usually a substitutional atom, replacing Si atoms as well. It can combine with vacancies to form stable centres like the VB centre, or oxygen to form $B_i O_i$.

After irradiation of a Si lattice, Frenkel-pairs either instantly recombine or create vacancies and interstitials; their subsequent migration leads in turn to more complex defects. Three main categories of radiation-induced defects in the silicon bulk are hereby summarized from [94] and [95]:

- **Vacancy-related defects:** the single vacancy comes with five different charge states; it is highly mobile at room temperature thus forming di-vacancies (V_2) or combine with impurities (e.g. VO or VP). Multi-vacancies defects V_n form clusters, and are produced especially after fast hadron irradiation.
- **Interstitial-related defects:** carbon interstitials are mobile and may combine with an immobile oxygen atom, forming $C_i O_i$. In oxygen lean material, a competing process is responsible for the introduction of $C_i C_s$ instead;

- **Cluster-related defects** are produced at the very end of a damage cascade. Clusters are highly disordered crystal regions; the exact nature and structure inside the cluster is not known at present. However, some defects are already attributed to clusters because they are not found after gamma irradiation, but only after hadron irradiation (this is the case of E4, E5 and E205a defects).

An overview of material and irradiation-induced defects is presented in tab. 3.2, listing the most important point-like and extended defects with impact on sensor properties and performance. On the contrary, the defects VO, V₂, C_i, C_iO_i, C_iC_s, IO₂ are already known not to be responsible for device degradation after ϕ_{neq} higher than 10^{12} cm^{-2} [96].

Despite the many possible defect structures, the net result is the introduction of energy levels (E_t) into the Si forbidden band gap, making the recombination of charge carriers¹ possible at k values differing from the k_m of the conduction band (as introduced in section 1.1.2). The transition probability depends on the energy differences between the state E_t and the conduction or valence band. Recombination centers near midgap yield the highest recombination rates, because processes involving high energy variation (with $E_t \gg E_V$ or $E_C \gg E_t$) are less probable. The theory regarding the role of such intermediate energy-level has been worked out by Shockley, Read and Hall [97] (see subs. 3.3.2).

Bulk defects resulting from displacement and nuclear interactions have then severe impact on sensor's properties and performance (as described in section 3.4).

3.3.2 SRH carrier statistics

In semiconductor materials, four recombination mechanisms are possible [99]: (I) Shockley-Read-Hall, (II) direct radiative (with the emission of a photon), (III) direct Auger (with three carriers involved) or (IV) trap-assisted Auger. For indirect-bandgap semiconductors like silicon (as discussed in section 1.1.2), the dominant recombination takes place via localized energy states in the forbidden energy bandgap [9]. Recombination of excess minority carriers with majority carriers processes act from non-equilibrium states ($np > n_i^2$), towards restoring equilibrium (according to the mass action law $np = n_i^2$), by recombination of the excess minority carriers with the majority carriers. Assuming excess carriers in the density Δn and Δp , the electron and hole densities are summed up as:

$$n = n_0 + \Delta n \quad \text{and} \quad p = p_0 + \Delta p. \quad (3.15)$$

¹Recombination of carriers takes place not only within the bulk of a semiconductor crystal but at its surface as well, where the periodicity of the crystal lattice is actually interrupted and in contact to other substances (e.g. air, SiO₂, metals) [2].

Defect	Structure	Energy level (eV)
Phosphorus	$P^{0/+}$	$E_C - 0.045$
E(30K) $^{0/+}$	unknown	$E_C - 0.100$
E(46K) $^{???$	unknown	$E_C - 0.143$
A-centre	$VO^{-/0}$	$E_C - 0.176$
E-centre	$VP^{-/0}$	$E_C - 0.400$
Divacancy	$V_2^{-/0}$	$E_C - 0.423$
H(152K) $^{0/-}$	unknown	$E_V + 0.420$
Carbon	C_iO_i	$E_V + 0.360$
H(140K) $^{0/-}$	unknown	$E_V + 0.360$
H(116K) $^{0/-}$	unknown	$E_V + 0.330$
Carbon	$C_i^{+/0}$	$E_V + 0.284$
H(40K) $^{0/-}$	unknown	$E_V + 0.108$
Carbon	$C_iC_s^{+/0}$	$E_V + 0.084$
Boron	$B^{-/0}$	$E_V + 0.045$

Table 3.2: Impurities and radiation induced defects in silicon of interest for the current work, summarized from [17] and [98]. The charge at room temperature is indicated together with the defect label and chemical structure, if known.

For instance, in the case of a p-type semiconductor, carrier injection is either low ($\Delta n = \Delta p \ll p$) or high ($\Delta n = \Delta p \gg p$). Generation-recombination centers can be donors or acceptors; we assume that the options for their charge state are:

- For donors: (0/+), if occupied by an electron/hole, respectively;
- For acceptors: (-/0), if occupied by an electron/hole, respectively.

We assume that all generation-recombination centers are either completely occupied by electrons or completely empty. The so-called amphoteric defects have both acceptor and donor energy levels; their possible charge states are neutral, single or double charged.

At thermal equilibrium, the electron occupation probability of a defect state with energy E_t is described by the Fermi-Dirac distribution function as already mentioned in eq. 1.8:

$$F(E_t) = \frac{1}{1 + \exp\left(\frac{E_t - E_F}{k_B T}\right)}, \quad (3.16)$$

here, $F(E_t)$ is the probability that a center with energy E_t is occupied by an electron. The occupation of the defects (with total concentration N_t) either with elec-

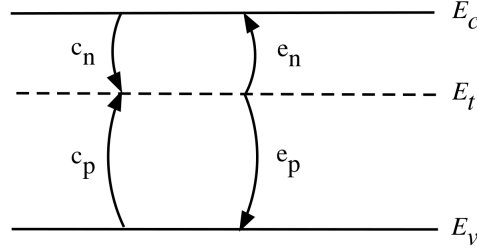


Figure 3.7: Recombination and generation processes: (c_p) hole capture from the valence band by a center, (c_n) electron capture from the conduction band by a center, (e_n) electron emission from the trap, (e_p) hole emission from the trap.

trons (n_t) or holes (p_t) can be calculated by:

$$n_t = N_t F(E_t) \quad \text{and} \quad p_t = N_t (1 - F(E_t)). \quad (3.17)$$

As far as the totality condition $N_t = n_t + p_t$ holds, each defect state could be either occupied by an electron or a hole. For instance, at room temperature, an acceptor occupied with an electron would contribute with negative space charge to the effective doping concentration. The change in level occupation has four contributions (see fig. 3.7): electron or hole emission, electron or hole capture.

$$\frac{dn_t}{dt} = R_a - R_b - R_c + R_d, \quad (3.18)$$

being the rates of electron and hole capture:

$$R_a = c_n n N_t (1 - F) \quad \text{and} \quad R_c = c_p p N_t F, \quad (3.19)$$

where $c_{n,p}$ are the capture coefficients for electrons and holes, respectively. Conversely, an emission is the inverse of the capture process:

$$R_b = e_n N_t F \quad \text{and} \quad R_d = e_p N_t (1 - F). \quad (3.20)$$

The proportionality constants $e_{n,p}$ are called emission probability. It is important to note that the capture rates are proportional to the concentration of centers occupied by holes; the other way around occurs for holes.

At thermal equilibrium, capture and emission rates must be the same ($R_a = R_b$), so that the emission probability is directly related to the capture coefficient:

$$e_n = \frac{c_n n (1 - F)}{F}. \quad (3.21)$$

It is more practical to express emission probabilities in terms of the intrinsic Fermi level E_i and the intrinsic carrier densities n_i :

$$e_{n,p} = c_{n,p} n_i \cdot \exp\left(\pm \frac{E_t - E_i}{k_B T}\right). \quad (3.22)$$

$n \cdot c_n \gg e_p$	$p \cdot c_p \gg e_n$	recombination center
	$p \cdot c_p \ll e_n$	electron trap
$n \cdot c_n \ll e_p$	$p \cdot c_p \gg e_n$	hole trap
	$p \cdot c_p \ll e_n$	generation center

Table 3.3: Overview on the nature of electron or hole traps, and generation-recombination centers.

Alternatively, the entropy factor can be introduced:

$$e_{n,p} = c_{n,p} N_{C,V} \cdot \exp\left(\pm \frac{E_t - E_{C,V}}{k_B T}\right) = c_{n,p} N_{C,V} X_{n,p} \cdot \exp\left(-\frac{\Delta H}{k_B T}\right). \quad (3.23)$$

The capture coefficients $c_{n,p}$ are related to the capture cross-section $\sigma_{n,p}$ [9] by:

$$X_{n,p} c_{n,p} = \sigma_{n,p} v_{th,n,p}, \quad (3.24)$$

being $v_{th,n,p}$ the thermal velocity (as defined in appendix A). Intuitively, the capture cross-section is a measure of how close to a center an electron must be in order to be captured. In conclusion, the emission probabilities are defined as follows:

$$e_{n,p} = \sigma_{n,p} v_{th,n,p} N_{C,V} \exp\left(-\frac{\Delta H'}{k_B T}\right). \quad (3.25)$$

The expression $\Delta H'$ indicates that the enthalpy was obtained under the assumption of a constant capture cross-section (the change of entropy is neglected). From now on, $\Delta H'$ will be referred as the activation energy. The eq. 3.25 is of fundamental importance for the analysis of the microscopic measurement presented in chapter 6. Eq. 3.25 holds also in non-equilibrium conditions since it does not depend on the Fermi energy.

According to the capture and emission rates, a center can be categorized as a generation or recombination center for holes or electrons (an overview is available in table 3.3). The interaction of the defect itself with the conduction and valence band determines the defect occupation. In the following, two cases of primary importance for spectroscopy measurements will be presented: reverse and forward bias in section 3.3.3 and section 3.3.4, respectively.

3.3.3 Defect occupation under reverse bias

A space charge region (SCR) builds up as a result of the application of a reverse bias. For low irradiated samples, the free charge carriers in the space charge are

neglected ($n \approx p \approx 0$); therefore, capture of charge carriers by the traps can be neglected in eq. 3.18 (i.e. $R_a = 0$ and $R_c = 0$):

$$\frac{dn_t}{dt} = -R_b + R_d = -e_n n_t + e_p p_t, \quad (3.26)$$

so that in steady state condition the defect occupation is reduced as:

$$n_t = N_t \frac{e_p}{e_n + e_p} \quad \text{and} \quad p_t = N_t \frac{e_n}{e_n + e_p}. \quad (3.27)$$

and it is a function of the emission probability for electron e_n and holes e_p . It is now possible to calculate the generation rate of electron-hole pairs from defect states:

$$G_t = e_n n_t = e_p p_t = N_t n_i \frac{c_n c_p}{c_n \exp\left(\frac{E_t - E_i}{k_B T}\right) + c_p \exp\left(-\frac{E_t - E_i}{k_B T}\right)}. \quad (3.28)$$

Assuming ($c_n = c_p = c$) and ($\sigma_n = \sigma_p = \sigma$), a simplification of the eq. 3.28 leads then to:

$$G_t = \frac{N_t n_i c}{2 \cosh\left(\pm \frac{E_t - E_i}{k_B T}\right)}. \quad (3.29)$$

Eq. 3.29 points out that “deep levels”, i.e. defects states with an energy level close to the intrinsic Fermi level, strongly contribute to the bulk generation current due to defect states in the SCR:

$$I = \sum_{traps} q_0 G_t V_{SCR}. \quad (3.30)$$

If the assumption ($n \approx p \approx 0$) is not valid anymore, i.e. free carriers are present in the SCR, the occupation of defect states becomes dependent not only on the emission probability (as if eq. 3.27), but also on the capture rates [94].

3.3.4 Defect occupation under forward bias

The application of a forward bias to a device is a common method with the aim of providing a large amount of free carriers to fill the traps with electrons and holes. This is also the case of the measurements performed in the present work (the TSC measurements, as described in chapter 4), where a high forward bias is applied at low temperatures ($T \approx 10$ K).

If a high number of carriers are injected into the silicon bulk, the emission rates become small in comparison to the capture rates ($e_n \ll c_n n$ and $e_p \ll c_p p$).

Under such conditions, the occupation probabilities under steady state condition for electron and hole traps are:

$$n_t = N_t \frac{1}{1 + \frac{c_p p}{c_n n}} \quad \text{and} \quad p_t = N_t \frac{1}{1 + \frac{c_n n}{c_p p}}. \quad (3.31)$$

The capture rates are the main factor for the occupation of the defects states, so that defects can get filled by electrons when the capture coefficient for electrons $c_n n$ is higher than the one for holes. Conversely, a defect state is only filled with holes when the capture coefficient $c_p p$ for holes is higher than the one for electrons.

3.4 Impact of bulk-defects on sensor properties

In this section the impact of bulk defects on three fundamental sensor properties is summarized with relevant information for the fluence range of interest for the present work; the impact of annealing is then addressed in section 3.4.1.

1. **Leakage current:** defects in the middle of the bandgap are able to generate and recombine electron-hole pairs by means of thermal excitation. Free electron-hole pairs can also be created in the depleted volume, thereby contributing to the reverse current. The increment of the volume-scaled leakage current is directly proportional to the radiation fluence ϕ_{neq} :

$$\frac{\Delta I}{Vol} = \frac{I(\phi_{neq}) - I(\phi_{neq} = 0)}{Vol} = \alpha \cdot \phi_{neq}, \quad (3.32)$$

where the proportionality factor α is not material-dependent. As a reference value for measurements performed at $T=293$ K, $\alpha_{80/60} = 4.0 \cdot 10^{-17}$ A $\text{cm}^{-1} \pm 5\%$ after annealing of 80 min at 60°C [17]. The increase of the concentration of current-generation centers leads not only to an increase of dark current, but also to an increase of power consumption and dissipation ($P=VI$), a voltage drop on bias resistors ($\Delta V=RI$) and a decreased Signal to Noise Ratio (SNR).

2. **Space charge:** after irradiation, the doping density is not a constant as a function of the depth inside the sensor bulk. The non-uniform space charge distribution therefore depends on the bias voltage. CV curves are frequency and temperature dependent: the CV(f,T) phenomenon is due to the presence of deep traps in the forbidden bandgap.

Here we recall that: deep traps have an ionization energy ΔE much greater than kT (that is $\Delta E \gg kT$). The opposite happens for shallow traps ($\Delta E \ll$

kT), so that they are ionized at equilibrium and contribute to the space charge in depleted region. Shallow traps always respond to the AC signal applied during CV measurements.

In other words, thermal activation is a slow process for deep levels at room temperature; the filling of deep levels is slow as well if the density of free carriers is low.

The reason for the CV(f,T) dependences becomes clearly by observing the band diagram in fig. 3.8. Traps (or donors) are empty above the Fermi level, while they are occupied below. Emission occurs at the Fermi level.

Due to the applied AC signal in the CV measurement, a periodic change in the occupation of the trap occurs where the Fermi level crosses a trap level. The maximum frequency for a deep-level charging depends on the temperature as follow:

$$f \propto T^2 \exp(-E_a/kT), \quad (3.33)$$

where the energy $E_a = \pm(E_{C,V} - E_t)$. If the AC frequency is lower or higher than the trapping-detrapping rate, then the space charge due to this trap is detected or not.

Deep traps near the edge of the depletion region switch between depleted and neutral regions. If they are located in the depletion region, they are empty thus not contributing to the space charge of the device; on the contrary, they are filled and charged if they are located in the neutral region. In short: the filling of deep levels by free carriers in the valence and conduction bands leads to a non-uniform charge distribution of deep levels. For heavily irradiated samples ($> 10^{14} \text{ cm}^{-2}$, according to [101]), the properties of deep levels in the forbidden band gap, together with the distribution of thermally generated free carrier concentrations in the silicon bulk, lead to a distribution of the electric field with two peaks near both contacts.

3. **CCE**: defects which are not occupied by charge carriers may act as traps, reducing the carriers mean free path, the CCE and SNR.

The effective trapping rate is defined as the inverse of the trapping time, which represents the mean time an electron or a hole spends in the space-charge region, before being trapped by a trap k . The effective trapping probability was parametrized by [102]:

$$\frac{1}{\tau_{eff,n,p}} = \phi_{eq} \sum_k g_k (1 - P_{k,n,p}) \sigma_{k,n,p} v_{th,n,p}, \quad (3.34)$$

where $\phi_{n,p}$ is the equivalent fluence, $v_{th,n,p}$ the thermal velocity of carriers, g_k is the introduction rate of the defect k with occupation probability $P_{k,n,p}$ and $\sigma_{k,n,p}$ is the cross-section for capturing electron and holes.

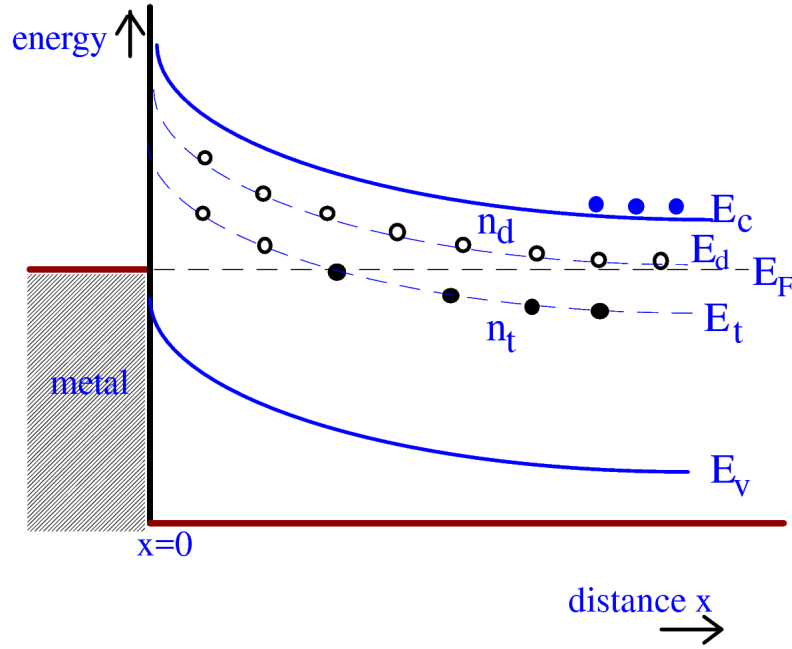


Figure 3.8: Schematic energy band diagram for a n-type diode with one trap level E_t , adapted from [100]. Traps (or donors) are empty above the Fermi level, while they are full below. Emission occurs at the Fermi level.

Assuming that the evolution of defects is governed by first-order dynamics, the effective trapping rates are proportional to the fluence with the proportionality constant $\beta_{n,p}$ at a given temperature and time after irradiation [102]:

$$\frac{1}{\tau_{eff,n,p}} = \beta_{n,p}(t, T)\phi_{eq}, \quad (3.35)$$

where $\beta_{n,p}$ depends on annealing time, annealing temperature and carrier type. For electrons, $\beta_e \approx 4 \times 10^{-16} \text{ cm}^2/\text{ns}$, while $\beta_h \approx 5 \times 10^{-16} \text{ cm}^2/\text{ns}$ for holes. Hence it follows that holes are more likely to be trapped [103]. After irradiations at fluences ϕ_{neq} in the order of 10^{15} cm^{-2} , τ_e is few ns, and the average drift length is shorter than the sensor thickness. As a result, the CCE of a $300 \mu\text{m}$ sensor drops from originally 23000 electrons to about few thousands only [103]. This is the reason why trapping is the ultimate limitation of silicon sensors.

3.4.1 Evolution of bulk-defects with annealing

The annealing process is defined as the irreversible thermal dissociation of defects, followed by motion of a defect or separation of one of its components, with irreversible drift to join one of the component of a Frenkel pair [104]. Defects in the silicon lattice like interstitials and vacancies are mobile through diffusion processes that depend on temperature. More practically: an annealing session of 4 min at 80°C resembles the yearly room temperature warm up periods during maintenance in LHC experiments [105].

Annealing processes can be limited by keeping sensors at low temperatures (less than 20°C) or accelerated by heating the sensor. In the following, the impact of the annealing on three main sensor properties are outlined:

1. **Leakage current** decreases with time (this is the so-called “beneficial” annealing), given the annealing behavior of the α parameter:

$$\alpha(t) = \alpha_0 + \alpha_I \exp\left(\frac{-t}{\tau_I}\right) - \beta \ln\left(\frac{t}{t_0}\right), \quad (3.36)$$

where $\alpha_I \approx 1.25 \cdot 10^{-17}$ A/cm, $\beta \approx 3.0 \cdot 10^{-18}$ A/cm and $t_0 = 1$ min.

The α_0 and τ_I parameters are temperature dependent, too; after annealing at 80°C, $\alpha_0 = 4 \cdot 10^{-17}$ A/cm, and $\tau_I = 9$ min [106].

2. **Space charge:** In contrast to the leakage current, the space charge is not only subject to a beneficial annealing but also to an adverse effect, called anti-annealing or reverse annealing. The variation ΔN_{eff} in the space charge with fluence and annealing time is parametrized by the Hamburg model [17]:

$$\Delta N_{eff}(\phi_{neq}, t, T) = N_C(\phi_{neq}) + N_A(\phi_{neq}, t, T) + N_Y(\phi_{neq}, t, T), \quad (3.37)$$

being N_C the stable damage, N_A the short term annealing and N_Y the reverse annealing components:

$$\left| \begin{array}{l} N_C(\phi_{neq}) = N_{C,0} (1 - \exp(-c\phi_{neq})) + g_c \phi_{neq}, \\ N_A(\phi_{neq}, t) = \phi_{neq} \sum_i g_{a,i} \exp(t/\tau_{a,i}), \\ N_Y(\phi_{neq}, t) = N_{Y,\infty} \left(1 - \frac{1}{1 + k_y N_{Y,\infty} t}\right). \end{array} \right.$$

Details about the model can be found in [17]; here we quote just two important consequences. Firstly, $N_{C,0}/N_{eff,0}$ is the fraction of removable donors, which depends on the oxygen concentration. An oxygen concentration

higher than 10^{16} cm^{-3} is expected to suppress the donor removal: many vacancies are caught in E-centres, with the $N_{C,0}/N_{eff,0}$ ratio dropping from about 80% down to even 10% [106]. Secondly, N_{eff} in n-type silicon initially decreases to the level of intrinsic silicon until type inversion can occur. On the contrary, p-type sensors do not undergo type inversion and show an ever increasing depletion voltage.

3. **CCE:** Trapping of electrons and holes is also the subject of annealing effects and experimental data indicates that the probability of electron trapping decreases, while hole trapping increases [107]. The relevant fit function is independent of the fluence [107]:

$$\beta_{n,p}(t) = \beta_{0n,p} \cdot \exp(-t/\tau_{n,p}) + \beta_{\infty n,p} \cdot (1 - \exp(-t/\tau_{n,p})), \quad (3.38)$$

with $\beta_{0n,p}$ and $\beta_{\infty n,p}$ the trapping constant at early ($t \rightarrow 0$) and late ($t \rightarrow \infty$) annealing times, respectively.

After the presentation of the performed proton irradiations of silicon sensors with different bulk material, the results of the measurements of leakage current and changes in the space charge due to deep defects will be shown in chapter 5. The annealing behavior of point-like and cluster defects will be then addressed in chapter 6.

Part II

Experimental work

Investigated silicon samples and experimental methods

After a review on the performed proton irradiations (section 4.1) and on the six test structures (section 4.2), the experimental techniques used for bulk damage characterization will be presented. On one hand, Current-Voltage (IV, section 4.3) and Capacitance-Voltage (CV(f,T), section 4.4) measurements are performed to provide leakage current, stability and breakdown characteristics, the depletion voltage and the space charge. On the other hand, Thermally Stimulated Current (TSC, section 4.5) are performed to detect and electrically characterize radiation-induced bulk-defects. The chapter ends with an overview on all the performed measurements (section 4.6).

4.1 Proton irradiations

As anticipated in chapter 2, the innermost pixel sensors of the HL-LHC experiments will have to be operated in a radiation field of photons, electrons, charged and neutral hadrons, for neutron equivalent fluences ϕ_{neq} of the order of 10^{16} cm^{-2} , and ionizing dose values of a few MGy.

Measurements on prototype sensors have shown that thin ($200 \mu\text{m}$ thick) n^+p silicon sensors may stand such harsh radiation environment [108]. However, the knowledge of radiation-induced defects in p-type silicon sensors is quite limited at present, and in particular studies of the effects of proton irradiation at different energies are lacking. In addition, it is needed to investigate the proton-energy dependent damage in silicon sensors since, up to now, irradiation studies are conventionally performed with protons of just one energy (23 GeV) which is not the average energy (of 1 GeV) as of simulations in LHC silicon trackers [55].

Therefore, in the present work, proton irradiations of silicon pad diodes were

performed with protons of 23 MeV, 188 MeV and 23 GeV kinetic energy. The irradiations were performed at three different irradiation facilities: at the cyclotron ZAG (Karlsruhe, Germany), for the lowest investigated proton energy (23 MeV, $\kappa = 2.00$)¹. Irradiation tests at the highest proton energy (23 GeV, $\kappa = 0.62$) were performed at the PS synchrotron of CERN, Switzerland. In the following, details are given in particular for the most recent irradiation with 188 MeV protons ($\kappa = 1.0$), at the KVI institute in Groningen.

4.1.1 23 MeV protons @ KIT

Irradiations of silicon pad diodes with 23 MeV protons were performed at the Karlsruhe Kompakt-Zyklotron KAZ, operated by the Zyklotron AG (ZAG). An uncertainty on the hardness factor of 15% has to be taken into account related to the beam extraction energy [80]. The typical proton flux is $2.5 \cdot 10^{13}$ p/(s·cm²). Given the small beam spot size (≈ 7 mm), the samples have to be scanned on an XY-stage [109]. The temperature in the irradiation station is approximately -40°C, thus annealing during the irradiation period is negligible.

Nickel foils are used for dosimetry by measuring the ⁵⁷Ni activity induced after (p,2n) reactions:



The subsequent β^+ plus decay of ⁵⁷Cu ($t_{1/2} = 199$ ms) produces ⁵⁷Ni (with $t_{1/2} = 35.6$ h):



The ⁵⁷Ni isotope in turn decays via electron capture, emitting 1377.6 keV photons. The error on the estimated proton fluences is 10% [88].

4.1.2 188 MeV protons @ AGOFIRM

Irradiations with 188 MeV protons took place at the superconducting cyclotron of KVI-CART in Groningen. The irradiation were performed at the maximum available proton energy (190 MeV). However, the proton energy at the device under test (DUT) is slightly lower than the nominal energy, due to energy losses in the vacuum exit window, the copper scatter foil, the Beam Intensity Monitor (BIM) and in the sample stock. The calculated energy at the DUT is 188 MeV.

During the irradiation, the proton fluence is controlled by monitoring the beam intensity with the BIM which produces a current that is linearly dependent on the beam intensity. The calibration of the BIM is performed with a scintillation detector at the DUT, with a radius of 0.5 cm. The total variation of the flux over a

¹the definition of the hardness factor κ is given in eq. 3.10.

Proton fluence (10^{14} cm^{-2})	Beam intensity (MU)	Duration (min)
1.0	424.11	42
0.5	212.06	53*
0.3	127.23	11

Table 4.1: Summary of irradiations performed at KVI (chronological order). (* delayed by issues with the radio protection system in the irradiation hall).

field with 1 cm diameter is 20 % (see fig. 4.1(a)). The relative fluence variation is shown in fig. 4.1(b). The average flux in per pulse from the BIM was determined to be $2.36 \times 10^5 \text{ p/cm}^2$ per Monitor Unit (MU).

All the silicon samples were placed on an XY table, remotely moved from the control room. The performed irradiation are summarized in table 4.1. The temperature in the irradiation room was 23°C ; after irradiation, the samples were stored in a fridge for approx. 4 months at -25°C to avoid further annealing.

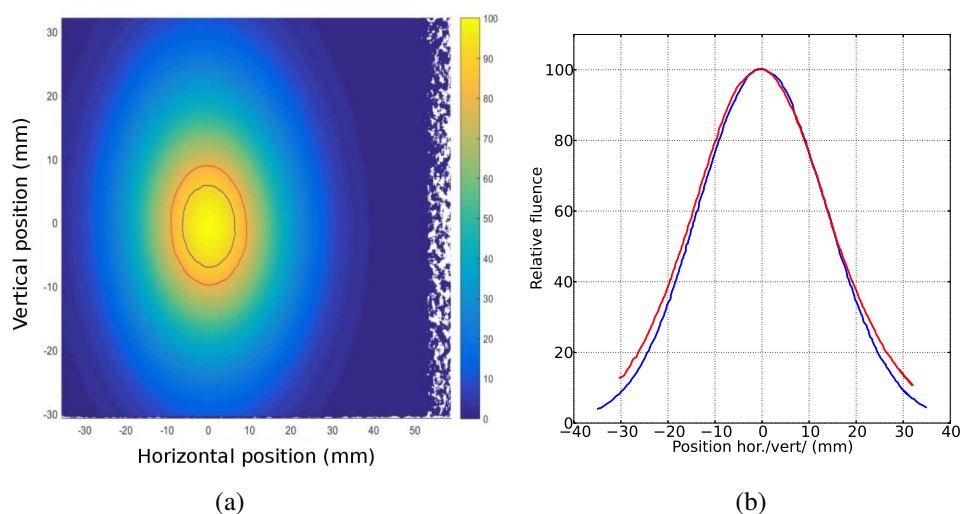


Figure 4.1: Irradiation at the KVI facility: (a) 2D map of the proton beam on the DUT and (b) relative fluence profile along the horizontal and vertical axes [110].

4.1.3 23 GeV protons @ CERN

The irradiations with 23 GeV protons were performed at the Proton Synchrotron (PS) CERN [111]. Proton spills with a kinetic energy of 23 GeV from the primary PS beam are delivered to the irradiation area, with a maximum beam intensity of

2×10^{11} protons per spill [111]. For instance, irradiations with a proton fluence of 10^{14} p/cm² lasts at least ≈ 2 days; furthermore, the temperature of the irradiation hall was around 27°C. Therefore, defect annealing takes place already during the irradiation itself. The samples are placed in cardboards of (5×5) cm² and scanned by the proton beam over an area of (2×2) cm². Together with a sample stock, (5×5) cm² aluminum foils are irradiated for dosimetry purposes. The induced activity of the ²²Na and ²⁴Na isotopes from the ²⁷Al(p,3p3n)²²Na and ²⁷Al(p,3pn)²⁴Na reactions are exploited to measure the proton fluence [112]. The ²²Na activity ($t_{1/2} = 2.6$ y) is measured via the gamma emissions of 1.27 MeV photons. The ²⁴Na isotope ($t_{1/2} = 15$ h) emits 1.37 MeV photons. The error on the fluence is 8% after irradiation at the CERN PS with 23 GeV protons [113].

4.2 Test Structures

Here we describe the geometry and bulk properties of the test structures which underwent the proton irradiations presented in section 4.1.

4.2.1 Geometry and bulk properties

The study of bulk damage in silicon requires a test structure with simple geometry and well-defined sensor volume. Silicon pad-diodes are planar diodes that fulfill these requirements and they are used as test structures for R&D on silicon detectors to be implemented in harsh radiation environments, such as in the case of HEP experiments. In the present work, silicon pad diodes are used to investigate the proton-energy dependent damage in the silicon bulk. Given the investigated proton energies (with $E_p > 23$ MeV) and being the surface not segmented, minor effects on the leakage current and the electric field are expected because of surface damage (i.e. from ionizing energy losses) [114].

All test structures used in this work are square silicon pad-diodes manufactured by Hamamatsu Photonics K.K. [115]. Top and cross sectional sketches are shown in fig. 4.2(a) and fig. 4.2(b), respectively. The square pad-diodes have an active area of 0.25 cm², defined by a guard-ring of 135 μ m width.

Various n-type (phosphorous-doped) and p-type (boron-doped) silicon $\langle 100 \rangle$ crystals were investigated: Magnetic Czochralski (MCz) and Physically Thinned (FTH), for which the physical thickness is nearly equal to the active thickness (a thickness of 1.2 μ m of both n⁺ and p⁺ implants has to be subtracted). Deep diffused Float Zone (FZ) diodes have a physical thickness of 320 μ m; the active thickness of 200 μ m is obtained via deep diffusion. In comparison to the standard backside processing, the deep diffusion process is responsible for the smooth increase of the doping towards the backside (thus a non-saturating capacitance)

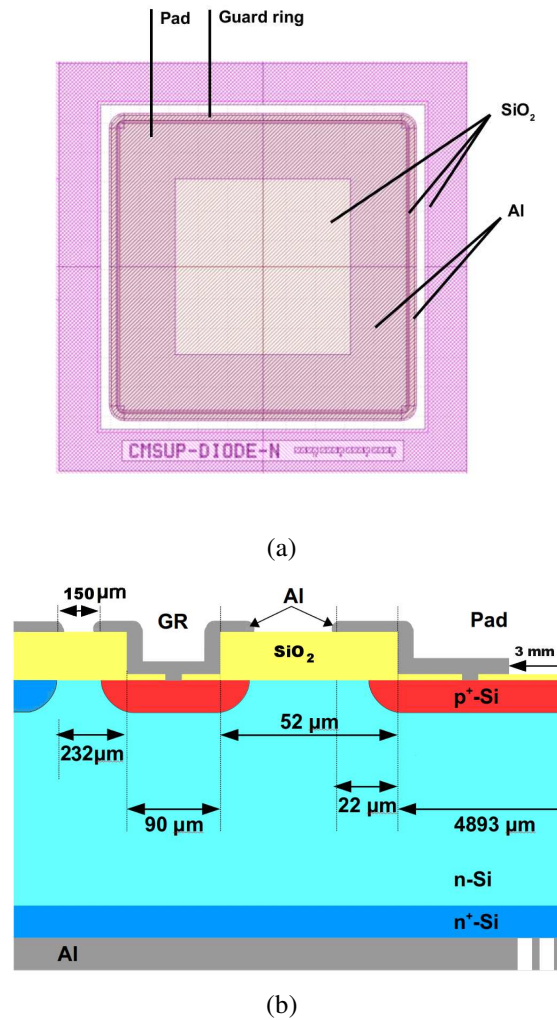


Figure 4.2: A n-type silicon pad-diode: (a) mask layout for p^+ -implant and aluminum contacts. (b) Cross-sectional view with dimensions of interest (not to scale). Adapted from [116].

and process-induced bulk-defects. The growth and production process of wafers are also responsible for the different oxygen content in the sensor bulk. Fig. 4.3 presents the oxygen profiles in the sensor bulk measured by Secondary Ion Mass Spectroscopy (SIMS). Since the profiles are not homogeneous over the thickness of the sensors, an average oxygen concentration [O] is included in tab. 4.2. MCz diodes come with the highest oxygen content (up to $5.6 \times 10^{17} \text{ cm}^{-3}$); deep diffused FZ sensors are characterized by a highly non-uniform oxygen content in the sensor bulk, with higher [O] at the sensor edges.

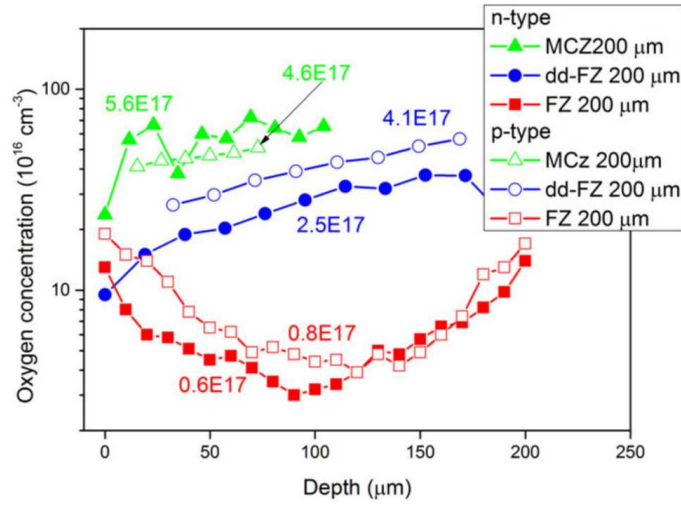


Figure 4.3: Oxygen profile in three different bulk material for silicon pad-diodes, obtained with Secondary Ion Mass Spectroscopy [117].

Sensor label	Type	ρ ($\text{k}\Omega \cdot \text{cm}$)	Average [O] (10^{17} cm^{-3})	V_{dep} (V)	N_{bulk} (10^{12} cm^{-3})
MCZ	p-in-n	0.5	5.6	160 ± 5	5.0
MCZ	n-in-p	2.0	4.6	90 ± 5	3.0
FZ	p-in-n	1.2–2.4	2.5	100 ± 10	3.0
FZ	n-in-p	3.0–8.0	4.1	90 ± 10	3.0
FTH	p-in-n	1.2–2.4	0.6	90 ± 5	3.0
FTH	n-in-p	3.0–8.0	0.8	120 ± 5	3.8

Table 4.2: Overview on bulk material and average oxygen concentration [117].

The front-contact is metalized with aluminum, a part from a central square (with 3 mm long edges) for light injection during TSC measurements. The back-contact metalization is deposited with a mesh-like structure, so that the resulting Al grid allows for light injection. Non-metalized parts are covered with silicon dioxide (SiO_2) which act as passivation as well as protection layer.

After irradiation, the samples were mounted with conductive silver glue on a $(2 \times 2.5) \text{ cm}^2$ ceramic support. Five thin gold metalizations with a pitch of 2.54 mm make the sample contacting straightforward during the three different type of measurements performed, and especially for the spectroscopic measurements. The central gold strip is usually bonded to the rear electrode; the outermost gold strips are connected to pad and guard ring.

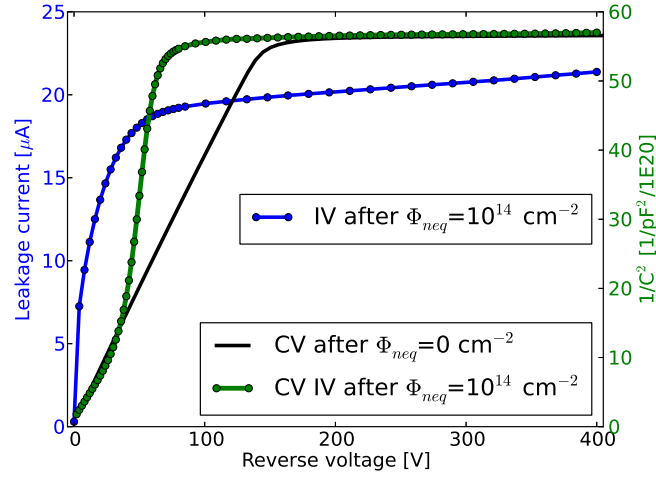


Figure 4.4: IV (blue curve) and CV(f,T) (green points) reverse characteristics measured with grounded guard-ring on n-type MCZ diode (after irradiation with 188 MeV protons at $\phi_{neq} = 10^{14} \text{ cm}^{-2}$ and no annealing. $T=293 \text{ K}$ and $f=10 \text{ kHz}$). The CV measured before irradiation is shown for comparison in black.

4.3 IV measurements

The measurement of Current-Voltage characteristics is performed by ramping-up the DC voltage to the back plane of the sensor; a Keithley Kei6517 (max 1000 V, 1 mA) is used as both bias source and current meter. The accuracy is in the order of 1% for low currents (up to 2 nA) and for currents up to 2 mA in the order of 0.1%. Another pico-amperemeter (Keithley 6485) is used for measuring the guard-ring current. The guard-ring is kept at the very same potential of the pad, thereby acting as boundary of the E-field and keeping well-defined the active sensor volume. Furthermore, it prevents surface or edge leakage currents from being collected by the pad. The IV measurements were performed in a light-tight and temperature-controlled probe-station (in the range [253, 293] K. The temperature is controlled with an accuracy of $\pm 0.1^\circ\text{C}$ by an ATT temperature controller).

An example of IV characteristic can be seen in fig. 4.4 (blue curve), for a n-type MCZ diode irradiated with 188 MeV protons. After irradiation, the current is dominated by generation current in the depleted region and is typically in the μA range after ϕ_{neq} in the order of 10^{14} cm^{-2} .

4.4 CV(f,T) measurements

Capacitance-Voltage measurements are performed by superimposing a small AC voltage to the reverse DC bias. The applied frequency is in the range between 100 Hz and 2 MHz. The admittance $Y = \frac{1}{R_p} + j\omega C_p$ is measured with an Agilent E4980A LCR meter [118], after calibration for the additional capacitances of cables and the isolation box.

The CV(f,T) measurements were performed inside a temperature-controlled probe station. CV(f,T) measurements provides a wealth of information about e.g. the depletion voltage, the effective doping concentration (before irradiation) or the density of free mobile majority carriers (after proton irradiation), as it will be shown in section 5.2. As a representative example, the CV characteristics of a n-type MCZ diode before and after irradiation are plotted in fig. 4.4 (black and green lines, respectively). Additionally, the information gained from IV and CV(f,T) measurements are of value for correctly setting the TSC measurements on the very same sample as pointed out in section 4.5.

4.5 Thermally Stimulated Current (TSC) measurements

In the present work, bulk defects in silicon diodes are detected and electrically characterized with the Thermally Stimulated Current (TSC) spectroscopy [119–123]. First, the spectroscopic technique (section 4.5.1), and second the TSC experimental setup (section 4.5.2) are outlined.

4.5.1 The TSC method

The TSC measuring procedure consists of a three-phase cycle (fig. 4.6):

1. **Cooling** from room temperature down to $T < 20$ K, under a bias V_c^{TSC} . By keeping the samples under 0 V bias, traps are filled with majority carriers (electrons in n-type and holes in p-type silicon), provided that the number of available carriers is larger than the number of traps. Otherwise, only those traps near to the midgap are filled. Alternatively, cooling under reverse bias (sufficient for a full sensor depletion) keep the traps free of charge carriers.
2. **Filling** at $T_{fill} < 20$ K can be performed either electrically (with forward bias for a current $I_{fill}^{TSC} \approx 1$ mA) or optically (by light illumination of a sample contact with $\lambda = 520$ nm). Under a forward bias V_{fill}^{TSC} , traps are filled with both majority and minority carriers; the occupation of a trap depends

on its individual capture cross-section for electrons and holes at T_{fill} . In the present work, filling with forward bias at $T_{fill} = 10$ K for $t = 30$ s is the choice for all the studies aiming at determining the defect concentrations.

On the contrary, optical filling is not intended to provide the absolute defect concentrations, but rather to determine whether a defect level is either an electron or a hole trap. In fact, the penetration depth of light increases at low temperatures but if $T < 20$ K the absorption length is not precisely known. Since the light-cone does not homogeneously illuminate the whole sensor, the measured volume is not well-defined.

If the penetration depth is large enough to penetrate the whole sample, defects are filled with both majority and minority carriers. If the penetration depth is restricted to few microns, either electrons or holes drift through the depleted volume and fill electron or hole traps, by illuminating either the n^+ or the p^+ junction side, respectively.

3. **Heating** (under a reverse bias V_h^{TSC}): after the filling phase, a reverse bias V_h^{TSC} is already applied to the diode and a delay time Δt_d is used to wait for the diode to relax back to a steady state. The TSC spectrum is recorded while the sample is heated back to room temperature, at a constant heating rate β . The provided thermal energy stimulates the detrapping of carriers from defect potentials. By recording the current as a function of the rising temperature, the resulting TSC spectrum in the temperature range (10 K, 200 K) shows peaks at specific temperatures related to the energy level of the radiation induced defects.

The steady state Leakage Current (LC) is the main limitation in performing TSC measurements; it has to be subtracted from the overall current signal for a proper analysis of the TSC spectrum. Therefore, in addition to a TSC spectrum under the reverse bias V_h^{TSC} , a dedicated TSC cycle has to be measured with the very same voltage applied during all the three measurements steps (i.e. $V_c^{LC} = V_f^{LC} = V_h^{LC} = V_h^{TSC}$). The TSC cycle is subsequently repeated at many different V_{fill}^{TSC} and V_h^{TSC} .

The sensitivity to bulk defects is limited by the dark leakage current and the instrumentation for current measurements (in the pA range, with $I_{min}^{TSC} > 0.1$ pA). Due to the large number of different defects, the signals from different traps can overlap. Further complications may arise from changes in the space charge sign during the TSC measurement itself: as a result, the shape and the magnitude of TSC peaks are substantially altered (see section 6.1). The most critical aspect is guaranteeing the full depletion of the diode so that the sample volume is well-defined for an accurate determination of defect parameters. In the present work, the TSC technique is applied to silicon pad diodes irradiated with proton fluences

up to $\phi_{neq} = 3.0 \cdot 10^{14} \text{ cm}^{-2}$, so that the maximal temperature at which the TSC signal can still be distinguished from the leakage current is about 200 K.

In the following, for a simpler notation, the applied voltages during cooling, filling and heating will be indexed simply as V_c , V_{fill} and V_h . Fig. 4.5 shows a typical TSC spectra (black line) recorded on a $200 \mu\text{m}$ FTH diode after irradiation with 23 MeV protons at $\phi_{neq} = 0.5 \cdot 10^{14} \text{ cm}^{-2}$. At least, 11 peaks can be clearly distinguished, with shallow defects in the low-T region and deep levels at higher temperatures. Traps in a n-type diode can be filled also by illumination with light injected at the front-side (green line in fig 4.5), to discriminate electron traps from hole traps. Finally, the dotted blue-line in fig. 4.5 represents the leakage current which is usually measured starting from 80 K and dominates the TSC signal at temperatures above ≈ 200 K.

4.5.2 The TSC setup

The TSC measurements are typically performed in the temperature range between 10 K and 290 K. Therefore, the sample is placed inside an evacuated cryostat chamber (model RDK-205D) and cooled by a close-cycle helium refrigerator-

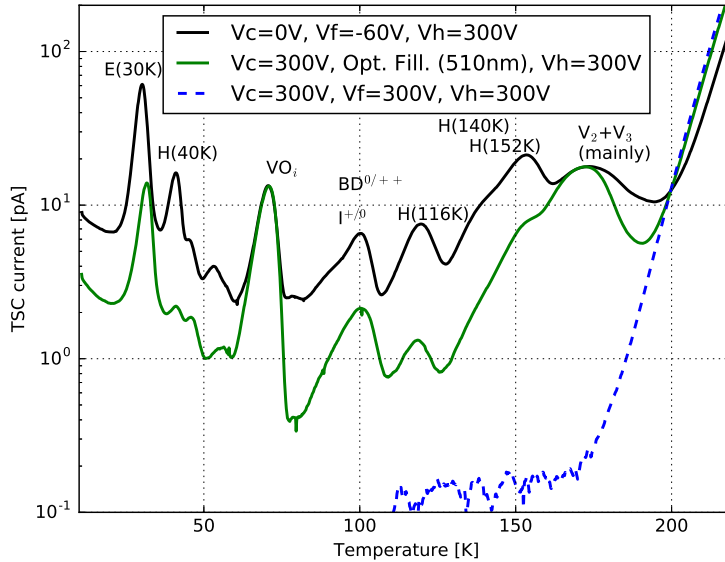
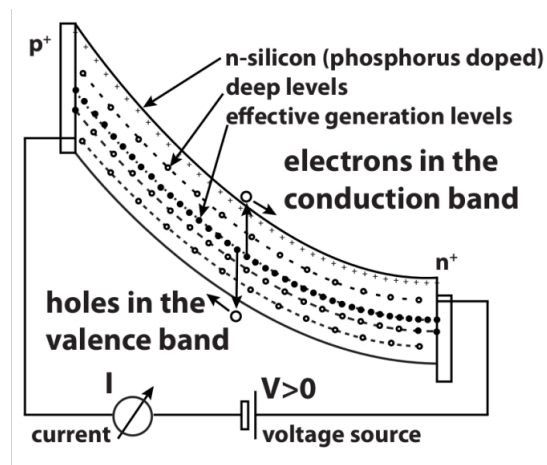
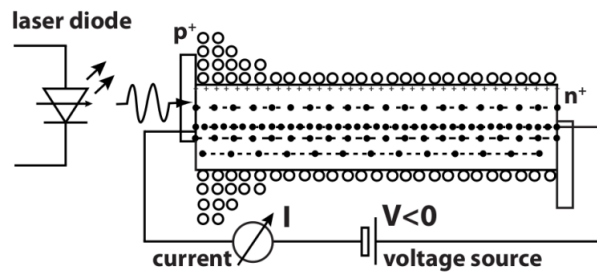


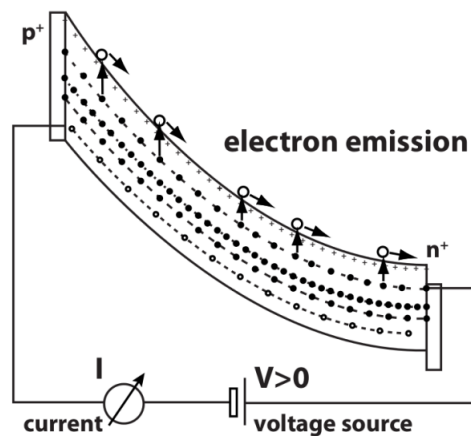
Figure 4.5: TSC spectra (black line) and leakage current (dotted blue line) for a n-type FTH diode, after irradiation with 23 MeV protons to $\phi_{neq} = 0.5 \cdot 10^{14} \text{ cm}^{-2}$ and annealing of 60 min at 80°C . The main electron traps can be identified by illumination of the front side with green light (green line).



(a)



(b)



(c)

Figure 4.6: The three steps for a TSC measurement cycle sketched for a n-type diode: (a) sample cooling, (b) injection of free charge carriers at $T < 20$ K and (c) sample heating while recording the TSC spectrum [124].

tor (model CKW-21), both from Sumitomo Heavy Industries Ltd. A two-staged Pfeiffer vacuum pump (model TMH 071P) is responsible for the evacuation of the cryostat chamber.

The silicon sample on the ceramic board is mounted to the TSC sample holder, on top of the cryostat chamber (fig. 4.7(a)). The sample holder is connected to the cold head via a hot copper stage, where a resistor of $30\ \Omega$ is used as heater ($30\ \text{W}$ is the maximum power). The connection between the hot stage and the cold head are provided by stainless steel rods. Temperature sensors are placed on the rear side of the sample holder and in the cold stage. The temperature of the sample holder is monitored via a Lake Shore 340 Temperature Controller. Voltage supply and current measurement are provided by a Keithley 6517A, with $10\ \text{fA}$ resolution.

Cables for contacting the sample and for temperature measurement are wrapped around cooling rods to avoid heating of the ceramic board, especially at low temperatures. The sample holder is enclosed in a radiation shield to avoid thermal radiation; two holes (with a diameter of $4\ \text{mm}$) in correspondence of front and rear sides are left for optical illumination. Green LEDs for optical filling are mounted on x-y tables outside of the cryostat chamber. The temperature and electrometer control uses a LabVIEW based program. Between consecutive TSC phases, the voltage is ramped in steps of $\pm 10\ \text{V}$. Temperature at the sample position, the TSC current signal and time information are stored every second.

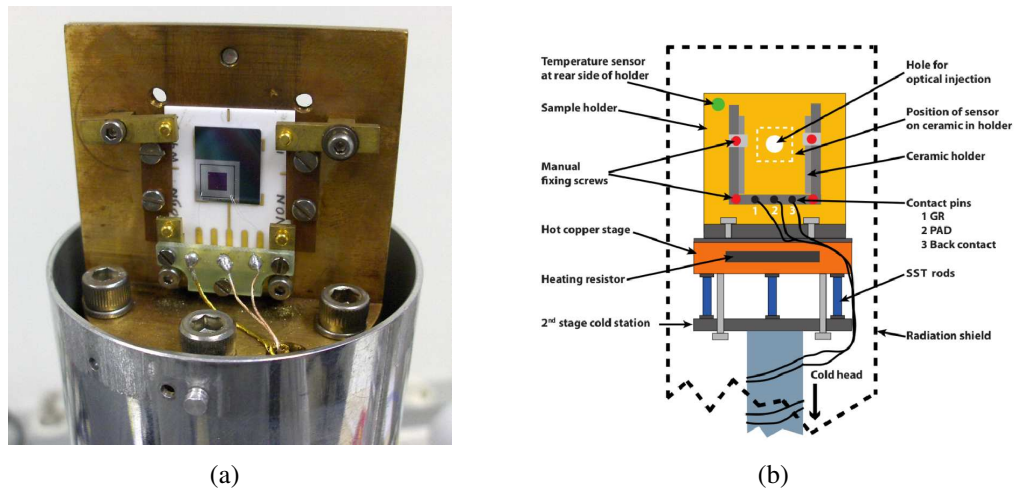


Figure 4.7: The TSC sample holder: (a) top part of the cryostat chamber showing the sample holder and (b) illustrative scheme of the subcomponents [95].

Proton beam		MCZ		FZ		FTH	
Energy	ϕ_{neq} (10^{14} cm $^{-2}$)	N	P	N	P	N	P
23 MeV	0.30	✓	✓	✓	✓	■	✓
	0.50	✓	✓	✓	✓	✓	✓
	1.00	✓	✓	✓	✓	✓	■
188 MeV	0.21	✓	✓	✓	✓	✓	✓
	0.35	✓	■	■	✓	✓	✓
	0.70	✓	✓	✓	✓	✓	✓
23 GeV	0.10	✓	✓	✓	✓	■	■
	3.00	✓	✓	✓	✓	■	■

Table 4.3: Summary of investigated 200 μm silicon n- and p-types pad diodes.

4.6 Summary of performed measurements

IV, CV(f,T) and TSC measurements were performed after irradiation with 23 MeV, 188 MeV and 23 GeV protons, reaching a maximum ϕ_{neq} of $3 \cdot 10^{14}$ cm $^{-2}$. In most of cases, all the measurements were performed at five subsequent annealing times (0, 8, 15, 30, 60) minutes at 80°C. A summary table and the corresponding legend can be found in tab. 4.3 and fig. 4.8. A list of complete diode labeling is available in appendix A. The results of IV, CV(f,T) and TSC measurements will be presented in chapter 5 and chapter 6, respectively.

	MCZ		FZ		FTH	
	N	P	N	P	N	P
23 MeV	●	○	▼	▽	■	□
188 MeV	●	○	▼	▽	■	□
23 GeV	●	○	▼	▽	■	□

Figure 4.8: Adopted legend for the 18 categories of investigated samples.

“Macroscopic” approach

The results of Current-Voltage in section 5.1 and Capacitance-Voltage measurements in section 5.2 are presented (both in reverse and forward bias). In reverse bias, the proportionality between the leakage current and ϕ_{neq} is demonstrated for all the investigated bulk material types and after all the irradiations with various proton-energies. Concerning the CV measurements, since the conventional analysis to determine the depletion voltage is found not to be applicable anymore, a possible method (the “initial rise method”) is proposed and tested, in view of comparing the space-charge related results from CV measurements with those obtained from TSC measurements (in chapter 7). In addition, the strong frequency and temperature dependences of the capacitance is exploited to obtain relevant information about deep defects in the silicon bulk.

Forward IV and CV measurements are performed to study the relaxation-likeness of silicon diodes after proton irradiations.

5.1 Results of IV measurements

The leakage current is investigated in silicon-pad-diodes before and after irradiation with protons of various energies E_p (23 MeV, 188 MeV and 23 GeV) and neutron equivalent fluences ϕ_{neq} in the range $[0.1, 3] \cdot 10^{14} \text{ cm}^{-2}$. Three different bulk materials (both n- and p-type bulk) were investigated (MCZ, standard FZ and deep-diffused FZ). IV characteristics are performed at $T=293 \text{ K}$, by applying to the sensor selected reverse DC voltages ($V_{reverse}$, in the range $[0, 400] \text{ V}$), and measuring the DC current. The current is measured after a delay time of 3 s from ramping up the reverse bias voltage. The pad and guard-ring currents are separately measured to decouple the bulk current from the current generated at the surface and cut edges. The IV measurements were repeated at subsequent an-

nealing steps at 80°C, from 0 to 60 min. The sensor thickness is obtained from the end capacitance in CV characteristics before irradiations. Accounting for the actual physical thickness d of the sensor is especially important for deep-diffused FZ silicon pad-diodes. The results from IV measurements are presented in the following sections:

- 5.1.1 Representative examples of IV characteristics after proton irradiation (with $E_p=188$ MeV and $\phi_p = 10^{14}$ cm⁻²), with an overview on the isothermal annealing studies (in five subsequent steps, between 0 and 60 min at 80°C);
- 5.1.2 The comparison between IV characteristics after proton irradiation for all the investigated materials, after scaling to $\phi_{neq} = 10^{14}$ cm⁻² the reverse current $I(\phi_{neq}, Vol, T, t_{ann})$, including the uncertainties on the four independent variables;
- 5.1.3 At the voltage V_{LL} (defined in section 5.2.1): the verification of the proportionality between leakage current and ϕ_{neq} , for the various investigated bulk materials and proton energies. The values of the damage rate α , as a function of the proton energy, are provided at five subsequent annealing steps and compared to the expectations from NIEL-based calculations in [17];
- 5.1.4 At selected reverse voltages above the voltage V_{LL} : the leakage current as a function of ϕ_{neq} . In particular, the results for the leakage current at a reverse-bias of $V=300$ V will be correlated to the results for cluster of defects from TSC measurements (performed at $V_h = 300$ V as well, as shown in chapter 6), in order to link “microscopic” defects to “macroscopic” effects (as shown later in chapter 7);
- 5.1.5 As a summary, the damage rate α as a function of the annealing time at 80°C, for the various investigated proton energies, with a comparison to the expected trend from [17];
- 5.1.6 Representative examples of IV measurements in forward bias, to prove the relaxation-likeness of silicon diodes after proton irradiations.

5.1.1 Representative examples of reverse IV

The aim of this paragraph is to provide representative examples of IV curves after proton irradiation. The cases of n-type and p-type MCz, standard FZ and deep-diffused FZ silicon pad-diodes are chosen, after irradiation with 188 MeV to a proton fluence of 10^{14} cm^{-2} .

The results are presented at five subsequent annealing steps (between 0 and 60 minutes at 80°C), for n- and p-type pad-diodes with three different bulk materials: MCz in fig. 5.1(a), standard FZ in fig. 5.1(b), and deep-diffused FZ in fig. 5.1(c). Initially, the current increases as $\sqrt{V_{reverse}}$, then it slightly increases with rates in the order of 5-2 nA/V for annealing between 0-60 minutes at 80°C (summarized in tab. 5.1). The current rate CR is defined as:

$$\text{CR} = \frac{I_{400\text{V}} - I_{200\text{V}}}{200\text{V}}. \quad (5.1)$$

Consequently, the current increase is in the order of $1 \mu\text{A}$ for a voltage change of 200 V above the voltage V_{LL} . Such increase can be explained by the trap-assisted tunneling model by G. A. Hurkx [125]. Moreover, the CR values are found to be similar for n- and p-type sensors of the same bulk material, and decrease with annealing time.

The kink between the two regimes in the IV characteristics indicates full depletion of the sensor, with n-type sensors typically reaching full depletion before p-type sensors. This is due to different radiation-induced defects with impact on the space charge density. Above the full depletion, an agreement between n- and p-type materials is found.

For all the investigated samples, no breakdown is found for $V_{reverse} \leq 400\text{ V}$.

Isothermal annealing time (min@ 80°C)	CR (nA/V) in FZ p-type	CR (nA/V) in FZ n-type	CR (nA/V) in MCz p-type	CR (nA/V) in MCz n-type
0	5.26	4.76	5.06	5.69
8	3.56	3.55	3.03	3.84
15	3.17	3.18	2.92	3.64
30	2.52	2.64	2.62	2.93
60	2.40	2.23	2.12	2.48

Table 5.1: Current Rate (CR) above depletion [200, 400] V for n- and p-type MCz and standard FZ pad-diodes, after irradiation with $E_p = 188 \text{ MeV}$ and $\phi_p = 10^{14} \text{ cm}^{-2}$, and at five subsequent annealing steps.

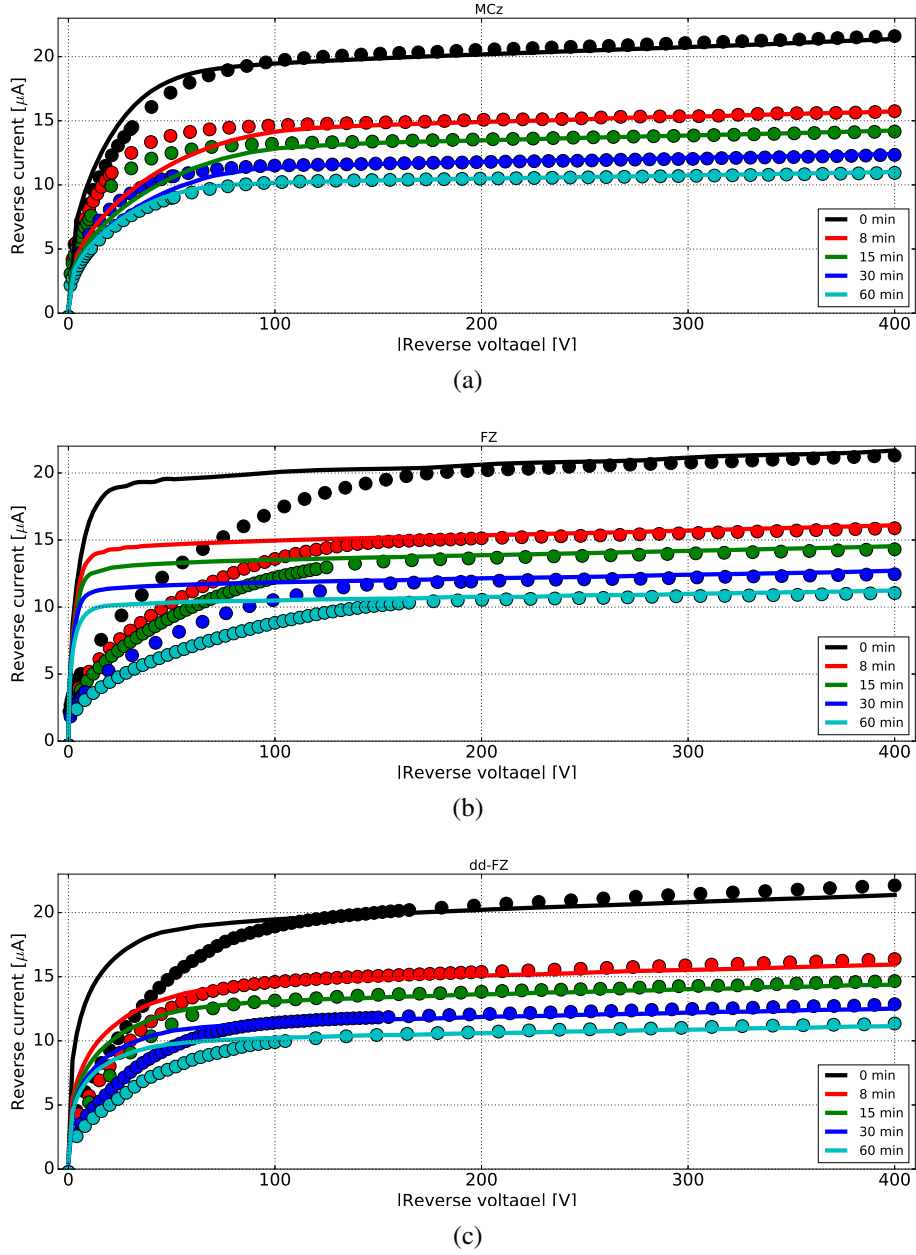


Figure 5.1: IV curves measured at $T=293$ K and at five subsequent annealing steps at 80°C , for (a) MCz silicon, (b) standard FZ and (c) deep-diffused FZ pad-diodes, after irradiation with $E_p = 188$ MeV and $\phi_p = 10^{14}$ cm^{-2} . Solid lines represent current values for n-type sensors, while dots are for p-type ones.

5.1.2 IV($E_{protons}$)

The impact of the proton energy on the leakage current is now presented for different bulk materials, after scaling the current values to the same ϕ_{neq} .

IV characteristics are shown in fig. 5.2(a)–5.2(c), after annealing of 30 minutes at 80°C, and after scaling to $\phi_{neq} = 10^{14} \text{ cm}^{-2}$ according to the results from subs. 5.1.3. A negative reverse bias is applied to p-type sensors, while a positive one is for n-type sensors.

It has to be noticed that the leakage current in the investigated sensors depends on:

$$I(\phi_{neq}, Vol, T, t_{ann}), \quad (5.2)$$

so that the error on the leakage current (for each $V_{reverse}$ step) was calculated as follows:

$$\Delta(I) = |I| \cdot \sqrt{\left(\frac{\Delta\phi_{neq}}{\phi_{neq}}\right)^2 + \left(\frac{\Delta Vol}{Vol}\right)^2 + \left(\frac{4k_B T + E_g}{k_B T} \cdot \frac{\Delta T}{T}\right)^2 + \left(\frac{\Delta t_{ann}}{\tau}\right)^2}. \quad (5.3)$$

The shadow areas around the leakage current values in fig. 5.2(a)–5.2(c) result from the error propagation on the four independent variables (see tab. 5.2). The annealing time is dominated by an estimation of the duration of the transportation of the samples from the irradiation facility to the laboratory. Potential annealing during the irradiation itself has to be considered for the irradiations with 23 GeV protons (thus the higher uncertainty on the annealing time), but expected to be negligible for the irradiations with 23 MeV and 188 MeV protons.

The calculated $\delta(I)$ are 9%, 9% and 15% for the investigated E_p of 23 MeV, 188 MeV and 23 GeV. From fig. 5.2(a)–5.2(c), it can be seen the leakage current does not show a proton-energy dependence, and it is found to scale with NIEL (as it was expected) with an accuracy at the 15% level.

Quantity	Uncertainty
ϕ_{neq}	10-20%
Sensor Volume	10%
Absolute T	0.1°C
Annealing time	10% (for 23 MeV and 188 MeV) 20% (for 23 GeV)

Table 5.2: Uncertainties on the leakage current $I(\phi_{neq}, Vol, T, t_{ann})$ resulting to the four independent variables.

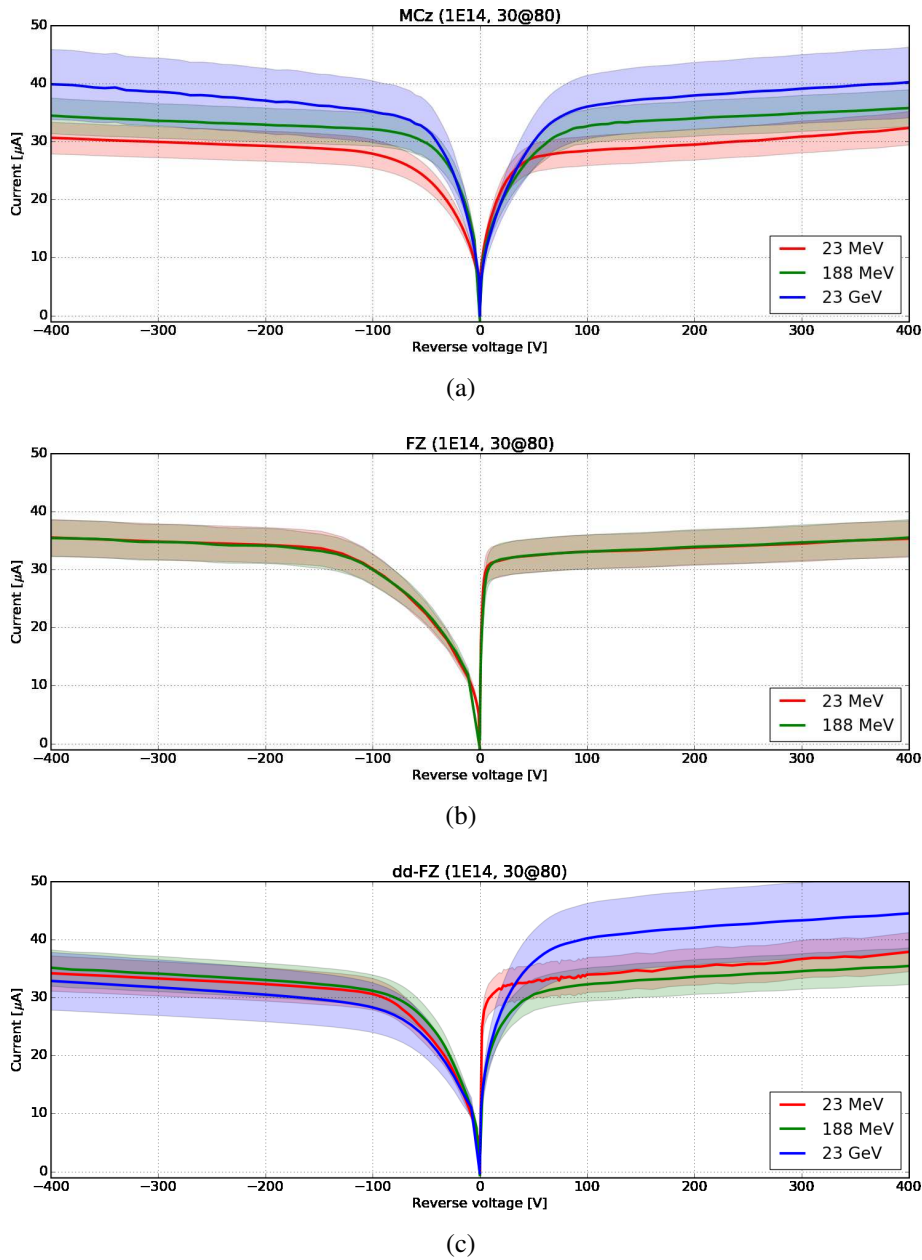


Figure 5.2: IV characteristics at reverse bias voltage ($V_{reverse} < 0$ for p-type sensors, while $V_{reverse} > 0$ for n-type sensors), as measured at $T=293$ K and at an annealing of 30 min at 80°C . Shadow areas are the spread obtained from error propagation for $I(\phi_{neq}, Vol, T, t_{ann})$ on ϕ_{neq} , sensor volume, temperature and annealing time.

5.1.3 $I(\phi_{neq})$ dependence at V_{LL}

The proportionality of the volume current (at the “depletion voltage” V_{LL}) with the neutron equivalent fluence was checked after irradiation with various proton energies.

The values of the volume current, obtained at the voltage V_{LL} , as a function of ϕ_{neq} are plotted in fig. 5.3(a)–5.3(e). For all the annealing steps, the expected proportionality from [17] is shown by dotted lines as a reference. The reference α values from measurements performed by [17] are provided in tab. 5.3.

The leakage current is set to be zero at $\phi_{neq} = 0 \text{ cm}^{-2}$. For all the different irradiations, the error on ϕ_{neq} is assumed to be 10%. The error on the leakage current is conservatively set to be 5%.

A large variation in the current values after irradiation with 23 GeV protons at $\phi_{neq} = 3 \cdot 10^{14} \text{ cm}^{-2}$ can be noticed, as already reported in [126] who mention a possible displacement of the samples with respect to the proton beam during the irradiations. Any material dependence of the radiation-induced current generation for MCz or FZ material was excluded by [126]. As a reference, shadow areas represent the 20% confidence band.

The resulting values of the damage rate α from the fit are summarized in tab. 5.3 as well, and are generally lower than the reference values (a part in the “as irradiated” case which are affected by uncertainties on the actual annealing status of the samples). In addition, the α values for each bulk material are presented as a function of the proton energy in fig. 5.4(a)–5.4(e).

A complete list of results is provided in appendix D (for various proton energies, annealing times, bulk materials and types).

Isothermal annealing time (min@80°C)	Fit to exp. data this work (10^{-17} A/cm)	Reference α measured in [17] (10^{-17} A/cm)
0	5.70 ± 0.20	5.03
8	4.08 ± 0.10	4.16
15	3.61 ± 0.10	3.77
30	3.30 ± 0.10	3.39
60	2.86 ± 0.10	2.94

Table 5.3: Calculated α values from IV measurements at $T=293 \text{ K}$, for five subsequent annealing times, and comparison with values from [17]. Fit errors are provided as well.

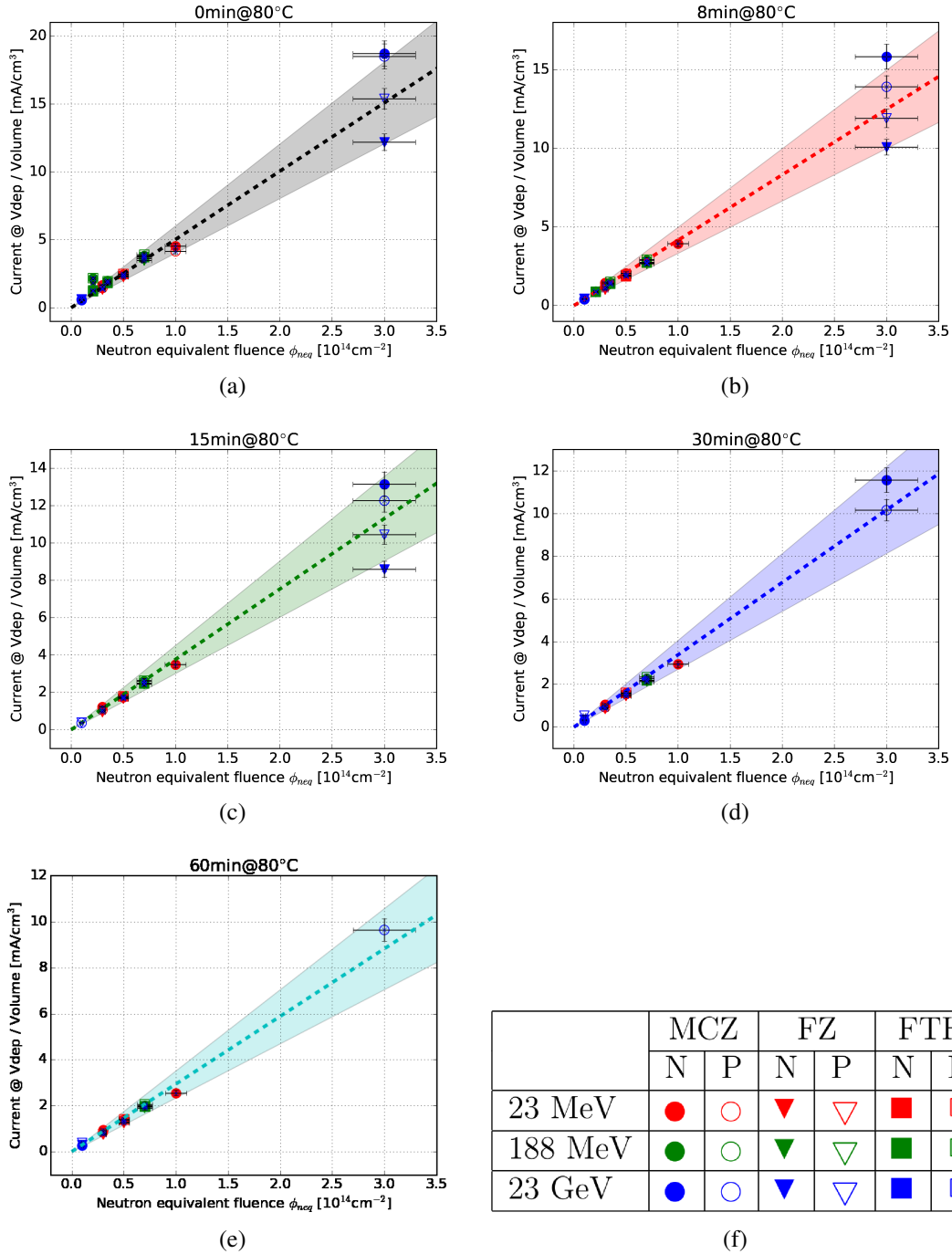


Figure 5.3: Volume-scaled leakage current at the voltage V_{LL} , as a function of ϕ_{neq} , for five subsequent annealing steps at 80°C. The symbol legend is provided in tab. 4.8 for the various investigated bulk materials and proton energies. Dotted lines are the expected trend from literature values by [17]. Shadow areas represent a 20% confidence band.

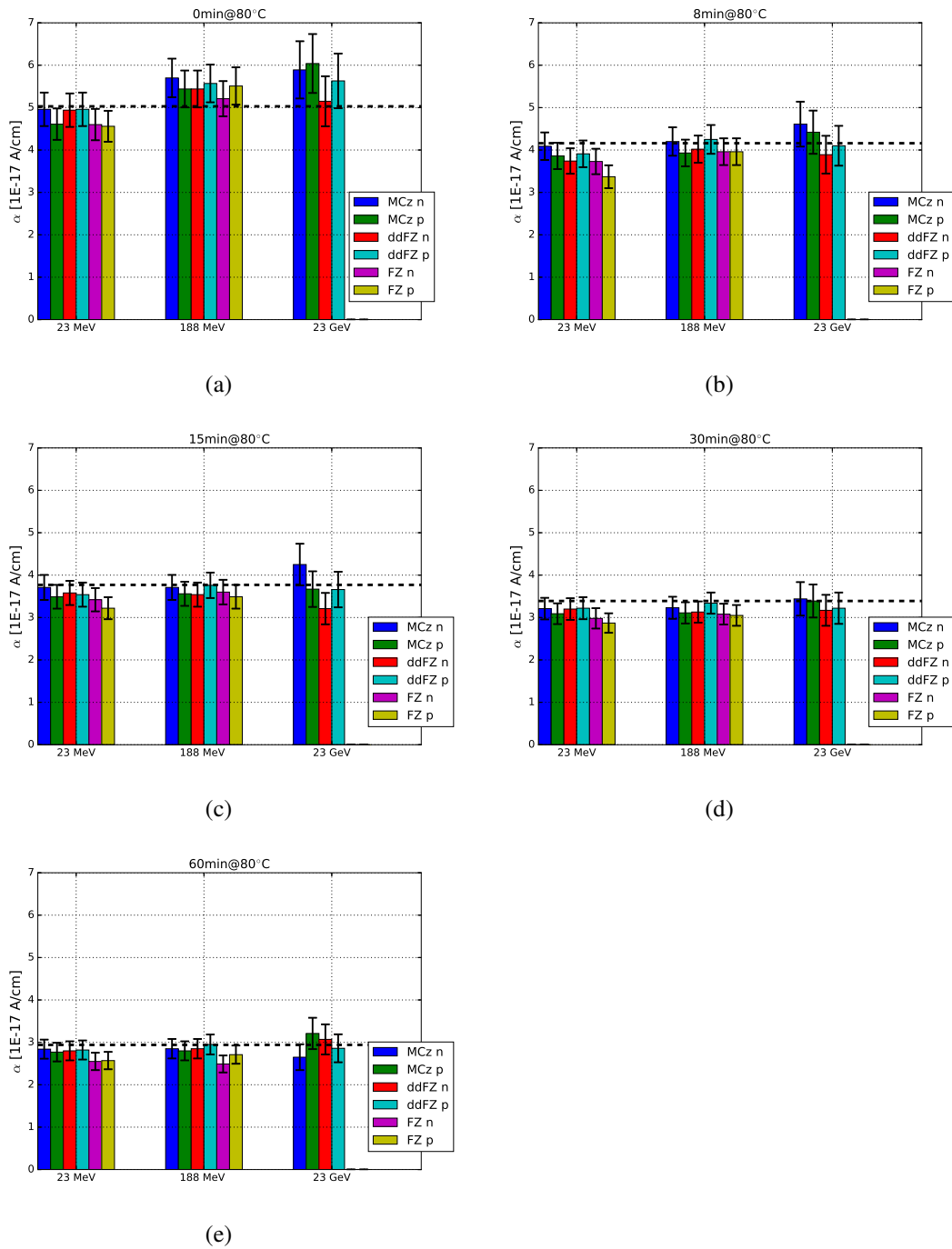


Figure 5.4: Damage rate α as a function of the proton energy, calculated for five subsequent annealing steps at 80°C. The dashed black lines are reference values from [17] (listed in tab. 5.3). The comprehensive list of results is provided in appendix D (for different proton energies, annealing times, and bulk materials and types).

5.1.4 $I(\phi_{neq})$ dependence above total depletion

The proportionality between the leakage current and the neutron-equivalent fluence ϕ_{neq} was checked also above full depletion. This subsection focuses on the results at $V_{reverse} = 300$ V, because this specific case will be useful for correlation studies (presented in chapter 7), between “macroscopic” sensor properties (from IV measurements) and “microscopic” bulk defect properties (from TSC measurements).

In the plots 5.5(a)–5.5(e), the volume current is plotted as a function of the ϕ_{neq} in the fluence range $[0.1, 3] \cdot 10^{14} \text{ cm}^{-2}$, for values of $V_{reverse} = 300$ V. The slope of the fit (with a function proportional to ϕ_{neq}) is defined to be $k_{LC,\phi}$:

$$\frac{I_{300V}}{Vol} = k_{LC,\phi} \cdot \phi_{neq}. \quad (5.4)$$

The resulting values of $k_{LC,\phi}$ are summarized in tab. 5.4, denoting a decreasing $k_{LC,\phi}$ for increasing annealing times. The obtained values for $k_{LC,\phi}$ at 300 V are slightly higher than the reference values at the depletion voltage, as expected from [17] and given the current rate above depletion (see tab. 5.1).

The leakage current is set to be zero at $\phi_{neq} = 0 \text{ cm}^{-2}$. For all the different irradiations, the error on ϕ_{neq} is assumed to be 10%. The error on the leakage current is conservatively set to be 5%, which is the maximum variation of the leakage current in the range [250, 350] V.

Isothermal annealing time (min@80°C)	$k_{LC,\phi}$ from fit for (MCz, FZ, dd-FZ) (10^{-17} A/cm)
0	5.73 ± 0.10
8	4.37 ± 0.10
15	3.88 ± 0.10
30	3.42 ± 0.10
60	3.01 ± 0.10

Table 5.4: Calculated values of $k_{LC,\phi}$ from IV measurements (at T=293 K and $V_{reverse} = 300$ V). Fit errors are provided as well.

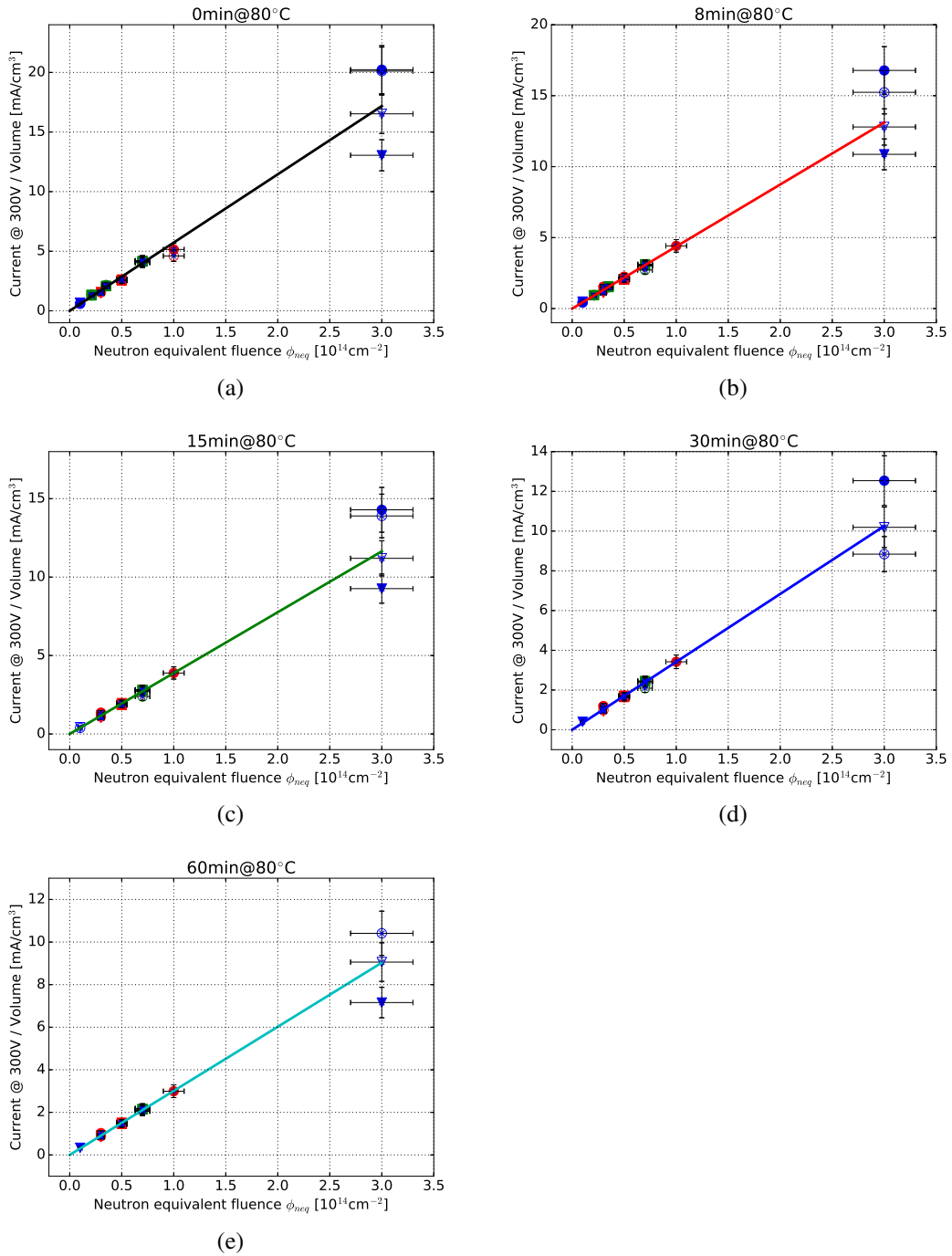


Figure 5.5: Volume-scaled leakage current at 300 V, as a function of ϕ_{neq} , for five subsequent annealing steps at 80°C. The symbol legend is provided in tab. 4.8. Solid lines are fit to data, with proportionality factors $k_{LC,\phi}$ presented in tab. 5.4.

5.1.5 Volume current annealing

Following the facts that the volume current scales with ϕ_{neq} and does not show a material dependence (therefore no dependence on the oxygen concentration), the mean values of the damage rate α (from the calculations presented in subs. 5.1.3) are now compared after irradiation with different proton energies and monitored as a function of the annealing time. The resulting values for $\alpha(t_{ann})$ are provided in tab. 5.5, with the corresponding plot in fig. 5.6(a). It can be noticed that the

	0min		8min		15min		30min		60min	
	$\bar{\alpha}$	STD								
23 MeV	4.77	0.20	3.78	0.24	3.49	0.17	3.10	0.14	2.73	0.13
188 MeV	5.48	0.16	4.05	0.14	3.61	0.10	3.16	0.11	2.78	0.16
23 GeV	5.68	0.39	4.26	0.32	3.70	0.43	3.31	0.13	2.95	0.25

Table 5.5: Mean ($\bar{\alpha}$) and standard deviation (STD) values (in 10^{-17} A/cm units) for the damage parameter α , calculated for three various proton energies and monitored at five isothermal annealing steps at 80°C.

$\bar{\alpha}$ decreases with increasing annealing time, while it increases with increasing proton energy. The latter observation is probably due to the fact that for higher energies more cluster defects are formed, therefore higher current and α values are found.

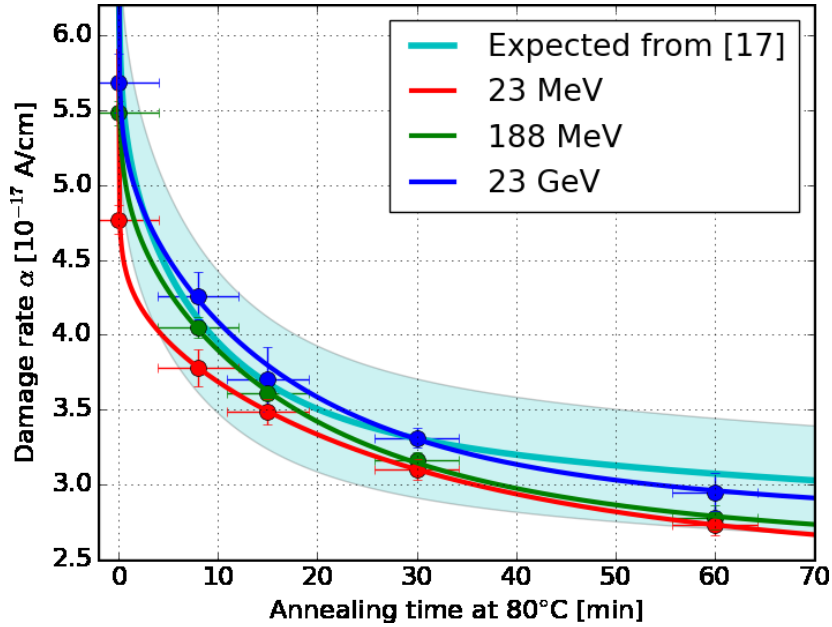
The values of $\bar{\alpha}(t_{ann})$ were fitted by the function [17]:

$$\alpha(t_{ann}) = \alpha_0 + \alpha_I \cdot \exp\left(-\frac{t_{ann}}{\tau_I}\right) - \beta \cdot \ln\left(\frac{t_{ann}}{t_0}\right), \quad (5.5)$$

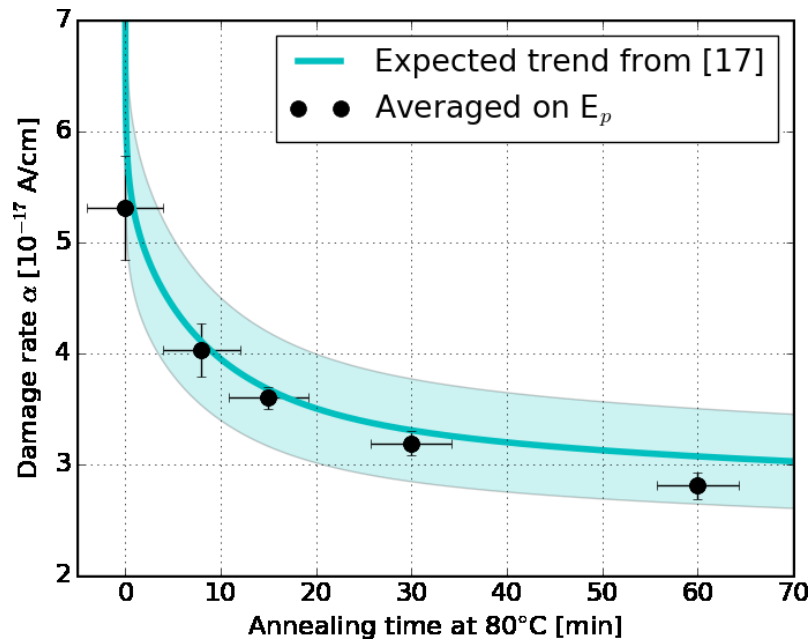
with the long term annealing at room temperature and the annealing at higher temperatures described by an exponential and a logarithmic term, respectively. The fifth parameter t_0 is set equal to 1 min. The resulting fit parameters for the various proton energies are provided in tab. 5.6. The higher values for $\alpha(t_{ann})$ after irradiation with 23 GeV protons results from higher values for α_0 and α_I with respect to irradiation by lower energy protons.

However, it must be kept in mind that the obtained alpha values depend on many physical quantities: the annealing time, the calculated neutron equivalent fluence, the measured sensor volume, the temperature during the irradiation itself and during the IV/CV and TSC measurements. If averaged over the proton energies, the alpha values are in agreement within 14% with the expectation from [17], as indicated in fig. 5.6(b) by the reference (cyan) area.

The damage constant can be considered as a measure of the concentration and generation rate of mid-gap centers. A detailed investigation of bulk defects with impact on the leakage current will be given in chapter 6.



(a)



(b)

Figure 5.6: Annealing evolution of the damage rate α for (a) various proton energies and (b) averaged on the proton energies. The reference trend from [17] is shown by the (cyan) line; the shadow (cyan) area represents a $\pm 14\%$ confidence band.

Parameter	Ref. from [17]	23 MeV	188 MeV	23 GeV
α_0 (10^{-17} A/cm)	4.2	3.3	3.7	3.8
α_I (10^{-17} A/cm)	1.1	1.1	1.3	1.4
τ_I (min)	9.0	28.2	18.0	16.7
β (10^{-17}) A/cm	0.28	0.16	0.22	0.21

Table 5.6: Fit parameters for the annealing of the volume current (specific for an annealing temperature of 80°C), according to [17]. The corresponding fit function is displayed in fig. 5.6(a) and fig. 5.6(b) as solid (cyan) lines.

5.1.6 Representative examples of forward IV

After proton irradiations, current-voltage characteristics in forward bias can be used to study the relaxation-likeness of silicon diodes due to the high density of generation-recombination centers. The transition from a lifetime material (before irradiation) to a recombination material (after irradiation) can be observed by comparing the value of the dielectric relaxation time τ_D to the value of the minority carrier recombination time τ_0 (see tab 5.7 for reference values).

On one hand, the dielectric relaxation time represents the time in which a space charge is neutralized by the flow of the produced free carriers that are slowed down by the resistance. In other words, it is the bulk equivalent of the time constant of an RC circuit. It is possible to compute τ_D from $\rho\epsilon\epsilon_0$ [127], and then to remember that the charge rapidly flows to restore the equilibrium phase.

On the other hand, the carrier recombination time τ_0 is the time constant for recombination of non-equilibrium electron-hole pairs or excess minority carriers. It is also the time needed to generate electron-hole pairs to reach equilibrium. Here, representative forward IV characteristics are presented after proton irradiation, and the underlying physical principles are summarized from [127].

If the Fermi level is pinned near the mid-gap position by intrinsic condition, the electron conductivity balances the hole conductivity ($\sigma_n = \sigma_p$), so that the carrier drift components $\mu_n n_{max}$ and $\mu_p p_{max}$ become equal. The quantities μ_n

MATERIAL	ρ	τ_D	τ_0
LIFETIME ($\tau_D \ll \tau_0$)	$\approx 2 \text{ k}\Omega\cdot\text{cm}$	$\approx 2 \text{ ns}$	$\approx \text{ms}$
RELAXATION ($\tau_D \gg \tau_0$)	$\approx \rho_{intrinsic} \approx 300 \text{ k}\Omega\cdot\text{cm}$	$\approx 0.3 \mu\text{s}$	$\approx 10\text{-}100 \text{ ns}$

Table 5.7: Reference values for the dielectric relaxation time τ_D and minority carrier recombination time τ_0 in lifetime- and relaxation-like materials.

and μ_p represent the electron and hole mobilities, respectively; n_{max} and p_{max} the corresponding carrier densities at maximum resistivity. Remembering that $n_i^2 = n_{max}p_{max}$, and that the following expression holds for ρ_{max} :

$$\frac{1}{\rho_{max}} = q_0 (\mu_n n_{max} + \mu_p p_{max}). \quad (5.6)$$

The maximum carrier relations for n_{max} and p_{max} can be exploited to evaluate the minimum conductivity σ_{min} in terms of the intrinsic carrier density n_i :

$$\begin{cases} n_{max} = (\mu_p/\mu_n)^{1/2} \cdot n_i \\ p_{max} = (\mu_n/\mu_p)^{1/2} \cdot n_i \end{cases} \rightarrow \sigma_{min} = 2q_0(\mu_n\mu_p)^{1/2} \cdot n_i.$$

Therefore, σ_{min} does not depend on the extrinsic doping. In the present calculations, the intrinsic carrier density n_i is obtained according to [128]:

$$n_i = 1.541 \times 10^{15} T^{1.712} \cdot \exp\left(-\frac{E_g^0}{2k_B T}\right), \quad (5.7)$$

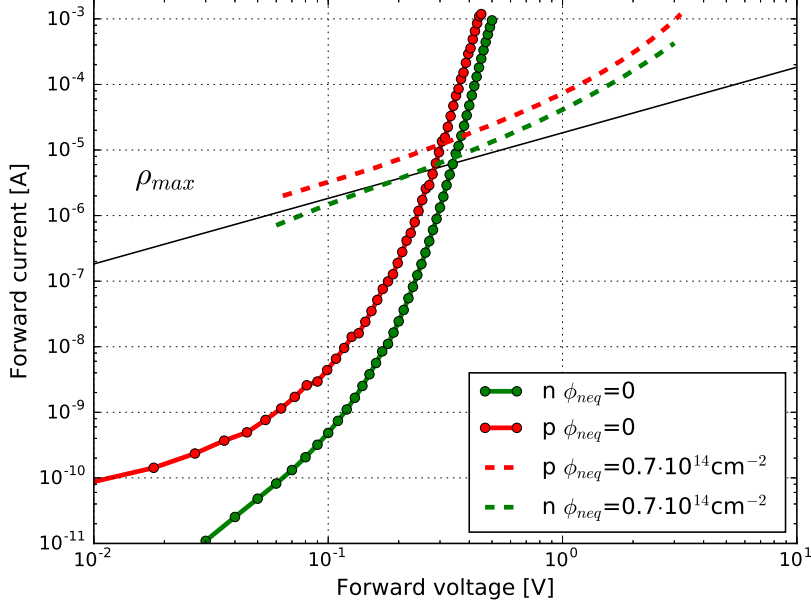
and $n_i = 5.3 \cdot 10^9 \text{ cm}^{-3}$ for silicon at $T=293 \text{ K}$. The resulting maximum resistivity ρ_{max} for silicon at $T=293 \text{ K}$ is $6.83 \times 10^5 \text{ } \Omega \cdot \text{cm}$; from such value of ρ_{max} it is possible to obtain the device resistance $R_{max} = d\rho_{max}A^{-1}$, for a sample with a thickness d and active area A (in this case, $d = 200 \text{ } \mu\text{m}$ and $A = 0.25 \text{ cm}^2$).

The double-logarithmic plot of fig. 5.7(a) presents the forward current at $T=293 \text{ K}$, as a function of the forward voltage in standard FZ diodes, before and after proton irradiation. The solid curves indicate that both n-type (in green) and p-type (in red) materials are lifetime-type prior to proton irradiations. Afterwards, the forward IV curves (dotted lines) tend to the maximum resistivity line for both material types. The same considerations are valid for MCz diodes; in the following the focus is on p-type diodes. For p-type MCz diodes, the forward current characteristics are measured before and after proton irradiation at six different ϕ_{neq} fluences in the range $[0.1, 3] \cdot 10^{14} \text{ cm}^{-2}$. In fig. 5.7(b), the orange curve indicates that the material was lifetime prior to radiation damage ($\phi_{neq} = 0 \text{ cm}^{-2}$). As the fluence increases, the current tends to the maximum resistivity line. Moreover, the current limit of 1 mA is reached at increasing forward voltage bias; this hints to a progression of the material to relaxation type, too.

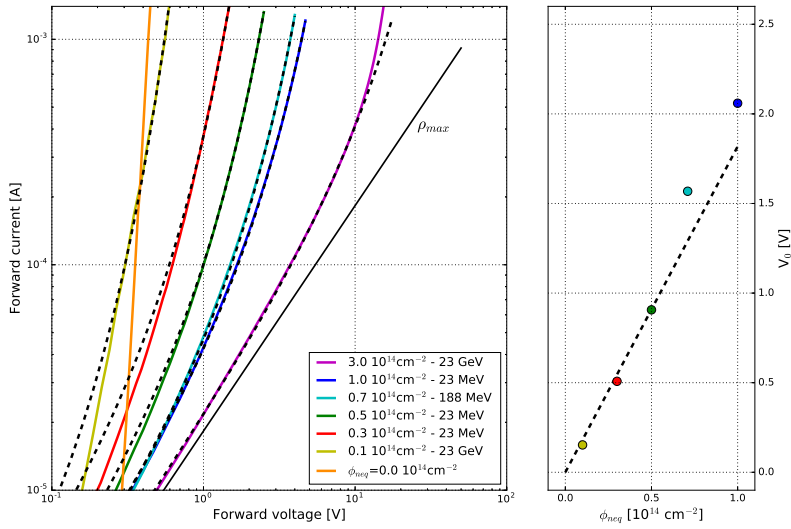
According to [127], it was found that forward IV-characteristics of irradiated diodes can be described by an empirical relation of the form:

$$I_F = G_0 V_F \exp(V_F/V_0), \quad (5.8)$$

being I_F the forward current resulting from a forward bias V_F . The voltage $V_0 = E_0/d$ and the conductance $G_0 = 1/R_0$ are fit parameters, and provide the degree of



(a)



(b)

Figure 5.7: (a) Forward IV for n-type (green) and p-type (red) standard FZ diodes, before (solid lines) or after (dotted lines) irradiation with 188 MeV protons and annealing of 60 min at 80°C. (b-left) Forward IV for p-type MCz diodes after proton irradiations and annealing of 60 min at 80°C; measured characteristics (solid coloured lines) are fitted (dotted lines) with eq. 5.8. (b-right) Corresponding V_0 as a function of ϕ_{neq} from fit (dotted black lines) with eq. 5.8. Black solid lines indicate the limit of maximum resistivity ρ_{max} (see eq. 5.6).

$\phi_{neq} [10^{14} \text{ cm}^{-2}]$	0.1	0.3	0.5	0.7	1.0	3.0
$V_0 [\text{V}]$	0.15	0.51	0.91	1.57	2.06	14.16
$G_0 [10^{-6} \Omega^{-1}]$	50	52	33	25	26	20

Table 5.8: Fit parameters V_0 and G_0 from eq. 5.8, for MCz p-type sensors after proton irradiation at increasing ϕ_{neq} , and annealing of 60 min at 80°C.

relaxation-likeness (see tab. 5.8). The factor G_0V_F represents the ohmic behavior at low forward bias V_F . At higher forward bias V_F , a rapid increase of the current occurs and $V_0 = F_0d$, with F_0 being the average electric field in a diode of thickness d . The quantity V_0 (or, alternatively, F_0) is assumed to be a good measure of the relaxation likeness of the material [127]. This relation fits the current data up to 10^{14} cm^{-2} (dotted black lines in fig. 5.7(b)), and the fitting parameter V_0 can be obtained from fit to data starting from 0.1 V, a lower limit posed by the sensitivity of the electrometer.

From the proportionality between V_0 and the fluence, it is found that:

$$dV_0/d\phi = 1.82 \cdot 10^{-14} \text{ V} \cdot \text{cm}^2, \quad (5.9)$$

in the fluence range $[0.1, 1] \cdot 10^{14} \text{ cm}^{-2}$ and after annealing of 60 min at 80°C. In such range the value of V_0 increases from 0.15 V to 2.06 V; the conductance G_0 is found to decrease from 50 to 20 $(\text{M}\Omega)^{-1}$.

It should be noted that after proton irradiation at $\phi_{neq} = 3.0 \cdot 10^{14} \text{ cm}^{-2}$, the data approaches the maximum resistivity line at low voltages, but deviates from the expected trend from eq. 5.8 in the final voltage range. Therefore in this case an upper limit at 10 V is set for the fit according to eq. 5.8. A dramatic increase is noted for V_0 ($=14.16 \text{ V}$, not shown in fig. 5.7(b)), with respect to those samples irradiated with $\phi_{neq} \leq 10^{14} \text{ cm}^{-2}$.

5.2 Results of CV measurements

CV(f,T) characteristics were measured in silicon pad-diodes before and after protons of various energies E_p (23 MeV, 188 MeV and 23 GeV) and neutron equivalent fluences ϕ_{neq} in the range $[0.1, 3] \cdot 10^{14} \text{ cm}^{-2}$. Three different bulk materials (both n- and p-type bulk) were investigated (MCZ, standard FZ and deep-diffused FZ). The CV(f,T) measurements were repeated at subsequent annealing steps at 80°C, from 0 to 60 min.

Several effects simultaneously occur and have an impact on the CV(f,T) characteristics of an irradiated diode: the effects of the relaxation region, the impact of deep traps and the effect of built-in charge at each contact. In the following subsections, the results from CV(f,T) measurements are presented with focus on:

- 5.2.1 The doping profile, obtained from CV measurements for non-irradiated diodes. The method is not valid for irradiated diodes because the space charge is not constant anymore as a function of the depth inside the sensor bulk;
- 5.2.2 The annealing studies, hinting to type inversion in n-type sensors after irradiation;
- 5.2.3 The deviation from the usual $V^{-1/2}$ dependence of the capacitance for irradiated diodes in reverse bias, to be analyzed with the initial rise method;
- 5.2.4 A method to analyze C(f,T) characteristics at low reverse bias;
- 5.2.5 The negative diffusion capacitance in forward bias.

5.2.1 Doping profiles before irradiation

Capacitance-voltage (CV) measurements of diodes are a standard method to determine doping profile and depletion voltage of non-irradiated diodes.

The assumptions used in deriving the junction capacitance for non-irradiated diodes include uniform doping in both p- and n-type regions, shallow donors and acceptors, an abrupt junction approximation and a planar junction. On each side of a p^+n junction, the incremental change of the charge dQ upon an incremental change of the applied voltage dV is:

$$C(V) = \frac{dQ}{dV} = \frac{dQ}{dW} \frac{dW}{dV} = A \sqrt{\frac{\epsilon_{Si} \epsilon_0 q_0 |N_{eff}|}{2V}} = \epsilon_{Si} \epsilon_0 \frac{A}{W(V)}, \quad \text{while } V < V_{dep}. \quad (5.10)$$

The capacitance shows a decrease with $V^{-1/2}$ until the applied reverse voltage $V = V_{dep}$ is enough to deplete the whole sensor. Once the depletion region reaches the

backplane ($W = d$), the junction capacitance is expected not to decrease anymore. The capacitance at full depletion is also called geometrical end capacitance C_{end} , since it depends only on the active area A and the thickness d of the diode:

$$C_{end} = \frac{\epsilon_0 \epsilon_{Si} A}{d}. \quad (5.11)$$

If $1/C^2$ is plotted as a function of the reverse voltage, two linear fits can be performed to obtain the voltage V_{LL} : one in the region of highest slope and one in the linear region of C_{end} . In the present work, the intersection point of the two fitted curves is defined as the depletion voltage V_{dep} for non-irradiated diodes. For non-irradiated diodes with known depletion voltage and active thickness d , the effective doping concentration N_{eff} in the bulk of the sensor can be calculated by using the equation:

$$N_{eff} = \frac{2\epsilon_0 \epsilon_{Si}}{q_0 d^2} \cdot V_{dep}. \quad (5.12)$$

A further analysis of CV-characteristics provides the doping density $N_D(x)$ as a function of the distance x from the p^+n junction:

$$x(V) = \frac{\epsilon_0 \epsilon_{Si} A}{C(V)} \quad \text{and} \quad N_D(x(V)) = \frac{2}{q_0 \epsilon_0 \epsilon_{Si} A^2} \frac{1}{\frac{d(1/C^2)}{dV}}. \quad (5.13)$$

Typical doping concentration in n-bulk silicon sensors are of the order of 10^{12} cm^{-3} , while the n^+ or p^+ implants have higher doping concentrations (with typical peak concentrations of $10^{18} - 10^{19} \text{ cm}^{-3}$).

The results are shown in fig. 5.8 for n- and p-type bulk materials, before irradiation. MCz and standard FZ are produced on $200 \mu\text{m}$ thick wafers, with sharp transition between low doped active sensor volume and the highly doped rear side, while deep-diffused FZ diodes have a physical thickness of $300 \mu\text{m}$. In the special case of dd-FZ diodes (after the deep-diffusion process), the transition between the (high doped) rear side and the (low doped) active volume is not as sharp as it can be observed for MCz and standard FZ diodes. In fact, due to the long diffusion times of the dopants, the transition is not abrupt.

It is worth specifying here that, in the present calculations, the area is assumed to be constant; for more accurate evaluations the edge effects have to be taken into account, since they were found to be voltage-dependent, and particularly relevant for smaller diodes in area than the ones considered in the present study [129].

5.2.2 Annealing and type inversion

Annealing studies of CV(f,T) characteristics were performed for a wealth of reasons. Practically, the CV(f,T) characteristics were always measured before TSC

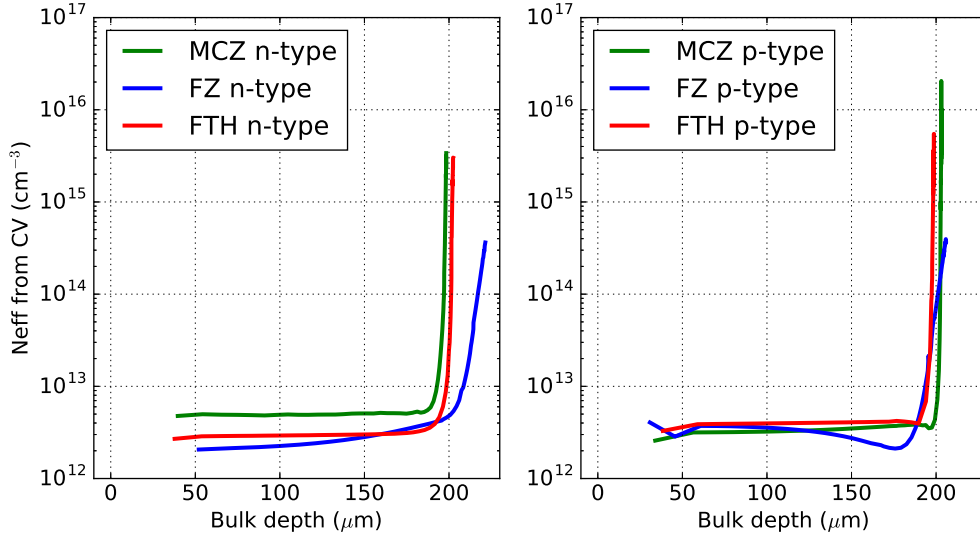


Figure 5.8: Depth profiles of the doping concentration from CV measurements ($T=293$ K, $f=10$ kHz): non-irradiated (left) n-type diodes and (right) p-type diodes.

measurements up to 400 V, in order to guarantee that a reverse bias of 300 V is enough to fully deplete the sensors during the heating phase. Any possible early breakdown was excluded by previously performed IV measurements. The reverse bias of 300 V is chosen as a reference for comparison of all the measured TSC spectra and it is a compromise for measuring well above depletion but below potential early breakdown. In fact, TSC measurements at reverse biases lower than 200 V are not always comparable because not all the investigated proton-irradiated samples are found to be fully depleted under such (lower) bias.

Fig. 5.9 shows an example of CV measurements for proton-irradiated n- and p-type MCz silicon diodes, measured at $T=293$ K and frequency of 10 kHz, and repeated at subsequent annealing steps at 80°C . Each CV curve is shifted by $5 \cdot 10^{-20} \text{ F}^{-2}$ for improving the visibility. As a general observation, the depletion voltage is slightly increased after proton-irradiation of a p-type MCz diode with 23 MeV protons and $\phi_{neq} = 10^{14} \text{ cm}^{-2}$ (the reference value of 160 V before irradiation is shown by the dashed black line in fig. 5.9(left)). The opposite effect is noted for the corresponding n-type sample.

The annealing studies provides also hints for the type inversion of n-type diodes, whose structure changes to p^+pn^+ and depletes from the the pn^+ junction.

Tab. 5.9 summarizes the information from annealing studies regarding the type inversion of n-type diodes, after proton irradiation. For all the three proton en-

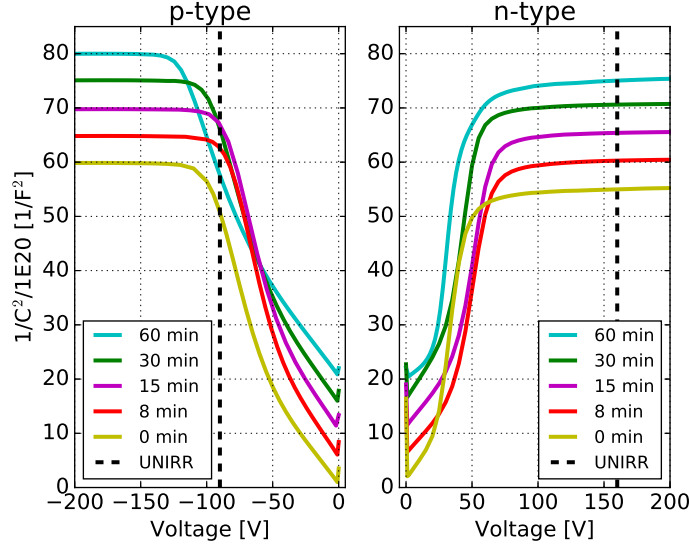


Figure 5.9: CV curves at subsequent annealing steps for MCz n- and p-type sensors, after irradiation with 23 MeV protons and $\phi_{neq} = 10^{14} \text{ cm}^{-2}$. Each CV curve is shifted by $5 \cdot 10^{-20} \text{ F}^2$ for improving visibility. The reference depletion value before irradiation is indicated by a dashed black line.

ergies, the highest ϕ_{neq} was considered; no type inversion is seen for MCz and dd-FZ diodes, while type inversion occur for standard FZ diodes already after irradiations with 188 MeV protons (at $\phi_{neq} = 7 \cdot 10^{13} \text{ cm}^{-2}$). Type inversion occurs instead for standard FZ diodes also after irradiation with 23 MeV protons (at $\phi_{neq} = 10^{14} \text{ cm}^{-2}$), and for such proton energies it was already reported after $\phi_{neq} = 7.8 \cdot 10^{13} \text{ cm}^2$ in [126]). The reason is explained in subs. 6.3.3.

E_p	MCz		dd-FZ		FZ	
	ϕ_{max} [10^{14} cm^{-2}]	Type	ϕ_{max} [10^{14} cm^{-2}]	Type	ϕ_{max} [10^{14} cm^{-2}]	Type
23 MeV	1.0	n	1.0	n	1.0	p
188 MeV	0.7	n	0.7	n	0.7	p
23 GeV	3.0	n	3.0	n		

Table 5.9: Summary of type inversion studies for n-type sensors at the highest ϕ_{neq} for various proton energies, after monitoring CV(f,T) measurements in 5 subsequent annealing steps.

5.2.3 The initial rise method

By looking at the CV measurements in fig. 5.9 and fig. 5.10(a), it is possible to note the deviation of the capacitance from the $V^{-1/2}$ dependence found in non-irradiated diodes: the conventional analysis to determine the depletion voltage from the slope of the curve is therefore not applicable.

Here, the initial rise method is proposed as a way to determine the space charge [NCV] from the slope of the $1/C^2$ characteristics (see eq. 5.13), in the low bias range (below 20 V), i.e. with insufficient concentration of free charge carriers to fill deep traps. The method is especially relevant at high fluences, and in particular after the irradiation with $E_p = 23$ GeV for which CV measurements are analyzed after $\phi_{neq} = 3 \cdot 10^{14} \text{ cm}^{-2}$ (fig. 5.10(b)). It should be noted that [NCV] is an average value of the space charge, i.e. no strong electric field dependence nor depth dependence are assumed.

The results about the space charge concentration from the application of the initial rise method ([NCV] in units of cm^{-3}), will be then compared to the results from TSC measurements ([NTSC] in units of cm^{-3}) in chapter 7.

5.2.4 Analysis of CV(f,T)

Here the focus is on the frequency dependency of the capacitance at low reverse bias which is due to the presence of deep levels. The scope is to obtain information about deep levels, by measuring the junction capacitance over a wide frequency

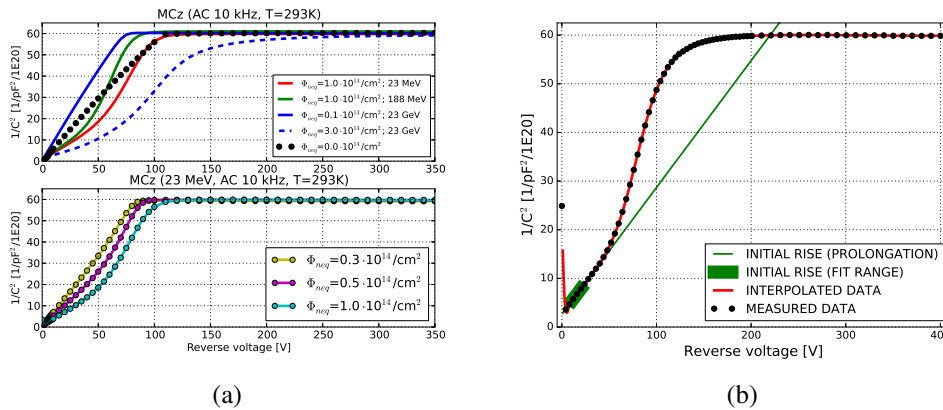


Figure 5.10: CV measurements in reverse bias for p-type MCz diodes: (a-top) after irradiation at various E_p and fluences; (a-bottom) after irradiation with $E_p = 23$ MeV and three ϕ_{neq} . (b) Application of the initial rise method for a p-type MCz diode irradiated with 23 GeV protons and $\phi_{neq} = 3 \cdot 10^{14} \text{ cm}^{-2}$.

range, and deduce the presence of two main categories of deep traps in the proton-irradiated samples. The analysis will be further developed in chapter 7 to obtain the activation energy.

The measurements of $C(f,T)$ are performed in parallel mode, with AC frequency in the range [100 Hz, 1 MHz] and 200 mV amplitude; the DC voltage is -5 V. The temperature varies between [253, 293] K. The applied method was derived by [130] for the analysis of neutron irradiated silicon diodes; here it is tested for p-type MCz diodes after proton irradiation (see fig. 5.11(a)–5.11(c)). According to the method by [130], the total capacitance is assumed to have two contributions:

$$C(f) = C_1(f) + C_2(f), \quad (5.14)$$

with

$$\left| \begin{array}{l} C_1(f) = C_\infty + \frac{(C_{L1} - C_\infty)}{1 + (f/f_1)^\alpha}, \\ C_2(f) = \frac{C_{L2}}{1 + (f/f_2)^\beta}. \end{array} \right.$$

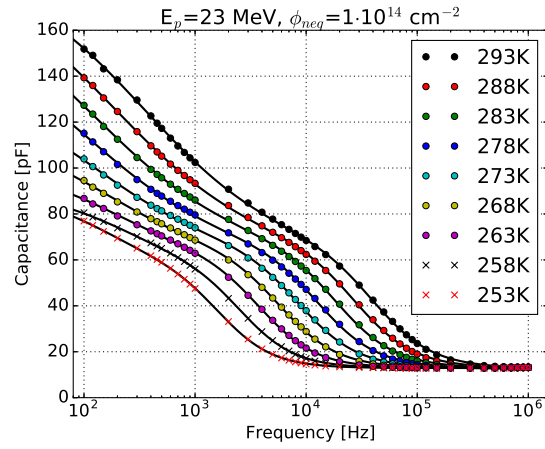
In the model by [130], C_{L1} and C_∞ are the low and high frequency junction capacitance. The frequency associated with the first deep level of finite concentration is f_1 . The same definitions are valid for the parameters in $C_2(f)$.

The low frequency capacitance is related to deep and shallow impurities, while the high frequency capacitance is related to the free carrier density [131]. In all the cases presented in fig. 5.11(a)–5.11(c), it is possible to note the strong frequency dependence of the junction capacitance; at a fix voltage, the total capacitance decrease with increasing frequency. At high frequency (or equivalently, and low temperature), the curves flatten to the value of the geometrical capacitance. The total capacitance is also found to increase with increasing temperature. In fact, the dependence of the capacitance on the frequency is directly related to the presence of shallow traps which respond to the AC test signal at low reverse voltage and low frequency ($f \ll e_n + e_p$). In the high frequency limit ($f \gg e_n + e_p$), no contribution from deep traps can be seen, but only the movement of free carriers at the edge of the depletion region. All the fit parameters for the measurements in fig. 5.11(a)–5.11(c) are available in tab. 5.10.

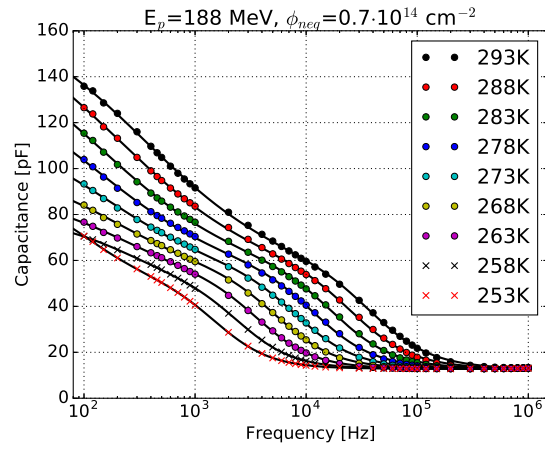
5.2.5 Capacitance in forward bias

One of the main effects of radiation damage in silicon is the establishment of a negative diffusion capacitance in forward bias. We report here the results for p-type MCz diodes as a representative example.

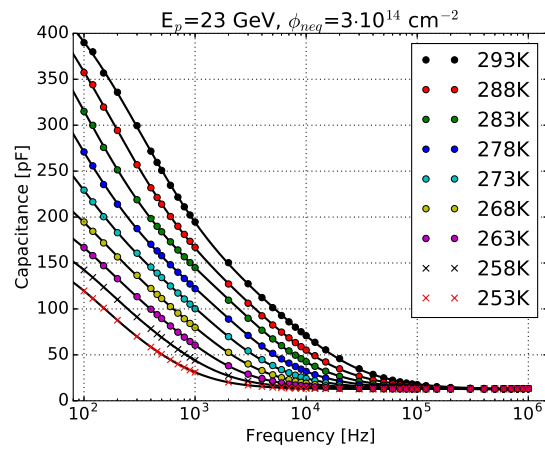
Fig. 5.12 shows the capacitance measured at $T=293$ K and AC test frequency of



(a)



(b)



(c)

Figure 5.11: $C(f,T)$ characteristics at low DC voltage (-5 V) and AC voltage (0.2 mV), for three samples irradiated with various proton energies and ϕ_{neq} . Lines are fits to data points with the method in eq. 5.14.

E_p	23 MeV	188 MeV	23 GeV
$\phi_{neq} [\text{cm}^{-2}]$	$1.0 \cdot 10^{14}$	$0.7 \cdot 10^{14}$	$3.0 \cdot 10^{14}$
253 K			
C_∞ [pF]	12.9	12.9	12.9
C_{L1} [pF]	58	50	57
f_1 [Hz]	1667	1583	602
α	1.787	1.75	1.62
C_{L2} [pF]	31.1	43.46	109
f_2 [Hz]	148	93	129
β	1.24	1.27	1.51
273 K			
C_∞ [pF]	12.7	12.7	12.6
C_{L1} [pF]	63.1	53.9	114.4
f_1 [Hz]	882	839	1804
α	1.67	1.64	1.30
C_{L2} [pF]	73.4	65.4	263
f_2 [Hz]	127	160	80.4
β	0.80	0.82	1.01
293 K			
C_∞ [pF]	12.4	12.3	12.3
C_{L1} [pF]	630	53.4	104
f_1 [Hz]	4097	3926	968
α	1.67	1.63	1.30
C_{L2} [pF]	125	117	383
f_2 [Hz]	349	354	311
β	0.72	0.69	0.96

Table 5.10: Fit parameters according to the model in eq. 5.14, for the three samples in fig. 5.11(a)–5.11(c).

10 kHz, in the voltage range $[-10, V_{f,max}]$, where $V_{f,max}$ is the forward reverse voltage at which a current of 1 mA is previously recorded from IV measurements on the same device in forward bias.

From fig. 5.12 it is possible to note that the capacitance of a non-irradiated diode is positive both in reverse and forward bias; moreover, the forward capacitance increases with increasing bias voltage. After proton irradiation with $0.3 \cdot 10^{14} \text{ cm}^{-2} \leq \phi_{neq} \leq 3 \cdot 10^{14} \text{ cm}^{-2}$, we note that the forward capacitance is negative instead, and the absolute value increases with increasing forward voltage. Recalling that $C = \frac{dQ}{dV}$, it follows that a negative capacitance has to be established because $\frac{\Delta Q}{\Delta V} < 0$.

The fact that the forward capacitance is negative is another evidence that the material has changed from lifetime to relaxation semiconductor, as it was already noticed by analyzing the IV measurements in forward bias (see subs. 5.1.6).

In fact, relaxation-like materials have high resistivity and also a large density of generation-recombination (GR) centers which are near to the middle of the band gap, and easily interact with E_C and E_V . Therefore, electron-hole pairs can be easily created or recombined (in lifetime materials, these are slow processes requiring thermal generation in the band gap instead). The (two steps) thermal excitation via GR centers is therefore more efficient than a direct (one step) thermal excitation of electrons in the valence band to the conduction band.

The phenomenon of negative diffusion capacitance in forward bias is explained in [100], and by considering the band diagram in fig. 5.13. The Fermi level is near the conduction band in the low resistance contact, while it is near midgap in the relaxation semiconductor (due to the presence of GR centers and the fast GR processes). The material is actually p-type only far from the n^+p junction.

A dipole with (+) pole in the highly doped contact, and (-) pole in the semiconductor with free electrons but few fixed ionized traps, induces a potential step of about half the band gap. In forward bias, holes are injected and readily recombine with negative free carriers near the junction: the dipole charge is reduced, and the recombination process is so strong that the capacitance eventually becomes nega-

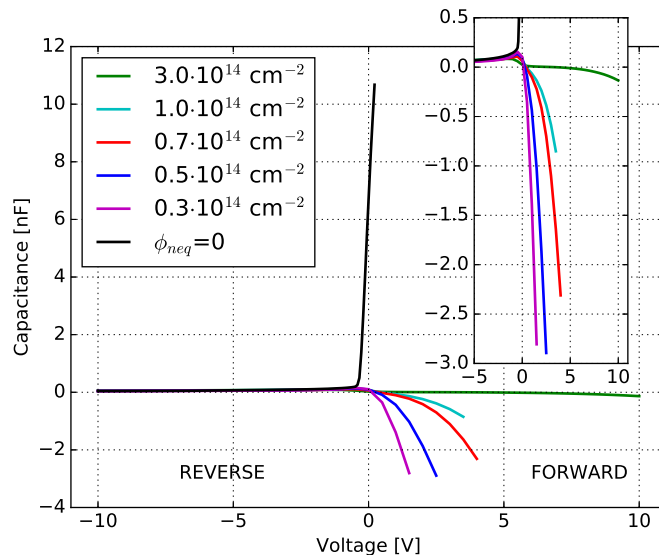


Figure 5.12: CV characteristics for p-type MCz diodes before and after irradiation; the inset shows a zoom in the forward reverse bias for irradiated diodes. The current limit is set at 1 mA.

tive.

From fig. 5.12 it is also possible to note that the higher the fluence the less negative the capacitance is. Once again, two competing effects shall be considered: on one hand, the increase in the density of GR centers tend to increase the recombination-generation rate, trying to enhance the negative capacitance effect. On the other hand, the density of deep levels increases as well, and “delays” the effect at higher frequencies (or, equivalently, at lower temperatures). The latter effect prevails on the former [132]; as a result, the capacitance is less negative at higher fluences (see the case of $3 \cdot 10^{14} \text{ cm}^{-2}$, i.e. the highest ϕ_{neq} presently considered, in fig. 5.12).

The relaxation effect is also responsible for reducing the positive capacitance at low reverse bias, thus introducing a characteristic peak at low reverse bias voltages [133] (equivalently, for the low valley in the $1/C^2$ characteristics, as it is possible to note in fig. 5.9).

It is worth recalling that CV characteristics after irradiation are temperature and frequency dependent (because of the presence of deep traps, see subs. 5.2.4); the scope here is to show the low frequency and high temperature limit: at high frequency (or, equivalently, at low temperature), the negative capacitance is expected not to be observable, because carriers would not be able to respond to the AC signal, resulting in a constant capacitance over a wide voltage range.

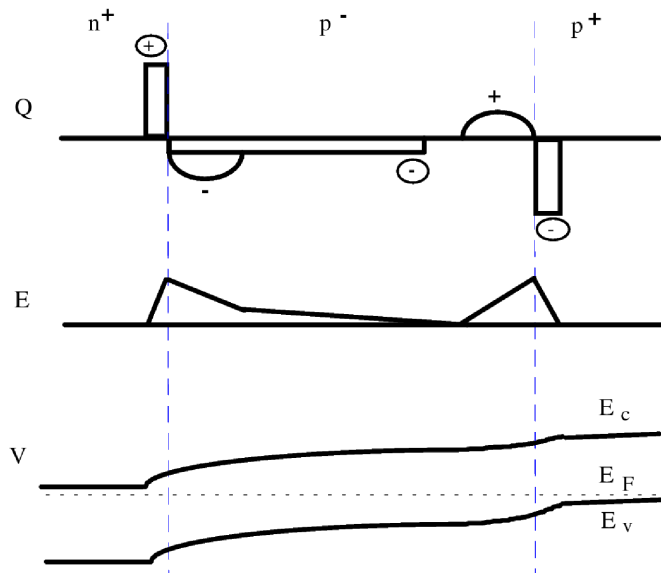


Figure 5.13: (top) Dipole near the junction between the highly doped n^+ contact and the relaxation-like part of a p-type semiconductor, and corresponding (middle) electric field and (bottom) band banding [100]. ($T=293 \text{ K}$, AC freq= 10 kHz).

“Microscopic” approach

The identification of the radiation-induced defects and their effects are of crucial importance for further development of radiation-hard silicon sensors. Projections for a successful long-term operation of silicon sensors are only possible if the damage parameters and their annealing dependence are known.

This chapter is dedicated to the results of Thermally Stimulated Current (TSC) measurements for bulk defects identification in proton-irradiated silicon diodes. In section 6.1, the most striking parameters for successfully performing a TSC scan are presented. Section 6.2 describes the standard approach to the analysis of TSC spectra at the conventional filling temperature of 10 K, and defect concentrations are provided in section 6.3, with focus on the introduction rates for defects affecting the space charge and the leakage current.

Additionally, TSC measurements are performed also with filling temperature higher than 10 K, and analyzed in section 6.4 according to the Multi-Phonon Emission model. A third analysis method is presented in section 6.5, for interpreting TSC measurements in the presence of proton-induced cluster-related defects.

6.1 TSC measurement settings

Setting up a TSC measurement for an irradiated silicon diode requires the knowledge of sample-related parameters (such as the forward voltage to provide a current of ≈ 1 mA at $T=10$ K), as well as optimal experimental conditions (such as the filling temperature, the reverse bias voltage and heating rate). The adoption of standard settings enables comparisons between measurements on different samples (with respect to the ϕ_{neq} , proton energy or the annealing step for example), but resulting from the very same experimental procedure. In the following, the most important TSC settings are presented, together with practical examples of

their impact on the TSC spectra and hints for the further analysis of TSC spectra: the filling temperature (subs. 6.4), the filling current (subs. 6.1.1), and the heating rate β (subs. 6.1.2).

6.1.1 Filling current

The most crucial phase during a TSC scan is the filling phase, when a forward voltage V_f has to be applied (at $T=10$ K) so that a forward current of at least 1 mA is guaranteed for filling the traps. The necessary V_f can not be determined *a priori*; it is the scope of the present paragraph to provide a way to experimentally find such striking value for the overall experiment. Other possible filling options were already described in section 4.5.1.

In fig. 6.1(a), the forward current I_f as a function of the (increasing) forward voltage V_f (measured at $T=10$ K) is shown, for the case of standard FZ p-type sensors, after irradiation with 188 MeV protons at three proton fluences. The annealing is only 8 minutes at 80°C . In all three cases, a threshold voltage of 1.5 V is found before a current of $\approx 1 \mu\text{A}$ can be measured. After such threshold, the current is found to increase from $\approx 1 \mu\text{A}$ to ≈ 0.1 mA, according to the eq. 5.8 already presented in section 5.1.6. As soon as the current is in the order of 0.1 mA, there is a (second) steep jump towards higher forward current (≈ 10 mA) which saturates for even higher forward bias, due to the range limit of the electrometer (Keithley 6517A). We consider this (second) threshold voltage V_{TH} is the minimum bias to be applied in order to fill the traps at $T=10$ K.

The dotted black lines in fig. 6.1(b) represent the fit according to eq. 5.8; the results of the analysis are shown in tab. 6.1, pointing out increasing V_0 and decreasing G_0 with increasing ϕ_{neq} , as expected for relaxation-like materials. In particular, the parameter V_0 is found to be proportional to the fluence, with $dV_0/d\phi = 1.21 \cdot 10^{-13} \text{ V}\cdot\text{cm}^2$, in the fluence range $[2.1, 7] \cdot 10^{13} \text{ cm}^{-2}$, after irradiation with 188 MeV protons and annealing of 8 min at 80°C . In addition, also the threshold voltage V_{TH} is found to be proportional to ϕ_{neq} (right plot in fig. 6.1(a)).

The forward current was monitored at subsequent annealing steps, at 290 K with the IV-setup and 10 K with the TSC setup (fig. 6.1(b)) as well. From both cases, it

$\phi_{neq} [10^{14} \text{ cm}^{-2}]$	0.21	0.35	0.7
$V_0 [\text{V}]$	2.8	4.5	8.23
$G_0 [10^{-3} \Omega^{-1}]$	1.5	0.5	0.15

Table 6.1: Fit parameters V_0 and G_0 from fit to measured forward IV at $T=10$ K with eq. 5.8, for standard FZ p-type sensors after proton irradiation for increasing ϕ_{neq} , and annealing of 8 min at 80°C .

is possible to see a recovery of the forward current with annealing and the sample tends to revert back from the relaxation-like phase to the lifetime-phase. Similarly, the threshold voltage V_{TH} decreases with increasing annealing time (right plot in fig. 6.1(b)). The double-injection current-voltage characteristic at high injection levels were already calculated in [134]. Here, we summarize two interesting aspects: firstly, a negative resistance originated from the increasing hole lifetime with increasing injection level, owing to electron depopulation of the recombination centers by hole capture. Secondly, the negative resistance arises from a decreasing current at increasing voltage over a voltage range from V_{TH} and $V_M \approx (\sigma_n/\sigma_p)V_{TH}$ [134].

Experimentally, in the present work it is found that such negative resistance is responsible for hysteresis in the current vs. voltage characteristic; for instance, fig. 6.2 presents the hysteresis effect in a standard FZ diode (p-type), after irradiation with 188 MeV protons $\phi_{neq} = 7 \cdot 10^{13} \text{ cm}^{-2}$ and annealing of 8 min at 80°C .

6.1.2 Heating rate β

The heating rate β , at which the temperature is increased during a TSC heating phase, has to be constant throughout the duration of the TSC measurement. To set the optimal heating rate, TSC measurements on the same sample, under the same bias conditions, were performed at various heating rates in the range [0.050, 0.500] K/s. The results point out that the measured TSC temperature is non-linear as a function of the time during the heating phase, if the heating rate is higher than 0.200 K/s. Therefore, an heating rate of 0.183 K/s is chosen for all the performed TSC measurements, if not stated otherwise. Such β value was checked and found to be independent of the bias during the heating phase V_H (up to the fourth decimal place). In the [75, 400] V range, the average β value is 0.18381 K/s.

As a general consideration from fig. 6.3, higher heating rates cause higher T_{max} and peak heights. Therefore, it was actually checked that $\int I_{TSC} dt \approx \int I_{TSC} / \beta dT$. The variation of the heating rate was exploited to obtain the activation energy E_a and capture cross-section $\sigma_{n,p}$ of defects in the approximation of [120]:

$$\ln \left(\frac{T_{max}^4}{\beta} \right) \approx \frac{E_{a, n,p}}{k_B} \cdot \frac{1}{T_{max}} + \ln \left(\frac{E_{a, n,p}/k_B}{B\sigma_{n,p}m_{dC,V}/m_0} \right), \quad (6.1)$$

which is shown for instance in fig. 6.3(a) for the VO_i defect.

In conclusion, all the measurements in this thesis are performed with a heating rate $\beta = 0.183$ K/s, filling temperature of 10 K and filling current of 1 mA if not stated otherwise. More details about the settings for TSC measurements can be found in appendix C, which can serve also as a check-list for planning a TSC scan.

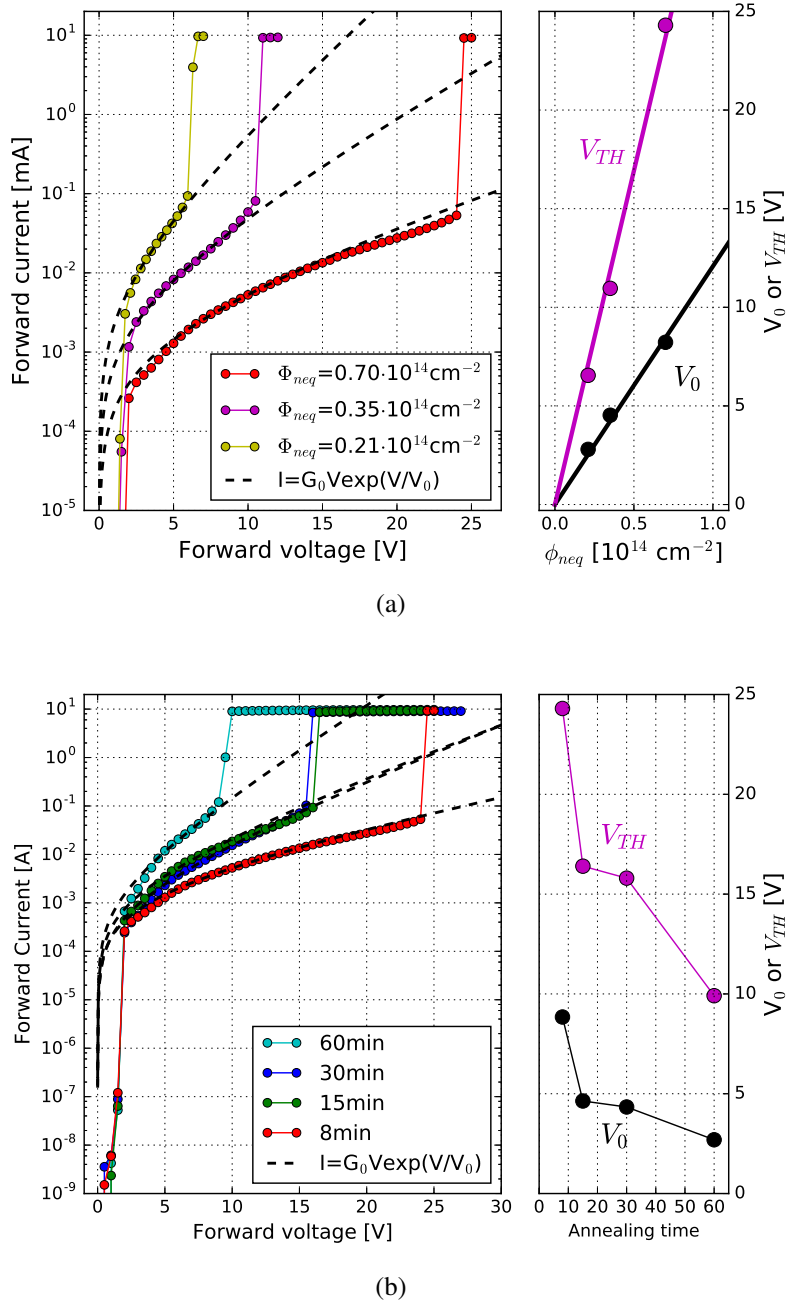


Figure 6.1: Forward IV characteristics at $T=10$ K for standard FZ diodes (p-type) after irradiation with 188 MeV protons and corresponding V_0 , V_{TH} values from fit with the theoretical trend (eq. 5.8, dotted black lines): (a) at different ϕ_{neq} (but same annealing of 8 min at 80°C), and (b) after $\phi_{neq} = 7 \cdot 10^{13} \text{ cm}^{-2}$ and subsequent annealing times at 80°C .

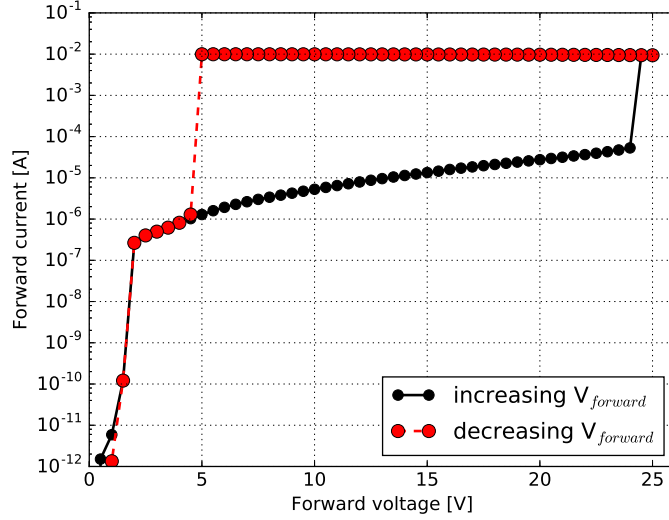


Figure 6.2: Hysteresis effect under forward bias at $T=10$ K, for a standard FZ diode (p-type), after irradiation with 188 MeV protons $\phi_{neq} = 7 \cdot 10^{13} \text{ cm}^{-2}$ and annealing of 8 min at 80°C .

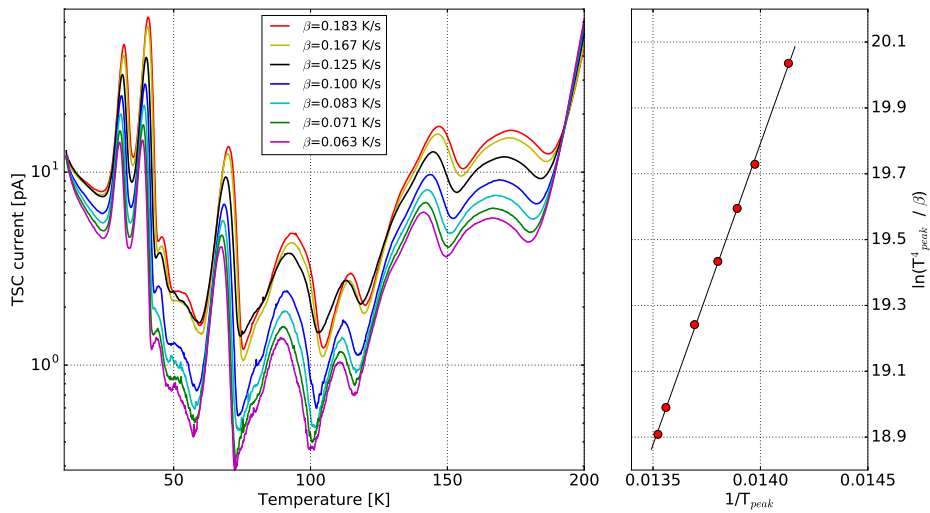


Figure 6.3: TSC spectra at various heating rates in the range $[0.063, 0.183]$ K/s, and evaluation of the activation energy for the VO_i defect (0.156 ± 0.027) eV. The sample is a FZ (p-type) diode, irradiated with 23 MeV protons, $\phi_{neq} = 5 \cdot 10^{13} \text{ cm}^{-2}$, and annealing of 8 min at 80°C .

6.2 Analysis of TSC spectra ($T_{fill} = 10$ K)

In this section, the method for analyzing TSC spectra obtained at the conventional $T_{fill} = 10$ K is presented. Such filling temperature was adopted in the past for the analysis of samples irradiated with electrons, photons, and neutrons. The wealth of measurements performed in the present work, under the same conventional experimental conditions in the last 20 years, are now available for comparison after irradiation with different particles. Moreover, for the first time the method is implemented in Python (version 2.7.12).

The analysis of TSC spectra requires the subtraction of the background (in the low temperature range, with $T < 60$ K) and of the dark current (in the high temperature range, with $T > 80$ K). This is the object of subs. 6.2.1. The method in subs. 6.2.2 aims at extracting defect concentrations.

6.2.1 Background and leakage current subtraction

In the low temperature range of a TSC spectrum ($T < 60$ K), the background has to be subtracted. In the present work, TSC current values up to $T = 20$ K and the first minimum after the H(40K) defect are used as starting and ending ranges for a linear fit (green lines in fig. 6.4). After the subtraction of the background in such range, the TSC spectra can be further analyzed to obtain the defect concentrations. The background in the low temperature range would otherwise lead to overestimation of the defect concentrations, especially for the E(30K) and H(40K) defects. The background at low temperature is affected by the time waited between the filling and the heating phases, the filling temperature, and it is found to increase at increasing heating rates, but decreasing after annealing.

In the high temperature range, the leakage current has to be subtracted as well. The leakage current has to be measured as a function of the temperature under the same V_H bias applied for the TSC measurement. After irradiation with ϕ_{neq} up to 10^{14} cm⁻², the leakage current dominates the TSC signal for $T > 200$ K. A proper subtraction of the leakage current is therefore necessary, as clearly visible from fig. 6.5. The leakage current is measured in the range [10, 290] K at different heating rates β (0.050 K/s $< \beta < 0.200$ K/s). It can be noticed that the leakage current is in the 0.1 pA range for temperatures below 150 K. To speed up the measurements, the leakage current was measured starting from 80 K. Since the dependence of the leakage current on the temperature is expected to follow the function in eq. 6.2:

$$I_{TSC}(T > 190 \text{ K}) = A \cdot T^2 \cdot \exp\left(-\frac{E_a}{k_B T}\right), \quad (6.2)$$

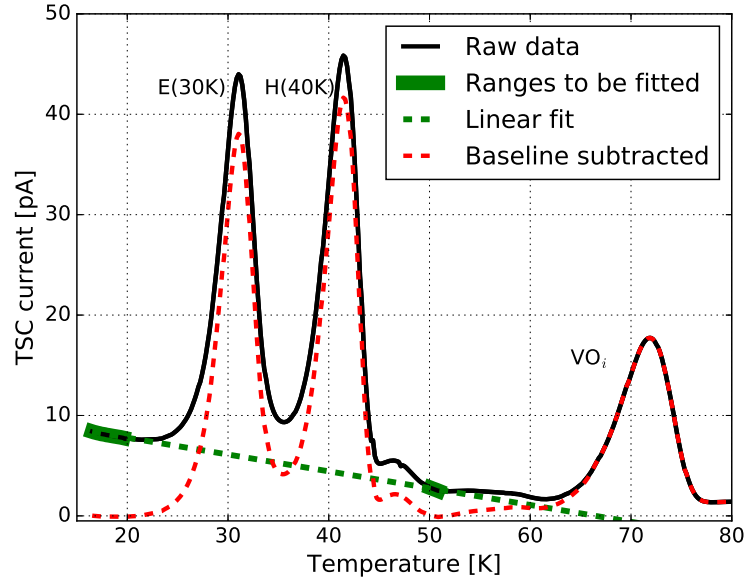


Figure 6.4: TSC spectra before (solid black line) and after (dotted red line) background subtraction in the low temperature range ($T < 60$ K).

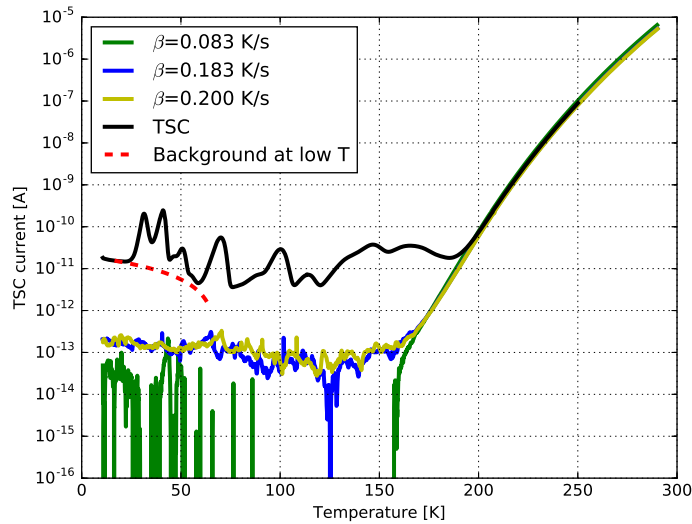


Figure 6.5: Leakage current measured at different heating rates β ($V_C = V_F = V_H = -300$ V). The sample is a dd-FZ irradiated with 23 MeV protons, $\phi_{neq} = 10^{14}$ cm $^{-2}$ and annealing of 60 min at 80°C. The TSC spectrum, and the background at low temperature, are indicated by solid black and dotted red lines, respectively.

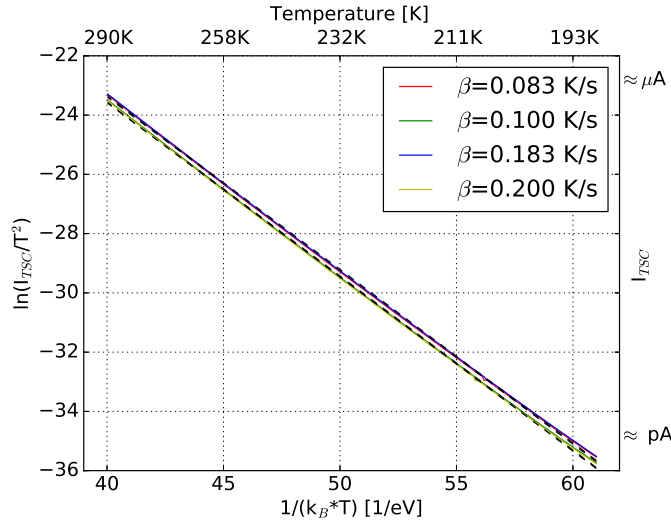


Figure 6.6: Fit (dashed black lines) to data (colored lines) according to eq. 6.2, for the sample presented in fig. 6.5.

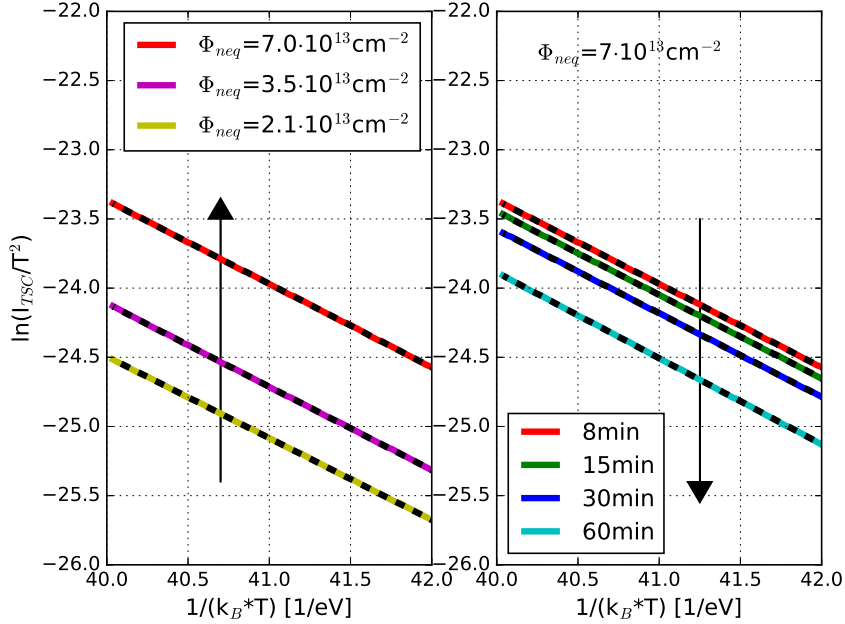
The value for the activation energy E_a for beta values in the [0.083, 0.200] K/s range is found to be 0.59 eV, averaging the results from a set of four β values. If compared to the band gap energy, E_a is near to $E_g/2$ (=0.56 eV), which indicates that generation centers are close to the mid-gap.

The leakage current was measured after proton irradiation at various fluences and fixed annealing of 8 min at 80°C. The left plot in fig. 6.7(a) shows the increasing leakage current in a p-type FZ diode, for increasing fluences. The corresponding activation energies E_a (fig. 6.7(b), left) are in general higher than $E_g/2$, as for n-type FZ diodes after irradiation under the same ϕ_{neq} , and are consistently close to the midgap also after annealing (up to 60 min at 80°C, as shown in fig. 6.7(b) (right)).

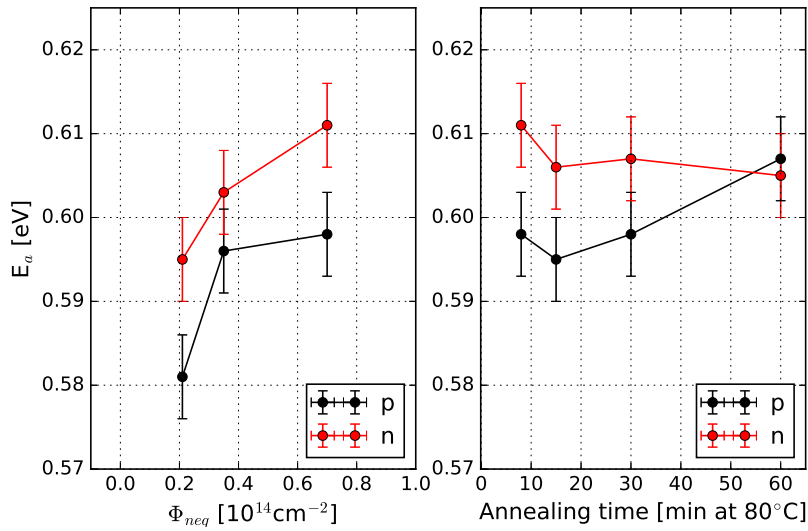
6.2.2 Defect concentrations

Hereby it is described the method for calculating concentrations of defects from measured TSC spectra, after the conventional filling under forward bias of defects at $T_{fill} = 10$ K. Each TSC peak is described via the following temperature-dependent $I_{TSC}(T)$ function:

$$I_{TSC}(T) = k \times f(T) \times g(T), \quad (6.3)$$



(a)



(b)

Figure 6.7: Leakage current (a) for standard p-type FZ diodes, 188 MeV protons: (left) at different ϕ_{neq} (but same annealing of 8 min 80°C), and (right) subsequent annealing ($\phi_{neq} = 7 \cdot 10^{13} \text{ cm}^{-2}$). Dashed lines are fit according to eq. 6.2. (b) Corresponding activation energy as a function of (left) ϕ_{neq} and (right) annealing, for p-type as well as for n-type FZ diodes under the same conditions.

where:

$$\left\{ \begin{array}{l} f(T) = 1 - \frac{1}{1 + \exp(-(T - T_c - \alpha/2)/\beta)}, \\ g(T) = \frac{1}{1 + \exp(-(T - T_c + \alpha/2)/\gamma)}. \end{array} \right.$$

The $f(T)$ and $g(T)$ functions are meant to replace the temperature dependent emission probabilities and the fraction of occupied traps, respectively.

According to eq. 6.3, five parameters are necessary for each defect: the peak amplitude Amp , the temperature value T_c corresponding to the peak center, α for the temperature shift, and γ and β for describing the rising and falling tails of a peak, respectively. The five parameters are under a constrained multivariate least-squared optimization, with $\alpha > \beta > \gamma$. Defect concentrations N_t are calculated from the peak area A_{peak} as follows:

$$N_t = \frac{2A_{peak}}{q_0V_{dep}}, \quad (6.4)$$

where V_{dep} is the depleted sensor volume and q_0 is the elementary charge. Fig. 6.9 shows an example of application of the fitting method for a TSC spectrum after irradiation of a p-type FZ diode with 23 MeV protons (for a total of 13 bulk defects). The bottom part of fig. 6.9 provides the ratio between measured and fitted values. The constrained multivariate least-squares calculations are optimized until

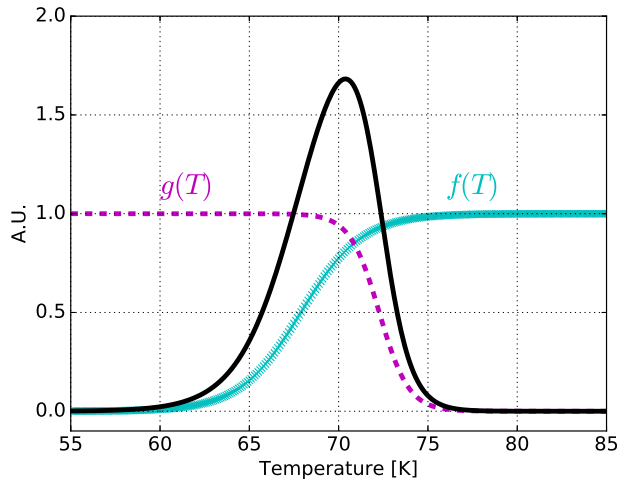


Figure 6.8: The fitting function $I_{TSC}(T)$ from method in eq. 6.3, to obtain defect concentrations. See eq. 6.3 for actual expressions of the $f(T)$ and $g(T)$ functions.

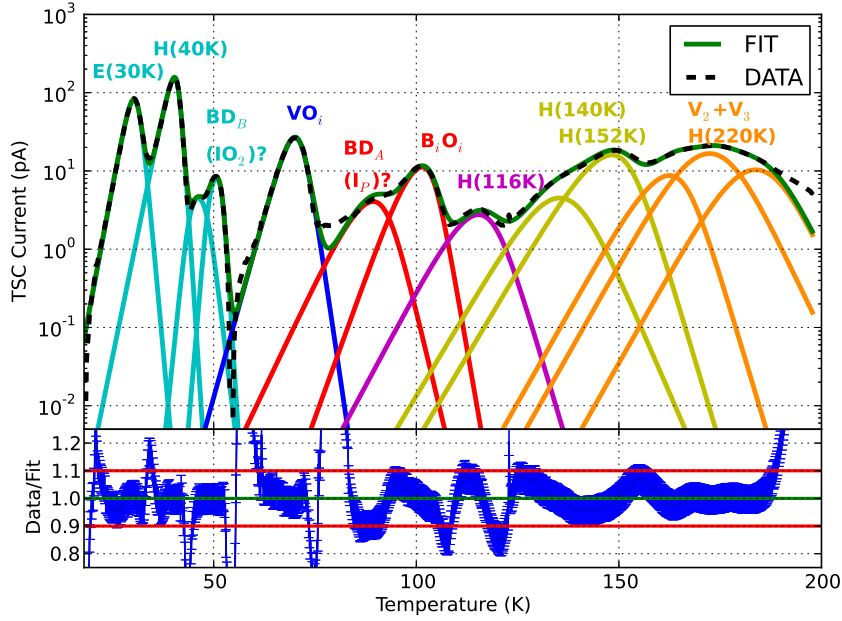


Figure 6.9: Example of TSC spectra fitted with the function in eq. 6.3, for a p-type FZ diode irradiated with 23 MeV protons at $\phi_{neq} = 0.5 \cdot 10^{14} \text{ cm}^{-2}$ and annealed for 15 minutes at 80°C . The log scale for the y-axis is meant for enhancing the visibility of defect peaks.

differences between measured and calculated values are less than $\pm 10\%$ for defects which have more than 10 pA in peak amplitude. This is especially the case for the defects labeled as E(30K), H(40K), and VO_i , which have clearly isolated peaks. At $T \approx 50$ K, the BD_B and possibly the IO_2 electron traps are found. In the temperature range [80, 110] K, the B_iO_i defect is present, together with possible contributions from $\text{BD}_A^{0/++}$ and $\text{I}_P^{+/0}$, that were previously identified in [135] and in [136]. The hole trap H(116K) at $T = 116$ K is followed at higher temperature by two other hole traps (the H(140K) and H(152K)). In the higher temperature region [160, 200] K the TSC spectrum is populated by many deep levels. Three defect states are assumed to be present (fitting functions in orange, as shown in fig. 6.9). The three states are representative for a double-vacancy $\text{V}_2^{-/0}$, a three-vacancy $\text{V}_3^{-/0}$ and the hole-trap $\text{H}^{+/0}(220\text{K})$ (as motivated in par .6.4).

6.3 Bulk defects after proton irradiation

This section focuses on electrically active defects generated by protons of different energies and $\phi_{neq} \leq 3 \cdot 10^{14} \text{ cm}^{-2}$. The results are obtained by performing TSC measurements without bias during the cooling phase, with the conventional $T_{fill} = 10 \text{ K}$, and a high enough $|V_F|$ to provide a filling current of $\approx 1 \text{ mA}$. The method in subs. 6.2.2 is applied to obtain the defect concentrations.

Firstly, a qualitative approach to TSC spectra is presented in order to give an overview on the many bulk defects found after irradiation with different proton energies, on various bulk material and subsequent annealing. The quantitative results are provided for the main bulk defects in subs. 6.3.1–6.3.4.

- **Proton energy E_p :** fig. 6.10 shows the TSC spectra after irradiation of MCz p-type diodes with 23 MeV, 188 MeV and 23 GeV, after normalizing the TSC current values to $\phi_{neq} = 10^{14} \text{ cm}^{-2}$. The annealing is 60 min at 80°C . At a first look, it can be noticed that the very same bulk defects are found after irradiation with protons of different energies. The apparent suppression of the E(30K) defect at 30K with increasing E_p will be discussed in section 6.3.1. Contrary to shallow defects in the lower temperature range, broader peaks appear in the higher temperature range. The broad peak above $T=160 \text{ K}$ results from overlapping V_n defects: the diva-

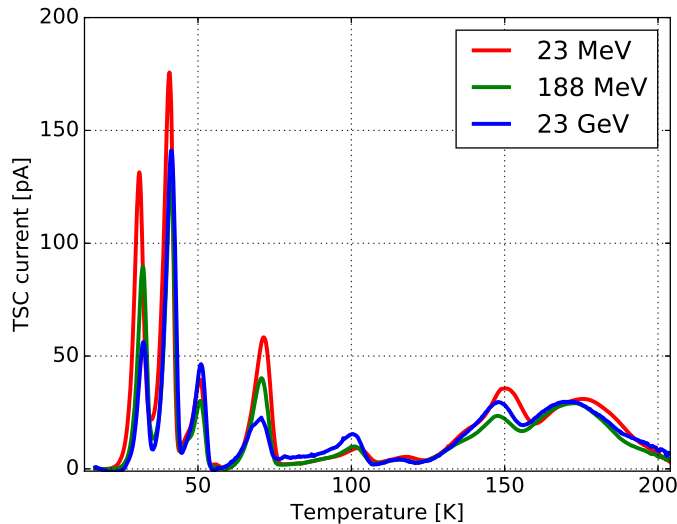


Figure 6.10: TSC spectra for MCZ p-type diodes, after irradiation with different proton energies, normalized to $\phi_{neq} = 10^{14} \text{ cm}^{-2}$, and annealing of 15 min at 80°C .

cancy V_2 , the trivacancy V_3 and the hole trap H(220K) (possibly a vacancy-related defect V_x defect), in view of the results presented in subs. 6.4.

In addition to the E(30K) and cluster defects, the most abundant defects are the hole traps H(116K), H(140K) and H(152K) which are not observed after ^{60}Co irradiation [135]; this is a clear indication that these five defects are all cluster-related defects.

It is worth noticing that, as a result of the proton irradiation of silicon sensors, at least 13 bulk defects can be detected with TSC measurements. It has to be noticed that the $I_p^{0/-}$, which is known from [135] to be responsible for space charge sign inversion in n-type sensors, is not visible because overwhelmed by the leakage current ($T_{peak} \approx 200$ K).

- **Bulk material:** The very same defects found after proton irradiation in p-type MCz diodes are found also in p-type FZ diodes, a part for the $\text{BD}_B + \text{IO}_2$ complex (at $T \approx 50$ K, to be noticed in the top plot of fig. 6.11). In fact, the

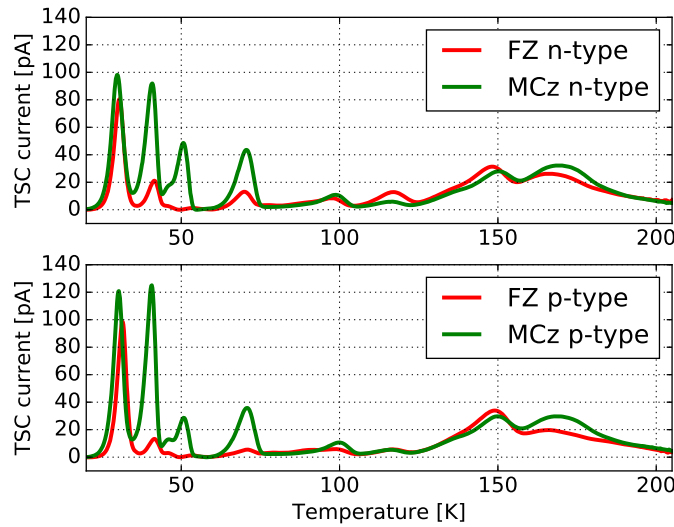


Figure 6.11: TSC spectra for different n and p-type materials, after irradiation with $E_p = 188$ MeV, $\phi_{neq} = 7 \cdot 10^{13} \text{ cm}^{-2}$, and annealing of 60 min at 80°C .

oxygen dimer IO_2 is strongly suppressed in materials with low oxygen content. It is worth noticing that the $\text{BD}_B^{+/++}$ defect is a donor and therefore is responsible for the introduction of positive space charge.

From the bottom plot of fig. 6.11, it can be noticed that the very same bulk defects are found also in p-type diodes. The only difference in the nomenclature has to be reported at $T = 100$ K: the appearing peak is labeled as the

BD_A or B_iO_i in n-type or p-type diodes, respectively. The latter defect is expected to be responsible for the boron removal in p-type sensors which are boron-doped. In other words, a boron-interstitial B_i bonded to an oxygen-interstitial O_i forms the detrimental B_iO_i defect which reduces the doping concentration of a p-type sensor.

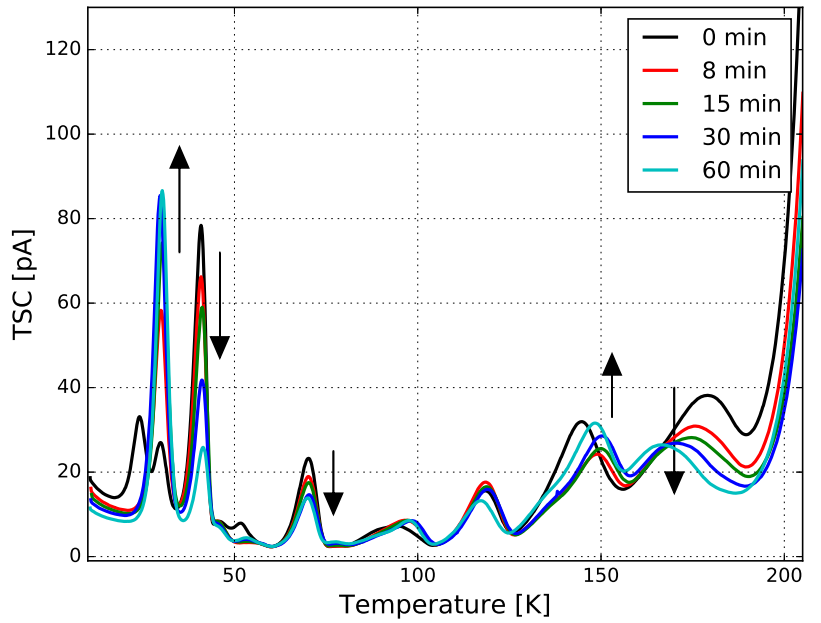
A clear oxygen dependence for the H(40K) defect has to be expected, whereas no strong oxygen dependence is observed for hole traps in the [116, 152] K range.

- **Annealing:** TSC measurements are repeated after annealing at 80°C in order to “accelerate” the long term evolution of defects and monitor their effects on the detector performance (addressed in chapter 7). As representative examples, fig. 6.12(a) and fig. 6.12(b) provide the results of annealing studies up to 60 min at 80°C for n-type and p-type FZ sensors, respectively, after irradiation with 188 MeV protons and $\phi_{neq} = 7 \cdot 10^{13} \text{ cm}^{-2}$. Starting from the results soon after irradiation (annealing of 0 min at 80°C), it can be seen that, in addition to the above mentioned bulk defects, a presently unknown defect can be seen at $T \approx 28 \text{ K}$ in both material types. This defect anneals out soon after 8 min at 80°C and allows for a clear detection of the E(30K) donor. Another defect is suddenly disappearing soon after irradiation: this the case of the peak at $T \approx 145 \text{ K}$ which is especially present in p-type sensors.

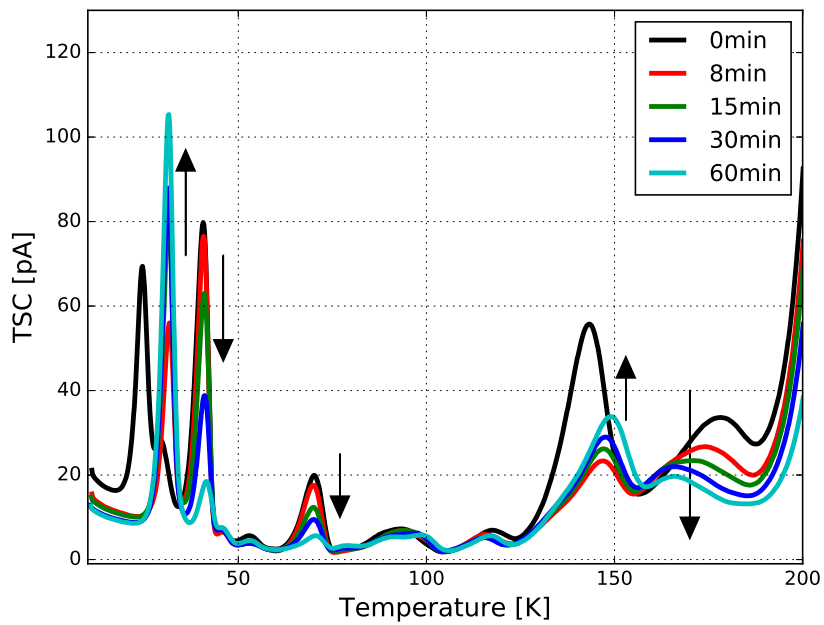
As a general trend, the leakage current decreases with annealing time, as well as the background in the low temperature range. Some defect concentrations are found to increase with annealing time (e.g. E(30K), H(140K) and H(152K)), while others decrease with annealing time (e.g. V_n -group and H(40K)).

Finally, at the very central part of the TSC spectra, on one hand we report the stable presence of B_iO_i , on the other hand the unstable concentration of the peak at $T \approx 70 \text{ K}$ which at first sight should be attributed to the VO_i defect. The VO_i is a well-known point-like defect which does not contribute to the space charge because $\sigma_n \gg \sigma_p$; it does not contribute to the leakage current since in the silicon band gap it is positioned at ($E_C - 0.176 \text{ eV}$).

At this point, it is interesting to remember here that, at room temperature, the vacancies are mobile and mainly trapped by interstitial oxygen to eventually form the VO_i state (energy level $E_C - 0.176 \text{ eV}$). The latter defect is expected to be stable up to high temperature during isochronal annealing (from the demonstrations in [136]), but the experimental observation points out that another defect is overlapping and annealing out. The fit to the peak concentration at $T \approx 70 \text{ K}$ (with a function of $\exp(-t_{ann}/\tau)$ in fig. 6.13)), gives



(a)



(b)

Figure 6.12: Annealing evolution of TSC spectra for (a) n-type and (b) p-type standard FZ diode, after irradiation with $E_p = 188$ MeV and $\phi_{neq} = 7 \cdot 10^{13} \text{ cm}^{-2}$.

a time constant of 20 min for FZ n-type, and of 27 min for FZ p-type samples. Similarly, a time constant at 80°C of 20 min is found for MCz p-type diodes irradiated with the same proton energy and ϕ_{neq} , while the concentration of the VO_i defect is found to be constant in MCz n-type diodes. We conclude that the reduction of the peak at $T \approx 70$ K is due to the annealing out of the C_iC_s defect in the oxygen lean material.

Similarly to the VO_i , the $H(40K)^{+/0}$ defect is a hole trap (neutral at room temperature), which decreases with annealing time (see fig. 6.14) and vanishes after 960 min at 80°C [136]). The activation energy and capture cross-section were calculated in [126] after 23 MeV proton irradiation, and found to be $E_a = (0.108 \pm 0.003)$ eV and $\sigma_p = (4.3 \pm 3.9) \cdot 10^{15}$ cm² [126]. The chemical structure is unknown up to now, but it is possibly oxygen-related in view of the above mentioned characteristics.

6.3.1 E(30K): oxygen-dependent IR

The electron trap $E(30K)^{0/+}$ is a shallow donor (located in the upper half of the silicon bandgap, at $(E_C - 0.1)$ eV), contributing in full concentration with positive space charge to N_{eff} . It was already detected after high-energy electron and neutron irradiations [135], but not after low-energy electron irradiation nor gamma irradiation. The electron capture cross-section σ_n is $2.3 \cdot 10^{-14}$ cm⁻² [135]. The

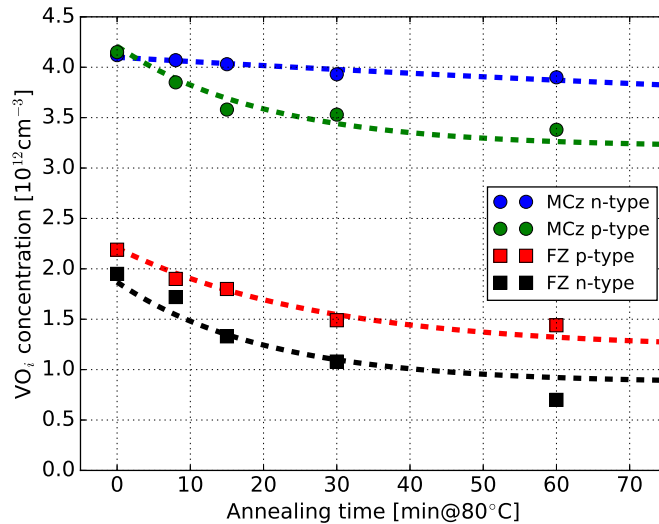


Figure 6.13: E(70K) peak evolution with annealing at 80°C, with fit functions over-imposed (dashed black lines), after irradiation with 188 MeV protons and $\phi_{neq} = 7 \cdot 10^{13}$ cm⁻².

chemical structure is unknown, but it is expected to be interstitial-oxygen related. The evolution of an E(30K) peak with the annealing time is presented in fig. 6.14 for a standard FZ p-type sensor, after irradiations with 188 MeV protons and $\phi_{neq} = 7 \cdot 10^{13} \text{ cm}^{-2}$. All the measurements were performed under the same bias conditions ($V_C = 0 \text{ V}$, and $V_H = -300 \text{ V}$) and $T_{fill} = 10 \text{ K}$.

After correcting the background for $T < 60 \text{ K}$ and subtracting the leakage current, the TSC spectra are fitted to obtain the E(30K) concentration as shown in fig. 6.14 (dashed black lines). Soon after irradiation, the E(30K) concentration is at the minimum, and an unknown defect with $T_{peak} \approx 25 \text{ K}$ suddenly disappears after the first annealing step of 8 min at 80°C . After an initial increase, the concentration reaches a saturation value, in all the investigated materials (n- and p-type FZ, dd-FZ and MCZ).

Since the E(30K) defect is expected to be oxygen-related, in the following the focus is on the oxygen-enhanced introduction of the E(30K) bulk defect after proton irradiation. The introduction of E(30K) is shown for the representative case of MCz and FZ diodes after irradiations with 188 MeV protons and $\phi_{neq} = 7 \cdot 10^{13} \text{ cm}^{-2}$ in fig. 6.15. The two extremes with respect to the oxygen concentration [O] in the sensor bulk are considered: low [O] for standard FZ (between $5 \cdot 10^{16} \text{ cm}^{-3}$), while high [O] for MCz materials ($5 \cdot 10^{17} \text{ cm}^{-3}$). The dd-FZ is not considered because of the not homogeneous [O] in the sensor bulk (as already pointed out in

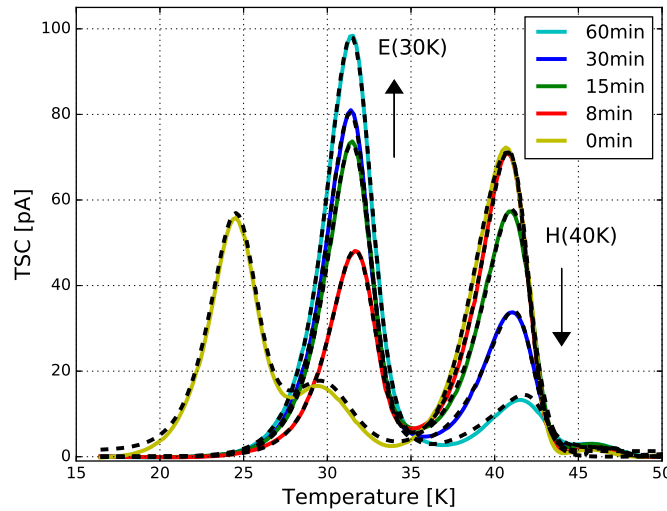


Figure 6.14: E(30K) evolution with annealing at 80°C , with fit functions over-imposed (dashed black lines), after irradiation with 188 MeV protons and $\phi_{neq} = 7 \cdot 10^{13} \text{ cm}^{-2}$ of a standard FZ p-type diode. The defect with T_{peak} at 25 K is unknown; the peaks at 40K belong to the hole trap H(40K).

fig 4.3). The lowest concentration of the E(30K) defect is found for the standard FZ diodes, whereas the highest concentration is found in MCz samples. In other words, the donor E(30K) introduces more positive space charge in oxygen rich materials.

In the special case of annealing of just 8 minutes at 80°C, the introduction rate of E(30K) is in the range $[0.02, 0.04] \text{ cm}^{-1}$ (lower and higher values are for FZ and MCz materials, respectively). This is higher than the introduction rate of E(30K) after neutron irradiation (0.015 cm^{-1} as calculated by [135]). The enhanced generation after proton irradiation might be an indication for an isolated “point defect” resulting from the (highly probable) low-energy transfers after Coulomb interaction [135]. The following results are related to the possibility for the E(30K) of being cluster-related, meaning that it is a point-like defect that might be “screened” by cluster defects.

The evolution of the E(30K) defect concentration (divided by the fluence) with the annealing time t_{ann} (expressed in minutes at 80°C) is parametrized as follows:

$$[E(30K)] = [E(30K)]_0 + s \cdot \left(1 - \exp\left(-\frac{t_{ann}}{\tau}\right) \right), \quad (6.5)$$

with $[E(30K)]_0$ the E(30K) concentration soon after irradiation ($t_{ann} = 0 \text{ min}$), s the saturation value, and τ a time constant characteristic of the bulk material. The parametrization applied to MCz diodes is shown in fig. 6.16(a), and to standard FZ in fig. 6.16(b). Higher saturation values at long annealing times are found in MCz material in comparison to standard FZ. This is a further confirmation that the E(30K) defect might be an oxygen-related defect which is especially produced in [O] rich materials. Moreover, a common time constant τ of 16 minutes is found

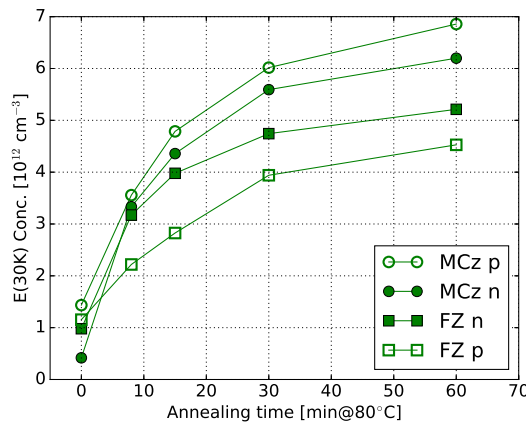


Figure 6.15: E(30K) concentrations as a function of the annealing time, after irradiation with 188 MeV protons and a $\phi_{neq} = 7 \cdot 10^{13} \text{ cm}^{-2}$.

for both the bulk materials, and expected because N_{eff} reaches a minimum after 8-15 min of annealing at 80°C, then the (negative) contributions from acceptors overcomes the saturated (and positive) contribution from the E(30K) defect. In fig. 6.16(c), the average values for FZ and MCz diodes are plotted as a function of the annealing time, and it is possible to note that MCz diodes have a higher saturation value with respect to standard FZ diodes.

We shall now focus on the case of the p-type material with maximum oxygen concentration (MCz) and at the maximum E(30K) concentration (after 60 min at 80°C). Under these conditions, the introduction rate of the E(30K) defect is studied as a function of the proton energy.

In fig. 6.17(left), the introduction rate is shown under two different filling conditions: at $T_{fill} = 10$ K and $T_{fill} = 20$ K. In fact, if $T_{fill} = 10$ K a decreasing intro-

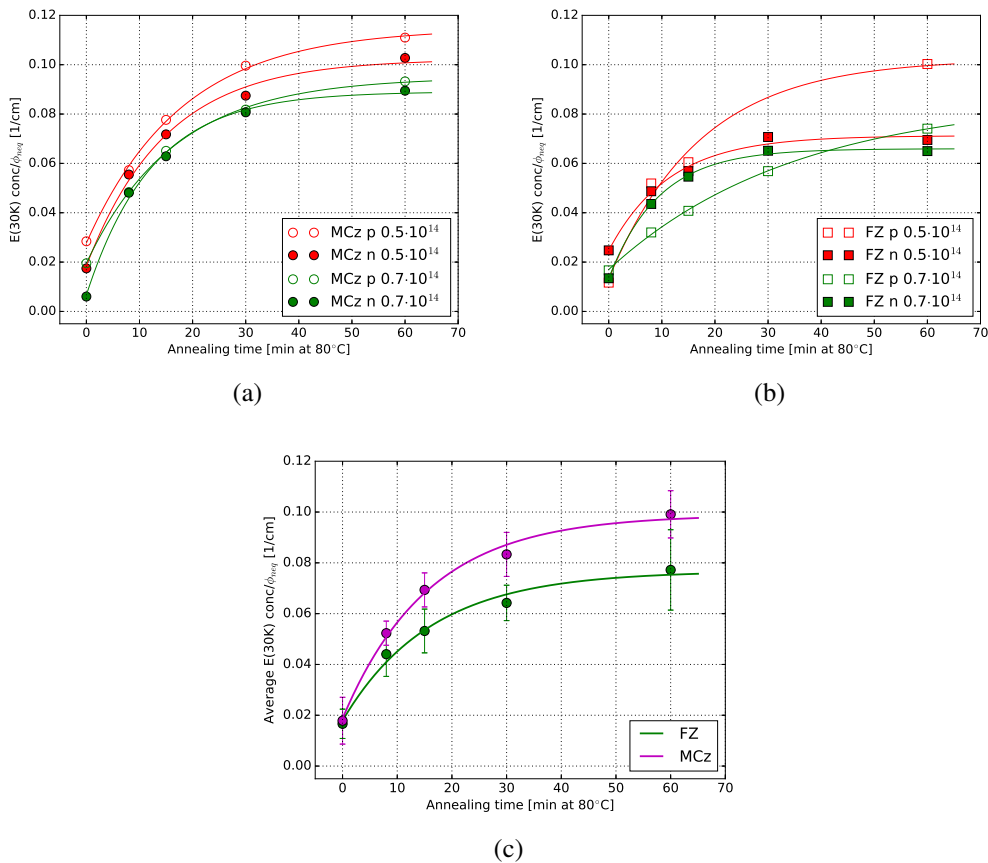


Figure 6.16: Fluence-scaled E(30K) concentration as a function of the annealing time after irradiation with 23 MeV protons (red) and 188 MeV protons (green), (a) for MCz diodes and (b) for standard FZ. (c) Averaged values.

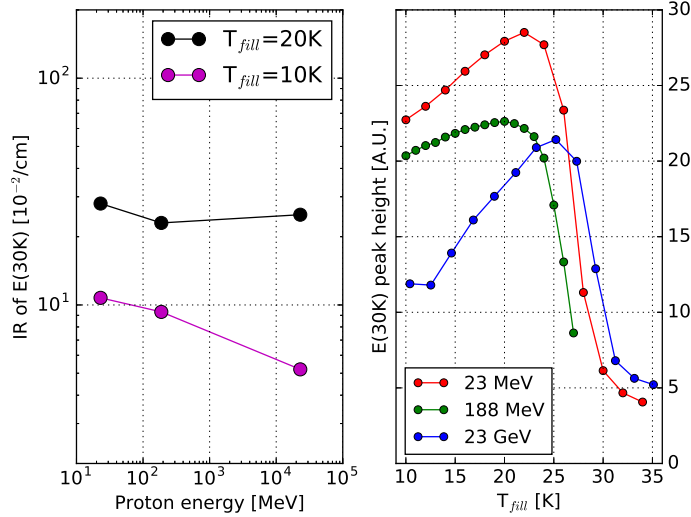


Figure 6.17: (Left) Proton-energy dependent introduction rate for the E(30K) defect, and (right) location of the E(30K) peak height as a function of the filling temperature T_{fill} .

duction rate is observed with increasing proton energies. However, higher concentrations of the E(30K) are found if T_{fill} is increased. This effect could be due to the presence of (other) clustered defects that are “screening” the E(30K) defects, and causing only a partial filling of the E(30K) traps at $T_{fill} = 10\text{K}$. Therefore the maximum E(30K) concentration (and introduction rate) are calculated, and plotted as well in fig. 6.17(right). From this second results, no proton-energy dependence of the introduction rate is found. This is in agreement with the expectation for a NIEL-scaling and cluster-related defect.

In conclusion: after proton irradiation, the E(30K) defect shows a oxygen dependent introduction rate, but not a bulk-material type dependence. In addition, the introduction rate does not depend on the proton energies, as it was noticed also after electron irradiations in the energy range from 15 to 27 MeV [136].

6.3.2 B_iO_i : boron removal

Limited information is available for radiation-induced degradation of boron-doped silicon sensors. In the present work, the very same bulk defects are found after proton irradiation in both n-type and p-type silicon sensors, apart for the interstitial boron-oxygen complex (B_iO_i). In fact, the B_iO_i is a donor (with energy level $E_C - 0.23\text{eV}$ [137], [138]) and removes negative space charge due to the boron-removal. Such defect is therefore expected to be detrimental for Low-Gain

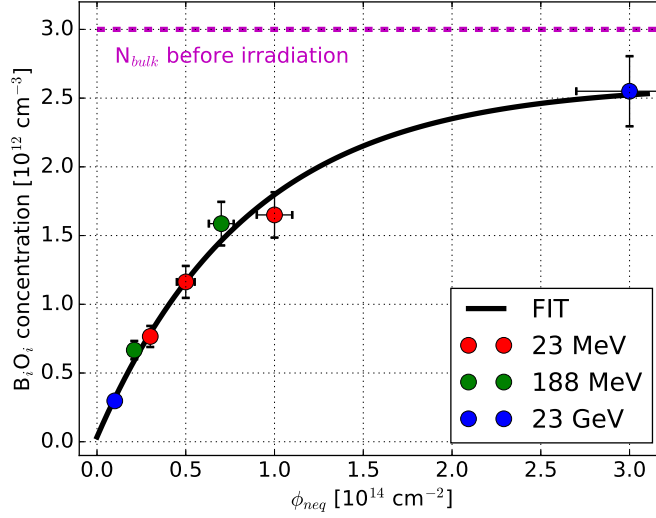


Figure 6.18: B_iO_i concentration as a function of ϕ_{neq} , for p-type MCz diodes, irradiated with different proton energies and after annealing of 60 min at 80°C. The dotted magenta lines recalls the p-doping content before irradiation.

Avalanche Detectors (LGAD) which are promising silicon radiation detector with an intrinsic multiplication of the charge [139]: in fact, LGAD are fabricated by diffusing a p-type layer, just below the n^+ electrode, to form a n^+ -p-p $^-$ junction. Under reverse bias, the multiplication takes place for electrons reaching the n^+ electrode. In particular, the p-layer is fundamental in order to enhance the electric field in such localized region; a reduction of the boron content in the p-type multiplication layer would therefore in turn limit the gain mechanism.

In addition, the B_iO_i is a possible precursor for light-induced degradation (LID) in solar cells produced from boron-doped oxygen-rich silicon [140].

The fluence-scaled concentration for the B_iO_i is found to be constant with annealing time, throughout the period from 0 to 60 min at 80°C. In MCz p-type diodes, an introduction rate of 0.021 cm $^{-1}$ is found, while standard FZ diodes are characterized by a smaller introduction rate (of 0.013 cm $^{-1}$). The introduction rates are valid after irradiation with different proton energies (see fig. 6.18), and dependent on the different oxygen content in the bulk materials. The introduction rates are one order of magnitude less with respect to the previous findings for the E(30K) defect (see subs. 6.3.1).

The B_iO_i concentration as a function of the neutron equivalent fluence is described with:

$$[B_iO_i] = [B_iO_i]_S \cdot (1 - \exp(-c\phi_{neq})). \quad (6.6)$$

The B_iO_i concentration is found to saturate to a value $[B_iO_i]_S = 2.5 \cdot 10^{12} \text{ cm}^{-3}$, with $c = 1.16 \cdot 10^{-14} \text{ cm}^2$ after 23 GeV proton irradiation with $\phi_{neq} = 3.0 \cdot 10^{14} \text{ cm}^{-2}$.

6.3.3 Deep hole-traps

After presenting the introduction rates for the E(30K) and B_iO_i defects, the focus is now on three hole traps which are expected to negatively contribute to the space charge: the H(116K), H(140K) and H(152K) defects. In fact, the group of deep acceptors in the lower part of the band gap was discovered and characterized in [135] and [141]. In particular, we report that the H(140K) and H(152K) hole traps show enhanced field emission; with a theoretical model of a 3D Poole-Frenkel effect, the zero field emission rates were obtained in [135] (see tab. 6.2). Moreover, it was found in [136] that the concentration of oxygen in the bulk does

	H(116K)	H(140K)	H(152K)
E_a (eV)	$E_V+0.33$	$E_V+0.36$	$E_V+0.42$
σ_p (cm ²)	$4 \cdot 10^{14}$	$25 \cdot 10^{14}$	$2.3 \cdot 10^{14}$

Table 6.2: Activation energy E_a and hole capture cross-section σ_p for deep acceptors [135].

not influence the introduction rate of the hole traps.

In the present work, a proportionality between the concentrations and ϕ_{neq} is observed. The total introduction rate for the three hole traps ($\Sigma(H - traps)$) was calculated for all the proton irradiated samples, and monitored at subsequent annealing step up to 60 min at 80°C.

For samples irradiated with 188 MeV, an initial contamination of the TSC signal in the temperature range of the $\Sigma(H - traps)$ was already noticed in fig. 6.12(b), especially in p-type samples. Such defect is highly suppressed already after 8 minutes of annealing, and was not detected soon after irradiation with 23 MeV protons nor 23 GeV protons. The unknown defect is possibly responsible for the slightly higher IR after 188 MeV protons, which is calculated to be $(0.12 \pm 0.02) \text{ cm}^{-1}$. If averaged on the proton energies, the IR for the $\Sigma(H - traps)$ is $(0.117 \pm 0.03) \text{ cm}^{-1}$ (dashed black line in fig. 6.19). If average over the annealing, the introduction rate is $(0.114 \pm 0.06) \text{ cm}^{-1}$ (dashed red line in fig. 6.19).

Given the consistently higher IR for the $\Sigma(H - traps)$ with respect to IR of defects positively contributing to the space charge, more acceptors (i.e. hole traps) than donors (i.e. electron traps) are created, so that in the case of n-type diodes the space charge sign inversion is possible [92]. The radiation fluence at which type inversion occurs is dependent upon the resistivity of the non-irradiated material.

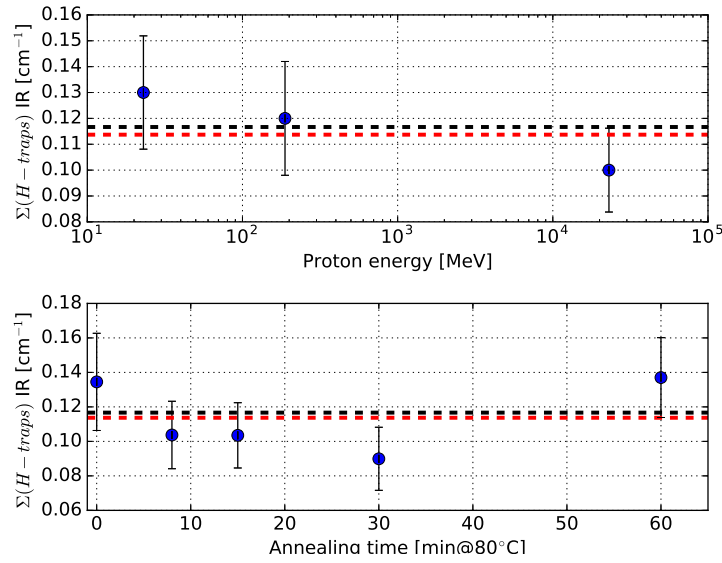


Figure 6.19: Dependence of the total introduction rate (IR) for H(116K), H(140K) and H(152K) defects on (top) the proton energy and (b) on the annealing time, for all the materials considered in the present study. Dashed lines represent in (black) the average IR on the proton energy (0.117 ± 0.03) cm^{-1} ; in (red) the average IR on the annealing of (0.114 ± 0.06) cm^{-1} .

6.3.4 The V_n -group

After addressing the defects with contributions to the space charge, the defect with impact on the leakage current are now presented. Following the results in section 6.4, three cluster-related defects are considered as part of the “ V_n -group” populating the high temperature range of the TSC spectra for a proton-irradiated silicon diode. In the present calculations they are assumed to be the divacancy V_2 , the trivacancy V_3 , and the hole trap H(220K) (possibly, of the type V_x).

In irradiated silicon, the divacancy (V_2) is a fundamental intrinsic defect either directly produced by irradiation or resulting from pairing of two vacancies. The production of the V_2 is independent on the oxygen concentration. Divacancies are stable at room temperature, but become mobile at high temperatures; they may migrate to form the V_2O defect if trapped by interstitial oxygen atoms in high oxygen materials. The transition from V_2 to V_2O occurs at $T > 200^\circ\text{C}$ [136], [95], and it is especially fast in oxygen rich materials. Oxygen atoms are efficient traps also for mobile trivacancies V_3 to form V_3O complexes. The trivacancies were experimentally identified and characterized in [142].

Fig. 6.20(a)-6.20(e) show the concentration of the V_n -group as a function of the ϕ_{neq} . The concentrations were obtained from TSC measurement performed at

Isothermal annealing time (min@80°C)	Average IR [10^{-2} cm^{-1}]
0	19.5 ± 2.0
8	18.0 ± 1.9
15	16.6 ± 1.5
30	16.1 ± 1.9
60	14.7 ± 1.7

Table 6.3: IR for cluster defects in the V_n -group, calculated for all the proton irradiated samples of different bulk and conduction types.

$V_{heating}$ of 300 V. From the proportionality between the concentration and ϕ_{neq} , the introduction rates are calculated and reported in tab. 6.3. The introduction rates for defect cluster as a function of the annealing time is found to be governed by the very same expression for the the annealing of the damage rate $\bar{\alpha}(t_{ann})$ (see fig. 6.20(f)), as previously stated by eq. 5.5. The introduction rates of cluster decrease with annealing, as expected from the annealing of cluster defects, mainly for the V_3 .

6.4 Analysis of TSC spectra (with $T_{fill} > 10 \text{ K}$)

It is the scope of the present paragraph to describe the impact of the filling temperature on a TSC spectrum for a proton-irradiated silicon sensors, and highlight the main bulk defects. In the present work, the lowest achievable T_{fill} is 10 K and a forward current of at least 1 mA is applied.

As a starting point, an experimental observation is demonstrated in fig. 6.21: it is an example of TSC spectra for a MCz p-type sample (after irradiation with 23 GeV protons, $\phi_{neq} = 1 \cdot 10^{13} \text{ cm}^{-2}$ and annealing of 60 min at 80°C). The filling temperature T_{fill} was increased from 10 K to 130 K (the different filling temperatures are grouped in steps of 10 K, and shown in different colors). As a result, increasing peak heights can be noticed in comparison to the standard TSC scan that is usually performed with $T_{fill} = 10 \text{ K}$ (indicated by the solid black line in fig. 6.21). The leakage current above $T=200 \text{ K}$ is not influenced by T_{fill} , being the result of the generation of carriers (electron-hole pairs) and not only of charge emission.

The peak enhancement with increasing T_{fill} is found to be especially relevant in the temperature range between 130 K and 160 K. More quantitatively, the increase of the peak at $T \approx 150 \text{ K}$ is about a factor 10 (solid points in the top plot

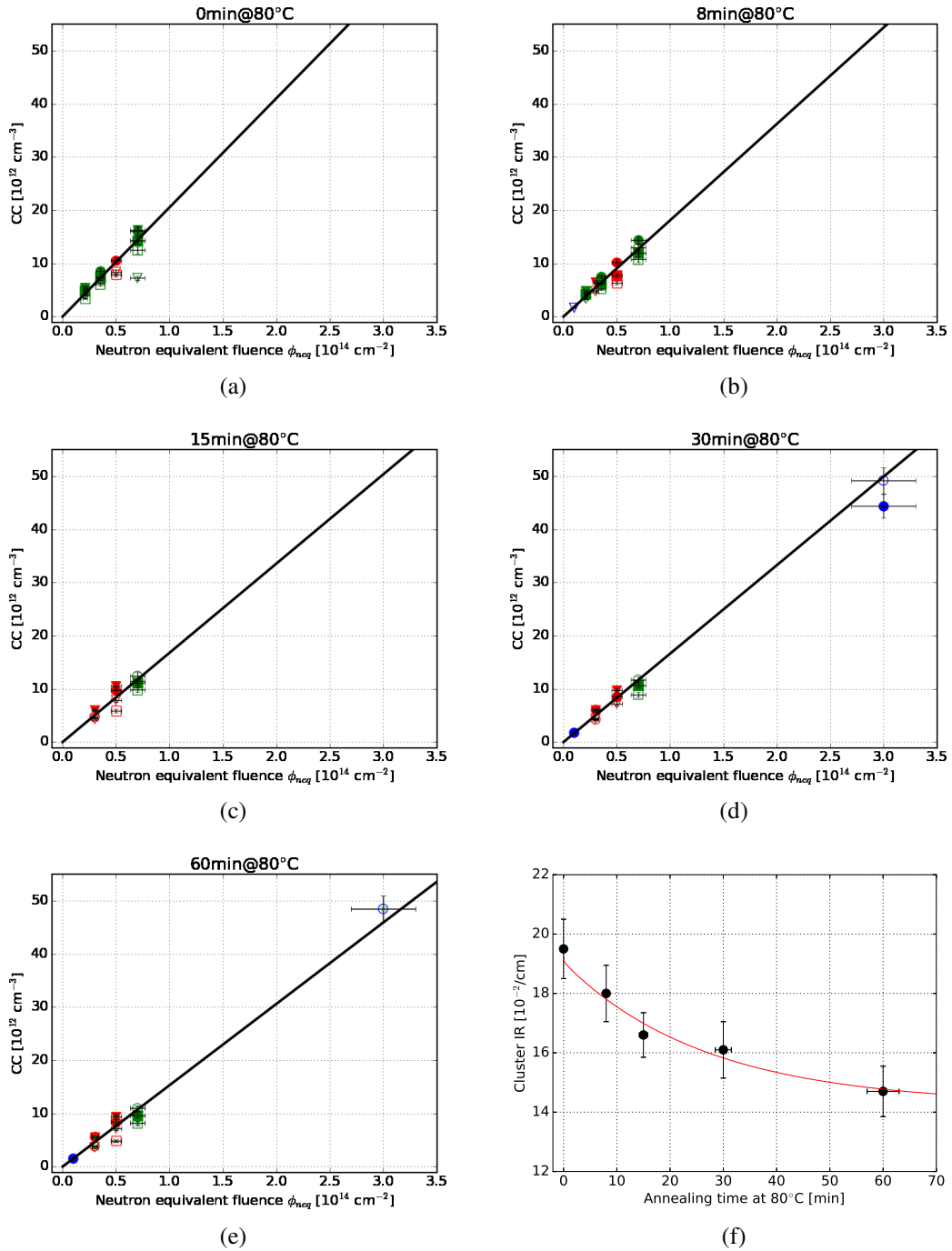


Figure 6.20: (a)-(e) Cluster concentrations (CC) as a function from TSC at $V_{heating}$ of 300 V, as a function of ϕ_{neq} , for five subsequent annealing steps at 80°C. The symbol legend is provided in tab. 4.8. (f) Cluster introduction rates for defect cluster as a function of the annealing time. Solid lines are fit to data as explained in text.

of fig. 6.22(a)). The experimental data can be described by accounting for three defects: the H(140K) and H(152K) acceptors, and additionally the $C_iO_i^{+/0}$ donor, whose energy levels are sketched in the bottom plot of fig. 6.22(a). In [124] it was demonstrated that the TSC peak height of the $C_iO_i^{+/0}$ defect results from a fractional occupation p_t/N_t with holes during the high injection ($n=p$) filling process, with $p_t/N_t = (1 + c_n/c_p)^{-1}$ (as calculated and presented in the bottom plot of fig. 6.22(a)). It can be deduced that $c_p \ll c_n$ in the low temperature range (as expected in the presence of the two acceptors only), while in the high temperature range the dominant defect is the $C_iO_i^{+/0}$ having $c_n \ll c_p$ instead. The two limits legitimate the parameterization of the maximum TSC current I_{max} as a function of the filling temperature as follows [17]:

$$I_{max}(T_{fill}) = I_{max}(T_{fill} = 10K) + k \cdot \frac{1}{1 + \frac{c_n}{c_p}}, \quad (6.7)$$

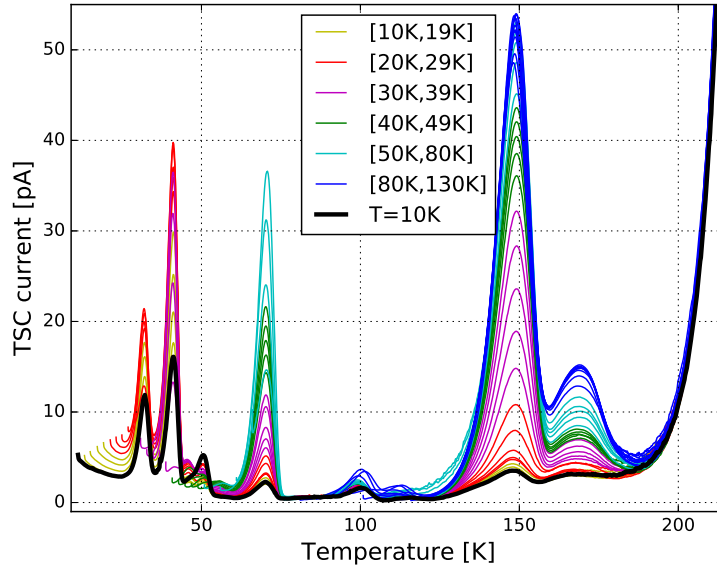


Figure 6.21: TSC spectra for a MCz p-type diode (after irradiation with 23 GeV protons, $\phi_{neq} = 10^{13} \text{ cm}^{-2}$ and annealing of 60 min at 80°C). The bias voltages during the TSC phases are: $V_C = 0 \text{ V}$, $V_F = 20 \text{ V}$ and $V_H = -180 \text{ V}$. The filling temperatures are in the range ($10 \text{ K} \leq T_{fill} \leq 130 \text{ K}$). The measurements last 80 hours.

as computed in the top plot of fig. 6.22(a) (red line). The ratio between the capture coefficients is assumed to be of the form:

$$\frac{c_n}{c_p} = a \cdot \exp\left(\frac{E_s}{k_B T_{fill}}\right), \quad (6.8)$$

resulting from the Multi-Phonon Process (MPP) [143]. After the capture process, the MPP emission model foresees a violent vibration of the defect and a subsequent emission of several phonons, and a final settling down to a new configurational state. The energy E_s represents the energetic barrier to be overcome for an actual capture of a free carrier. For the specific case of the $C_iO_i^{+/0}$ shown in fig. 6.22(a), $E_s = 27$ meV. The resulting value for E_s is comparable to values obtained by [124] and [17] after neutron irradiation.

The very same MPP emission process can be exploited for investigating how many cluster-related defects (V_n -clusters) overlap in the high temperature range of fig. 6.21. The analysis of the peak amplitude and occupation as a function of the filling temperature is provided at the top and bottom plot of fig.6.23(a), respectively. The increase of the V_n -cluster with increasing T_{fill} is about a factor 3, and it can be described by accounting for the divacancy $V_2^{-/0}$, the trivacancy $V_3^{-/0}$, and a hole trap H(220K) (possibly, of the form V_X). Their energy levels are sketched in the bottom right corner of fig. 6.23(a). A global E_s of 13 meV is

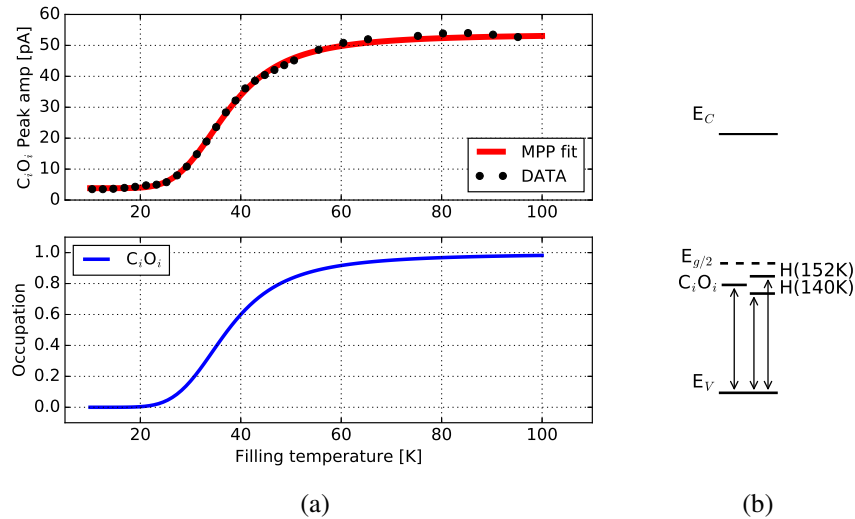


Figure 6.22: (a) $C_iO_i^{+/0}$ peak amplitude and occupation as a function of the filling temperature. Irradiation and annealing conditions are the same as of fig. 6.21. (b) Sketch of the energy levels for the defects of interest (not to scale).

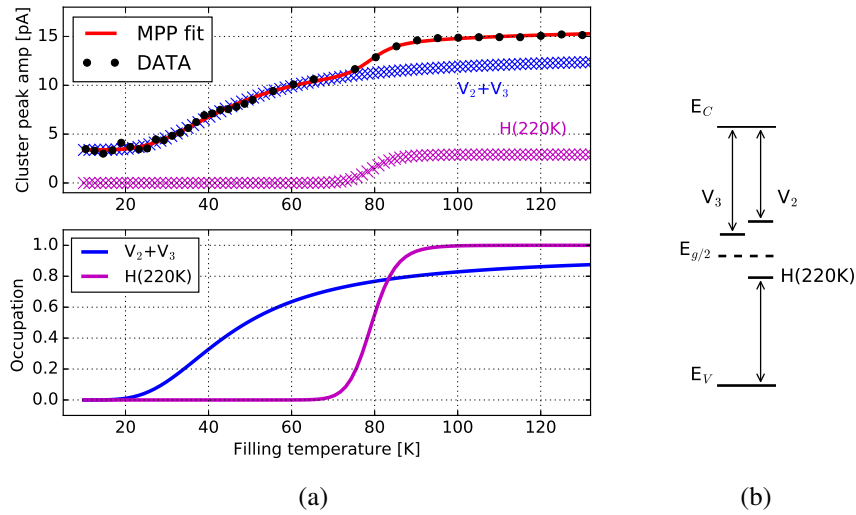


Figure 6.23: (a) Cluster peak amplitudes and occupations as a function of the filling temperature. Irradiation and annealing conditions are the same as of fig. 6.21. (b) Sketch of the energy levels for the defects of interest (not to scale).

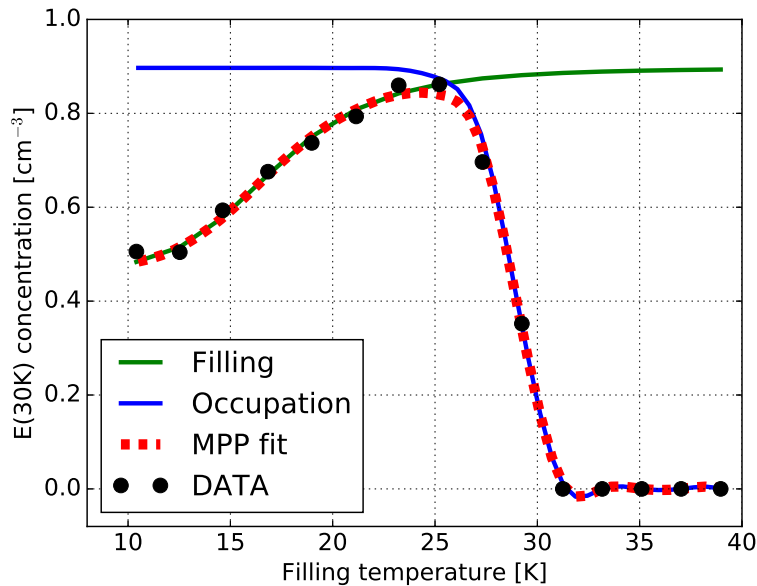


Figure 6.24: MPP process applied to the E(30K) defect. Irradiation and annealing conditions are the same as of fig. 6.21.

found for the $V_2^{-/0}$ and $V_3^{-/0}$ defects, while a higher E_s of 95 meV is found for the H(220K) defect.

By observing once again the TSC spectra in fig. 6.21, two main peaks at $T=30$ K and 40 K can be noticed in the low temperature range, for which the peak heights increase only up to certain T_{fill} , and sharply drop to zero afterwards. It is therefore necessary to firstly compute the occupation of such traps as:

$$f_{occ}(T_{fill}) = \exp\left(-\frac{1}{\beta} \int_{T_0}^{T_{fill}} e_n(T) dT\right), \quad (6.9)$$

and secondly, to fold the $f_{occ}(T_{fill})$ function into the expression for the concentration $n_t(T_{fill})$:

$$n_t(T_{fill}) = n_{t,0} \times f_{fill}(T_{fill}) \times f_{occ}(T_{fill}). \quad (6.10)$$

The $f_{fill}(T_{fill})$ function represents the dependence of the above mentioned trap filling on the filling temperature T_{fill} , according to the MPP emission process. The parameterization in eq. 6.10 is applied to describe the concentration of the E(30K) defect as a function of the T_{fill} , as shown in fig. 6.24. The energy barrier for the E(30K) is $E_s = 22$ meV. It can be seen that the E(30K) concentration after $T_{fill} = 25$ K is nearly twice the value at $T_{fill} = 10$ K.

As a final remark, we conclude that care must be taken in evaluating the properties of bulk defects, and especially defect concentrations, from TSC measurements at low filling temperature ($T_{fill} \leq 10$ K). The C_iO_i donor is expected to be responsible for trapping (thereby less CCE) in radiation-damaged silicon sensors, but it would not be detected with TSC measurements if $T_{fill} < 30$ K.

6.5 Impact of defect clusters

The method presented in this section aims at calculating defect concentrations from TSC measurements and the impact of cluster of defects on the activation energy. The activation energy is fixed (and obtained from literature), the majority capture cross-sections is taken from literature for variable initialization (so it is a free parameter). It is applied to a relatively simple TSC spectrum, obtained with cooling and filling under no bias, nor forward injection and no light illumination, so that only electron traps appear in the TSC spectrum. In the presence of many overlapping peaks and defects with unknown properties, the procedure would be less straightforward in comparison to the method already presented in section 6.2. According to the SRH statistics [97], a TSC peak for a point-like electron (n) or hole trap (p) is given by:

$$I_{TSC_n}(T) = \frac{Adq_0}{2} e_n(T) n_n(T), \quad (6.11)$$

with the concentration $n_n(T)$ of occupied traps calculated as:

$$n_n(T) = n_{n,0}(T) \times \exp\left(-\frac{1}{\beta} \int_{T_0}^T e_n(T') dT'\right), \quad (6.12)$$

where $n_{n,0}(T)$ denotes the fraction of occupied electron or hole traps during the filling process. Furthermore, q_0 is the elementary charge, A the pad area of the diode, d the thickness, β the heating rate, T_0 the starting temperature for the emission of the trapped charge carriers. The emission probability $e_{n,p}(T)$ for electron is given by eq. 3.25. The same calculations in eq. 6.11 can be written for hole traps. The calculations for the density of states in the conduction or valence band $N_{C,V}(T)$ are explicitly provided in appendix B.

In fact, the shape of TSC peaks after proton irradiation is remarkably different from those of point-like defects which were already extensively investigated with DLTS after gamma (from ^{60}Co) or electron irradiations (with $E < 6$ MeV).

Process-induced cluster defects (so-called dislocation loops) were noticed also in DLTS results by [144]. Estimation of cluster sizes in silicon after irradiation with 23 GeV protons were already shown in [87]. We only recall here, as a reference, that the most probable value in the probability distribution of vacancy-vacancy distances is ≈ 18 nm after irradiation with 23 GeV protons. In the following, a cluster is assumed to be an accumulation of point-like defects, changing the local potential according to the fraction of filled states.

As a starting point for including cluster defects in the model, the dependence of the potential on the fraction of filled states was studied for the case of charges uniformly distributed on a straight line. For instance, if only acceptors are present, then the traps can be occupied only by electrons. The repulsive potential can be iteratively computed, emission after emission of single negative charges; the resulting repulsive potential as a function of trap occupation is shown in fig. 6.25 (blue line). The Coulomb repulsion due to the negatively charged defects is:

$$E_{Coulomb} = \frac{q_0}{4\pi\epsilon_S\epsilon_0 l} = 0.121 \text{ eV}/d, \quad (6.13)$$

where l is the distance between point-like defects in a cluster and it is expressed in nm. It follows that $E_{Coulomb}$ is typically in the order of 0.01 eV for typical l values of 10-20 nm. The same computations can be performed for positively charged defects (i.e. attractive potential), as plotted in fig. 6.25 (red line). The main conclusion is that the potential energy does depend on the occupation of traps, so that the emission probability in eq. 3.25 is now replaced with:

$$e_{n,p}(T) = \sigma_{n,p} \nu_{th,n,p}(T) N_{C,V}(T) \exp\left(-\frac{E_a^*}{k_B T}\right). \quad (6.14)$$

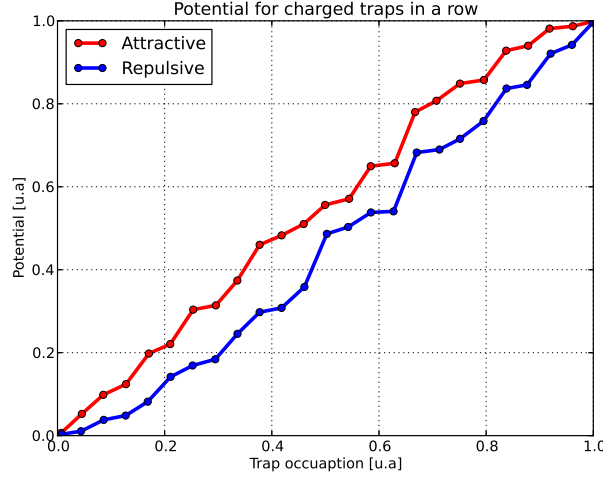


Figure 6.25: Attractive (red) and repulsive (blue) potentials after charge emission from traps which are ideally located on a straight line [145].

The activation energy E_a is set to be a function of the fraction of filled traps $f_{n,p}(T) = n_{t,n,p}(T)/n_{t,0,n,p}$ as follows:

$$E_a^*(f_{n,p}) = \begin{cases} E_a^0 - f_n \cdot \delta E^0 & \text{for acceptors,} \\ E_a^0 + (1 - f_p) \cdot \delta E^0 & \text{for donors.} \end{cases} \quad (6.15)$$

We recall here that the activation energy is fixed (taken from literature), the majority capture cross-section is taken from literature for variable initialization (so it is a free parameter); the defect concentration and shift in activation energy are left free. Two case limits are possible for the value of the activation energy:

- $E_{a,max}$ i.e. ($n_t^* \rightarrow 0$) \rightarrow this is the case limit of a point defect,
- $E_{a,min}$ i.e. ($n_t^* \rightarrow 1$) \rightarrow all the traps are occupied, so the trap level is shifted maximally to the conduction band.

The temperature dependence of the effective energy E_a^* leads to a shift and broadening of the TSC peak (see fig 6.26). The variation of the activation energy δE^0 for cluster-related defects is typically in the order of 10 meV, and it is expected to decrease with annealing according to the shrinking cluster. Once again, the limit $\delta E^0 = 0$ eV would represent the case of point defects. It should be noted that, after each charge emission, no redistribution of the trapped charges to an equidistant situation is included in the presented model. Coupling of defect levels due to interaction between close by defects (also known as inter-defect charge exchange)

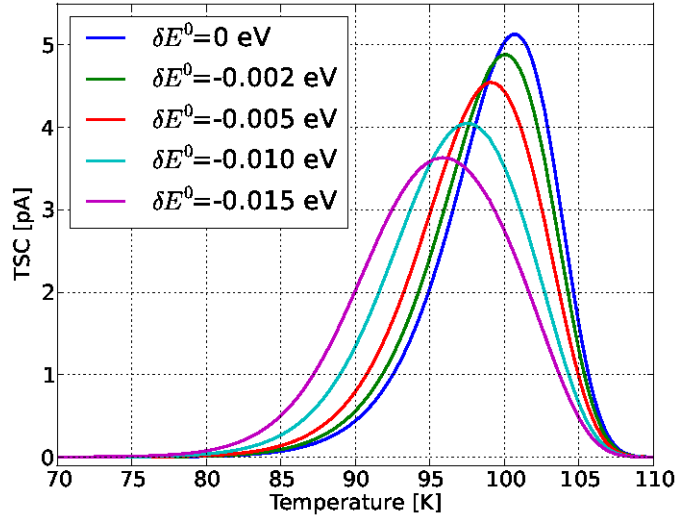


Figure 6.26: Shift and broadening of a (calculated) TSC peak due to the temperature dependence of the effective energy E_a^* via $f_{n,p}(T)$.

seems to be unlikely [144].

The usefulness of the method can be appreciated when in need of distinguishing point-like defects from cluster ones. The method was applied for an epitaxial n-type diode (75 μm thick), after irradiation with 23 GeV protons at fluence of 10^{13} cm^{-2} and annealing of 120 minutes at 80°C. The TSC spectra in fig. 6.27 was acquired under the bias conditions ($V_C = 0 \text{ V}$, $V_F = 0 \text{ V}$ and $V_H = 150 \text{ V}$). As a result, only electron traps are filled. The TSC spectrum shows the presence of isolated point-like defects such as the VO_i , but also much broader peaks like for the double vacancy $\text{V}_2^{(-/0)}$. This is found to be the most abundant defect after irradiation with 23 GeV protons, with a peak located at $T \approx 170 \text{ K}$ that can not be described as a point-like defect. Therefore, the E205a defect is introduced for explaining the long tail in the rising edge of the peak. The picture is completed by the inclusion of the E4 and E5 defects which are triple vacancies (double or single negatively charged, respectively). The resulting values for the activation energy, concentration and capture cross-section can be found in tab. 6.4. It is worth noticing that divacancies and trivacancies present δE^0 of 14-17 meV, while for point-like defects δE^0 is one order of magnitude less.

In fig. 6.27, the fit function (dashed red line) resulting from the computed six defect contributions is overlaid to the measured TSC current values (solid black line). It should be noted here that the parameter δE^0 and the cross-section σ_n are strongly correlated, while the values for E_a^0 are fixed to literature values.

Defect	E_a^0 [eV]	δE^0 [meV]	σ_n [10^{-15} cm ²]	N_t [10^{12} cm ⁻³]
$VO_i^{(-/0)}$	0.176	1.2	11.5	1.40
$V_2^{(=/-)}$	0.244	2.9	1.5	1.58
E4 ($V_3^{(=/-)}$)	0.359	14.0	1.5	0.72
E205a	0.393	15.9	0.78	2.89
$V_2^{(-/0)}$	0.425	13.0	0.60	10.20
E5 ($V_3^{(-/0)}$)	0.460	16.8	0.73	1.65

Table 6.4: Complete list of parameters for electron traps found after irradiation with 23 GeV protons, $\phi_{neq} = 10^{13}$ cm⁻² and annealing of 120 minutes at 80°C. Concentrations are provided according to results of the method in subs. 6.2.2.

The very same sample presented in fig. 6.27 was analyzed with also the method previously presented in subs. 6.2.2. The resulting fit parameters from the two independent methods are written in tab. 6.5.

The defect concentrations obtained from the latter method are slightly smaller with respect to the results from the first method (last column in tab. 6.5), possibly due to the trapezoidal rule applied to A_{peak} in eq. 6.4. The different description

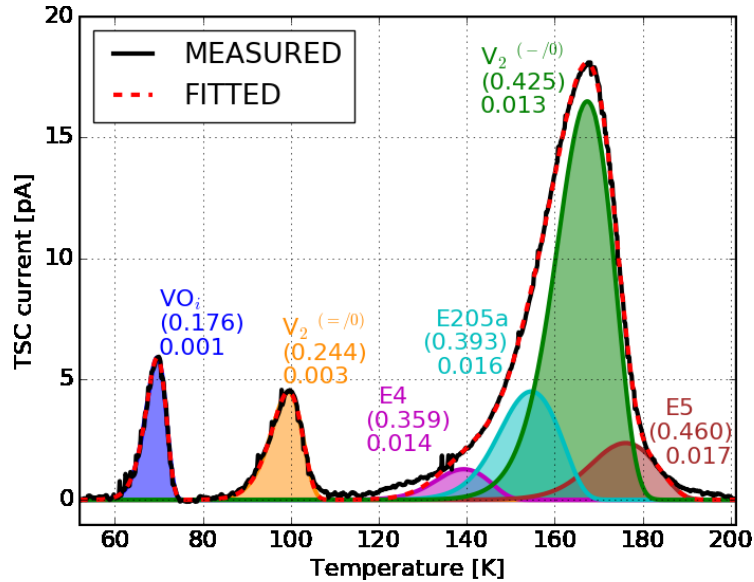


Figure 6.27: TSC spectra for an epitaxial n-type diode (75 μ m thick), after irradiation with 23 GeV protons, $\phi_{neq} = 10^{13}$ cm⁻² and annealing of 120 minutes at 80°C. Activation energy E_a are provided in eV and in brackets, together with δE^0 .

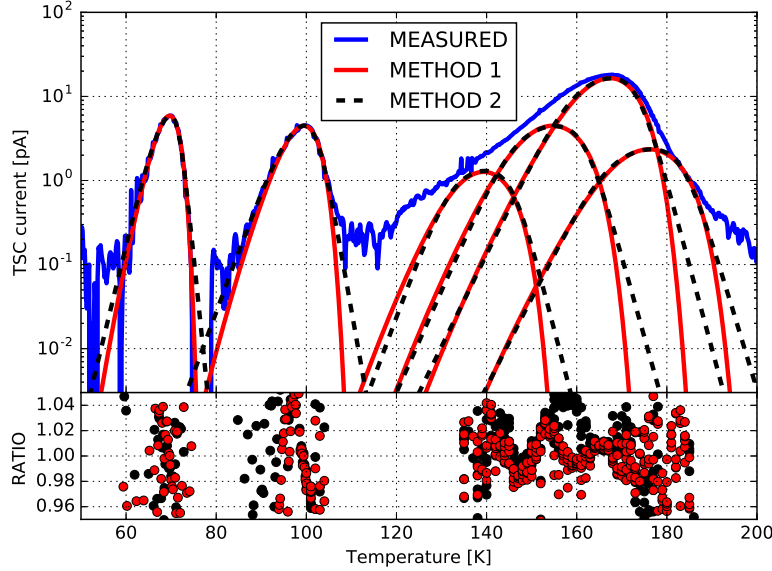


Figure 6.28: Comparison between the fit functions presented in section 6.2 and 6.5, together with the ratio to measured data. Fluence ϕ_{neq} and annealing are for the same sample described in fig. 6.27.

(for TSC current values below 0.1 pA) of peak tails can be appreciated in the log plot of fig. 6.28.

Method Parameter	Method 2						Method 1
	T_c	α	β	γ	Amp	$N_t [10^{12} \text{ cm}^{-3}]$	
$\text{VO}_i^{(-/0)}$	69.64	3.76	1.96	0.82	8.90	1.31	1.40
$\text{V}_2^{(=/-)}$	99.43	5.38	3.00	1.43	7.27	1.57	1.58
E4 ($\text{V}_3^{(=/-)}$)	138.99	13.20	3.00	2.10	1.5	0.72	0.72
E205a	154.12	14.98	3.59	2.26	5.13	2.82	2.89
$\text{V}_2^{(-/0)}$	166.6	13.65	3.95	2.18	20.00	10.05	10.20
E5 ($\text{V}_3^{(-/0)}$)	175.40	16.20	4.01	2.45	2.75	1.63	1.65

Table 6.5: Complete list of parameters of bulk defects found after irradiation with 23 GeV protons, $\phi_{neq}=10^{13} \text{ cm}^{-2}$ and annealing of 120 minutes at 80°C. The corresponding TSC peaks are shown in fig. 6.28 (dotted black lines).

Microscopic vs. Macroscopic

This chapter aims at merging the information from all the possible measurement types (IV, CV(f,T), and TSC) performed in the present work and from the two possible approaches to data analysis (“macroscopic” or “microscopic”). Firstly, the information from IV and TSC measurements regarding the leakage current are presented in section 7.1: the expected NIEL-scaling leakage current is proved as expected for all the analyzed bulk materials and types, after exposure to various proton energies. Next, the results from the initial rise method are compared to those from TSC measurements regarding the space charge concentration. In addition, a “microscopic” approach to C(f,T) measurements at low bias is proposed in section 7.2: the method is tested to obtain the activation energy of the main acceptor level produced after proton irradiation. Finally, the knowledge of relevant bulk defects from TSC and their properties make it possible to select a set of (six) relevant bulk defects to be used in TCAD simulations, in view of future developments of a radiation damage model based on actual bulk defects (see section 7.4).

7.1 TSC vs. IV

This sections deals with the correlation between cluster concentrations (obtained from TSC measurements at $V_H = 300$ V), and the leakage current $I_{leakage}$ (obtained from IV measurements at at 253 K and $V_{reverse} = 300$ V, as well). The leakage current is considered to be mainly due to the weighted concentration of three main cluster-related defects (V_2 , V_3 and H(220K)):

$$I_{leakage} \propto (w_{V_2} \cdot N_{V_2} + w_{V_3} \cdot N_{V_3} + w_{H(220K)} \cdot N_{H(220K)}) . \quad (7.1)$$

The weights are available in literature and set equal to $2.88 \cdot 10^{-2}$ for the divacancy [17], to $8.85 \cdot 10^{-1}$ [146] for the trivacancy, and to $8.60 \cdot 10^{-2}$ for the

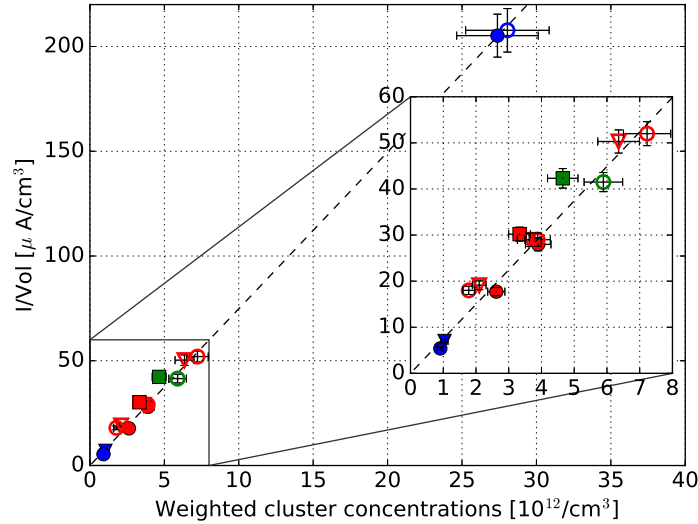


Figure 7.1: Correlation between cluster-related concentrations (from TSC measurements at $V_H = 300$ V) and leakage current (from IV measurements at 253 K and $V = 300$ V), after annealing of 30 min at 80°C .

H(220K) defect [136]. The main contribution is clearly due to trivacancies V_3 . After irradiation at various proton energies, the leakage current is found to be scaling with NIEL, as expected. In fig. 7.1 all the available IV and TSC results for the three type of bulk material, irradiated with three different proton energies and various ϕ_{neq} are reported after annealing of 30 min at 80°C . The proportionality between the leakage current (from IV measurements) and the weighted cluster concentrations (from TSC measurements) is valid for all the (various) investigated bulk materials and types, ϕ_{neq} , proton energies and annealing steps.

In the calculations, the inter-defect charge exchange between cluster defects is not considered, but it might be responsible for an additional increase of the generation of charge carriers, especially at higher fluences than the presently considered ones [147].

7.2 TSC vs. CV (initial rise method)

In this section, the results regarding the space charge concentration from CV measurements (in terms of [NCV]) are compared to those from TSC measurements (in terms of [NTSC]). In particular, CV measurements at $T = 253$ K and AC frequency 455 Hz are analyzed with the initial rise method (presented in chapter 5.2.3), while [NTSC] is calculated from TSC measurements at $V_{reverse} = 300$ V in the following

way:

$$[NTSC] = N_{eff,0} + [E(30K)] + [B_iO_i] - [H(116K)] - [H(140K)] - [H(152K)], \quad (7.2)$$

being $N_{eff,0}$ the effective doping concentration obtained from CV measurements before irradiation. The positive contribution $[B_iO_i]$ is accounted for only p-type sensors. The E(30K) donor is considered to positively contribute to the space charge, while the three hole traps are negatively contributing.

The results at five consecutive annealing times are presented in fig. 7.2(a)–7.2(e). Dotted black lines in fig. 7.2(a)–7.2(e) are the reference line, if $[NTSC]$ was equal to $[NCV]$.

Soon after irradiation it can be noticed that $[NTSC] \ll [NCV]$, then the general tendency with annealing is $[NTSC] \approx [NCV]$ for most of the samples. We recall that soon after irradiation with 188 MeV protons, a huge TSC peak, from an unknown defect and overimposed to the H(152K) peak, was seen. Such defect might be responsible for the overestimation of negative contributions to the space charge. The defect was found to anneal out after few minutes of annealing, and this might be the reason why $[NTSC] \approx [NCV]$ after few annealing minutes.

Few results are available regarding 23 GeV protons, however it is clear that after irradiation at high fluence ($3 \cdot 10^{-14} \text{ cm}^{-2}$) and long annealing times (30 min at 80°C) $[NTSC]$ is still way smaller than $[NCV]$. These results indicates that the negative contribution to the space charge are way higher than the positive ones at the highest fluence considered in the present study. In other words, the $[E(30K)]$ is way less than the sum of the concentrations from the hole traps considered in eq. 7.2. It would be necessary to repeat the calculations with defect concentrations obtained from TSC measurements performed with $T_{filling} > 10 \text{ K}$, in order to confirm or not the underestimation of $[E(30K)]$.

Another possibility is that deeper defects (positively contributing to the space charge) should be added in eq. 7.2. In addition, it would be interesting to check if $[NTSC]$ keeps on being equal to $[NCV]$ at longer annealing times.

7.3 TSC vs. C(f) at low bias

As noticed in subs. 5.2.4 at low reverse voltage, a strong dependence of the junction capacitance as a function of the frequency is due to radiation induced deep levels in the silicon bulk. In this section, the method developed by [148] is adapted to analyze C(f,T) curves of diodes after irradiation of p-type diodes with protons of various energy, and extract the activation energy of the dominant donor after proton irradiation. The result serve as input for the simulations in section 7.4.

The C(f,T) measurements already presented for p-type diodes in fig. 5.11(a)-5.11(c) are further analyzed by assuming the presence of a dominant deep donor.

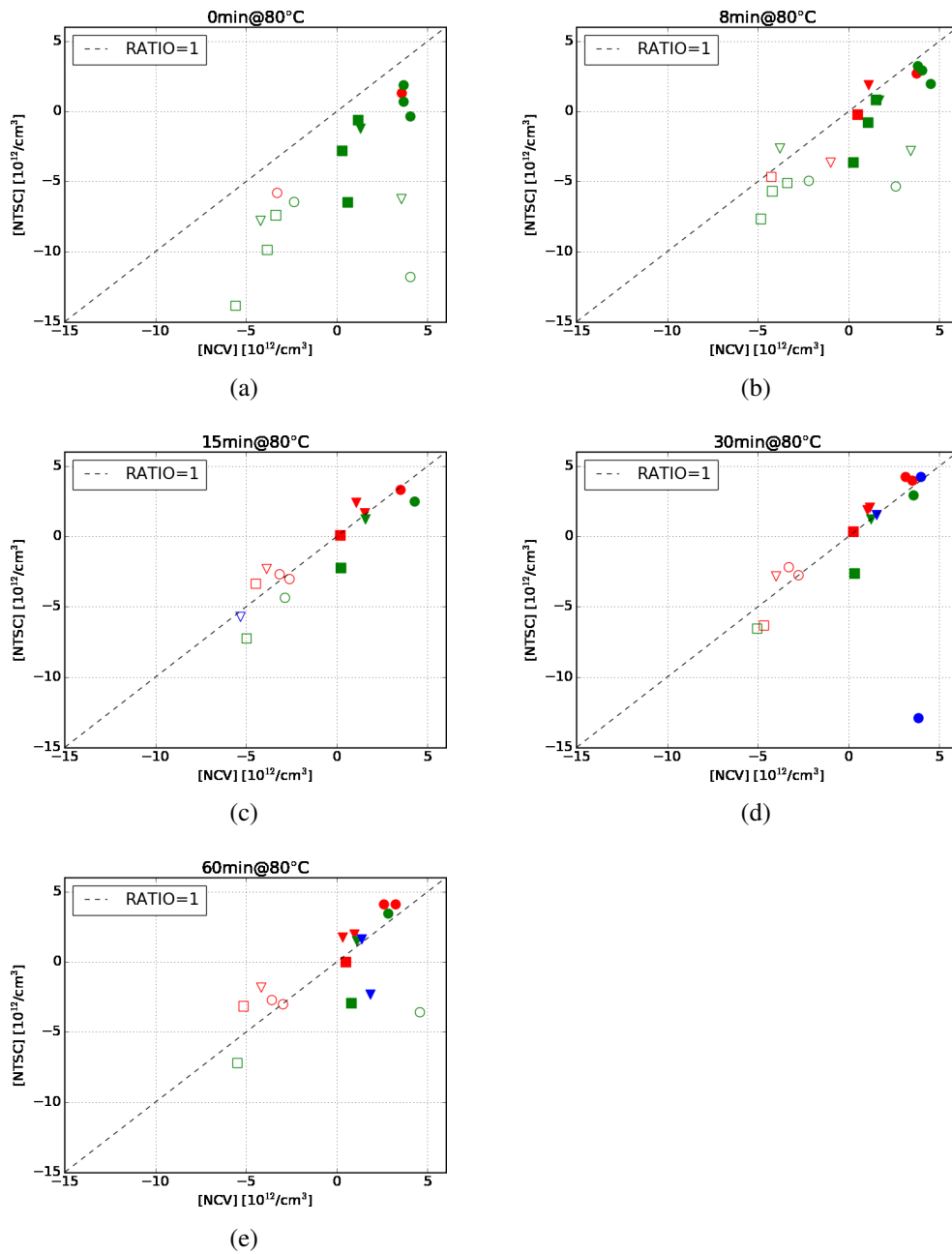


Figure 7.2: Comparison between [NTSC] and [NCV] at five subsequent annealing steps. Dotted black lines represent the reference for [NTSC]=[NCV].

An energy level possess a time constant τ related to its emission and capture coefficients for electrons and holes [148]:

$$\tau = \frac{1}{c_p(p_0 + p_1) + c_n(n_0 + n_1) + e_n + e_p}, \quad (7.3)$$

where p_0 and n_0 are the steady state hole and electron concentrations, and p_1, n_1 are:

$$p_1 = N_V \cdot \exp\left(\frac{E_V - E_t}{k_B T}\right), \quad n_1 = N_C \cdot \exp\left(-\frac{E_C - E_t}{k_B T}\right). \quad (7.4)$$

It is assumed that one dominant donor influences the junction capacitance, with a concentration $N_t > N_d$ and energy level in the upper half of the forbidden band. Since $(E_c - E_t) > (E_c - E_F)$, then $p_0 \ll p_1$ in eq. 7.3. In addition, for a deep donor it follows that $e_n \ll e_p$, and $n \cdot c_n \ll e_p$ (see tab. 3.3), so that eq. 7.3 is reduced to:

$$\tau \approx \frac{1}{c_p p_1 + e_p} = \frac{1}{2 \cdot e_p(T)}. \quad (7.5)$$

The hole emission rate is calculated as:

$$e_p(T) = \sigma_{v_{th}} N_C \exp(E_V - E_t)/k_B T = \sigma \gamma T^2 \exp(E_V - E_t)/k_B T. \quad (7.6)$$

In the eq. 7.6, γ is not temperature dependent and is obtained as $16\pi k^2 m_e^*/h^3$. The estimation of the activation energy of the dominant donor defect can be obtained considering that where the maximum slope of the C(T) curve is observed, the expression $f \approx 1/\tau = 2 \cdot e_p(T)$ is valid. The following expression is used to fit the f_1 values extracted from the fit in fig. 5.11(a)- 5.11(c):

$$\ln\left(\frac{f_1}{T^2} [K^2 \cdot s]\right) = \frac{E_V - E_t}{k_B T} + \ln(\sigma \gamma [K^2 \cdot s]). \quad (7.7)$$

The results from the fit with the model in eq. 7.7 after proton irradiation (with various proton energies and maximum ϕ_{neq}) are shown in fig. 7.3(a)- 7.3(c) and recapitulated in tab. 7.1. After 23 MeV and 188 MeV proton irradiation of the MCz p-type sensors, it is deduced that the dominant donor level has an activation energy $E_t - E_V = 0.463 \pm 0.02$ eV and $E_t - E_V = 0.469 \pm 0.02$ eV, respectively. After 23 GeV and much higher fluences ($\phi_{neq} = 3.0 \cdot 10^{14} \text{ cm}^{-2}$), the assumption of only one dominant deep donor is not enough. Two possible regimes are noted and, from the application of the fit in eq. 7.7, two separate values for the activation energies are obtained, which are either smaller or higher than the value obtained after lower irradiations.

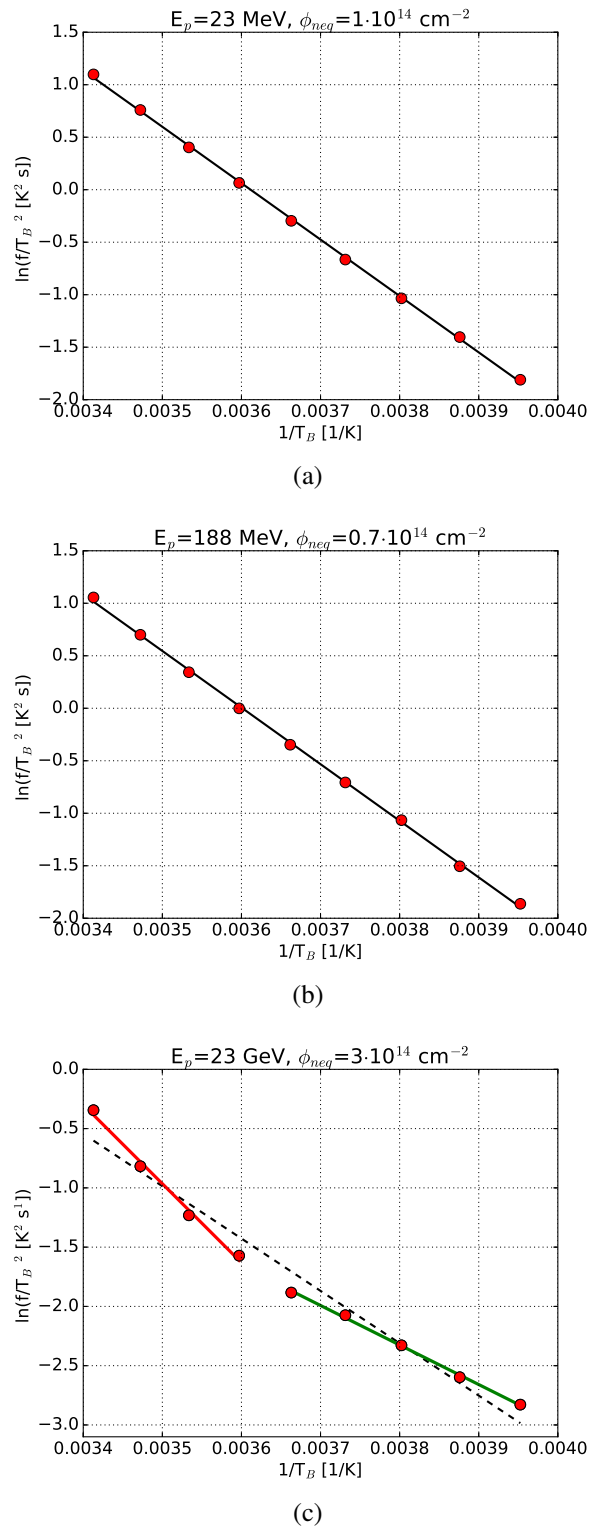


Figure 7.3: Arrhenius plot for three MCz p-type silicon diodes (the corresponding $C(f,T)$ measurements are shown in fig. 5.11(a)- 5.11(c). The fit (solid lines) to data (points) are performed with the method in eq. 7.7 by [148]. Fit errors are smaller than the points.

E_p	Φ_{neq}	$E_t - E_V$ (eV)
23 MeV	$1.0 \cdot 10^{14} \text{ cm}^{-2}$	0.463 ± 0.020
188 MeV	$0.7 \cdot 10^{14} \text{ cm}^{-2}$	0.469 ± 0.020
23 GeV	$3.0 \cdot 10^{14} \text{ cm}^{-2}$	0.633 ± 0.030 (?), 0.300 ± 0.010 (?)

Table 7.1: Activation energies obtained by applying the method in eq. 7.7 by [148], after proton irradiation of MCz p-type sensors.

7.4 Simulations vs. Measurements of bulk defects

On one hand, several models of bulk damage in silicon sensors are currently available for instance from [101] and [149], but they rely on “effective” defect states and not on actual radiation-induced defects. In addition, none of the models is able to simultaneously predict IV/CV and CCE characteristics for a given sensor design and definite operating parameters, after irradiation at a certain Φ_{neq} with specific particle type(s). On the other hand, including all the bulk defects obtained from TSC measurements is challenging in view of developing a radiation damage model, especially because not all the properties of bulk defects (e.g. the minority capture cross-sections) are always measurable.

All in all, it should be noticed that only point defects are calculated in TCAD simulations, while the TSC results presented in this work (chapter 6) clearly point out the presence of defect clusters in the silicon bulk after proton irradiation.

In this section, guidelines for selecting the most relevant bulk defects from TSC measurements are suggested. Defects which do not have any impact on sensor performance (e.g. the VO_i) are excluded from the discussion at the very beginning. As a starting point, the impact of one bulk defect at a time on IV/CV characteristics is reported in subs. 7.4.2; next, a set of six relevant bulk defects is then suggested in subs. 7.4.3. Finally, simulated and measured IV/CV characteristics are compared for three p-type standard FZ diodes, irradiated with 188 MeV protons and Φ_{neq} in the range of $[2.1, 7] \cdot 10^{13} \text{ cm}^{-2}$.

7.4.1 TCAD Input files

Three main input files are used in the present simulations with Synopsys TCAD (version 2012.06):

1. `Silicon.par`: The dielectric constant ϵ for silicon is set equal to 11.9; the carrier recombination lifetimes of electrons and holes are 5 ms and 2.5 ms, respectively.

The widely used definitions of thermal electron and hole velocities for the

evaluation of DLTS or TSC spectra are:

$$v_{n,p}(T) = \sqrt{\frac{3 \cdot k_B \cdot T}{m^*(T)}}, \quad (7.8)$$

with $m^*(T)$ representing the density of state effective masses for electrons or holes.

However, the default thermal velocities for electrons or holes have a different parameterization [150] in TCAD simulations:

$$v_{n,p}^{TCAD}(T) = v_{n,p}(T = 300 \text{ K}) \cdot \sqrt{\frac{T}{300 \text{ K}}}, \quad (7.9)$$

with the following constant values for $v_{n,p}(T = 300 \text{ K})$:

$$\left| \begin{array}{l} v_n(T = 300 \text{ K}) = 2.0420 \cdot 10^7 \text{ cm/s}, \\ v_p(T = 300 \text{ K}) = 1.563 \cdot 10^7 \text{ cm/s}. \end{array} \right.$$

Therefore, correction factors $CF_{n,p}$ have to be applied to majority and minority capture cross-sections of bulk defects. The $CF_{n,p}$ factors are available from [150] and reported in tab. 7.2 for defects of interest in the present work. It can be noticed that $CF_n \approx 1.8$ for electrons while $10 \text{ K} < T < 290 \text{ K}$, whereas for holes a stronger temperature dependence of CF_p can be seen from fig. 7.4. In the picture, data points are obtained from [150], while solid lines are interpolations to 20 data points available from literature.

2. `sde_dvs.cmd`: For specifying the diode thickness (known from CV measurements before irradiation), and the doping profile of the n^+ implant. The doping concentration of the bulk is $N_{eff,0} = 3.8 \cdot 10^{12} \text{ cm}^{-3}$, and the depletion voltage of $V_{dep,0} = 115.4 \text{ V}$. Fig. 7.5 shows a zoom on the n^+ implant;
3. `diode_CV_des.cmd`: For a 2D simulation, a factor of $25 \cdot 10^6 \text{ } \mu\text{m}^2$ is included to account for the actual diode area. Since the pad-size is large, effects of the boundaries are neglected. It takes 1 min for each IV/CV simulation. The simulations are performed at a temperature of $T = 293.15 \text{ K}$ and with AC frequency of 10 kHz, under reverse bias in the range of $[0, -400] \text{ V}$. The results are compared to measured IV/CV measurements performed under the same conditions.

The steering file (`diode_CV_des.cmd`) for the present simulations is made available in app. F; the most relevant part in the “Physics” section is the specification of traps in the silicon bulk region. The effects of one trap at a time is the object of subs. 7.4.2.

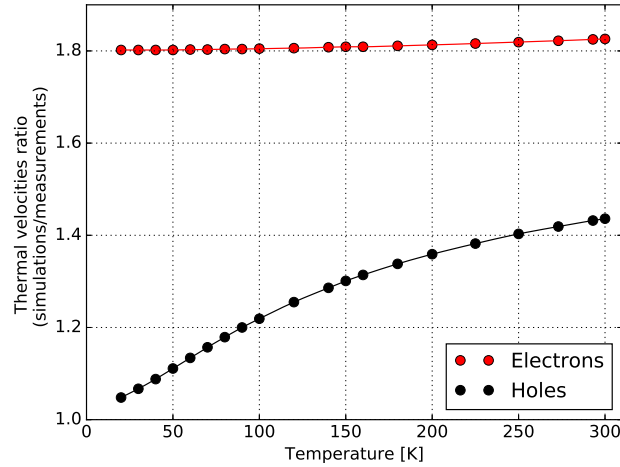


Figure 7.4: Ratio of thermal velocities from simulations and measurements, for electrons and holes. Data points are obtained from [150], while lines are interpolations to the 20 data points available from literature.

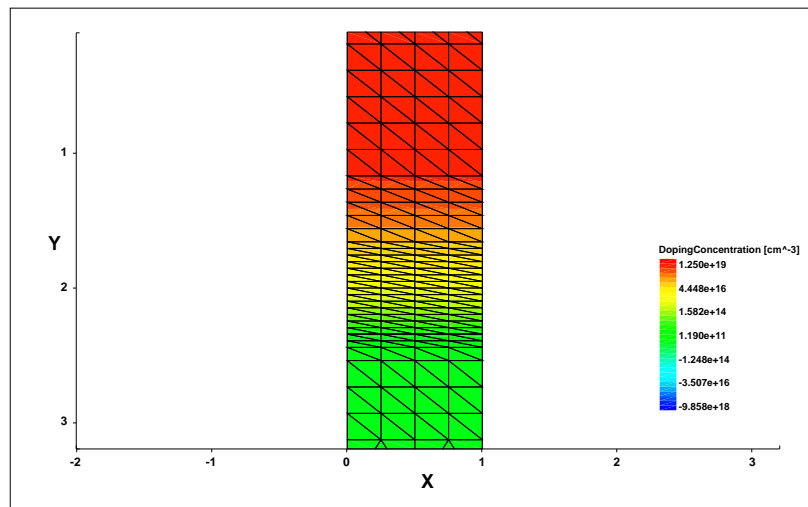


Figure 7.5: 2D simulation of a p-type standard FZ diode: the zoom (with $0 < Y < 3.1 \mu\text{m}$) is on the n^+ implant and the adopted mesh. The Y coordinate (with $0 < Y < 200 \mu\text{m}$) refers to the diode thickness. The X coordinate (with $0 < X < 1$) has to be multiplied for a factor of $25 \cdot 10^6 \mu\text{m}^2$ to account for the actual diode area.

7.4.2 Simulation of single trap

For each bulk defect, four parameters have to be declared: activation energy, concentration, majority σ_{maj} and minority σ_{min} capture cross-sections. As a starting

	E_a [eV]	$\sigma^{measured}$ [cm ²]	CF_n	CF_p	Impact	Fig.
E(30K)	$E_C - 0.1$	$\sigma_n = 2.30 \cdot 10^{-14}$	1.802	1.067	+SC	7.6(a)-7.6(b)
H(152K)	$E_V + 0.42$	$\sigma_p = 2.30 \cdot 10^{-14}$	1.809	1.303	-SC	7.6(c)-7.6(d)
B_iO_i	$E_C - 0.23$	$\sigma_p = 2.48 \cdot 10^{-16}$	1.805	1.219	B-removal	7.6(e)-7.6(f)
V_3	$E_C - 0.46$	$\sigma_n = 2.4 \cdot 10^{-15}$ $\sigma_p = 2.15 \cdot 10^{-13}$	1.811	1.338	+LC	7.7

Table 7.2: Simulated bulk defects, corresponding (fixed) parameters for the present simulations, correction factors for capture cross-sections ($CF_{n,p}$) and impact on sensor properties. Legend: SC=space charge, LC = leakage current.

point, one bulk defect is simulated at a time in order to understand its impact on:

- the space charge (SC), e.g. by the E(30K) donor and the H(152K) acceptor, and affected *in primis* by the boron removal by the B_iO_i donor;
- the leakage current (LC), mainly from the trivacancy V_3 , as previously observed in section 7.1.

In addition to the above mentioned defects (which can be clearly detected in TSC measurements via their emission peaks), the unmissable inclusion of two other deep defects (a deep donor and a deep acceptor) will be presented in subs. 7.4.3. The known activation energies and majority capture cross-sections σ_{maj} are declared in tab. 7.2 for the E(30K), H(152K), B_iO_i and V_3 bulk defects. These properties are fixed for all the performed simulations. Unfortunately, the minority capture cross-sections σ_{min} are not known for the E(30K), H(152K) and B_iO_i bulk defects. Therefore one bulk defect is simulated at a time, with fixed activation energy, σ_{maj} and concentration (obtained from TSC with $T_{fill} = 10$ K for a p-type FZ diodes, after irradiation with 188 MeV protons and $\phi_{neq} = 7.0 \cdot 10^{13}$ cm⁻²). The minority cross-section σ_{min} is varied in the range [$\sigma_{maj}/100$, $\sigma_{maj} \cdot 100$] for donors, and [$\sigma_{maj}/100$, σ_{maj}] for acceptors. The results are summarised in tab. 7.3.

Despite the variation of σ_p for the E(30K) donor over the wide range ($\frac{\sigma_n}{100} \leq \sigma_p \leq 100 \cdot \sigma_n$), no changes in the depletion voltage are noted, nor in the leakage current (which is found to be less than 1 nA). The same conclusions are valid for σ_n of the H(152K) acceptor. We conclude that the missing knowledge of the minority capture cross-section for the E(30K) donor and the H(152K) acceptor is not an issue; it is therefore decided to set the minority capture cross-sections for the E(30K) and H(152K) defects ten time smaller than the majority ones.

Next, the concentrations of bulk defects are increased, while fixing the activation energy and cross-sections. The simulated CV characteristics for increasing [E(30K)] and [H(152K)] are shown in fig. 7.6(a) and fig. 7.6(c), respectively. The

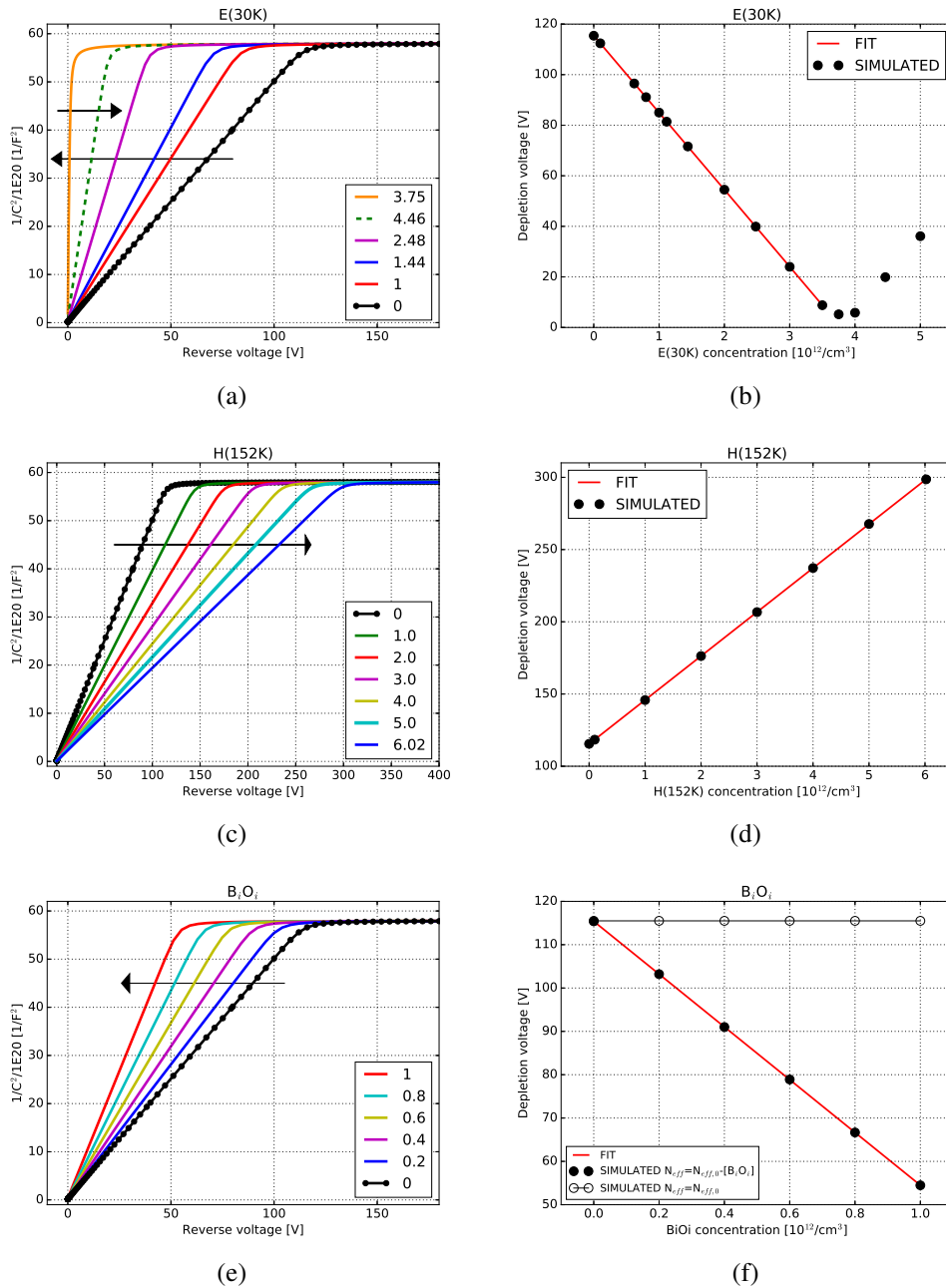


Figure 7.6: Simulated CV characteristics for a p-type standard FZ diode, at increasing (a) [E(30K)], (c) [H(152K)] and (e) [Bi_iO_i] (expressed in 10^{12} cm^{-3}), and (b)-(d)-(f) corresponding depletion voltage as a function of defect concentrations. (Left) Two linear fit are applied in the two regimes (the rising and constant ranges) of the $1/C^2$ curves to extract the depletion voltage V_{dep} ; (right) a linear fit is applied to obtain the rate of increase/decrease of V_{dep} with defect concentrations.

	N_t [$10^{12}/\text{cm}^3$]	Variation of σ_{min}	Produced LC [A]	Shift of V_{dep}
E(30K)	2.48	$\frac{\sigma_n}{100} \leq \sigma_p \leq 100 \cdot \sigma_n$	$\leq 8 \cdot 10^{-10}$	No
H(152K)	6.02	$\sigma_n \leq \sigma_p$	$\leq 8 \cdot 10^{-8}$	No
B_iO_i	0.84	$\frac{\sigma_n}{100} \leq \sigma_p \leq 100 \cdot \sigma_n$	$\leq 8 \cdot 10^{-10}$	No

Table 7.3: Impact of (unknown) σ_{min} on IV/CV characteristics.

depletion voltage is extracted from the intersection point between two linear fit, one for the rising part of the $1/C^2$ curve and the second one to the end capacitance. The corresponding depletion voltage as a function of [E(30K)] and [H(152K)] are shown in fig. 7.6(b) and fig. 7.6(d), with evident +SC and -SC contribution, respectively. The rate at which the depletion voltage increases as a function of [H(152K)] is $30 \cdot 10^{-12} \text{ V} \cdot \text{cm}^3$, while in the case of [E(30K)] is $-30 \cdot 10^{-12} \text{ V} \cdot \text{cm}^3$ until [E(30K)] = $N_{eff,0}$.

Since the present simulations are performed for p-type diodes, it is recommended to include the B_iO_i donor in the simulations. As in the case of the E(30K) and H(152K) defects, almost no impact on the IV is found due to the presence of the B_iO_i . Moreover, no visible changes are obtained after varying the minority cross section between $[\sigma_{maj}/100, \sigma_{maj} \cdot 100]$. However, an increase in the $[B_iO_i]$ leads to a decreasing depletion voltage, only if the original effective doping concentration is reduced by $[B_iO_i]$, i.e.:

$$N_{eff} = N_{eff,0} - [B_iO_i], \quad (7.10)$$

as shown in fig. 7.6(e). The depletion voltage would otherwise stay constant if the boron removal is not properly taken into account. From fig. 7.6(f) it is possible to note that the depletion voltage decreases as a function of the $[B_iO_i]$ with a rate of $-60.9 \cdot 10^{-12} \text{ V} \cdot \text{cm}^3$, a factor two with respect to the rate due to the other donor E(30K).

In the interest of simulation at higher fluences than $7 \cdot 10^{13} \text{ cm}^{-2}$, we recall that $[B_iO_i]$ saturates to a value of $[B_iO_i]_S = 2.4 \cdot 10^{12} \text{ cm}^{-3}$, after irradiation with 23 GeV protons and $\phi_{neq} = 3.0 \cdot 10^{14} \text{ cm}^{-2}$, as reported in subs. 6.3.2.

Up to now, no deviation from the typical $1/\sqrt{V_{reverse}}$ is observed in the $1/C^2$ plot, after including the E(30K), H(152K), and B_iO_i defects. Such deviation is expected from measured CV characteristics, and it is expected to be due to a high density of generation-recombination centres, which are even deeper than the defects discussed up to now in this subsection (see subs. 7.4.3). Such deep bulk defects are expected to be responsible not only for changes in the space charge, but also on the leakage current, together with the trivacancy V_3 . As opposed to the E(30K),

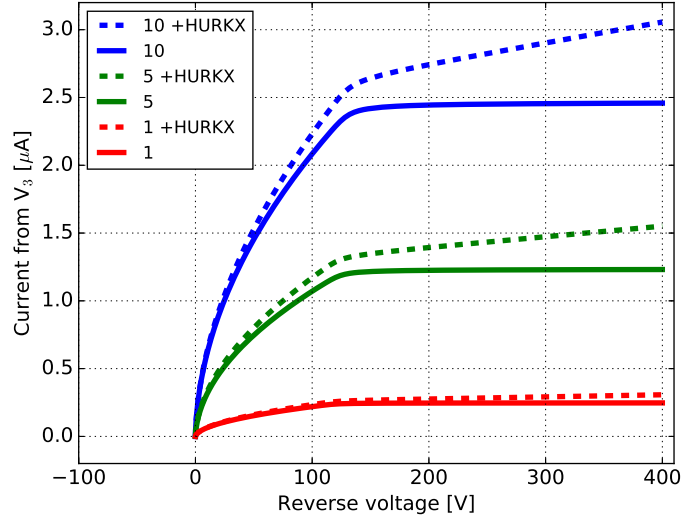


Figure 7.7: Simulated IV characteristics for three values of V_3 concentration (expressed in 10^{12} cm^{-3}), with or without the inclusion of Hurkx tunneling.

H(152K) and B_iO_i , the V_3 defect has little impact on the space charge, but is (mainly) responsible for the leakage current.

All the known properties for the V_3 are reported in tab. 7.2. From fig. 7.7, it is worth noticing that the unique properties of the V_3 (having $\sigma_p \approx 100\sigma_e$) lead to a leakage current in the order of few μA if $[V_3] \geq 10^{12} \text{ cm}^{-3}$, as found after irradiation with $\phi_{neq} = 7 \cdot 10^{13} \text{ cm}^{-2}$.

At this point it is worth remembering that, different types of leakage current flow to the diode bulk, according to the bias conditions. Current generation can be increased from I_{gen} to I_{Hurkx} by trap assisted tunneling with phonon interactions, for which a two step mechanism was proposed by Hurkx [151], [152] and [153]. Firstly, a charge carrier at one main defect center is thermally enhanced, and then it tunnels through the remaining potential barrier. The enhancement of the thermal generation current (I_{gen} , i.e. the current emitted from traps in the band gap) is analytically approximated as [152]:

$$I_{Hurkx} = I_{gen} \cdot B_{Hurkx}, \quad (7.11)$$

being B_{Hurkx} the electric field factor for the diode leakage current by the Hurkx mechanism; it is derived from the ratio of the emission probability with and without tunneling [151]. The tunneling component factor B_{Hurkx} depends on the effective mass, the depletion width (W), the effective electric field (F_{eff}) and the

temperature:

$$\left| \begin{array}{l} B_{Hurkx} = \sqrt{3\pi} \frac{F_{\Gamma}}{F_{eff}} \left[\exp\left(\frac{F_{eff}}{F_{\Gamma}}\right)^2 - \exp\left(\frac{F_{eff} \cdot W(0V)}{F_{\Gamma} \cdot W}\right) \right], \\ F_{\Gamma} = \frac{\sqrt{24m^* \cdot (kT)^3}}{e\hbar}. \end{array} \right.$$

Practically, in the simulations, the Hurkx model is included for deep defects, and the effective electric field at every grid point of the 2D simulation is taken into account [154]. The trap energy determines the temperature dependence of the leakage current, while the effective mass parameter affects the slope of the leakage current (see fig. 7.7). In addition, the capture cross section of the generation current is decreased by:

$$\sigma_{Hurkx} = \frac{\sigma_{n,p}}{1 + B_{Hurkx}}. \quad (7.12)$$

In addition to the trap assisted tunneling, other possible mechanisms for the leakage current are band to band tunneling [151] and the Poole-Frenkel effect [155].

7.4.3 Simulation with a set of bulk defects

In this section, a set of six bulk defects is considered in order to compare the simulated IV/CV characteristics (with six bulk defects) to measured ones, for three p-type standard FZ diodes irradiated with 188 MeV protons. The approach is inspired by the results of TSC measurements: the starting point is presented in fig. 7.8, showing the TSC spectra after three ϕ_{neq} . The defect included in the simulations are: the E(30K), H(152K), B_iO_i , V_3 , a deep donor (DD, which is possibly the H(220K) defect) and a deep acceptor (DA). The initial doping concentration is reduced by the $[B_iO_i]$.

All the activation energies are obtained from the universally adopted values, available in literature, a part for the DA defect whose activation energy is the same as in [101]. This value is close to midgap and, within experimental errors, the same for the activation energy obtained in this work (subs. 6.2.1) for the leakage current.

Concerning the capture-cross sections, all the known values from literature are included; if unknown, the minority capture cross-section is set to be 10 times smaller than the majority one, as motivated in subs. 7.4.2. For the deepest defect (DA) it is assumed that $\sigma_{maj} = \sigma_{min} = 10^{-14} \text{ cm}^2$, which is the typical value used for the cross-sections of GR centers [156] – [157]. The concentrations of the deepest defects are ten times higher than the concentration of the other (four) defects, and

in the same order of magnitude for the defects obtained by [158] who developed a deep level model starting from pulse shapes (TCT). Moreover, the concentration of the deepest defects were found to be at least one order of magnitude higher than the initial doping concentration also in [159], with a linear increase in the concentration with the fluence. The capture cross-sections are corrected by $CF_{n,p}$, as recommended in subs. 7.4.2.

Concerning the defect concentrations, $[H(152K)]$ and $[B_iO_i]$ are obtained from TSC measurements at $T_{fill} = 10$ K, while it is strongly recommended to consider the highest peak occurring with $T_{fill} > 10$ K for the $[E(30K)]$ and $[V_3]$. In fact, $[E(30K)]$ and $[V_3]$ can be up to +80% and +180% higher if $T_{fill} > 10$ K, respectively (after irradiation in the 10^{13} cm^{-2} range, see section 6.4). For the deepest defects, we recall that the generation current at 300 V is assumed to be due to three deep defects as follows:

$$I_{TSC}(T) = q_0 \cdot A \cdot d \cdot \left(\sum_{i=V_3, \substack{DA, \\ DD}} N_i \cdot \frac{e_{n,i}(T) \cdot e_{p,i}(T)}{e_{n,i}(T) + e_{p,i}(T)} \right). \quad (7.13)$$

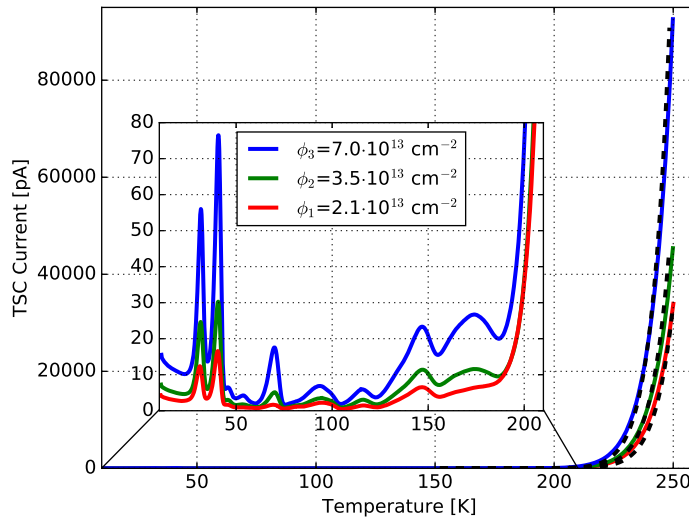


Figure 7.8: TSC measurements for p-type standard FZ diodes, irradiated with 188 MeV protons at three ϕ_{neq} and annealing of 8 min at 80°C . The inset shows the TSC peaks after $V_H = 300$ V, spanning over $[0, 80]$ pA in a temperature range of $[10, 190]$ K, while the generation current spans over $[0, 80]$ nA in a temperature range of $[200, 250]$ K and is fitted with eq. 7.13 (dashed black lines).

with the emission rates $e_{n,i}$ or $e_{p,i}$ of the i -defect with concentration N_i given by:

$$e_{n,p} = c_{n,p}(T) \cdot N_{C,V}(T) \cdot \exp\left(\pm \frac{E_T(T) - E_{C,V}}{k_B T}\right). \quad (7.14)$$

In fact, the deepest defects (V_3 , DA and DD) are expected to be responsible for the TSC current increase from the ≈ 100 pA range to the ≈ 80 nA range, as notable in the [200, 250] K temperature range of fig. 7.8.

It is also assumed that $[DA] > [DD]$, and their concentrations are obtained from the fit with eq. 7.13 to the generation current in the [200, 250] K temperature range of the TSC spectra (dotted black lines in fig. 7.8).

The complete list of input parameters are reported in tab. 7.4 for three p-type standard FZ diodes irradiated with three different ϕ_{neq} in the range of $[2.1, 7] \cdot 10^{13} \text{ cm}^{-2}$. The comparison between simulated and measured IV/CV characteristics are presented in fig. 7.9(a)–7.9(f) after three ϕ_{neq} . It is worth noticing that a good agreement is found if the concentrations after $\phi_{neq} = 7 \cdot 10^{13} \text{ cm}^{-2}$ are scaled at lower ϕ_{neq} by the ratio of neutron equivalent fluences.

In fig. 7.10(a)–7.10(f) the electric field (at three reverse bias) and the trap occupations (at just one reverse bias of -400 V) are reported for the three analyzed samples. It is possible to note that the E(30K), H(152K) and B_iO_i are full, whereas the all the other deeper defects (the DD, DA, and V_3) are only partially filled.

It would be interesting to test such scaling for samples irradiated at higher fluences. It is strongly recommend to include also the C_iO_i defect (see subs. 6.4) to account for trapping and in view of comparing simulated to measured CCE characteristics as well.

		σ_n	σ_p	N_t [10^{12} cm^{-3}]		
	E_a (eV)	[cm^2]	[cm^2]	ϕ_1	ϕ_2	ϕ_3
E(30K)	$E_C - 0.1$	$1.276 \cdot 10^{-14}$	$1.276 \cdot 10^{-15}$	1.34	2.23	4.46
H(152K)	$E_V + 0.42$	$1.768 \cdot 10^{-15}$	$1.768 \cdot 10^{-14}$	1.086	1.81	3.62
B_iO_i	$E_C - 0.23$	$1.37 \cdot 10^{-16}$	$1.37 \cdot 10^{-17}$	0.252	0.42	0.84
V_3	$E_C - 0.46$	$1.104 \cdot 10^{-15}$	$1.606 \cdot 10^{-13}$	3.405	5.68	11.35
DD	$E_V + 0.48$	$3.3 \cdot 10^{-16}$	$3.99 \cdot 10^{-15}$	14.9	24.9	49.8
DA	$E_C - 0.525$	10^{-14}	10^{-14}	18.0	30.1	60.1
[$\max_{T_{fill}} > 10 \text{ K}$] (this work)	from DLTS	from TSC (this work)	incl. $CF_{n,p}$ (this work)	from literature	$\sigma_{maj}/10$ (this work)	from GR (this work)

Table 7.4: Input parameters for simulations of IV and CV characteristics (shown in fig. 7.9(a)-7.9(f)) of p-type standard FZ diodes, after irradiation with 188 MeV protons and annealing of 8 min at 80°C. Legend: $\phi_1 = 2.1 \cdot 10^{13} \text{ cm}^{-2}$, $\phi_2 = 3.5 \cdot 10^{13} \text{ cm}^{-2}$ and $\phi_3 = 7.0 \cdot 10^{13} \text{ cm}^{-2}$. The color code is explained at the bottom of the table.

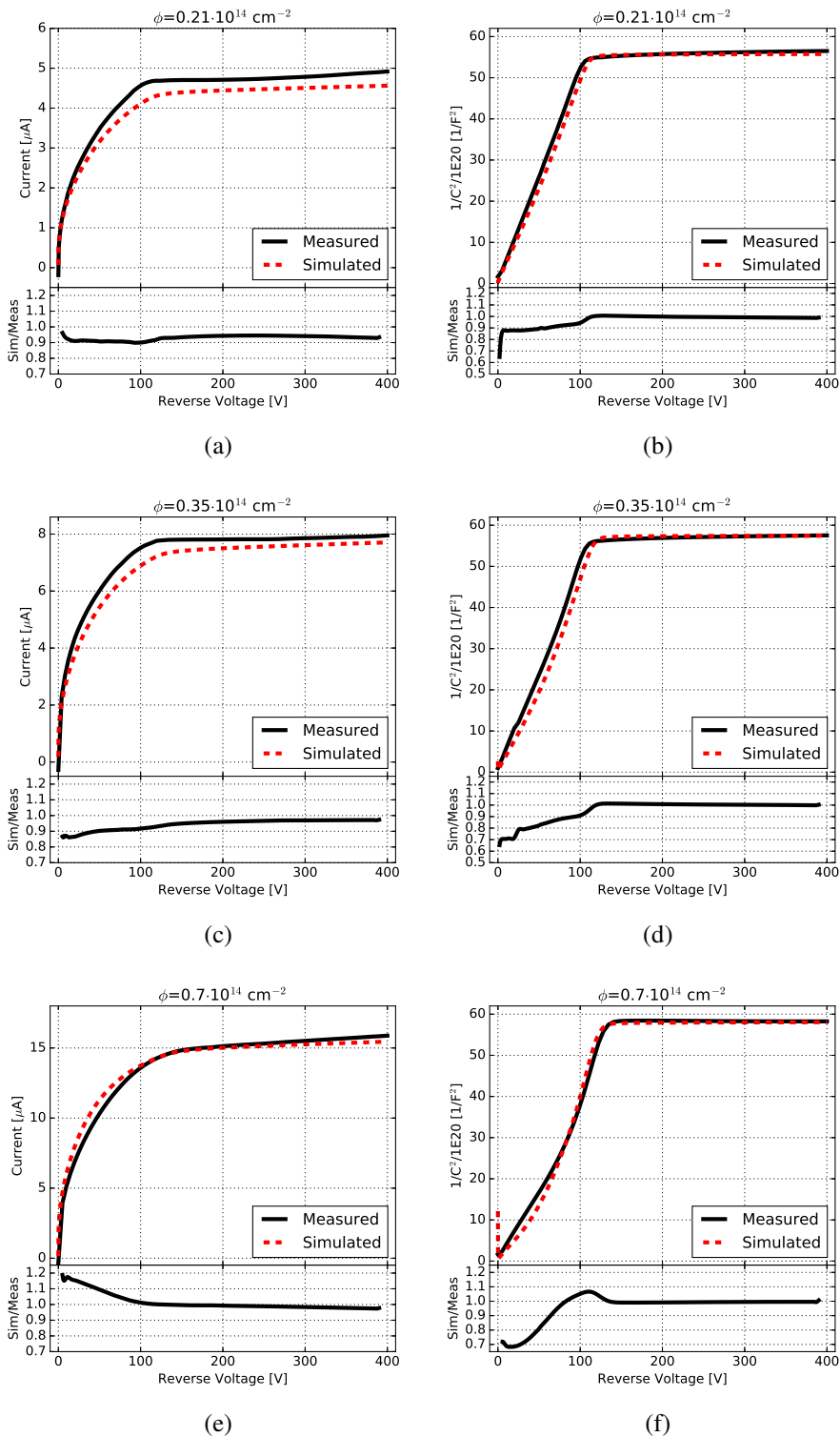


Figure 7.9: Comparison between simulated and measured IV/CV characteristics for p-type standard FZ diodes, after irradiation with 188 MeV protons and annealing of 8 min at 80°C, at three ϕ_{neq} fluences.

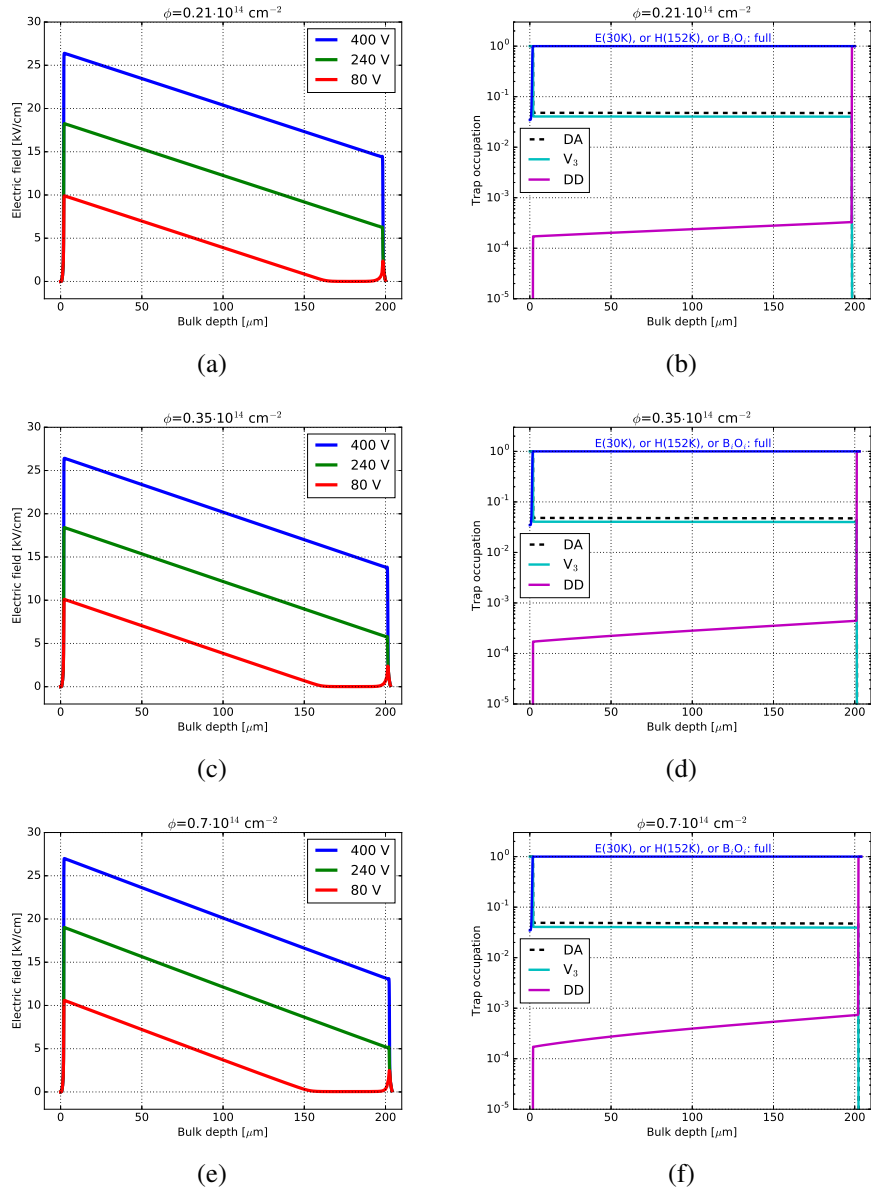


Figure 7.10: Electric field and trap occupation relative to the simulations under the conditions described for the simulations presented for fig. 7.9(a)–7.9(f).

Conclusion & Outlooks

The study was set to explore the proton-energy dependent damage to silicon pad diodes, after irradiation with 23 MeV, 188 MeV and 23 GeV protons, with corresponding hardness factors of 2, 0.7 and 1 (available in literature). The samples were irradiated with 1 MeV neutron equivalent fluences at selected values in the range $[1 \cdot 10^{13}, 3.0 \cdot 10^{14}] \text{ cm}^{-2}$. Three different bulk materials were investigated: MCz, standard FZ and deep-diffused FZ. The study sought to identify proton-induced bulk defects not only in n-type, but especially in p-type silicon sensors for which a quite limited amount of data was available before the present work. The relevance of the investigations are evident due to the growing interest for p-type sensors in HEP experiments in the past few years, and due to the issue of boron removal, namely the reduction of p-doping concentration due to trapping from the B_iO_i defect. On one hand, bulk defects have been identified both in n-type and p-type materials with Thermally Stimulated Current measurements (TSC); on the other hand, Current-Voltage (IV) and Capacitance-Voltage (CV) measurements were performed in order to link the presence of bulk defects to their impact on the sensor properties and performances.

The concluding part is structured in four sections, dealing with:

- 1 Performed measurements and new approaches to IV/CV and TSC techniques;
- 2 Analysis methods, together with a synthesis of their usefulness and key findings;
- 3 Guidelines for TCAD simulations in view of merging relevant information from the above mentioned measurements;
- 4 Outlooks and suggested further investigations.

1) Measurements

Three type of experimental techniques are used for the present thesis work:

1. IV measurements in reverse bias, at three selected temperatures (253 K, 273 K, 293 K), to be correlated with TSC results about defects with impact of the leakage current;
2. CV measurements in reverse bias, at three selected temperatures (253 K, 273 K, 293 K) and selected AC frequencies (455 Hz, 1 kHz, 10 kHz), to be correlated with TSC results about space charge concentration. In addition $C(f,T)$ were performed at low bias voltage and over a wide frequency range (100 Hz, 1 MHz) to obtain the activation energy of the dominant deep level. Forward IV/CV characteristics are additionally performed;
3. For all the samples, Thermally Stimulated Current measurements were performed at the conventional $T_{fill} = 10$ K, in order to obtain the defect concentrations. For some samples TSC spectra were performed also at many higher T_{fill} (up to 130 K); such measurement type is extremely time consuming (lasting at least 3 days), but provides a further insight on the temperature-dependent capture coefficients. The forward bias at all the various T_{fill} should be carefully selected in order to guarantee enough filling current in all the filling steps. Differences in defect concentrations are observed between filling at the conventional temperature of 10 K and higher temperatures. Such differences are especially relevant for the E(30K) and the V_3 defects, and up to +80% and +180%, respectively, after irradiation in the 10^{13} cm⁻² fluence range (see section 6.4).

2) Data analysis

The analysis of the above mentioned measurements is central to provide relevant information about bulk defects and their effect on the irradiated samples. In particular:

1. IV measurements in reverse bias were analyzed with focus on the damage-related parameter α . In fact, the leakage current after irradiation is found to scale with NIEL for the various proton energies, fluences and for all the investigated bulk material and types;
2. CV measurements were necessarily analyzed with the initial rise method, in order to calculate the average space charge concentration. The fundamental assumption is that at low bias the concentration of free charge carriers is not sufficient to fill deep traps: in fact, at low current the occupation of traps is not changed due to the free-charge carriers.
From the temperature and frequency dependences of the capacitance, it is

possible to obtain the activation energy of dominant deep levels. The analysis of $C(f,T)$ provides complementary information with respect to TSC measurements. In fact, the last clearly distinguishable peak in TSC measurements is ≈ 0.43 eV (i.e. the activation energy of the V_3 defect); while from $C(f,T)$ measurements it is possible to note that another deep defect is located in the $[0.443, 0.489]$ eV energy range. This is valid after irradiations with 23 MeV and 188 MeV protons with fluences less than 10^{14} cm $^{-2}$; after 23 GeV protons irradiated with fluences of $3 \cdot 10^{14}$ cm $^{-2}$, the method indicates that at least two defects play a role (see section 7.3);

3. The analysis of forward IV/CV characteristics suggested that the irradiation has so much altered the semiconductor material that it is not lifetime- but relaxation-like. The proposed explanations were based on the relaxation theory for the occurrence of ohmic IV and negative capacitance (see subs. 5.1.6 and 5.2.5, respectively);
4. For the analysis of TSC spectra, three different analysis methods were implemented in Python. In the first case, a simplified model was implemented for obtaining bulk defect concentration from TSC measurements with the conventional filling temperature of 10 K, under the assumption that all the defects are fully filled at the same temperature. The simplified model is used in many studies of this thesis for historical reasons, and can be easily adapted for analysis of TSC spectra for different materials, bulk type, and particle type and energy.
 The second analysis method is an extension of the first (simplified) method and aims to analyze TSC spectra after $T_{fill} > 10$ K. The second method accounts for the temperature-dependent capture coefficients according to the multi-phonon process.
 The third method is an innovative approach to the analysis of TSC spectra in the presence of defect clusters. The new formalism is based on the SRH statistics, modified to account for the occupation-dependent activation energy of cluster defects. The method allows for distinguishing point- from cluster-like defects: in fact, it has been found that the variation of the activation energy δE^0 for cluster-related defects is typically in the range of $[10, 20]$ meV, while for point-like δE^0 assumes one order of magnitude lower values. The method is being tested for analysis of TSC spectra after irradiation with different particles and it is the object to a next publication [160]. The maximum variation in the concentration between the (first) simplified model and the (third) SRH-based model is 6% for VO_i defect, otherwise it is less than 2 % for all other defects.
5. Thanks to annealing studies, it was possible to correlate the leakage current

with the weighted concentrations of three main defects responsible for the leakage current (V_3 , V_2 , and H(220K)). Comparing the information from CV and TSC is more challenging, and pointed out that at least 4 or 5 defects are contributing to the space charge in n- and p-type sensors, respectively. In particular, positive contributions to the space charge of p-type sensors are mainly due to the E(30K) and the B_iO_i defects, while three deep acceptors (namely H(116K), H140K, and H(152K)) negatively contribute to the space charge.

3) Simulations

It was instructive to simulate one bulk defect at a time, with all the possible information at the best of the present knowledge from DLTS or TSC measurements: this was the case for the E(30K) donor, the B_iO_i donor, and the H(152K) acceptor. At the investigated $\phi_{neq} < 7 \cdot 10^{13} \text{ cm}^{-2}$, it was confirmed that the three defects are responsible for changes in the space charge concentration, but not on the leakage current which is mainly due to the trivacancy defects.

For the four above mentioned defects, the concentrations are obtained from TSC measurements, while activation energies and majority capture cross-sections are taken from literature (if available). The minority capture cross-sections for the E(30K), H(152K) and B_iO_i defects are unknown, but, if varied over a wide range with respect to the majority capture cross-section, they have no impact on IV nor CV characteristics.

The implemented concentrations were corrected for the values obtained from TSC spectra at $T_{fill} > 10 \text{ K}$; the capture cross-sections were corrected for the ratio of thermal velocities for electrons and holes.

To complete the set of relevant bulk defects, it was suggested to obtain from $C(f,T)$ curves at low bias and TSC spectra at high temperature (i.e. the so-called “generation current”), the activation energies of the dominant deep defects (one deep donor and one deep acceptor).

As noted from [80] and [161], the CCE is reduced by 15% and 10%, after 23 MeV protons and 23 GeV protons at fluences of $3 \cdot 10^{14} \text{ cm}^{-2}$, respectively. Therefore, extrapolations to the lower fluences considered in the present simulations (i.e. $7 \cdot 10^{13} \text{ cm}^{-2}$) point out that the reduction in CCE is transcurable. This is the reason why CCE measurements and simulations were not compared.

4) Outlook

From the experimental point of view, a (practical) limitation has to be mentioned: on one hand TSC measurements are time consuming, but on the other hand they provide a wealth of information about bulk defects that are necessary in view of developing a radiation damage model based on actual bulk defects. TSC measurements at higher filling temperatures were even more time consuming, but misleading conclusions about defect concentrations and proton-energy dependent

introduction rate of defects could be avoided. Moreover, they provided information of defects which are expected to be responsible for trapping (this is the case of the C_iO_i defect, which is not detected with the conventional $T_{fill} = 10$ K because of its temperature dependent capture coefficient). In regard of simulations of CCE characteristics, it is suggested to include the C_iO_i defect (detected in TSC measurements with $T_{fill} > 10$ K) to account for trapping in future simulations at higher fluences than the presently considered.

TSC measurements demonstrated that after high fluences ($\phi_{neq} > 3 \cdot 10^{14} \text{ cm}^{-2}$) defects with negative contribution to the space charge are more abundant than those with positive contribution. More work is necessary in order to sort out an underestimation of [E(30K)] or undetected deep defects with positive contribution to the space charge.

It should be noted that TSC measurements for highly irradiated samples are challenging ($\phi_{neq} > 10^{14} \text{ cm}^{-2}$) because deep level emissions are indistinguishable from the background current. The issue might be overcome by performing Zero-Bias TSC (ZB-TSC) i.e. with no bias applied during the heating phase.

It is possible that the C_iO_i defect should be added in order to account for trapping. More investigations about the boron removal at higher fluences are necessary in order to confirm the saturation at high fluences, and correctly taking into account the effect of such defect.

Detailed investigations are also needed for the H(40K) defect which in the present study is not considered as contributor to the leakage current nor to the space charge. From TSC measurements it is clear that it vanishes after 60 min at 80°C . Defect engineering is needed in order to fight the occurrence of cluster of defects after proton irradiation. It is planned to investigate the potential suppression of vacancy and interstitial aggregates with nitrogen enrichment.

A

List of measured devices

Proton beam		FZ		MCz		FTH	
Energy	Fluence [10^{14} cm^{-2}]	n	p	n	p	n	p
23 MeV	0.30	01/9	05/9	09/5	05/9		03/5
	0.50	04/11	06/8	03/5	06/11	23/8	02/5
	1.00	01/11	04/9	04/5	07/8	23/9	
188 MeV	0.21	6g_3E13	2g_3E13	5g_3E13	3g_3E13	1g_3E13	4g_3E13
	0.35		8g_5E13	10g_5E13		7g_5E13	9g_5E13
	0.70	16g_1E14	12g_1E14	15g_1E14	13g_1E14	11g_1E14	14g_1E14
23 GeV	1.00	04/8	04/8	03/11	05/8		
	3.00	05/9	05/8	10/11	06/8		

Table A.1: Summary of investigated 200 μm silicon n- and p-types pad diodes. Black cells point out not available samples. In most of cases, IV/CVf and TSC measurements were successfully accomplished at five subsequent annealing times (0, 8, 15, 30, 60) minutes at 80°C.

Density of states

In the following, the formalism accounting for the temperature dependence of the electron and hole masses is introduced, and it is needed for the TSC peak fitter method presented in section 6.5.

First of all, the temperature dependence of the band gap in silicon is computed according to the Varshni equation [162]:

$$E_{gap}(T)[eV] = E_{gap,0} - \frac{\alpha T^2}{T + \beta}, \quad (\text{B.1})$$

where:

$$\left| \begin{array}{l} E_{gap,0} = 1.1696, \\ \alpha = 4.73 \cdot 10^{-4}, \\ \beta = 636. \end{array} \right.$$

The temperature dependence of the electron mass is computed as follows:

$$m_e(T) = 6^{2/3} (m_{te}(T) \cdot m_{le})^{1/3}, \quad (\text{B.2})$$

where:

$$\left| \begin{array}{l} m_{te}(T) = 0.1905 \frac{E_{gap,0}}{E_{gap}(T)}, \\ m_{le} = 0.9163. \end{array} \right.$$

The temperature dependence of the hole mass is:

$$m_h(T) = \left(\frac{a + bT + cT^2 + dT^3 + eT^4}{1 + fT + gT^2 + hT^3 + iT^4} \right), \quad (\text{B.3})$$

where:

$$\left\{ \begin{array}{ll} a = 0.443587, & f = 0.4683382E - 2, \\ b = 0.3609528E - 2, & g = 0.2286895E - 3, \\ c = 0.1173515E - 3, & h = 0.7469271E - 6, \\ d = 0.1263218E - 5, & i = 0.1727481E - 8, \\ e = 0.3025581E - 8, & \end{array} \right.$$

Thermal velocity for electrons or holes have the same temperature dependence:

$$v_{n,p}(T) = v_{n,p}(T = 300K) \cdot \sqrt{\frac{T}{300}}, \quad (\text{B.4})$$

$$\left\{ \begin{array}{l} v_n(T = 300 \text{ K}) = 2.0420 \cdot 10^7 \text{ cm/s}, \\ v_p(T = 300 \text{ K}) = 1.563 \cdot 10^7 \text{ cm/s}. \end{array} \right.$$

The density of states in the conduction and valence bands are:

$$N_C(T) = 2 \cdot \left(\frac{2\pi m_e(T) k_B T}{\hbar^2} \right)^{3/2} \quad \text{and} \quad N_V(T) = 2 \cdot \left(\frac{2\pi m_h(T) k_B T}{\hbar^2} \right)^{3/2}. \quad (\text{B.5})$$

Finally, the emission rates for electron for electrons and holes are computed as:

$$e_{n,p}(T) = \sigma_{n,p} v_{n,p}(T) N_{C,V}(T) \exp\left(\frac{-\Delta E_a}{k_B T}\right). \quad (\text{B.6})$$

where $\sigma_{n,p}$ are the capture cross section for electrons or holes, respectively. The activation energy for the emission of charge carriers from one trap is ΔE_a .



List of TSC parameters

A quick overview and check-list before starting a TSC measurement is presented in tab. C.1.

The ID number refers to the input parameter in the steering file for a TSC scan.

ID	Parameter	Options	Comments
1	Filling T	5–10 K	Precision ± 1 K
2	Cooling rate	1.0 K/s	$\Delta t \approx 2$ h for $\Delta T = 280$ K
3	Cooling bias	0 V or reverse	Mandatory
4	Cryostat on	32	Mandatory
5	Filling bias	0 V or forward	To be set after IV at 10 K
6	Filling duration	30 s	Recommended
7	Waited time	30 s	Recommended
8	Optical filling	520 or 670 nm	Optional
9	Cryostat off	0	Mandatory
10	Final T	250 K/290 K	TSC spectrum/LC
11	Heating rate	0.183 K/s or < 0.200 K/s	TSC current linear with time
12	Heating bias	0 or reverse	Higher than V_{dep}
13	Cryostat off	0	Mandatory

Table C.1: Summary of parameters to be used for setting a TSC scan.



List of α values

E_p	bulk	type	0 min		8 min		15 min		30 min		60 min	
			$\bar{\alpha}$	σ								
23 MeV	MCZ	n	4.96	0.79	4.09	0.65	3.71	0.59	3.21	0.51	2.84	0.45
	MCZ	p	4.61	0.74	3.86	0.62	3.49	0.55	3.09	0.49	2.77	0.44
	FZ	n	4.94	0.79	3.74	0.60	3.58	0.57	3.20	0.51	2.80	0.45
	FZ	p	4.96	0.79	3.91	0.63	3.54	0.57	3.22	0.51	2.82	0.45
	dd-FZ	n	4.60	0.74	3.73	0.60	3.42	0.55	2.98	0.48	2.55	0.41
	dd-FZ	p	4.56	0.73	3.37	0.54	3.22	0.52	2.87	0.46	2.57	0.41
188 MeV	MCZ	n	5.70	0.91	4.2	0.67	3.71	0.59	3.23	0.52	2.85	0.46
	MCZ	p	5.44	0.87	3.93	0.63	3.56	0.57	3.11	0.50	2.80	0.45
	FZ	n	5.44	0.87	4.02	0.64	3.54	0.57	3.13	0.50	2.85	0.46
	FZ	p	5.57	0.89	4.25	0.68	3.76	0.60	3.34	0.53	2.95	0.47
	dd-FZ	n	5.21	0.84	3.96	0.63	3.60	0.58	3.08	0.49	2.49	0.40
	dd-FZ	p	5.51	0.88	3.96	0.63	3.49	0.56	3.05	0.49	2.71	0.43
23 GeV	MCZ	n	5.89	1.35	4.61	1.03	4.25	0.98	3.44	0.79	2.65	0.61
	MCZ	p	6.04	1.39	4.42	1.02	3.67	0.84	3.39	0.78	3.21	0.74
	dd-FZ	n	5.15	1.18	3.89	0.90	3.21	0.74	3.17	0.73	3.07	0.71
	dd-FZ	p	5.63	1.29	4.10	0.94	3.66	0.84	3.10	0.74	2.84	0.66

Table D.1: List of α values for different proton energies E_p , bulk material and annealing times. Mean $\bar{\alpha}$ values are provided in units of 10^{-17} A/cm, together with the corresponding standard deviation.

Error from trapezoidal rule

We recall that, in the present work, the concentrations N_t of bulk defects from TSC measurements are obtained via eq. 6.4:

$$N_t = \frac{2A_{peak}}{q_0V_{dep}}, \quad (\text{E.1})$$

where the area $A_{peak} = \int_{T_{min}}^{T_{max}} I_{TSC}(T)dT$ under a TSC peak is approximated with the trapezoidal rule with n intervals. The largest error σ_A on the computed area by such type of numerical integration is [163]:

$$\max(\sigma_A) \leq \frac{|\max(\frac{d^2}{dT^2}I_{TSC}(T))|(T_{max} - T_{min})^3}{12n^2}, \quad (\text{E.2})$$

and it is directly proportional to the largest possible absolute value of the second derivative for the function $I_{TSC}(T)$. The integration range is between $[T_{min}, T_{max}]$ and an appropriate binning has to be adopted in order to minimize the overall error.

In the present work, the second derivative has to be calculated for eq. 6.3, representing a TSC peak. To make the calculations easier, we rearrange eq. 6.3 as follows:

$$I_{TSC}(T) = \frac{k \left(1 - \frac{1}{e^{-\frac{T-T_c-\frac{\alpha}{2}}{\beta}} + 1} \right)}{e^{-\frac{T-T_c+\frac{\alpha}{2}}{\gamma}} + 1}. \quad (\text{E.3})$$

The first derivative of $I_{TSC}(T)$ is:

$$\frac{d}{dT}I_{TSC}(T) = -\frac{ke^{\frac{T-T_c+\frac{\alpha}{2}}{\gamma}} \left(\gamma e^{\frac{T-T_c+\frac{\alpha}{2}}{\gamma}} + \frac{T-T_c-\frac{\alpha}{2}}{\beta} + (\gamma-\beta) e^{\frac{T-T_c-\frac{\alpha}{2}}{\beta}} - \beta \right)}{\beta\gamma \left(e^{\frac{T-T_c-\frac{\alpha}{2}}{\beta}} + 1 \right)^2 \left(e^{\frac{T-T_c+\frac{\alpha}{2}}{\gamma}} + 1 \right)^2}. \quad (E.4)$$

The second derivative of $I_{TSC}(T)$ is:

$$\frac{d^2}{dT^2}I_{TSC}(T) = ke^{\frac{T-T_c+\frac{\alpha}{2}}{\gamma}} \cdot \frac{Numerator}{Denominator}, \quad (E.5)$$

with numerator and denominator defined as follows:

$$\begin{aligned} Numerator &= \left(\gamma^2 e^{\frac{2(T-T_c-\frac{\alpha}{2})}{\beta}} - \gamma^2 e^{\frac{T-T_c-\frac{\alpha}{2}}{\beta}} \right) e^{\frac{2(T-T_c+\frac{\alpha}{2})}{\gamma}} \\ &+ \left((2\gamma^2 - 2\beta\gamma - \beta^2) e^{\frac{2(T-T_c-\frac{\alpha}{2})}{\beta}} + (-2\gamma^2 - 2\beta\gamma - 2\beta^2) e^{\frac{T-T_c-\frac{\alpha}{2}}{\beta}} - \beta^2 \right) e^{\frac{T-T_c+\frac{\alpha}{2}}{\gamma}} \\ &+ (\gamma^2 - 2\beta\gamma + \beta^2) e^{\frac{2(T-T_c-\frac{\alpha}{2})}{\beta}} + (-\gamma^2 - 2\beta\gamma + 2\beta^2) e^{\frac{T-T_c-\frac{\alpha}{2}}{\beta}} + \beta^2. \\ Denominator &= \beta^2\gamma^2 \left(e^{\frac{T-T_c-\frac{\alpha}{2}}{\beta}} + 1 \right)^3 \left(e^{\frac{T-T_c+\frac{\alpha}{2}}{\gamma}} + 1 \right)^3. \end{aligned}$$

For instance, the method is now applied to the VO_i defect, found after irradiation of a p-type MCz diode with 188 MeV protons and $\phi_{neq}=7 \cdot 10^{13} \text{ cm}^{-2}$. The VO_i concentration is $3.38 \cdot 10^{12} \text{ cm}^{-3}$ resulting from a peak area $A_{peak}=1353 \text{ C}$. As it can be noticed in fig. E.1, the largest possible absolute value of the second derivative is 14.95. Entering in eq. E.2 the obtained values leads to a maximum error of 1% on the obtained concentration for the VO_i defect.

Larger uncertainties up to 6% are found for the dominant defects soon after irradiations (i.e. those belonging to the V_n group), or the E(30K) and H(40K) defects which are the dominant ones after annealing of 60 min at 80°C.

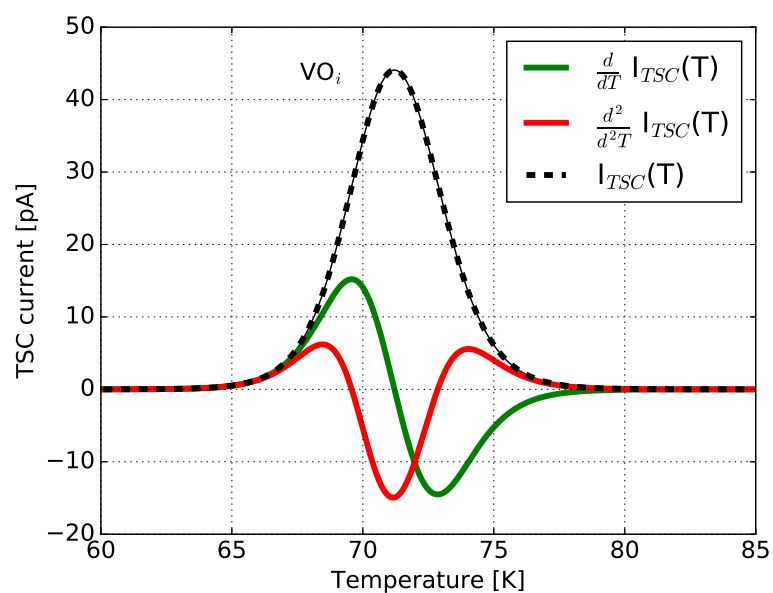


Figure E.1: First and second derivative applied to the fitting function $I_{TSC}(T)$ for the VO_i peak, in a p-type MCz diode irradiated with 188 MeV protons and $\phi_{neq}=7 \cdot 10^{13} \text{ cm}^{-2}$.



TCAD steering file

The TCAD version 2012.06 is used for running `sdevice` and `inspect`, while the more recent version 2016.03 is used for `svisual`. In the calculations, the dielectric constant for silicon is $\epsilon=11.9$; the thermal velocity is already declared in eq. 7.9. The lifetime of electrons and holes are 5 ns and 2.5 ns, respectively. Hereby the TCAD steering file (`diode_CV_des.cmd`) is reported, as input file for simulations of IV and CV characteristics in the presence of (six) bulk defects (see Traps section).

```
Device diode {
File {* input files
Grid = "diode_msh.tdr"
Doping = "diode_msh.tdr"
Parameter = "Silicon.par"
Plot = "diode_CV_des.dat"
Current = "diode_CV_des.plt"}

Electrode {
{Name = "p-side" voltage = 0.0 Material = "Aluminum"}
{Name = "n-side" voltage = 0.0 Material = "Aluminum" }}

Physics {
    areafactor = 2.5e7
    Temperature = 293.15
    Fermi
    Mobility (DopingDependence
              HighFieldSaturation)
```

```

    Recombination (
      SRH (DopingDependence
          TempDependence
          ElectricField (Lifetime=Hurkx DensityCorrection=none))
      eAvalanche (vanOverstraeten)
      hAvalanche (vanOverstraeten))
      EffectiveIntrinsicDensity (Slotboom)
    )

    Physics (material="Silicon")
    {
      Traps(
    * DA
      (Acceptor Level fromCondBand EnergyMid=0.525
      Conc=6e13 eXsection=1e-14 hXsection=1e-14)
    * DD
      (Donor Level fromValBand EnergyMid=0.48
      Conc=5e13 eXsection=3.3e-16 hXsection=3.99e-15)
    * E30K
      (Donor Level EnergyMid=0.1 fromCondBand
      Conc=4.464e12 eXsection=1.276e-14 hXsection=1.276e-15)
    * H152K
      (Acceptor Level EnergyMid=0.42 fromValBand
      Conc=3.62e12 eXsection=1.768e-15 hXsection=1.768e-14
      Tunneling(Hurkx))
    * BiOi
      (Donor Level EnergyMid=0.23 fromCondBand
      Conc=0.84e12 eXsection=1.37e-16 hXsection=1.37e-17)
    * V3
      (Acceptor Level EnergyMid=0.46 fromCondBand
      Conc=11.35e12 eXsection=1.104e-15 hXsection=1.606e-13
      Tunneling(Hurkx))
    )}

    Plot {ElectricField/Vector Potential SpaceCharge
      Doping DonorConcentration AcceptorConcentration
      eLifetime hLifetime
    *--Traps
      TotalTrapConcentration }
    CurrentPlot {
      TrapOccupation (Average(Everywhere))}

```

```

} * end of diode def.
File {
Output = "diode_CV"
ACExtract = "diode_CV"}
System {
  diode sample ( "p-side"=cp "n-side"=cn)
  Vsource_pset vn (cn 0) {dc=0}
  Vsource_pset vp (cp 0) {dc=0}}
Math {
  Method = Blocked
  SubMethod = Pardiso
  ACMethod = Blocked
  ACSubMethod = Pardiso
  Number_of_Threads = 8
  Derivatives
  AvalDerivatives
  RelErrControl
  Digits=7
  ErrRef(electron)=1.0e3
  ErrRef(hole)=1.0e3
  Extrapolate
  Iterations=15
  Notdamped=50
  ExitOnFailure
  MetalConductivity
  BreakCriteria {
    Current ( Contact = "n-side" Absval = 1e-3)}}
Solve {
  * 1) initial solution
  coupled (iterations=100) { Poisson }
  Coupled (iterations=100) { Poisson Electron Hole }
  Save(FilePrefix="diode_init")
  QuasiStationary ( InitialStep=1e-7
    Minstep = 1e-10
    MaxStep = 0.01
    Increment = 1.25
    Decrement = 4
    Goal {Parameter=vp.dc voltage = -400 })
  { ACCoupled ( Iterations=10
    StartFrequency=10000 EndFrequency=10000
    NumberOfPoints=1 Decade

```

```
        Node(cp cn) Exclude(vp vn))
        {Poisson Electron Hole}
Plot (FilePrefix = "diode_"
Time = (Range = (0.0 1) Intervals = 10)
NoOverwrite) }}
```

List of Acronyms

ADC	Analog to Digital Converter
AGILE	A Large Ion Collider Experiment
ALD	Atomic-Layer Deposited
ALICE	A Large Ion Collider Experiment
ATLAS	A Toroidal LHC ApparatuS
ASIC	Application-Specific Integrated Circuit
BIM	Beam Intensity Monitor
BIFM	Beam Induced Fluorescence Monitor
CCC	Clatterbridge Cancer Center
CCD	Charged Coupled Device
CCE	Charge Collection Efficiency
CERN	European Organization for Nuclear Research (Conseil Europeen pour la Recherche Nucleaire)
Cf	Capacitance-frequency
CMS	Compact Muon Solenoid
CT	Computed Tomography
CVf	Capacitance-Voltage-frequency
DAQ	DATA AcQUISITION
DLTS	Deep Level Transient Spectroscopy
DSSD	Double Side Strip Detector
DUT	Device Under Test
ECAL	Electromagnetic CALorimeter
FLUKA	Fluktuierende Kaskade
FWHM	Full Width Half Maximum
GCR	Galactic Cosmic Ray

GR	Generation-Recombination
GLAST	Gamma-ray Large Area Space Telescope
HEP	High Energy Physics
HESS	High Energy Stereoscopic System
HL-LHC	High-Luminosity Large Hadron Collider
IMP	Ionization Profile Monitors
IV	Current-Voltage
KAZ	Kompakt-Zyklotron
KVI	Kernfysisch Versneller Instituut
LED	Light Emitting Diodes
LEP	Large Electron Positron
LGAD	Low-Gain Avalanche Detector
LHC	Large Hadron Collider
LHCb	Large Hadron Collider - Beauty
LID	Light-Induced Degradation
MCNPX	Monte Carlo N-Particle eXtended Code
MIP	Minimum Ionizing Particle
MU	Monitor Unit
MWPC	Multi-Wire Proportional Chamber
NIEL	Non Ionizing Energy Loss
NCV	SC Concentration from CV (from initial rise)
NRT	Norbert-Robinson-Torrens
NTSC	SC Concentration from TSC
PAMELA	a Payload for Antimatter Matter Exploration and Light-nuclei Astrophysics
PECVD	Plasma-Enhanced Chemical Vapor Deposition
pCT	proton Computed Tomography
PMT	Photo-Multiplier Tube
PS	Proton Synchrotron
PSI	Paul Scherrer Institut
QA	Quality Assurance
R&D	Research and Development
RICH	Ring Imaging CHerenkov
RMS	Root Mean Square
ROC	Read Out Circuit
SAA	South Atlantic Anomaly
SCP	Scribe Cleave Passivate
SC	Space Charge
SCR	Space Charge Region
SCSI	Space Charge Sign Inversion
SEE	Single Event Effects
SEL	Single Event Latch-up

SLAC	Stanford Linear Accelerator Center
SLC	SLAC Linear Collider
SM	Standard Model
SNR	Signal to Noise Ratio
SPS	Super Proton Synchrotron
SSD	Single Side Detector
SST	Silicon Strip Tracker
ToT	Time Over Threshold
TRIM	TRajectories of Ions in Matter
TSC	Thermally Stimulated Current
UFSD	Ultra Fast Silicon Detector
VELO	VERtex LOCator
VLSI	Very-Large-Scale Integration
WEPL	Water-Equivalent Path Length
WET	Water Equivalent Thickness
ZAG	Zyklotron AG

Bibliography

- [1] G. Lutz. *Semiconductor radiation detectors*. Springer, Berlin, 2009.
- [2] J. P. Shimura. *Physics of semiconductor devices*. Kluwer Academic publishers, 2002.
- [3] G. E. Moore. Cramming more components onto integrated circuits. *Electronics*, 14:114–117, 1965.
- [4] G. E. Moore. Progress in digital integrated electronics. *IEEE technical international digest*, pages 11–13, 1975.
- [5] R. Nave. Abundances of the elements in the Earth’s crust, Georgia State University, 2016.
- [6] K. Abraham et al. Variation of stable silicon isotopes: analytical developments and applications in Precambrian geochemistry, Mainz University Thesis, 2010.
- [7] G. Faure and T. M. Mensing. *Isotopes: principles and applications*. Wiley, 2005.
- [8] C. C. Hu. *Modern semiconductor devices for integrated circuits*. Prentice Hall, 2010.
- [9] S. M. Sze. *Physics of semiconductor devices*. John Wiley and Sons, 1985.
- [10] F. Shimura. *Semiconductor silicon crystal technology*. Elsevier, 2012.

- [11] N. W. Ashcroft and D. N. Mermin. Solid state physics, HRW international editions, 1963.
- [12] D. A. Neamen. *Semiconductor physics and devices*. Mc Graw Hill, University of New Mexico, 2003.
- [13] Microelectronics I lecture notes, Faculty of Electrical Engineering, University Technology Malaysia, 2016.
- [14] M. Podesta. *Understanding the properties of matter*. Taylor and Francis, 2002.
- [15] F. Hartmann. *Evolution of silicon sensor technology in particle physics*. Springer, Berlin Heidelberg, 2009.
- [16] V. Alex et al. Temperature dependence of the indirect energy gap in crystalline silicon. *J. Appl. Phys.*, 79(9):6943–6946, 1996.
- [17] M. Moll. Radiation damage in silicon particle detectors - microscopic defects and macroscopic properties, DESY-THESIS-1999-040, 1999.
- [18] A. Peisert. *Silicon microstrip detector, Instrumentation in High-Energy Physics*. World Scientific, 1992.
- [19] D. Bortoletto. How and why silicon sensors are becoming more and more intelligent? *Journ. Instr.*, 10(08), 2015.
- [20] H. Spieler. *Semiconductor detector systems*. Oxford University press, 2005.
- [21] H. F. W. Sadrozinski. Application of silicon detectors, Presentation for the IEEE 2000 Conference, 2000.
- [22] <http://www.pravda.uk.com/index.php/78-pgeneral/71-phone>, 2016.
- [23] S. Weinberg et al. A model for leptons. *Phys. Rev. Lett.* , 19(21), pages 1264–1266, 1967.
- [24] A. Salam et al. Elementary Particle Physics: Relativistic Groups and Analyticity. *Eighth Nobel Symposium*, page 367, 1968.
- [25] J. Kemmer. Fabrication of a low-noise silicon radiation detector by the planar process. *Nucl. Instr. Meth. Phys.*, 169:499–502, 1980.

- [26] G. Barbiellini. Application of silicon detector technology to the space laboratory experiment. *Proceedings of Physics and Astrophysics in the space station era, Venice*, 1987.
- [27] A. Chen et al. Population studies: prospects for AGILE and GLAST. *X-ray and gamma ray astrophysics of galactic sources*, 2004.
- [28] S. Takeda. Double sided silicon strip detector for x-ray imaging, SPIE 2015.
- [29] P. Picozza. PAMELA - A Payload for Antimatter Matter Exploration and Light-nuclei Astrophysics. *Astrop. Phys.*, 27:296–315, 2007.
- [30] <https://directory.eoportal.org/web/eoportal/satellite-missions>, 2016.
- [31] O. Adriani et al. PAMELA mission: heralding a new era in cosmic ray physics. *EPJ Web Conf.*, 71, 2014.
- [32] <http://www.asdc.asi.it/pamela/>, 2016.
- [33] E. G. Stassinopoulos. Forty-year drift and change of the SAA, NASA/TM-2015-217547, 2015.
- [34] E. do Couto e Silva. Space experiments with silicon strip detectors. *SLAC-PUB-8750*, 2001.
- [35] HESS collaboration. Acceleration of PeV protons in the galactic centre - HESS collaboration. *Nature 531*, pages 476–479, 2016.
- [36] S. Yoshida et al. Performance of large area silicon strip sensors for GLAST. *SLAC-PUB-9643*, 2003.
- [37] R. Bailey et al. A silicon strip detector telescope for the measurement of production and decay of charmed particles. *Nucl. Instr. Meth. Phys.*, 226:56–58, 1984.
- [38] R. Bailey et al. A silicon counter telescope to study short-lived particles in high-energy hadronic interactions. *Nucl. Instr. Meth. Phys.*, 205:99–105, 1983.
- [39] J. T. Walker et al. Development of high density readout for silicon strip detectors. *Nucl. Instr. Meth. A*, A226, 1984.
- [40] C. Adolphsen et al. The Mark-II silicon strip vertex detector. *Nucl. Instr. Meth.*, A(313), 1991.

- [41] A. Litke et al. A silicon strip vertex detector for the Mark-II experiment at the SLAC linear collider. *SLAC-PUB-4400 SCIPP87/89*, 1987.
- [42] S. Tkaczyk et al. The CDF silicon vertex detector. *Nucl. Instr. Meth.*, A(342), 1994.
- [43] T. Altonen et al. Operational experience, improvements, and performance of the CDF Run II silicon vertex detector. *arXiv:1605.00778*, 2016.
- [44] ALICE collaboration. The ALICE experiment at the CERN LHC. *Jinst.*, 3:S08002, 2008.
- [45] LHCb collaboration. The LHCb detector at the LHC. *Jinst.*, 3:S08005, 2008.
- [46] ATLAS collaboration. The ATLAS experiment at the CERN LHC. *Jinst.*, 3(08):S08003, 2008.
- [47] CMS collaboration. CMS detector performance and software. *CMS-TDR-008-1*, 2006.
- [48] M. Friedl. The CMS silicon strip tracker and its electronic readout, Vienna University of Technology Thesis, 2001.
- [49] CMS collaboration. The CMS tracker system project. *CMS-TDR-005, CERN-LHCC-98-006*, 1997.
- [50] M. C. Vignali. Silicon sensors for the upgrades of the CMS pixel detector, University of Hamburg thesis, 2015.
- [51] CMS collaboration. Description and performance of track and primary-vertex reconstruction with the CMS tracker. *JINST, vol. 10009*, 2014.
- [52] M. Kroupa et al. A semiconductor radiation imaging pixel detector for space radiation dosimetry. *Life Sciences in Space Research*, pages 69–78, 2015.
- [53] F. Hartmann. Silicon tracking detectors in high-energy physics. *Nucl. Instr. Meth.*, A(666):25–46, 2012.
- [54] M. E. Dinardo. The pixel detector for the cms phase-II upgrade. *Journal of Instrumentation*, 10(04):C04019, 2015.
- [55] <https://twiki.cern.ch/twiki/bin/view/cmspublic/brilrs1d1mevneqattracker>, 2015.

- [56] R. Schulte et al. Design of a proton computed tomography system for applications in proton radiation therapy. *Nucl. Sci. Symposium Conference Record IEEE*, 3, 2003.
- [57] The LCHb VELO group. Radiation damage in the LHCb vertex locator CERN. *LHCb-DP-2012-005*, 2013.
- [58] C. P. Welsch et al. Non-invasive beam profile monitoring, Richmond, VA, USA , 2015.
- [59] H. Bichsel. *Passage of charged particles through matter*. American Institute of Physics Handbook, McGraw-Hill, New York, 1972.
- [60] H. F. -W. Sadrozinski et al. Issues in proton computed tomography. *Nucl. Instr. Meth. A*, pages 275–281, 2003.
- [61] G. Poludniowski et al. Proton radiography and tomography with application to proton therapy. *Br. J. Radiol.*, 88, 2015.
- [62] R. W. Schulte. Conceptual design of a proton computed tomography system for applications in proton radiation therapy. *IEEE Trans. Nucl. Sci.*, page 866, 2004.
- [63] J. M. Garland. Normal-conducting scaling fixed field alternating gradient accelerator for proton therapy. *Phys. Rev. Accel. Beams.*, 18, 2015.
- [64] C. Bopp. Quantitative proton imaging from multiple physics processes: a proof of concept. *Phys. Med. Biol.*, 60, 2015.
- [65] U. Schneider et al. Spatial resolution of proton tomography: methods, initial phase space and object thickness. *Z. Med. Phys.*, 22:100–108, 2012.
- [66] E. Reichwein. <http://ericreichwein.com/research.php>, 2017.
- [67] R. W. Schulte et al. Density resolution of proton computed tomography. *Med. Phys.*, pages 1035–1046, 2005.
- [68] U. Schneider et al. Multiple coulomb scattering and spatial resolution in proton radiography. *Med. Phys.*, 21:1657–1663, 1994.
- [69] A. M. Cormack. Representation of a function by its line integrals with some radiological applications. *J. Appl. Phys.*, pages 2722–2777, 1963.
- [70] V. A. Ba et al. Development of proton computed tomography detectors for application in hadron therapy. *Nucl. Instr. Meth. A*, pages 120–129, 2016.

- [71] M. Yoshida et al. Alumina and silicon oxide/nitride sidewall passivation for p- and n-type sensors. *Nucl. Instr. Meth. A699* , pages 14–17, 2013.
- [72] R. Mori et al. Charge collection measurements on slim-edge microstrip detectors. *SCIPP 12/02*, 2012.
- [73] H. F. -W. Sadrozinski et al. Development of a head scanner for proton CT. *Nucl. Instr. Meth. A (699)*, pages 205–210, 2016.
- [74] P. Wang et al. Proton compute tomography using 1D silicon diode array. *Med. Phys.*, 43(10), 2016.
- [75] I. Randall. Silicon diode array lines up for proton CT, 2016.
- [76] J. F. Ziegler et al. The stopping and range of ions in solids, Pergamon Press, 1985.
- [77] G. W. Simon et al. Energy dependence of proton damage in silicon. *Phys. Rev.*, 129(6):2454–2459, 1963.
- [78] S. Vayrynen. Irradiation of silicon particle detectors with MeV-protons, University of Helsinki Thesis, 2010.
- [79] P. J. Griffin. Detailed description of the derivation of the silicon damage response function, 2016.
- [80] J. Erfle. Irradiation study of different silicon materials for the CMS tracker upgrade, University of Hamburg Thesis, 2014.
- [81] M. Huhtinen. Pion induced displacement damage in silicon devices. *Nucl. Instr. Meth. Phys. Res. A*, 335, 1993.
- [82] G. P. Summers et al. Damage correlations in semiconductors exposed to gamma, electron and proton radiations. *IEEE Trans. Nucl. Sci.*, 40(6), 1993.
- [83] I. Jun et al. Proton nonionizing energy loss (NIEL) for device applications. *IEEE Trans. Nucl. Sci.*, 50(6), 2003.
- [84] M. Guthoff et al. Simulation of beam induced lattice defects of diamond detectors using FLUKA. *Nucl. Instr. Meth. A*, 735:223–228, 2014.
- [85] A. Fasso et al. FLUKA realistic modeling of radiation induced damage. *Nucl. Sci. Tech.*, 2:769–775, 2011.

- [86] I. Jun. Effect of secondary particles on the total dose and the displacement damage in space proton environments. *IEEE Trans. Nucl. Sci.*, 48(1):162–176, 2001.
- [87] M. Huhtinen. Simulation of non-ionizing energy loss and defect formation in silicon. *Nucl. Instr. Meth. Phys. Res. A*, 491(1-2), 2002.
- [88] A. Dierlamm. Proton Irradiation in Karlsruhe, 16th RD50 Workshop, 2010.
- [89] G. Lindstroem et al. Radiation hard silicon detectors-developments by the RD48 (ROSE) collaboration. *Nucl. Instr. Meth. Phys. Res.*, A466, 2001.
- [90] M. J. Norget, M. T. Robinson, I. M. Torrens. A proposed method of calculating displacement dose rates. *Nucl. Eng. Des.*, 33, 1975.
- [91] E. M. Donegani. Calculation of the radiation damage to the MEGAPIE window and other structural components, PSI internal report, 2010.
- [92] R. Wunstorf. Systematische Untersuchungen zur Strahlenresistenz von Silizium-Detektoren fuer die Verwendung von Hochenergie-Experimenten, University of Hamburg thesis, 1992, 1992.
- [93] Y. Shi et al. A numerical study of cluster center formation in neutron-irradiated silicon. *Journ. App. Phys.*, 67(2):1116–1118, 1990.
- [94] F. Hoenniger. Radiation damage in silicon: defect analysis and detector properties, University of Hamburg thesis, 2007.
- [95] A. Junkes. Influence of radiation induced defect clusters on silicon particle detectors, University of Hamburg thesis, 2011.
- [96] I. Pintilie et al. Experimental techniques for defect characterization of highly irradiated materials and structures. *Proceedings to the Vertex conference 2016*, 2016.
- [97] W. Shockley et al. Statistics of the recombinations of holes and electrons. *Phys. Rev. Vol.*, 87(5), 1952.
- [98] Wodean project. Summary Report, 2010.
- [99] P. Bradley. The development of a novel silicon microdosimetry high LET radiation therapy, University of Wollongong Thesis, 2000.
- [100] RD48 collaboration. Irradiated silicon detectors: a relaxation semiconductor analysis, RD48 Technical notes ROSETN982, 1998.

- [101] V. Eremin et al. The origin of double peak electric field distribution in heavily irradiated silicon detectors. *Nucl. Instr. Meth.*, A(476):556–564, 2002.
- [102] G. Kramberger et al. Annealing studies of effective trapping times in silicon detectors. *Nucl. Instr. Meth. A*, 571, 2007.
- [103] H. G. Moser. Silicon detector systems in high energy physics. *Progress in Particle and Nuclear Physics*, 63:186–237, 2009.
- [104] G. P. Gaidar et al. Annealing of radiation induced defects in silicon. *Surf. Eng. and App. Chem.*, 48(1):78–89, 2012.
- [105] CERN RD48 (ROSE) collaboration. Developments of radiation hard silicon detectors by defect engineering. *ROSE*, TN/2000/06, 2000.
- [106] A. Dierlamm. Study on the radiation hardness of silicon sensors, IEKP-KA-THESIS-2003-23, 2003.
- [107] G. Kramberger et al. Impact of annealing of trapping times on charge collection in irradiated silicon detectors. *Nucl. Instr. Meth. A*, 579(2), 2007.
- [108] E. M. Donegani et al. Defect spectroscopy of proton-irradiated thin p-type silicon sensors. *RADECS 2016 Conference proceedings*, pages 323–329, 2016.
- [109] A. Dierlamm. <http://www.ekp.kit.edu/english/264.php>, 2016.
- [110] M. J. van Goethem. Private communication, 2016.
- [111] M. Glaser et al. Dosimetry assessments in the irradiation facilities at the cern-ps accelerator. *Nucl. Sci. IEEE Transactions*, 53(4):2016–2022, 2006.
- [112] M. Glaser et al. New irradiation zones at the CERN-PS. *Nucl. Instr. Meth. in Phys. Res. A*, 426:72–77, 1999.
- [113] <http://irradiation.web.cern.ch/irradiation/Dosimeter/Sets-2011.htm>, 2016.
- [114] B. Tohermes. Investigation of edge effects of radiation damaged silicon pad diodes, University of Hamburg thesis, 2016.
- [115] Hamamatsu HPK, <http://www.hamamatsu.com>, 2016.
- [116] M. Hufschmidt. Data analysis of high precision capacitance measurements of large area pn-diodes, University of Hamburg Thesis, 2016.

- [117] A. Junkes et al. Energy dependence of proton radiation damage in sensors. *2014 IEEE Nuclear Science Symposium and Medical Imaging Conference (NSS/MIC)*, 2014.
- [118] Agilent E4980 LRC manual, <http://www.agilent.com>, 2016.
- [119] L. Forbes et al. On the determination of deep level center energy and concentration by TSC measured using reversed-biased p-n junctions. *Solid State Electronics*, 14:182–183, 1971.
- [120] M. G. Buehler. Impurity centers in pn junctions determined from shifts in the TSC and capacitance response with heating rate. *Solid State Electronics*, 15:69–79, 1995.
- [121] A. Baldini et al. TSC spectroscopy: experimental techniques for the investigation of silicon detectors. *Rev. Sci. Instr.*, 64(4):932–936, 1992.
- [122] C. J. Li et al. Development of current-based microscopic defect analysis methods and associated optical filling techniques for the investigation on highly irradiated high resistivity silicon detectors. *Nucl. Instr. Meth. in Phys. Res. A*, 364:108–117, 1995.
- [123] H. Feick et al. Analysis of TSC spectra measured on silicon pad detectors after exposure to fast neutrons. *Nucl. Instr. Meth. in Phys. Res. A*, 388:323–329, 1997.
- [124] H. Feick. Radiation tolerance of silicon particle detectors for high-energy physics experiments, DESY-THESIS-1997, 1997.
- [125] G. A. Hurkx et al. A new recombination model for device simulation including tunneling. *Nucl. Sci. IEEE Transactions*, 39:331–338, 1992.
- [126] C. Neubueser. Impact of irradiations by protons with different energies on silicon sensors, University of Hamburg thesis, 2013.
- [127] M. McPherson et al. Fermi level pinning in irradiated silicon considered as a relaxation-like semiconductor. *Phys. B. (344)* 52-57, 2004.
- [128] R. Couderc et al. Reassessment of the intrinsic carrier density temperature dependence in crystalline silicon. *Journ. App. Phys.*, 2014.
- [129] M. Hufschmidt et al. The influence of edge effects on the determination of the doping profile of silicon pad diodes. *Nucl. Instr. Meth.*, A(313), 2016.

- [130] W. G. Oldham et al. Admittance of pn junction containing traps. *Sol. St. Electr.*, 15, 1972.
- [131] E. Schibli et al. Effects of deep impurities on n⁺p junction reverse-biased small-signal capacitance. *Sol. St. Electr.*, 11, 1968.
- [132] M. McPherson et al. Capacitive effects in neutron-irradiated silicon diodes. *Nucl. Instr. Meth. A* , 488 , 2002.
- [133] B. K. Jones et al. Negative capacitance effects in semiconductor diodes. *Sol. St. Comm.*, 107(2):47–50, 1998.
- [134] N. Holonyak et al. Double injection with negative resistance in semi-insulators. *Phys. Rev. Lett.* 8(11), 1962.
- [135] I. Pintilie et al. Radiation-induced point- and cluster-related defects with strong impact on damage properties of silicon detectors. *Nucl. Instr. Meth. A* (52) 611, 2009.
- [136] R. Radu et al. Investigation of point and extended defects in electron irradiated silicon - Dependence on the particle energy. *Journ. Appl. Phys.* 117, 2011.
- [137] M. Yamaguchi et al. Deep level analysis of radiation-induced defects in Si crystals and solar cells. *J. Appl. Phys.* 86, 1999.
- [138] L. F. Makarenko et al. Formation and annealing of boron-oxygen defects in irradiated silicon and silicon-germanium n-p structures. *AIP Conference Proceedings* 1583 (123), 2014.
- [139] G. Pellegrini et al. Technology developments and first measurements of Low Gain Avalanche Detectors (LGAD) for high energy physics applications. *Nucl. Instr. Meth. A*, 765, 2014.
- [140] L. I. Murin et al. Local vibrational modes of interstitial boron-interstitial oxygen complex in silicon. *Phys. Stat. Sol. A*(213), 2016.
- [141] K. Koch. Strahlenhaerte von epitaktischen, Floatzone und Magnetic Czochralski-Siliziumdioden nach Neutronenbestrahlung, University of Hamburg, Diploma Thesis, 2007.
- [142] V. P. Markevich et al. Trivacancy and trivacancy-oxygen complexes in silicon: experiments and ab initio modeling. *Phys. Rev. B* 80, 235207, 2009.

- [143] C. H. Henry et al. Non radiative capture and recombination by multi-phonon emission in GaAs and GaP. *Phys. Rev. B* 15(2) 989, 1977.
- [144] A. Scheinemann et al. A comprehensive study of the impact of dislocation loops on leakage currents in Si shallow junction devices. *Phys. Stat. Sol. A*, 211, 2014.
- [145] R. Klanner. Private communication, 2016.
- [146] K. G. McKay et al. Lifetime in proton irradiated silicon. *J. App. Phys.*, 79, 2015.
- [147] K. Gill et al. Bulk damage effects in irradiated silicon detectors due to clustered divacancies. *Journ. Appl. Phys.*, 82(126):296–315, 1997.
- [148] E. Borchini et al. Temperature and frequency dependence of the capacitance of heavily irradiated silicon diodes. *Sol. Stat. Electr.*, 42(11), 1998.
- [149] R. Dalal et al. Simulation of irradiated si detectors. *PoS (Vertex2014)*, 030, 2014.
- [150] M. A. Green. Intrinsic concentration, effective densities of states, and effective mass in silicon. *Journ. Appl. Phys.*, page 2944, 1990.
- [151] D. B. M. Klaasen et al. A new recombination model for device simulation including tunneling. *IEEE Trans. El. Dev.*, 39(2):331–338, 1992.
- [152] H. C. de Graaff et al. A new analytical diode model including tunneling and avalanche breakdown. *IEEE Trans. El. Dev.*, 39(9):2090–2098, 1992.
- [153] A. Schenk et al. Rigorous theory and simplified model of band-to-band tunneling in silicon. *Sol. Stat. El.*, 36(1):19–34, 1993.
- [154] Synopsys. Sentaurus device user guide (version D-2010.03), 2010.
- [155] M. J. J. Theunissen et al. Analysis of the soft reverse characteristics of n⁺p source drain diodes. *Sol. Stat. El.*, 28(5):417–424, 1985.
- [156] A. Saadouni et al. Modelling of semiconductor diodes made of high defect concentration, irradiated, high resistivity and semi-insulating material: the capacitance-voltage characteristics. *Sol. St. Electr.*, 50, 2006.
- [157] C. Betancourt et al. Analysis of deep level parameters in irradiated silicon detectors. *Nucl. Instr. Meth.*, 612, 2010.

- [158] O. Krasel et al. Electric fields in irradiated silicon pad detectors, 4th RD50 Workshop, CERN, 2004.
- [159] U. Biggeri. A comparative study of heavily irradiated silicon and non irradiated Si LEC GaAs detectors. *IEEE Nuclear Science Symposium*, 1997.
- [160] E. M. Donegani et al. Study of point- and cluster-defects in radiation-damaged silicon. *RADECS 2017 Conference proceedings*, 2017.
- [161] T. Poehlsen. Charge losses in silicon sensors and electric-field studies at the Si-SiO₂ interface, University of Hamburg thesis, 2013.
- [162] P. Varshni. Temperature dependence of the energy gap in semiconductors. *Physica*, 34, 1967.
- [163] E. Bender. Derivation of the error bounds, Math 20B Fall 2016, Calculus for science and engineering, UC San Diego, 2016.

Acknowledgements



*Erika Garutti, Eckhart Fretwurst, and the Defense Committee.
The UHH Detector Lab, with special thanks to:
Heike Biskop, Peter Buhmann, Reiner Peter Feller, Magdalene Hack,
Alexandra Junkes, Robert Klanner, Stephan Martens, Michael Matysek,
Gundula Serbser, Jörn Schwandt, Jory Sonneveld, Georg Steinbrück.*

*Annina Anzani, Gabriella Anzani, Benzi Anna, Benzi Loris, Bernaschina Carlo,
Massimo Caccia, Marco Confortola, CPG-1937, Chiara Donegani, Maria Grazia
Donegani, Paolo Donegani, Dieter Haidt, Felice Rainoldi, Luca Zanin.*



Eidesstattliche Versicherung/Declaration on oath

Hiermit versichere ich an Eides statt, die vorliegende Dissertationsschrift selbst verfasst und keine anderen als die angegebenen Hilfsmittel und Quellen benutzt zu haben.

Die eingereichte schriftliche Fassung entspricht der auf dem elektronischen Speichermedium.

Die Dissertation wurde in der vorgelegten oder einer ähnlichen Form nicht schon einmal in einem früheren Promotionsverfahren angenommen oder als ungenügend beurteilt.

Hamburg, den

Unterschrift

Publications related to this dissertation:

1. *E. M. Donegani et al.* Study of point- and cluster-related defects in radiation-damaged silicon, Proceedings to the RADiations Effects on Components and Systems “RADECS” conference, 10/2017
2. *E. M. Donegani et al.* Defect spectroscopy of proton-irradiated thin p-type silicon sensors, Proceedings to the RADiations Effects on Components and Systems “RADECS” conference, 9/2016
3. *A. Junkes et al.* Energy dependence of proton radiation damage in Si-sensors, Proceedings to the 2014 IEEE Nuclear Science Symposium and Medical Imaging Conference “NSS/MIC”, 11/2014

